UNIVERSITY OF SOUTHAMPTON

Faculty of Engineering and Physical Sciences
School of Physics and Astronomy

Strongly Coupled Physics from the Gauge Gravity Duality

by

Matthew James Russell

A thesis for the degree of
Doctor of Philosophy

December 2021

University of Southampton

Abstract

Faculty of Engineering and Physical Sciences
School of Physics and Astronomy

Doctor of Philosophy

Strongly Coupled Physics from the Gauge Gravity Duality

by Matthew James Russell

The gauge/gravity duality links the fields of string theory and quantum field theory. The duality states that systems that are strongly coupled in one theory are weakly coupled in the other. Thus, intractable problems in strongly coupled physics can instead be calculated using the gravity side of the duality. In this thesis we study three areas of strongly coupled physics: quantum chromodynamics, condensed matter theory and (non)-hydrodynamic physics.

First, we study quantum chromodynamics (QCD), where we attempt to gain insight into the temperature chemical potential QCD phase diagram by extending an exactly soluble holographic model into imaginary chemical potential. We then look for structure at small real μ and imaginary μ that help to reconstruct the large real μ phase diagram. We find that the phase diagram has boundaries of regions where metastable vacua exist and these boundaries, as well as the phase boundaries, converge at the holographic QCD critical point.

We then move on to condensed matter theory where we study a top-down holographic Weyl semi-metal where we find the defining characteristic of a Weyl semi-metal: a quantum phase transition from a topological state with non-zero anomalous Hall conductivity to a trivial insulator. Unlike previous models, we find that the anomalous Hall conductivity is independent of model parameters at zero temperature and is also first order. At non-zero temperature the transition remains first order, and the anomalous Hall conductivity acquires non-trivial dependence on model parameters.

Finally, we study the transition between non-hydrodynamic modes and hydrodynamic modes in holographic strange metals, where the microscopic description of the collective excitations is unknown but departs from the standard weakly-coupled Fermi liquid theory. We find that by including translational symmetry breaking the propagating non-hydrodynamic modes are damped, until at sufficiently large symmetry breaking parameters the mode transitions to the purely imaginary diffusive hydrodynamic mode.

Contents

List of Figures

List of Tables

Declaration of Authorship

I declare that this thesis and the work presented in it is my own and has been generated by me as the result of my own original research.

I confirm that:

1. This work was done wholly or mainly while in candidature for a research degree at this University;
2. Where any part of this thesis has previously been submitted for a degree or any other qualification at this University or any other institution, this has been clearly stated;
3. Where I have consulted the published work of others, this is always clearly attributed;
4. Where I have quoted from the work of others, the source is always given. With the exception of such quotations, this thesis is entirely my own work;
5. I have acknowledged all main sources of help;
6. Where the thesis is based on work done by myself jointly with others, I have made clear exactly what was done by others and what I have contributed myself;
7. Parts of this work have been published as:

Signed:..... Date:.....

Acknowledgements

I would first like to thank my supervisors Nick Evans and Andy O'Bannon who have helped guide and shape the work in this thesis, as well as impart with decades of experience. I am also grateful to Ronnie Rodgers for his patience and help throughout my PhD, as well as collaborations with Kazem Fadafan.

Southampton would not have been as nearly as fun to live in over the past four years without my fellow Phd students, including Lorenzo Zanisi, Adam Forster, Billy Ford, Michele Santagata, Sami Rawash, Hao Fu, Ross Glew, Alessandra Costantino and many more.

Finally, I would like to give thanks to my parents and family who have always supported everything I do.

Part I

Introduction

Chapter 1

Motivation

From humanities earliest foray into the study of nature we have always been lured to an irresistible question - what is the fundamental *thing* that makes up all else? In every century of scientific advancement there has always been opposing ideas and opinions, from the pre-Hellenistic philosophers of whether it is changing or unchanging, to modern day mathematicians and theoretical physicists who squabble of string theory, loop gravity and quantum field theory. There may simply be no answer, something that should be locked away in a vault of metaphysics...but it won't stop people pondering - what is our reality?

Some first attempts at defining the Fundamental was with the philosophers of the Milesian school over two and half thousand years ago. They began with Thales, who asserted that everything was made of water. His successor Anaximander said hold on a minute - it isn't water, it's the apeiron! a concept of infinity or something indefinite, and then came Anaximenes who thought it to be of air. After the Militians came the Ionian Xenophanes (earth and water), and Heraclitus (fire).

Heraclitus was also known for another idea, one that to this day is still of great interest - he thought everything was in a state of flux - 'you cannot step twice into the same river for fresh waters are ever flowing in upon you'. His Fundamental fire was always changing: 'all things come out of the one, and the one out of all things.' This goes straight to the heart of the question of what is our reality. Is it changing, or is it unchanging? At first this might seem bizarre, of course everything is changing, but what about at the level of the Fundamental, is it in motion or is it fixed? What is its motion relative to?

Paramenides went against Heraclitus and coined the concept of eternity, that nothing changes. What we see as many different things is only an illusion of our senses, that base reality is indivisible and infinite. The different substances making up the Fundamental were finally combined by Empedocles who said that it was made from the four classical elements of earth, fire, water and air.

A middle ground was taken up by the atomists near the end of the rein of Athens; first, in a way, by Anaxagoras who asserted that everything is divisible to the minute, and second by the original atomists Leucippus and Democritus. They lived

around the fifth century B.C prior to the Peloponnesian War that annihalited the power of Athens and with it the city states that had been so important in the rise of philosophical thought. Their theories were remarkable and of curious interest to any modern physicist in that they invented the concept that everything was made of indivisible, indestructible atoms that were composed of mostly empty space. Their atoms came in different shapes and sizes and were constantly in motion, however they were deterministic rather than probabilistic. Their atomic theory is balanced between the changing and unchanging - changing in that the atoms are always in flux, unchanging in that they are indestructible.

The pre-Hellinistic philosophers had started a process of deductive reasoning into one of the most profound questions of humanity. They were also arguably the most scientific of the whole period of antiquity, and after the fall of the city-states and the rise of Alexander's empire, the subsequent baseness of the Roman empire and the beginning of the Christian dark ages, the progress of science, the progress of the search of the Fundamental, stalled[1].

It is testament to how advanced the Grecian civilisation was that it was about two thousand years later that the idea that the Fundamental was made up of atoms was again taken seriously with chemist and physicist John Dalton and his atomic theory. He, like the atomists, theorised that elements are made up of tiny particles, that atoms of a given element are identical and that they cannot be created or destroyed nor made smaller. The difference between the two eras was that mathematical modelling and scientific experiments had become far more advanced, and with the invention of the kinetic theory of gases the idea that our world was made up of atoms and molecules was accepted by the scientific community.

But the quest for the Fundamental was not finished.

Next came Thomson's electron and Rutherford's nucleus, and at the beginning of the twentieth century a paradigm shift started to emerge. Planck and Einstein discretised light energy into quanta and Bohr incorporated it into an early theory of quantum physics. Shortly after, the fully fledged quantum mechanics was devised by de Broglie, Schrodinger, Born and co. that among other things showed an early and intriguing example of duality – that the fundamental quanta could be described as particle or waves, known as the wave-particle duality. Whatever we thought was making up our reality, it was proving to be stranger and more counter-intuitive than we imagined – it was probabilistic, not deterministic.

Quantum mechanics was combined with special relativity utilising the framework of classical field theory into the quantum theory of fields – a framework that birthed the standard model: the current best description of what our reality is and how it interacts. The standard model predicts that the Fundamental is made up of 17 particles obeying various symmetries. It combines the fundamental forces of

[1] There were other advancements of note in Plato's mathematical Forms and in Hellenistic Alexandria in Euclid and others, but not much in the way of the search of the nature of reality (except perhaps for the Arabic alchemists and the Islamic Golden Age) and this introduction is already long enough.

electromagnetism, the weak nuclear force and the strong nuclear force into six quarks (up, down, charm, strange, top, bottom), six leptons (electron, muon, tau plus their neutrinos), four gauge bosons (gluon, photon, W and Z boson) and one scalar boson (Higgs).

Surely that was it – the fundamental particles that make up reality, joining together and falling apart...but a look at history would say that there always seems to be more to discover – were there issues with the standard model? Or is it complete? Of course, there are problems.

For a start there isn't a mention of gravity, either classical general relativity or quantum gravity. And what of neutrino oscillations, or the hierarchy problem? There are hints of discrepancies with experiments such as in the $g-2$ calculation [2]and B meson decay [3]. Not to forget that calculations using QFT are notoriously difficult and can often only be performed using perturbation theory at weak coupling – what happens at strong coupling? There is lots of interesting phenomena at strong coupling, such as the QCD phase diagram and exotic materials in condensed matter physics – how are we to describe them if the calculations are intractable? Perhaps, when we are far into the strong coupling regime, we are being told by nature that we are simply using the wrong theory and that there is a better solution.

The potential answer to some of the above questions comes as the foundation of this thesis. When the standard model was being built a theory to describe the quarks and gluons was required, one such idea, before quantum chromodynamics was adopted, was string theory. The Fundamental here is not of point particles but of strings and their higher-dimensional branes. Something else appeared, notably a massless spin-2 particle: the graviton – instead of finding a theory of quarks and gluons, a quantum theory of gravity was discovered! Was this string theory a theory of everything? Could it be used to describe everything in the universe?

A difficulty appeared (surprise!) – there wasn't just one string theory, but 5 encapsulated in another theory: M-theory. Moreover, string theory was right at the pinnacle of the energy scale. That is, it described physics at the smallest known distances, so how exactly do we go from strings down the energy ladder (and up the distance ladder) to get to the particles described in the standard model? It turns out there are a humongous amount of theories that the string theory could describe at the low energy level, a problem called the swampland – from one string theory model, many theories can arise at the standard model level. Further, string theory calculations are just as difficult, if not more so than QFT calculations. So although we have found a (consistent) theory of quantum gravity, what on earth do we do with it? We can't test it, and we struggle to relate it to the standard model even in theory. It looked like string theory might be an interesting discovery but perhaps of little use to particle physicists.

Nevertheless, hints appeared as to how to relate string theory to quantum field theory. The theories that make up the standard model are gauge theories with a

symmetry group $SU(N)$ and 't Hooft showed that in the large N limit, and using his 'double-line notation' [4], that the large N gauge theory had striking similarities with string theory. The holographic principle was taken up by Susskind [5], the idea that all the information of the universe could be held in a boundary of one less dimension (like a black hole's entropy). These ideas were combined by Maldecena in 1997 in the first example of the gauge/gravity duality – a d+1 dimensional string theory is dual to a d dimensional gauge theory [6].

Therefore there is a route to connect the physics of the standard model with the physics of string theory via the duality. Moreover, the duality is a strong/weak duality meaning that if one of the theories is strongly coupled, the other is weakly coupled – hence it is possible that the intractable calculations of strongly coupled QFT can instead be performed in the dual string theory and pro bono interpreting that physics in a geometrical way.

There are unfortunately certain issues with the gauge/gravity duality that will be fleshed out in later sections, for now we simple state a few. One is that the duality is only conjectured, that is there is no mathematical robust proof. However there is enough evidence to secure its claim to reality in academic circles. Another is a question of what gauge theory do we have exactly? It is not that of the standard model, nevertheless it is somewhat relatable and there are ways to make it more so.

Finally, we can come to the goal of this thesis: we investigate strongly coupled physics using the gauge/gravity duality. In section II we outline the formalism of the gauge/gravity duality. In part II we have new research. In section III we take a look at the phase diagram of QCD. At large chemical potential and large temperature QCD is in a state called the quark-gluon plasma where the quarks and gluons are deconfined and are (approximately) chiral symmetric [7]. In this regime the strong coupling constant is small and perturbation theory can be used. At low temperature and small chemical potential the quarks and gluons are instead in a confined state, bound together into baryons and mesons and chiral symmetry is completely broken. Therefore there is a phase transition in the $T - \mu$ plane of QCD. There is however an issue. The theory for the mesons and baryons, chiral perturbation theory, does not extend to the location of the phase transition, nor does perturbative QCD due to the coupling becoming strong. There is no known theory that can accurately predict the full phase transition of QCD. The best that can be achieved is using lattice QCD but due to the sign problem it cannot extend far into the real chemical potential axis [8]. There is however no such problem with lattice QCD working at imaginary chemical potential and the results can be analytically continued into a small region of the real chemical potential – such calculations have led to the discovery that at zero chemical potential the QCD phase transition is a cross-over. Noting that at zero temperature the chemical phase transition is expected to be first order, there must be a critical end point to the phase transition[9]. It is one of the outstanding questions of QCD to predict this end point, as well as to work out when and where confinement and chiral

symmetry breaking take place – do they occur at the same time, or separately? A potential answer to these questions was addressed using the gauge-gravity duality that, as mentioned above, can tackle difficult strongly coupled problems. There have been many conjectured phase diagrams using the duality all utilising different set ups and hence with different results. What we aim to do instead is try to gleam universal behaviour that could be of use in searches for the phase transition. We do this by extending previous duality phase diagrams into the imaginary plane, motivated by lattice simulations. Is there information in the imaginary plane that could be used to predict what is happening in the real plane? We find that the solutions only extend so far into the imaginary plane before instabilities arise (potentially related to the Roberge-Weiss transition) – however it is enough for our purpose as we discover that the phase transition lines are surrounded by bubbles of local minimums of the action. These local solutions extend out from the phase transition lines and can be used to track the locations of critical points. That is, by finding the local minimums on the imaginary side of the phase diagram, the locations and phase content of the real side can be approximated. It would be of great interest if such minimums can be found using experiments or lattice QCD.

In section IV we switch gears away from QCD and into condensed matter physics. Almost one hundred years ago Dirac published his work describing spin-1/2 particles. It was quickly followed up by Hermann Weyl in 1928 with a simplified massless framework that predicted the existence of Weyl particles. It wasn't until 2015 until these particles were actually discovered in tantalum arsenide [10, 11, 12, 13]. This opened up the field of Weyl semi-metals. Weyl semi-metals have numerous interesting properties. They are topological, meaning that the excited states are protected from deformations. They also have an anomalous Hall conductivity that can be thought of as an order parameter – it is zero in the trivial insulating phase (gapped electron bands) and non-zero in the Weyl semi-metal phase (electron bands touching forming Weyl points where the Weyl semi-metal excitations are found). The usual low energy theory that describes these particles is at weak coupling, a question is then what happens at strong coupling? Does the Weyl semi-metal phase still exist? Do its properties change? Can it be realised in experiment? Some of these questions have been addressed using gauge-gravity Weyl semi-metal models [14, 15], and we add to these discussions with a new top down Weyl semi-metal with probe branes that is formed using an axial gauge field. Not only do we find a Weyl semi-metal state, indicated by the presence of an anomalous Hall conductivity, but we also find that the transition is first order, contrary to previous models. We also find that at low temperature the anomalous Hall conductivity is independent of certain parameters of the theory, and that there is strong evidence of a sound mode in the spectrum of fluctuations. It would be of great interest to construct strongly coupled Weyl semi-metals in an experiment to test our predictions and those coming from the gauge-gravity duality in general.

Finally, in section VI we study the hydrodynamics of probe brane systems. In the standard probe brane set up there is a propagating mode called holographic zero sound [16], sharing the name of the zero sound mode found in experiments and theoretically modelled by Landau – a mode that exists at zero temperature [17, 18]. Zero sound is not a density wave but instead it is a fluctuation of the Fermi-surface. Although probe brane systems do not exhibit Fermi surfaces the mode found was dubbed Holographic zero sound as it is also apparent at zero temperature. We add an important ingredient in modelling real systems, namely that of translational symmetry breaking, or in more physics language in adding impurities to the system. We do this via incorporating various previous methods such as massive gravity, Stueckelberg fields and three-form fields into one model with symmetry breaking parameters [19, 20, 21, 22]. We find that the system does indeed act as expected. Increasing the symmetry breaking causes the holographic zero sound mode to stop propagating and transition to a diffusive mode. We show this in two ways, first via numerics and second by analytical results. We also comment on the effect TSB has on the AC and DC conductivities.

Before leaving this motivation section it is worth bringing the discussion back to the overall goal. We discussed philosophers, mystics, theologians, physicists – all asking the same question, albeit with different methods – what is the Fundamental of reality? Only the later can be trusted , formed outside of the environment and society whims that it finds itself in, whether of plenty or little, war or peace, only in science do we find true progress. And although our theories have become more complex and imaginative – a creativity bounded by the laws of physics and maths – the basic underlying questions and principle has not changed. Perhaps, through the duality of string theory and field theory, we take a step closer to answering this question, and perhaps by linking the theoretical predictions of the gauge-gravity duality to experiments we can take another.

In this thesis we start at the end of the road with the penultimate and ultimate in quantum field theory and string theory and the miraculous discovery that in fact they can be seen as two sides of the same coin.

Chapter 2

Introduction to the Gauge-Gravity Duality

A duality is the concept that two seemingly disparate things are actually exactly the same. In physics, this means that two theories can be used to describe the same system. One of most well known is the particle-wave duality outlined in the motivation section - that the constituent quanta of the universe can be modelled either as particles or waves. This isn't simply the statement that particles can be approximated or viewed as waves, the duality states that the quanta as waves is a complete and rigorous way to define the quanta and its dynamics. By discovering and understanding such dualities concepts that might be difficult to comprehend or calculate by viewing the quanta as particles might become clear or tractable using the other theory. For example by viewing the quanta as waves we can use all the theoretical understanding of wave physics - but now applied to the quanta, such as the Heisenberg uncertainty principle being a special case of the bandwidth theorem, or ultilising reflection and transmission properties of waves off boundaries.

Similarly, there is the Montonen-Olive duality [23], or electric-magnetic duality, that can be seen in Maxwell's equations when electric sources are neglected under the change of $\mathbf{E} \to \mathbf{B}$ and $\mathbf{B} \to -\mathbf{E}$, or when magnetic sources are introduced. In the later case something else of interest occurs, namely that the duality is a strong-weak duality (or S-duality) - the electric coupling constant is inversely proportional to the magnetic coupling constant. For now, magnetic monopoles remain undiscovered; however in mathematical models that are used for their high degree of symmetry we can realise the electric-magnetic duality [24].

The gauge-gravity duality, like the Montonen-Olive duality, is a strong-weak duality, but it also exhibits holography: the theories have a different number of dimensions. Concretely, the gauge-gravity duality maps between a $d+1$ dimensional superstring theory and a d dimension superconformal field theory. That is, there is a quantum gravity theory on one side of the duality, and a gauge theory without gravity on the other. This at first might seem startling, however there were hints that such a

duality could be realised. In section 2.1 we begin with the link between large N gauge theories and string theory, before stating the first example as given by Maldecena in 1997 [6] in section 2.2, alongside the dualities disctionary and properties. The duality at this point is still fairly unrealistic and in danger of being confined to mathematical curiosity. In section 2.3 we introduce some additional properties that can pull the duality towards the world that we think we reside in.

2.1 From Large N Gauge Theories to String Theory

Gauge theories are all around us. They are the mathematical framework that physicists use to describe particles and their interactions, in turn they are used to formulate the fundamental forces of nature. Gauge theories are a subset of a more general framework called quantum field theory (QFT) where particles are represented as excitations of some underlying field. QFT combines the subjects of quantum mechanics and classical field theory such that special relativity and quantum mechanics can themselves be combined. Four famous examples of gauge theories are quantum electrodynamics, the weak interaction, quantum chromodynamics and gravity, where the first three are of 'Yang-Mills' type and the later under diffeomorphisms. In what follows in this section we shall generally make use of standard lecture material such as [25, 26] and textbooks such as [27].

Specifically, Yang-Mills theories have actions of type

$$S_{YM} = -\frac{1}{4g_{YM}^2}\int d^4x F^{\mu\nu a}F^a_{\mu\nu} \tag{2.1}$$

where g_{YM} is the coupling constant and $F^{a\mu\nu}$ the gauge field tensors. Greek indices run over spacetime coordinates and latin indices over the generators of the Lie group of $N_c \times N_c$ unitary matrices with determinant 1: the special unitary group $SU(N_c)$. That is, the action is invariant under the symmetry group $SU(N_c)$ with $N_c^2 - 1$ generators indexed by a. To see this we first write out the field tensors,

$$F^{a\mu\nu} = \partial^\mu A^{a\nu} - \partial^\nu A^{a\mu} + g_{YM} f^{abc} A^{\mu b} A^{\nu c} \tag{2.2}$$

which is invariant under the following transformation,

$$F^{\mu\nu} \to U F^{\mu\nu} U^\dagger \qquad\qquad U = exp(i\omega^a T^a) \tag{2.3}$$

where T^a are the generators of the Lie group $SU(N_c)$ that span the associated Lie algebra. They obey the commutation relation,

$$[T^a, T^b] = i f^{abc} T^c \tag{2.4}$$

with group structure constants f^{abc}.

The above construction is non-abelian and is the correct formalism for QCD and the weak interaction, with symmetry groups $SU(3)$ and $SU(2)$ respectively. For QED we instead have the abelian formalism with symmetry group $U(1)$. Together they form the standard model $SU(3) \times SU(2) \times U(1)$ the basis of modern particle physics: we have 8 gluons as the gauge bosons of QCD, 3 W/Z bosons of the weak interaction and 1 photon from QED.

Gauge bosons only make up part of the standard model - we still have to include the fermions. To do this we add the following matter term to our Yang-Mills Lagrangian,

$$\mathcal{L}_f = \sum_{f=1} \bar{\psi}_f (i\gamma^\mu D_\mu - m_f)\psi^f \tag{2.5}$$

where f is the flavour index and ψ_f is the fermion of flavour f with corresponding mass m_f. The inclusion of such a term is what accounts for the quarks and leptons in the standard model [1].

It is worth emphasising what representations the gauge fields and matter fields transform under. The gauge fields transform as,

$$A_\mu \to A'_\mu = UA_\mu U^\dagger - ig_{YM}(\partial_\mu U)U^\dagger \tag{2.6}$$

which is the adjoint representation of the gauge group: the gauge fields live in the Lie algebra of $SU(N_c)$ that has the $N_c^2 - 1$ generators as its basis. Therefore we can expand the gauge field as,

$$A_\mu = \sum_a A_\mu^a T^a \tag{2.7}$$

where we see that we have a vector fields corresponding to the a gauge bosons. The generators T^a themselves can be in different representations, however in the standard model they are given in the fundamental representation, i.e they are $N_c \times N_c$ complex objects.

Finally, the matter fields can be in various representations, some examples are: electrons in QED are in the trivial representation; quarks in QCD are in the fundamental representation, and matter fields in supersymmetric Yang-Mills are in the adjoint representation.

There can be other symmetries associated with the (classical) Lagrangian, for example if all the matter fields are of equal mass there is a global $SU(N_f)$ symmetry with $N_c^2 - 1$ associated conserved currents and conserved charges, where the charges are the generators of the global symmetry. Furthermore, if the matter fields are massless they can be decomposed into left and right handed parts each with a global symmetry, i.e we have $SU(N_f)_L \times SU(N_f)_R$. The left and right handed parts mix to

[1] Strictly, the mass term should be generated via the Higgs mechanism, but the above will suffice for our purposes.

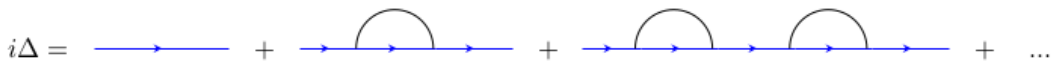

FIGURE 2.1: Example of loops in the calculation of a propagator.

form vector and axial conserved currents of which the aforementioned vector flavour symmetry $SU(N_f)$ is a subgroup. Indeed, under approximate chiral symmetry breaking in QCD we have the spontaneous breaking of $SU(3)_L \times SU(3)_R \to SU(3)_V$ where the 3 represents the u, d, s quarks only. That is, if we approximate the u, d, s as being massless they form a $SU(3)_L \times SU(3)_R$ approximate chiral symmetry that is then spontaneously broken via the formation of a quark-antiquark condensate. More details of chiral symmetry in QCD are given in section 3.1. Finally, we note that there is also a global $U(1)_B$ baryon symmetry.

We have a gauge field term in our Lagrangian and a matter field term, but what about interactions and how do we describe them? The probability amplitude for an interaction to take place is given by a summation of all possible allowed interactions with given initial and final states. This set of interactions can be ordered using the coupling strengths of the interaction in terms of loops. The amplitude of a particle to simply go from one position to another can therefore be given diagrammatically by fig. 2.1. As the number of vertices increases so does the power of the coupling strength associated with that diagram. Clearly, as long as the coupling strength is small perturbation theory will give accurate results in a timely fashion - however if the coupling strength is large, and we are in the strongly coupled regime of the theory, we instead have to turn to non-perturbative techniques of which there are few - one such technique is the gauge/gravity duality that we shall turn to in due course.

For now let's continue with our discussion of $SU(N_c)$ gauge theories. For such theories what can we say about the Feynman rules and diagrams? It turns out to be helpful to first write Feynman diagrams in t'Hooft's 'double-line' notation [4] where we make explicit that the adjoint fields are made up of two fundamental fields i.e one fundamental one anti-fundamental (just like in QCD where gluons have one quark and one anti-quark that can be seen by $\mathbf{3} \times \bar{\mathbf{3}} = \mathbf{8} + \mathbf{1}$). This is ultimately because for $SU(N_c)$ gauge theories the Feynman diagrams organise themselves in terms of the two parameters of the theory: N_c and g_{YM} (also N_f). In fact, when we go to large N_c it will be convenient to use the t'Hooft coupling $\lambda = g_{YM}^2 N_c$ such that the diagrams organise themselves in powers of λ and N_c.

To see this we consider a simple example. The Feynman rules for $SU(N_c)$ Yang-Mills are proportional to factors of λ and N_c: propagators are $\sim \lambda/N_c$ and vertex's $\sim N_c/\lambda$ (plus colour factors f^{abc}) that can be calculated from the Yang-Mills action given previously [25].

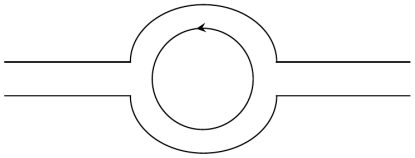

FIGURE 2.2: Gluon self interaction in double-line notation.

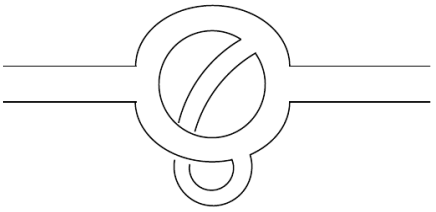

FIGURE 2.3: A non-planar diagram. Notice that there is no longer an internal loop.

In fig. 2.2 we sketch the one loop correction to the gluon propagator in double-line notation. The arrow on the internal circle indicates that there is an internal colour loop where colour factor indices have been contracted giving a factor of N_c ($f^{abc}f_{abc} = C_A = N_c$). We have 2 vertices, one colour factor and four propagators giving a total contribution of $\sim \lambda^2/N_c$. Fig. 2.2 is known as a planar diagram, essentially meaning it can be drawn flat on the page. Instead, in fig. 2.3 we sketch a non-planar diagram. With 7 propagators and four vertices (but now no colour contraction) it has a contribution of $\sim \lambda^3/N_c^3$. Therefore, if we took a large N_c limit, we see that the non-planar diagram is subleading and can be neglected - a great simplification. Moreover, if we consider vacuum bubble diagrams (essentially cut off the external arms and complete the circles in the sketches) the contributions are $\sim N_c^2$ and λ respectively. In fact, if we drew out more bubble diagrams, we would find that we can get the correct answer just by counting the number of Vertices, internal colour loops (Faces) and propagators (Edges):

$$\mathcal{A} = N^{F+V-E}\lambda^{E-V} \tag{2.8}$$

with the following relation,

$$F + V - E = 2 - 2g = \chi \tag{2.9}$$

The 'number of bridges' (i.e like the one in fig. 2.3) is g and χ is a topological invariant (continuous deformations do not affect it while the symmetry of the system remains unchanged) and is a property of Riemann manifolds. For example, in our first bubble-ified sketch we have that $g = 0, \chi = 2$ with $F = 2, V = E = 0$. In the second we have $g = 1, \chi = 0$ and $F = 1, V = 2, E = 3$.

We have therefore found that Feynman diagrams can be related to geometrical objects.

Concretely, we can write the amplitude as,

$$\mathcal{A} = \sum_g N_c^\chi \sum_n p_{g,n} \lambda^n \tag{2.10}$$

where $p_{g,n}$ are constants. The Feynman diagram expansion of a $SU(N_c)$ gauge theory in terms of the t'Hooft coupling λ and N_c can instead be viewed as an expansion in Riemann surfaces where g corresponds to the genus, or number of holes in the surface.

This is remarkably similar to the expansion of a closed string scattering amplitude with the identification of $g_s \sim 1/N_c$. That is, the large N_c limit is now identified as only considering tree level diagrams.[2]

Is the similarity of a $SU(N_c)$ gauge theory and a closed string theory just a coincidence? Can a map, a *duality*, really be formulated between gauge theories and string theories?

2.2 Gauge/Gravity Duality

Before answering that question we should first take a closer look at string theory and some of its properties. The following is a brief discussion of string theory and the duality, for more details see [6, 28, 29, 30, 31, 32].

2.2.1 String Theory

String theory is the idea that the fundamental constituents of nature are not point particles but one-dimensional objects called strings. The strings can either be open, where both ends of the string are free to propagate, or closed, where the endpoints of two strings are joined together. In the case of open strings the endpoints can have two types of boundary conditions; Neumann and Dirichlet. Dirichlet boundary conditions imply that the string endpoint is fixed in the geometry, that is there are potential hyperplanes that the endpoint is attached to. These hyperplanes are called Dp-branes, strings that are extended in more than one spatial direction indexed by p.

By studying the solutions to the string fluctuations we can find the spectrum of the theory. The spectrum is quantised and the various excited states can be separated into those that are massive and those that are massless. The massive states have mass proportional to $1/\sqrt{\alpha'}$, where α' is the Regge slope, related to the string length by $\alpha' = l_s^2$. Therefore, by considering energy scales $E \ll 1/\sqrt{\alpha'}$ the massive states will decouple from the theory and we only have to focus on the massless ones. What these massless fields are depends on what string theory we are considering.

[2] Although neglected here, fundamental particles can also be included by adding a factor $-b$ to χ that act as boundaries in the Riemann manifold.

Specifically, we first note that string theory only contains bosonic fields, and if we wish to include fermionic fields we need to invoke supersymmetry, leading to superstring theory. Superstring theory is only consistent in ten-dimensions to avoid anomalies [28]. Moreover, there are various different types of superstring theory that are themselves related by another theory, M-theory [33, 34]. There is a choice of 5; Type I, IIA, IIB, $SO(32)$ and $E_8 \times E_8$. Type I has both open and closed superstrings, type IIA and IIB only have closed superstrings, and $SO(32)$ and $E_8 \times E_8$ have closed heterotic strings that are composed of one superstring and one bosonic string. In what follows we will be exclusively interesting in type IIB. The low energy superstring spectrum is called supergravity and the type IIB supergravity spectrum includes bosonic fields; the graviton (metric), $g_{\mu\nu}$, an antisymmetric two-form gauge field, $B_{\mu\nu}$, a scalar field, ϕ, called the dilaton, and n-form gauge fields C_n with $n = 0, 2, 4$ (in type IIA n is odd) where $F_5 = dC_4$ is self-dual, and fermionic fields; the Majorana-Weyl gravitinos and dilatinos.

The Dp-branes mentioned above are charged under the n-form gauge fields C_n. Since only n odd/even is allowed for type IIA/IIB we see that only p even/odd branes are respectively allowed. The Dp-branes can also be massive, and therefore deform the geometry they reside in, as well as carry a $U(1)$ gauge field. If we stack N Dp-branes on top of each other we will instead have a $U(N)$ gauge group. As an example, the solution for a stack of N D3-branes in type IIB is given by [35],

$$\begin{aligned} ds^2 &= \left(1 + \frac{L^4}{\rho^4}\right)^{-1/2} \eta_{\mu\nu} dx^\mu dx^\nu + \left(1 + \frac{L^4}{\rho^4}\right)^{1/2} (d\rho^2 + \rho^2 d\Omega_5^2) \\ C_4 &= \left(1 + \frac{L^4}{\rho^4}\right)^{-1} dx^0 \wedge dx^1 \wedge dx^2 \wedge dx^3 \qquad F_5 = dC_4 \end{aligned} \tag{2.11}$$

where $d\Omega_5$ is a five sphere with radius ρ that is transverse to the $D3$ brane, and the Greek indices run over the coordinates longitudinal to the brane.

2.2.2 The Duality

To show that there is indeed a map between string theory and gauge theory we will make use of the Dp-branes outlined above.

As we have already mentioned, the Dp-branes can deform the spacetime around them - that is, they can act as sources for the gravitational field. As an example, let's take the stack of N $D3$-branes above. There are two distinct limits. First we see that far away from the branes, $\rho \gg L$, the metric is that of 10D Minkowksi spacetime. Second we take the limit, $\rho \ll L$, where the metric reduces to,

$$ds^2 = \frac{L^2}{\rho^2} d\rho^2 + \frac{\rho^2}{L^2} (\eta_{\mu\nu} dx^\mu dx^\nu) + L^2 d\Omega_5^2 \tag{2.12}$$

This is a specific type of geometry that is called $AdS_5 \times S^5$, where AdS stands for anti di-Sitter and S^5 labels the 5-sphere with radius ρ. More details on AdS are given

in the next section, for now it is enough to notice that when the D3-branes backreact and in the limit $\rho \ll L$ our theory is reduced to type IIB supergravity in $AdS_5 \times S^5$.

Instead, if the stack of Dp-branes do not backreact, we can focus on their surfaces and the attached open strings. The appropriate theory to describe the open strings is that of four-dimensional $\mathcal{N} = 4$ SYM, the supersymmetric extension of the Yang-Mills theory introduced in section 2.1. The field content consists of a gauge field, A_μ, that lies longitudinal to the brane, six real scalar fields, ϕ, that are transverse, as well as their supersymmetric partners. These fields can be described by the Dirac-Born-Infeld (DBI) action [28],

$$S_{D3} = \frac{1}{(2\pi)^3 \alpha'^2 g_s} \int d^4x e^{-\phi} \sqrt{-\det(g^* + B^* + 2\pi\alpha' F)} \tag{2.13}$$

where g^* and B^* are the pullback of the metric and 2-form field on the brane and F is the gauge field tensor with symmetry group $U(N)$.

We therefore have two ways of picturing D-branes; we can imagine that their effect is to deform the geometry they reside in, or we can instead imagine that they do not backreact and inspect the field content on their surfaces. To quantify the difference between the two pictures it is best to look at the parameters of the theory. First of all we have Newton's constant, G, that can be related to the string length scale, l_s, by

$$16\pi G = (2\pi)^7 g_s^2 l_s^8 \tag{2.14}$$

or in terms of N,

$$\frac{G}{L^3} = \frac{\pi}{2N^2} \tag{2.15}$$

where we have used,

$$\frac{L^4}{l_s^4} = 4\pi g_s N \tag{2.16}$$

with radius of curvature L.

When $g_s N \gg 1$ the backreaction of the branes cannot be neglected and we get the case of a curved geometry. This also implies that $l_s/L \to 0$ which suppresses all string quantum fluctuations and the theory reduces to the low energy point particle supergravity description (along with taking gravity to be weak i.e $g_s \to 0$ which implies $N \to \infty$).

Conversely, when $g_s N \ll 1$ the underlying geometry is unperturbed by the Dp-branes. However we are now in the limit $l_s/L \to \infty$ which would be in the non-perturbative string regime. It is therefore necessary to take the low energy massless limit $E \ll l_s^{-1}$ such that the open strings ending on the Dp-brane are described by a supersymmetric gauge theory. As advertised previously, the natural parameter of a $U(N)$ gauge theory is the t'Hooft coupling $\lambda = g_{YM}^2 N$ that can be related to the string coupling by $g_{YM}^2 = 2\pi g_s$.

Since these two limits describe the same underlying object, it is feasible that they are dual to one another. In fact, the above description is an example of the *weak* form of the gauge/gravity duality where classical supergravity ($g_s \to 0$, $l_s/L \to 0$) is dual to a strongly coupled, large N gauge theory. However there is nothing stopping a more general form, other than intractable calculations, where we relate a full quantum string theory to a supersymmetric gauge theory with arbitrary N and λ.

Therefore, for the example of D3-branes in type IIB superstring theory we have the following statement [6, 31, 32]:

$\mathcal{N} = 4$ SYM with $SU(N)$ and coupling g_{YM} is dual to IIB superstring theory with string length l_s and coupling g_s on $AdS_5 \times S^5$ with radius of curvature L.[3]

In what follows we shall be interested in the weak form of the duality, specifically the case of $D3$-branes in type IIB. Although the duality is not proven there is a large amount of evidence for its existence. As a first step, we should see that the symmetries on both sides are the same and that the field content can be mapped across.

2.2.3 Symmetries

AdS stands for anti-di Sitter, where the spacetime is hyperbolic rather than spherical (di Sitter), that is the spacetime has negative curvature rather than positive. A $d+1$ dimensional anti-di Sitter spacetime can be represented by embedding it in a $d+2$ Minkowksi space $\mathbb{R}^{d,2}$,

$$ds^2 = -dX_0^2 + \sum_{i=1}^{d} dX_i^2 - dX_{d+1}^2 \tag{2.17}$$

where AdS_{d+1} is given by the hypersurface,

$$-L^2 = -X_0^2 + \sum_{i=1}^{d} X_i^2 - X_{d+1}^2 \tag{2.18}$$

where the radius of curvature of the AdS space is L. One feature of this spacetime is that it has a conformal boundary, ∂AdS_{d+1}, at large values of X.

A standard coordinate system in the gauge/gravity duality is Poincaré patch coordinates. These parameterise the spacetime by

$$\begin{aligned} X_0 &= \frac{L^2}{2\rho}\left(1 + \frac{\rho^2}{L^4}(\bar{x}^2 - t^2 + L^2)\right) \\ X_i &= \frac{\rho x_i}{L} \\ X_d &= \frac{L^2}{2\rho}\left(1 + \frac{\rho^2}{L^4}(\bar{x}^2 - t^2 - L^2)\right) \\ X_{d+1} &= \frac{\rho t}{L} \end{aligned} \tag{2.19}$$

[3] Note both theories also have a region far away from the brane that becomes type IIB on $\mathbb{R}^{9,1}$ that are matched together.

where i runs from 1 to $d-1$ and ρ only has support $\mathbb{R}_+$ such that the coordinates only cover half of the AdS_{d+1} spacetime with a second Poincaré patch required to cover the whole space. In these coordinates the metric becomes,

$$ds^2 = \frac{L^2}{\rho^2}d\rho^2 + \frac{\rho^2}{L^2}(\eta_{\mu\nu}dx^\mu dx^\nu) \tag{2.20}$$

The Ricci scalar and cosmological constant are,

$$R = -\frac{d(d+1)}{L^2} \qquad \Lambda = -\frac{d(d-1)}{2L^2} \tag{2.21}$$

Therefore the AdS spacetime can be thought of as simply d-dimensional Minkowski space with an additional warp coordinate ρ [29]. Taking the case of the $D3$-brane induced $AdS \times S^5$ geometry we have,

$$ds^2 = \frac{L^2}{\rho^2}d\rho^2 + \frac{\rho^2}{L^2}(\eta_{\mu\nu}dx^\mu dx^\nu) + L^2 d\Omega_5^2 \tag{2.22}$$

that we previously related to the ten-dimensional $D3$-brane solution in the $\rho \ll L$ limit.

What are the symmetries of the metric in (2.22)? We see that we have a $SO(4,2)$ isometry group for the AdS_5 part as well as a $SO(6)$ rotation symmetry from the 5-sphere. This $SO(4,2) \times SO(6)$ symmetry is a subgroup of the string diffeomorphisms. In fact, it is the subgroup of large gauge transformations (and therefore act as global symmetries) that acts on the near boundary metric.

So far we have only acounted for half of the bosonic symmetries since the theory is supersymmetric, to include the fermionic contributions we simply have to go to the double cover, $SU(2,2) \times SU(4)$. Finally, including the conserved supercharges we arrive at $PSU(2,2|4)$ [28].

On the other hand we have $\mathcal{N} = 4$ SYM that is both supersymmetric and conformal. Conformal symmetry enlarges the standard Poincaré symmetry group of a field theory by including extra generators. Specifically we have the addition of dilatations and special conformal transformations. Conformal transformations are coordinate transformations $x \to x'$ that leave the metric invariant up to a scale factor [36],

$$g_{\mu\nu}(x) \to \Omega^{-2}(x) g_{\mu\nu}(x) \tag{2.23}$$

such that, although the length of a spacetime interval is altered, angles are preserved. Since we are interested in $\mathcal{N} = 4$ SYM in 4d we are interested in the conformal symmetries in $d > 2$ dimensions that form the group $\mathrm{Conf}(3,1)$ isomorphic to $SO(4,2)$. This group contains the Poincare group of translations, $P^\mu : x^\mu \to x^\mu + a^\mu$ and Lorentz transformations, $J_{\mu\nu} : x^\mu \to \Lambda^\mu_\nu x^\nu$, as well as dilatations $D : x^\mu \to \lambda x^\mu$ and special conformal transformations, $K_\mu : x^\mu \to \frac{x^\mu + b^\mu x^2}{1+2b\cdot x+b^2x^2}$, the later two of which can be combined to create an inversion symmetry where $x^\mu \to x^\mu/x^2$.

Supersymmetry further enlarges the symmetry group from $Conf(3,1)$ to $PSU(2,2|4)$ by the addition of a $SU(4)_R$ group, the bosonic subgroup of which being $SO(6)_R$ that rotates the 6 scalar field of $\mathcal{N}=4$ SYM, ϕ^i, into each other. The other fields of $\mathcal{N}=4$ SYM are four complex Weyl fermions, λ^a_α, where α labels the spacetime spinor index and a labels the distinct supercharges $a=1,...,\mathcal{N}$, and a gauge field, A_μ; that with the 6 scalars form a vector multiplet with all fields transforming in the adjoint representation. The generators of the $SU(4)_R$ group are the Poincaré supercharges Q^a_α, $\bar{Q}^a_{\dot{\alpha}}$ and the special conformal supercharges S^a_α, $S_{a\dot{\alpha}}$, of which there are 32 in total.

Therefore we see that the full symmetry group on both sides of the duality is $PSU(2,2|4)$ with the various subgroups also matching, notably the bosonic AdS_5 $SO(4,2)$ acts asymptotically as the conformal group on the spacetime coordinates x^μ and the $SO(6)$ as the supersymmetry on the scalars.

Some other properties of the symmetries are worth pointing out. First is that the asymptotic global symmetries of the gravity side ultimately arise as large gauge transformations. Therefore there is a gauge/global duality, a general feature of all gauge/gravity dualities. An immediate question is then what becomes of the $SU(N)$ gauge group of SYM on the gravity side? It turns out it becomes a flux through the 5-sphere, that is there are N units of 5 form flux on the S^5 [28],

$$\int_{S^5} F_5 = N \tag{2.24}$$

Second is how do we interpret the radial coordinate on the boundary? A hint can be given by looking at how the radial coordinate transforms, specifically under dilations. The field theory coordinates in the bulk transform under D as in the boundary, $D : x^\mu \to \lambda x^\mu$, however for the bulk metric to remain invarient the radial coordinate must scale as $D : \rho \to \rho/\lambda$. That is, it scales as if it were energy. This implies that short distance physics (UV) in the gauge theory is related to physics near the boundary of AdS, whereas long-distance physics (IR) takes place in the deep interior (horizon). However from the point of view of an observer at the horizon in AdS, the UV physics takes place at the horizon instead, and therefore by the time it reaches the boundary it is IR. In other words, the gauge/gravity duality is also a IR/UV duality where the radial coordinate plays the role of a renormalisation group scale in the gauge theory. We can then picture r-slices of the AdS space as setting a scale to the gauge theory.

2.2.4 Field/Operator Map

We have seen how to picture the two theories geometrically, we have seen the field content and symmetries on both sides. But if we wish to make calculations on one side and match them to the other, then we shall have to match the observables on both sides. On the field theory side physical observables are correlation functions made up

of composite operators that can be calculated from varying the generating functional with respect to the fields it contains. On the supergravity side the physical observables are the fields. Therefore if we wish to link the two we can instead define the correlation functions of the field theory in terms of the string fields defined at the boundary [31, 32]:

$$\langle \mathcal{O}(x_1)\mathcal{O}(x_2)...\mathcal{O}(x_n)\rangle = \frac{\delta^2 S_{sugra}}{\delta\phi_0(x_1)\delta\phi_0(x_2)...\delta\phi_0(x_n)} \tag{2.25}$$

In this way, we read the string fields at the boundary as the sources for the operators of the field theory. From this we can write a statement of the gauge/gravity duality,

$$\langle exp(\int d^4x \phi_{(0)}(x)\mathcal{O}(x)\rangle = Z_{CFT}[\phi_{(0)}] \equiv Z_{string}[\phi|_\partial] \sim exp(-S_{sugra}[\phi|_\partial]) \tag{2.26}$$

where the field ϕ is a classical solution to the supergravity equation of motion with boundary conditions $\phi(x,\rho) \to \phi_0(x)$ as $\rho \to \infty$. Some important examples of this field/source mapping is the current operator J_μ being sourced from a vector field A^μ and the energy-momentum tensor $T_{\mu\nu}$ being sourced by the metric $g^{\mu\nu}$. We will see some of these mappings in action later.

How, precisely, do we find the boundary value of the fields? It is easiest to consider a toy example with scalar field ϕ. The action term containing the scalar fields' dynamics is,

$$S \sim \frac{1}{2}\int dz d^d x \sqrt{-g}(g^{mn}\partial_m\phi\partial_n\phi + m^2\phi^2) \tag{2.27}$$

where we have switched to radial coordinate z and Fefferman-Graham coordinates [37],

$$ds^2 = g_{mn}dx^m dx^n = \frac{L^2}{z^2}(dz^2 + \eta_{\mu\nu}dx^\mu dx^\nu) \tag{2.28}$$

where the boundary is now at $z = 0$. The equation of motion for ϕ is,

$$(\Box_g - m^2)\phi = 0 \tag{2.29}$$

where,

$$\begin{aligned}\Box_g &= \frac{1}{\sqrt{-g}}\partial_m(\sqrt{-g}g^{mn}\partial_n) \\ &= \frac{1}{L^2}(z^2\partial_z^2 - (d-1)z\partial_z + z^2\eta_{\mu\nu}\partial^\mu\partial^\nu)\end{aligned} \tag{2.30}$$

Taking a boundary ansatz of $\phi(x,z) = z^\Delta\phi(x)$ and keeping only the leading terms as $z \to 0$ i.e keeping only $\mathcal{O}(z^\Delta)$ we find a constraint,

$$\Delta(\Delta - d) = m^2 L^2 \tag{2.31}$$

with solutions,

$$\Delta = \frac{d}{2} \pm \sqrt{\frac{d^2}{4} + m^2 L^2} \equiv \Delta_\pm \tag{2.32}$$

Clearly $\Delta_+ \geq \Delta_-$ and $\Delta_- = d - \Delta_+$. Furthermore, near the boundary the field $\phi(z, x)$ can be expanded as,

$$\phi(z, x) = z^{\Delta_-}\phi_{(0)}(x)(1 + ...) + z^{\Delta_+}\phi_{(+)}(x)(1 + ...) \tag{2.33}$$

where ellipses stand for subleading terms in z.

In the boundary theory a scalar operator will have conformal dimension Δ_c with source dimension $d - \Delta_c$. In general, to satisfy the conformal unitarity bound for a scalar field, $\Delta_c \geq 1/2(d-2)$, we define $\Delta_c \equiv \Delta_+$ such that ϕ_+ is related to the operator for a scalar field with dimension Δ_c. Therefore ϕ_0 must have dimension $d - \Delta_c$ and is identified as the source of the operator. It is also possible to instead choose $\Delta_c \equiv \Delta_-$, where the roles of operator/source are then interchanged, as long as the mass range is $-\frac{d^2}{4} \leq m^2 L^2 \leq -\frac{d^2}{4} + 1$. That $m^2 L^2 \geq -\frac{d^2}{4}$ is called the Breitenlogner-Freedman bound and is unique for AdS spacetimes [38, 39, 40].

In this way we can relate the fields in the bulk to sources and operators in the boundary.

2.3 Towards Reality

The brief introduction to the gauge/gravity duality above gives some credence to the conjecture, as well as some of the techniques of mapping calculations from one theory to the other. However, we still lack much of the details we find in a standard field theory system such as temperature, fields in the fundamental representation and a departure from the highly symmetric $\mathcal{N} = 4$ SYM. In this section we show how to bring the gauge/gravity towards reality.

2.3.1 Thermodynamics

A natural object to consider thermodyanimcs with in a theory of gravity is a black hole with Hawking temperature T_h [41, 42]. In supergravity this can be introduced via non-extremal black branes. For the case of $D3$ black branes, in the near-horizon limit, the only part that changes is the AdS metric,

$$ds^2 = \frac{L^2}{\rho^2 f(\rho)} d\rho^2 + \frac{\rho^2}{L^2}(-f(\rho)dt^2 + d\bar{x}^2) \tag{2.34}$$

with the emblackening function given as

$$f(\rho) = 1 - \frac{\rho_H^4}{\rho^4} \tag{2.35}$$

such that $f(\rho_H) = 0$. This is known as the AdS_5-Schwarzchild solution. The radial coordinate is now bounded by $[\rho_h, \infty]$.

In QFT at finite temperature the object of interest is the partition function $Tr[e^{-\beta H}]$. A simple way to make use of all the machinery of zero temperature QFT is to notice that this is exactly the same as a time evolution operator e^{iHt} if $t = i\beta$ with $\beta = 1/T$ - i.e we consider imaginary times. We therefore move to Euclidean time $\tau = it$ and the trace now signifies that bosons/fermions have to be periodic/ anti-periodic in the time directions with period $\beta = 1/T$. In other words we have compactified Euclidean time.

To connect this to the black hole we should first move to Euclidean time,

$$ds^2 = \frac{L^2}{\rho^2 f(\rho)} d\rho^2 + \frac{\rho^2}{L^2}(f(\rho)d\tau^2 + d\bar{x}^2) \tag{2.36}$$

where there is a conical singularity in the Euclidean time-direction. To make the metric regular, τ can be made periodic with period β - i.e we compactify the Euclidean time direction. We can then interpret the field theory temperature with the compact direction of the black hole,

$$T_{QFT} = \frac{1}{\beta_{BH}} = \frac{\rho_H^2 f'(\rho_H)}{4\pi L^2} \tag{2.37}$$

where the explicit period can be found by investigating the conical singularity. Using (2.35) we then find,

$$T = \frac{\rho_H}{\pi L^2} \tag{2.38}$$

Note, that by turning on a temperature we have added a scale to the theory and thus broken the conformal symmetry at the boundary.

Once again we are faced with the question of conjecture - does the correspondence still hold now that we have turned on a temperature? One possible check is to calculate the entropy. However, in the boundary theory it isn't possible to calculate the strongly coupled entropy, instead we can take a look at the non-interacting result [43]

$$S_{free} = \frac{2\pi^2}{3} N^2 T^3 Vol(\mathbb{R}^3) \tag{2.39}$$

Since the entropy can run, we do not expect the gravity calculation to be exactly the same, but it should take the same form. The natural entropy of a theory with a black hole is the Bekenstein-Hawking entropy, a semi-classical result,

$$S_{BH} = \frac{A}{4G} \tag{2.40}$$

where A is the horizon area and G is Newton's constant. The area of the horizon can be easily computed to be $A = \pi^6 L^8 T^3 Vol(\mathbb{R}^3)$ such that the entropy becomes [41],

$$S_{BH} = \frac{\pi^2}{2} N^2 T^3 Vol(\mathbb{R}^3) \tag{2.41}$$

Alternatively the same result can be calculated via the free energy $S = -\partial F/\partial T$. We see that the result is very similar to that of the free theory up to a multiplicative constant,

$$S_{BH} = \frac{3}{4} S_{free} \tag{2.42}$$

This is more than just a check; it is a result - it tells us how the entropy of a plasma of deconfined gluons runs between the free theory and the theory of infinite coupling $\lambda \to \infty$.

Another important thermodynamic quantity is chemical potential. In the grand canonical ensemble (GCE), where the potential can be calculated from the renormalised action $\Omega = -S_r$, there is a term that looks like:

$$dG \ni \sum_i \mu_i dN_i \tag{2.43}$$

where the i can run over different chemical species. This term can be explicitly seen in the GCE partition function in statistical field theory,

$$Z = \sum_i e^{-\beta(E_i - N_i \mu)} \tag{2.44}$$

That is, the partition function contains a term that couples the chemical potential to a number density operator. Such a term can also be introduced to the path integral of a QFT. If there is some global symmetry associated with the chemical potential, for example $U(1)_B$ baryon symmetry, we will get a conserved charge:

$$Q = \int d^3x J^t(x) = \int d^3x d(x) \tag{2.45}$$

where $d(x)$ is some density like the number density above. Therefore, we can write:

$$\mu Q = \int d^3x \mu(x) d(x) = \int d^3x \mu(x) J^t(x) \tag{2.46}$$

Recall that a conserved global current in the boundary CFT is sourced by a gauge field. Taking only the time component we can say that J^t is sourced by A_t. Comparing this to what we have above we see that we can associate $\mu = A_t$ at the boundary.

	x^0	x^1	x^2	x^3	x^4	x^5	x^6	x^7	x^8	x^9
D3	×	×	×	×						
D7	×	×	×	×	×	×	×	×		

TABLE 2.1: D3/D7 brane setup in $AdS_5 \times S^5$ where × signifies that the brane extends in that direction.

2.3.2 Flavour

So far we have considered $\mathcal{N} = 4$ SYM with some symmetry breaking via temperature. However in SYM all the fields are in the adjoint representation. To take a step toward reality we should include fields that transform in the fundamental representation. This can be achieved by including $\mathcal{N} = 2$ hypermultiplets that transform in the N_f representation of some gauge group $U(N_f)$ where 'f' stands for flavour (also called matter fields) to signify that the fields are fundamental. In this sense they can then be thought of as 'quarks'. More specifically, the field content of the hypermultiplet is of a Dirac fermion ψ and a pair of complex scalar fields q and $\tilde{q}$ - the Dirac fermion plays the role of the 'quark' or 'electron'. The fields of $\mathcal{N} = 4$ transform in the singlet representation of $U(N_f)$.

This addition is mapped to the gravity side by the inclusion of a stack of N_f D7 branes with gauge group $U(N_f)$, a specific example of a more general technique of embedding Dq-branes into a Dp-brane background [44, 45]. The symmetries of the theory change depending on how the Dq-branes are inserted into the background. In fact, suspersymmetry restricts the possibilities. For our D7-branes we choose to orient them such that they lie along all of the field theory directions. The set up is summerised in table 2.1.

We now have additional degrees of freedom. Previously, we only had 3-3 (p-p) strings with both ends attached to the D3-brane. We now also have 3-7 (p-q), 7-3 (q-p) and 7-7 (q-q) strings, however the 7-7 strings decouple from the other excitations in the $\alpha' \to 0$ limit that we are considering [29]. Since the 3-7 strings have one end on the $SU(N_c)$ D3 branes and one on the $U(N_f)$ D7 branes, they transform fundamentally under both groups. Note, the $U(N_f)$ has an important subgroup, the baryon symmetry $U(1)_B$. Only the fundamental fields are charged (± 1) under the baryon symmetry.

The first obvious change in the symmetry is that the $SO(6)$ of the 5-sphere is now broken down to $SO(4) \sim SU(2) \times SU(2)$ acting on the x^4, x^5, x^6, x^7 directions and $SO(2) \sim U(1)$ on the x^8, x^9. Therefore by introducing the $D7$ branes we have broken the $SO(6)_R \to SU(2)_L \times SU(2)_R \times U(1)_A$ where we indicate that the $U(1)_A$ acts as an *axial* symmetry on the quarks. If the $D7$ branes are separated in the x^8 or x^9 direction the $U(1)_A$ is also broken, for example we can choose $x^8 = l_q$ and $x^9 = 0$. Furthermore by separating the 3-7 and 7-3 strings in this way we have introduced a mass m_q associated with the separation distance,

$$m_q = \frac{l_q}{2\pi\alpha'} \tag{2.47}$$

Since the 3-7/7-3 strings are related to the $\mathcal{N} = 2$ hypermultiplet we can say that by separating the branes we are introducing mass to the 'quarks'. The angle of separation in the 8-9 plane plays the role of the phase of the hypermultiplet mass.

The *D7* brane action is given in part by a Dirac-Born-Infield (DBI) term and a Wess-Zumino (WZ) term:

$$S_{D7} = -N_f T_7 \int d^8\xi e^{-\phi}\sqrt{-det(P[G]_{ab} + 2\pi\alpha' F_{ab})} + \frac{(2\pi\alpha')^2}{2} T_7 \int P[C_{(4)}] \wedge F \wedge F \tag{2.48}$$

where $T_7 = 1/(2\pi)^7\alpha'^4$ is the tension of the *D7* brane, F is the field strength tensor for a $U(1)$ gauge field living on the brane, P denotes the pull-back of a background field on the brane and G, $C_{(4)}$ and ϕ are the background fields outlined previously. We should, however, be careful here. Since we have included a new term into the overall systems action, can we still use the type IIB background fields in $AdS_5 \times S^5$? In general the *D7* branes will backreact and we will have corrections to the background fields, however the situation is simplified if we instead consider *probe* branes. The full action is given by,

$$S = S_{\text{IIB}} + S_{D7} \tag{2.49}$$

Given that $g_s = e^{\phi}$ we have that $S_{D7} \propto N_f/(2\pi)^7\alpha'^4 g_s$ and $S_{IIB} \propto 1/2\kappa_{10}^2 = 1/(2\pi)^7\alpha'^4 g_s^2$. If we wish the contributions coming from S_{D7} to be small compared to S_{IIB}, and therefore the backreaction can be neglected, then we see that we want $g_s N_f \to 0$. During the set-up of the semi-classical formulation of the correspondence we also took $g_s N_c \gg 1$, hence the probe limit is satisfied when $N_f \ll N_c$. In other words, the number of probe branes is small compared to the branes that originally deformed the geometry.

The second part of this thesis is devoted to such probe-brane systems, therefore it will be helpful to consider a simple example to showcase some important features [46]. The metric for a black hole in $AdS_5 \times S^5$ was given by,

$$ds^2 = \frac{L^2}{\rho^2 f(\rho)} d\rho^2 + \frac{\rho^2}{L^2}(-f(\rho)dt^2 + d\vec{x}^2) + L^2 d\Omega_5^2 \tag{2.50}$$

where the boundary is located at $\rho = \infty$. It will be useful to make explicit the $SO(4)$ and $SO(2)$ symmetries. We do this by splitting the 5-sphere into a 3-sphere and a 1-sphere with $\rho^2 = r^2 + R^2$,

$$L^2 d\Omega_5^2 = \frac{L^2}{\rho^2}(dr^2 + r^2 d\Omega_3^2 + dR^2 + R^2 d\Omega_1^2) \tag{2.51}$$

The separation of the $D3$ and $D7$ branes is then given by the field R. It will also be helpful to make a coordinate transformation,

$$\frac{\rho d\rho}{(\rho^4 - \rho_H^4)^{1/2}} \equiv \frac{dw}{w} \tag{2.52}$$

$$2w^2 = \rho^2 + \sqrt{\rho^4 - \rho_H^4} \tag{2.53}$$

with $\sqrt{2}w_H = \rho_H$ and $\rho_H = \pi L^2 T$. The metric becomes,

$$ds^2 = \frac{w^2}{L^2}(-g_t dt^2 + g_x d\vec{x}^2) + \frac{L^2}{w^2}(dr^2 + r^2 d\Omega_3^2 + dR^2 + R^2 d\Omega_1^2) \tag{2.54}$$

where

$$g_x = \left(\frac{w^4 + w_H^4}{w^4}\right) \qquad g_t = \frac{(w^4 - w_H^4)^2}{w^4(w^4 + w_H^4)} \tag{2.55}$$

Turning on only the A_t component of the gauge field (to act as the chemical potential) the $D7$ action is, after integrating over the wrapped 3-sphere,

$$S_{DBI} = -\mathcal{N} \int d^4x dr \; g_x^{3/2} g_t^{1/2} r^3 \sqrt{1 + R'^2 - \frac{\widetilde{A}_t'^2}{g_t}} \tag{2.56}$$

Where the pre-factor is $\mathcal{N} = N_f T_{D7} \mathrm{Vol}(\Omega_3)$, $\widetilde{A}_t = 2\pi\alpha' A_t$ and the WZ term is zero (in chapter 4 we shall see an example with the WZ term non-zero). Since only A_t' appears in the action we have a conserved charge,

$$\frac{\delta S_{DBI}}{\delta A_t'} = \mathcal{N} r^3 g_x^{3/2} g_t^{1/2} \frac{(2\pi\alpha')\widetilde{A}_t'}{\sqrt{1 + L'^2 - \frac{\widetilde{A}_t'^2}{g_t}}} \equiv d \tag{2.57}$$

To identify the charge 'd' recall (2.25) and the argument below (2.46): the density one point function $\langle J_t \rangle$ is sourced by A_t at the boundary,

$$\langle J_t \rangle = \frac{\delta S_{DBI}}{\delta A_t(\infty)} \tag{2.58}$$

If we vary $A_t(\rho)$ we will find that $\langle J_t \rangle = d$.

Legendre transforming with respect to the conserved charge we can write the action in terms of the density,

$$\widetilde{S}_{DBI} = -\mathcal{N} \int dr \; g_x^{1/2} g_t^{1/2} r^3 \sqrt{1 + R'^2} \sqrt{g_x^2 + \frac{d^2}{g_x r^6 \mathcal{N}^2}} \tag{2.59}$$

where we have used,

$$A_t' = \frac{\sqrt{1 + R'^2}}{\sqrt{g_x^2 \mathcal{N}^2 + \frac{d^2}{g_x r^6}}} \frac{d g_t^{1/2}}{g_x^{1/2} r^3} \tag{2.60}$$

such that the chemical potential is:

$$\mu = \int_{r_0}^{r_H} A_t' dr \tag{2.61}$$

Finally the Gibbs free energy will be:

$$\Omega = \mathcal{N} \int dr\, g_x^{1/2} g_t^{1/2} r^3 \frac{\sqrt{1+R'^2}}{\sqrt{g_x^2 + \frac{d^2}{g_x r^6 \mathcal{N}^2}}} g_x^2 \tag{2.62}$$

To solve for the chemical potential and free energy we need to find solutions, and therefore boundary conditions, for R. There are two different boundary conditions that we should consider [47]. The first are called 'black hole' solutions where the D7 brane falls into the black hole (or in the case of zero temperature ends at the Poincaré horizon). The second are called 'Minkowski' embeddings that do not reach the black hole horizon. These solutions have different topological origins. In both cases the S_3 that wraps the S_5 does so equatorially at the boundary. However as we move into the bulk via the radial coordinate ρ the position of the S_3 on the S_5 can change. In the case of Minkowski embeddings the S_3 collapses on the S_5 before reaching the black hole horizon, it's volume has shrunk to zero and we have that $\rho > \rho_H$. Alternatively, for the black hole solutions, the S_3 shrinks but never collapses, therefore the D7 brane can extent to the black hole. We can therefore expect a topology changing phase transition between the two solutions. Furthermore this phase transition should be evident from inspecting the density. In the case of Minkowski embeddings the only stable solutions are those with a constant chemical potential and therefore zero density, whereas in the case of the black hole embeddings a non-zero density is allowed and is also thermodynamically favoured. In part II we shall see many examples of free energies and phase diagrams using this model as a baseline.

As previously mentioned the mass of the field theory hypermultiplets is given by the separation between the $D3$ and $D7$ branes. We can explicitly see this by considering the embedding function $R(r)$ near the boundary where it takes the expected form of 'source + operator',

$$R(r) = m + \frac{c}{r^2} \tag{2.63}$$

where $m_q = m/2\pi\alpha'$. More specifically the scalar field R is holographically dual to an operator $\langle \mathcal{O}_m \rangle$ at the boundary,

$$\langle \mathcal{O}_m \rangle = -(2\pi\alpha') \frac{\delta S_{DBI}}{\delta R(\infty)} \tag{2.64}$$

Varying $R(r)$ we find that $\langle \mathcal{O}_m \rangle \propto -c$. What is the role of 'c' here? In the field theory $\langle \mathcal{O}_m \rangle$ contains a vacuum expectation value $\langle \bar{\psi}\psi \rangle$ of the hypermultiplet fields. We therefore identify 'c' as a condensate of the hypermultiplets that is sourced by a non-zero mass term m. In chapter 3 we shall see a case where the D7 branes do not lie

flat and therefore have non-zero condensate even though the UV mass is zero.

2.3.3 Some Applications: Two-point Functions

It is important in physics to not only understand the static properties of a system, but to also understand how that system can change when influenced from the outside, for example, by turning on an electric or magnetic field. In general, it will be difficult to work out how the system evolves, especially if the influence is time dependent. The solution is to instead consider small changes and use the theory of linear response where we consider the response of an operator $\langle \mathcal{O}_i \rangle$ to small changes in the source of $\langle \mathcal{O}_j \rangle$ [48],

$$\delta \langle \mathcal{O}_i(x) \rangle = \int d^d y G_{ij}(x,y) \delta \phi_j(y) \tag{2.65}$$

where by neglecting terms with $\mathcal{O}(\phi^2)$ and higher we make explicit that we are working in linear response. The term $G_{ij}(x,y)$ is called the Green's function and the retarded part is given by [29],

$$G^R_{ij}(x,x') = -i\Theta(t-t')\langle \mathcal{O}_i(x)\mathcal{O}_j(x')\rangle + i\Theta(t'-t)\langle \mathcal{O}_j(x')\mathcal{O}_i(x)\rangle \tag{2.66}$$

where the heavy-side function Θ ensures causality. In Fourier space the Green's function is,

$$G(\omega,k) = \int d^d x e^{i\omega t - ikx} G_{ij}(t,x) \tag{2.67}$$

such that (2.65) becomes,

$$\delta \langle \mathcal{O}_i(\omega,k) \rangle = G_{ij}(\omega,k)\delta\phi_j(\omega,k) \tag{2.68}$$

or,

$$G_{ij} = \frac{\delta \langle \mathcal{O}_i \rangle}{\delta \phi_j} \tag{2.69}$$

Greens function, such as the ones defined above, are immensely useful in physics. This is because many properties of a system can be deduced from them - for example, via Kubo formulas we can calculate transport coefficients like the electric conductivity,

$$\sigma(\omega) = \frac{G^R_{J_x J_x}}{i\omega} \tag{2.70}$$

where the operator $\langle J^x \rangle$ is sourced by the spatial component of a gauge field A_x.

Another example is that the poles of the Green's function tell us about the allowed modes of the system, defined by their dispersion relation. The Green's function takes the approximate form,

$$G_{ij} \sim \frac{1}{\omega - \Omega + i\Gamma} \tag{2.71}$$

where Ω is the real 'propagating' part of the mode and Γ the imaginary 'dissipative' part. Examples of modes are the purely imaginary diffusion mode, $\omega = -iDk^2$ and propagating sound modes, $\omega = \pm vk - i\Gamma k^2$, where k is momentum and D is the diffusive constant. Note, we expect to find stable modes only in the negative imaginary frequency plane, otherwise the mode has unbounded increasing frequency and is thus unstable.

Clearly exploring Green's functions holographically will prove to be pivotal in understanding the systems that we are trying to describe. They will lead the way in relating what we do holographically to experiment and strongly coupled physics. How then do we go about calculating holographic Green's functions? This was first done using the Schwinger-Keldysh formulism [49, 50]. However here we shall instead use a technique that follows from (2.69).

First we must introduce fluctuations in the field content,

$$\phi_i(\rho) \to \phi_i(\rho) + \delta\phi_i(\rho)e^{-i\omega t + ikx} \tag{2.72}$$

Substituting the fields fluctuations into the bulk or DBI action we can then linearise and find the equation of motion for the fluctuation with appropriate boundary conditions. At the boundary we have an asymptotic $\rho \to \infty$ expansion as in (2.33). At the black hole horizon $\rho \to \rho_H$ we find that there are in fact two solutions to the equations of motion that relate to ingoing and outgoing modes. We choose the regular ingoing mode that corresponds to the retarded Green's function (the outgoing mode being unstable and corresponding to the advanced Green's function).

We can now see how to calculate the Green's function. Since we are looking for the source ϕ_j of an operator it makes sense to take the leading term of $\delta\phi(\rho)_j$ in the near boundary expansion, $\delta\phi_{j(0)}$,

$$G_{ij} = \frac{\delta\langle\mathcal{O}_i\rangle}{\delta\phi_j} = \frac{\delta}{\delta\phi_{j(0)}}\frac{\delta S_{ren}[\phi_{i(0)}]}{\delta\phi_{i(0)}} = \frac{2\Delta_i - d}{L}\frac{\delta\phi_{i(+)}}{\delta\phi_{j(0)}} \tag{2.73}$$

where we have instead switched to the *renormalised* action S_{ren}, that, when varied with respect to $\phi_{i(0)}$, results in a factor $\propto \phi_{i(+)}$ [51, 52]. More details of holographic renormalisation are given in the appendices of the chapters in part II.

A simple way of obtaining the dispersion relation is then to look for where $\delta\phi_{j(0)} = 0$, that is, the poles of the Green's function. As mentioned, these poles are ingoing fluctuations about a black hole background, so-called *quasi-normal modes*. Since the quasi-normal modes fall into the black hole it is of no surprise that the modes that we find in the QFT are damped and therefore can decay [53]. In addition, there are also normal modes that come from the Minkowski solutions that are instead long-lived excitations.

In part II we will see explicit examples of calculating quasi-normal modes, dispersion relations and conductivities.

Part II

Research

Chapter 3

Holography and Imaginary Chemical Potential: A Phase Diagram

Holography has allowed the exact solution of a small number of large N_c gauge theories. Amongst these is an $\mathcal{N}$=2 SYM theory of quarks interacting with $\mathcal{N}$=4 gauge fields. The temperature chemical potential phase diagram for this theory in the presence of a magnetic field is exactly known and shows first and second order chiral symmetry restoration transitions and a critical point. Here we extend this phase diagram to imaginary chemical potential to seek structure at small real μ and imaginary μ that help to reconstruct the large real μ phase structure. We also explore a phenomenologically deformed version of the theory where the critical point can be moved into the imaginary chemical potential plane. In particular we observe that when the transition is second order in these theories there are naturally two distinct transitions - one for the onset of density and one for chiral symmetry restoration. In addition, the phase diagram has boundaries of regions where metastable vacua exist and these boundaries, as well as the phase boundaries, converge at the critical point. These observations may point to techniques for the study of the QCD critical point either on the lattice or using heavy ion collision data.

3.1 Strongly Coupled: QCD

Quantum Chromodynamics, the theory of interacting quarks and gluons, is one of the three fundamental forces that make up the standard model of particle physics, the other two being the weak nuclear force and quantum electrodynamics.

Before taking a look at the problems of strongly coupled QCD let's first discuss two important properties: confinement and chiral symmetry.

Confinement - Confinement in QCD is the statement that the potential energy between a static quark-antiquark pair grows linearly with separation up until a certain

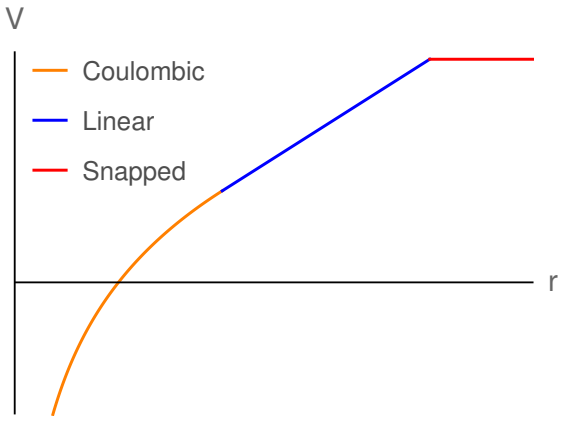

FIGURE 3.1: Quark-antiquark potential at different seperation lengths.

point where it flattens and we enter the deconfined region [54]. We can picture this by imagining a flux tube between the two quarks that at a certain separation snaps and produces two new quark-antiquark pairs. More formally what is happening is that there comes a point in length separation where it is energetically more favourable to pull two external colour sources in the fundamental representation in from infinity than it is to continue stretching the tube. In fig 3.1 we plot a cartoon of what the quark-antiquark potential looks like against separation distance. At small distances the interaction is Coulombic and goes as $V \sim 1/r$ where we are in the regime of asymptotic freedom. At intermediate distance we have a 'confined' linear potential, and at large distances we have a flat potential where the flux tube has snapped.

Chiral Symmetry - In QCD the the kinetic terms can be written as [25],

$$\sum_f \bar{q}_f i\not{D} q_f = \sum_f \bar{q}_{L,f} i\not{D} q_{L,f} + \bar{q}_{R,f} i\not{D} q_{R,f} \tag{3.1}$$

where $q, \bar{q}$ are the quarks/anti-quarks of flavour f, $\not{D} = \gamma_\mu(\partial_\mu - i\alpha_s A_\mu)$ is the covariant derivative, and by projecting out the left and right handed parts we see that there is a $U(N_f)_L \times U(N_f)_R \sim SU(N_f)_L \times SU(N_f)_R \times U(1)_B$ symmetry. $U(1)_B$ is the vector baryon symmetry and the $U(1)_A$ is neglected due to being broken at the quantum level. This symmetry is known as *chiral symmetry*. It is an exact symmetry at zero quark mass, breaks to an exact $SU(N_f)_V$ symmetry at non-zero but equal quark mass, and is broken explicitly when the masses are non-zero and not equal.

Even in the case that we have masssless quarks the QCD vacuum spontaneously breaks the $SU(N_f)_L \times SU(N_f)_R \to SU(N_f)_V$ due to the formation of a quark condensate, $\langle \bar{q}_{R,f_i} q_{L,f_j} \rangle = \Lambda^3 \delta_{ij}$ where we associate the dimensionfull $[\Lambda] = 1$ parameter Λ with Λ_{QCD} [1]. The $N_f^2 - 1$ broken generators have turned into massless Goldstone bosons made up of quark-antiquark pairs (i.e mesons) called pions.

[1] Λ_{QCD} is the only dimensionfull parameter in QCD, furthermore it is roughly the scale where non-perturbative effects are no longer negligible at around $200 - 300 MeV$.

However, as we know, the quarks are not massless, so what happens to the Goldstone bosons?

The point is that the three lightest quarks u, d, s are much lighter than the heavier quarks t, b, c and have mass well below Λ_{QCD}. We can say that the chiral symmetry $SU(3)_L \times SU(3)_R$ is approximately obeyed. Furthermore the u, d quarks mass are noticeable smaller than s and form a stronger chiral symmetry $SU(2)_L \times SU(2)_R$. When $SU(2)_L \times SU(2)_R \to SU(2)_V$ spontaneously breaks due to the condensate we get 3 massive pseduo-Goldstone bosons - the pions. When $SU(3)_L \times SU(3)_R \to SU(3)_V$ spontaneously breaks we instead get 4 kaons, 3 pions and an eta meson, the eight lightest mesons.

Standard practice of making predictions in QCD follows perturbation theory where interactions are expanded in loop-order with each order of loop carrying higher powers of coupling parameter α_s. In QCD α_s can be calculated from the β function as,

$$\alpha_s = \frac{\alpha_0}{1 + \frac{\alpha_0[11/3N_c - 2/3N_f]}{4} \ln|\frac{\mu^2}{\mu_0^2}|} \tag{3.2}$$

where μ (not to be confused with the chemical potential) is the renormalisation energy scale, $N_{c/f}$ the number of colours and flavours in the theory and α_0/μ_0 give a reference scale at some μ_0. Following convention, we use the mass of the Z-boson as the reference scale and relate the renormalisation energy scale to the momentum transfer Q. The resulting running of α_s is plotted in fig. 3.2.

While α_s is small we say that we are in the perturbative regime of QCD (i.e with energies much larger than Λ_{QCD}) and QCD is therefore a good model of the system that we wish to calculate. However, at low energies we do not find individual quarks and gluons but instead bound objects like mesons and baryons. This is due to the aforementioned property of confinement and is reflected in the fact that α_s grows with decreasing energy. Ultimately this means that QCD, a theory of quarks and gluons, is the wrong effective description at low energy, and instead we should have a theory of bound particles. This is what is done in chiral perturbation theory (χPT) [55]. However, we then have the opposite problem, when energies are increased we expect χPT to break down as we transition back to a theory of quarks and gluons. There is therefore a middle ground where neither an effective field theory description nor QCD works. It is this middle ground that is of extreme theoretical and experimental interest.

As an example, we take a look at the conjectured phase diagram for QCD in fig 3.3. There are various different phases of matter. At low temperature and baryon chemical potential we are in the regime with confinement; the degrees of freedom are mesons, baryons and other bound pairs of quarks and gluons like tetraquarks, pentaquarks and even hypothetical glueballs. This is also the regime where chiral symmetry (χS) is broken and a fermion-fermion condensate has formed. As temperature or chemical potential is increased the bound pairs 'melt' (or are so tightly

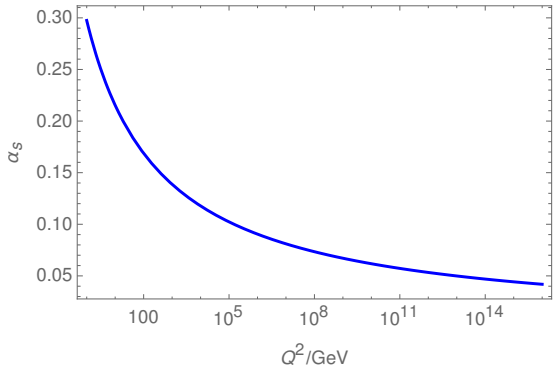

FIGURE 3.2: Running of the QCD coupling parameter, α_s as a function of energy scale Q. The Z-boson mass has been used as the reference scale. We see that at high energies that we are in the regime of asymptotic freedom. At small energies the coupling parameter increases signaling a breakdown of the theory.

packed they cannot tell which pair they are bound to) and we transition into a phase of matter called the quark-gluon plasma (QGP). The QGP is a phase of matter where the quarks and gluons are now deconfined and χS has been restored. The existence of such a phase has been experimentally verified via the Relativistic Heavy Ion Collider (RHIC) and the Large Hadron Collider (LHC) at low μ [7]. At $\mu = 0$ the phase transition has been calculated using lattice QCD and is found to be a cross-over for massive quarks and second-order for massless [8]. However since lattice QCD breaks down in the positive chemical potential regime due to the sign problem it can tell us little more [2]. In the other direction QCD models predict a first-order transition at lower temperature that is represented by the blue line in fig 3.3 [57, 58]. A critical end point should therefore link the change in transition order [9].

The location of the phase transition is exactly where neither perturbative QCD or χPT work - it is in the strong coupling regime. Therefore nearly all the phase diagram in that regime is merely conjectured. Where is the critial point? Is the phase transition really first order? Do confinement and chiral symmetry breaking occur at the same scale, or are they separate?

Furthermore there are theorised exotic phases of matter with high chemical potential. Moving along the μ axis at low temperature we first encounter a liquid-gas nuclear phase transition (red line) where the hadronic gas transitions into the normal liquid-like phase of nuclear matter [59]. What happens beyond that is somewhat of a mystery and depends on whether the blue first order line does indeed extend all the way to $T = 0$. It is possible that χS restoration and confinement/deconfinement transitions occur at different locations on the phase diagram, as well as for a density for the quarks to switch on. This could lead to deconfined χSB phases as well as confined χS 'quarkyonic' matter [46, 60]. At high μ we enter the the colour superconducting phase. At low temperatures certain metals can transition to a

[2] There are some efforts in extending lattice QCD to μ_R see [56] for details.

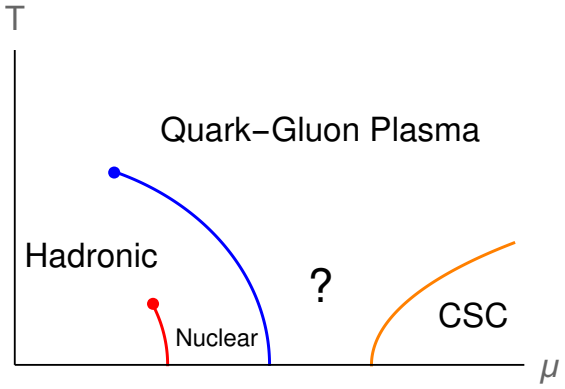

FIGURE 3.3: Conjectured phase diagram of QCD with temperature plotted against bayon chemical potential. At high temperature and chemical potential we are in the quark-gluon plasma phase (deconfined + χS). At low temperature and chemical potential we are in the hadronic phase (confined + χSB). At low temperature but growing chemical potential we first enter a nuclear phase before enevntually reaching a colour superconductor phase with potential colour locking dynamics. The quastion mark denotes a potentially new and unknown phase.

superconducting phase where electrons pair up to form a condensate of Cooper pairs. At high μ and low T it is theorised that quarks can do the same thing, see [61] for details.

For the middle ground of the QCD phase diagram it looks like we have no tractable theory. Clearly this is a good place to make use of the gauge-gravity duality. But before going any further we should set off some alarm bells. In what follows it is impossible to say that what we are studying *is* QCD - for a start, in the basic $\mathcal{N} = 4$ SYM theory there is no confinement, nor is there a chiral condensate or fundamental matter. Instead, the aim must be to look for universalities or expose hitherto unknown properties and structure of the system that can then be exploited to make progress with real QCD.

There are various different gauge-gravity duality phase diagrams. Here we make use of the phase diagram outlined in [46] where the $D3/D7$ system was used with zero quark mass in the UV and a magnetic field turned on to spontaneously break chiral symmetry. The system is outlined in the next section. We then proceed to turn on an imaginary chemical potential, μ_I. The goal of doing so is to ask how clearly, if at all, can we identify the position of the critical point from the study of the phase diagram at imaginary chemical potential, μ_I, low values of real chemical potential, μ_R, or from isolated data points as if from heavy ion collision data. The hope is that by asking these questions in a solved theory we might generate new ideas that might apply to QCD.

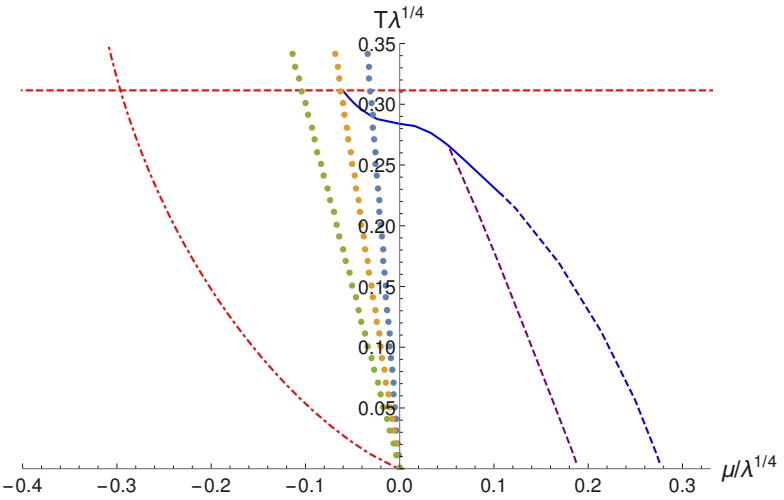

FIGURE 3.4: The phase diagram of the $\mathcal{N} = 2$ theory with a magnetic field. T and μ here are expressed in units of the magnetic field $\sqrt{B}$. The positive μ axis is real μ_R whilst negative μ correspond to imaginary μ_I values. The blue line is the chiral restoration transition (solid is first order, dashed second order); the purple line is the second order transition associated with the onset of density. The horizontal red dashed line shows where the chirally broken vacuum ceases to be a turning point of the effective potential - in the imaginary μ_I plane above this line the effective potential is unbounded. The curved red dashed line shows where vacua with density becomes unstable - to the left in the imaginary μ_I plane there are again instabilities. The dotted lines show the positions of the Roberge Weiss transition for $N_c\lambda^{1/2} = 10\pi$ (blue), 5π (orange) and 3π (green).

3.2 Spontaneous chiral symmetry breaking in D3/D7

Recall that in the introduction we outlined a basic $D3/D7$ model: $\mathcal{N}$=2 SYM theory consisting of a small number of quarks interacting with $\mathcal{N}$=4 gauge fields [44]. For the particular case of introducing a baryon number magnetic field [62], which breaks the supersymmetry and conformal symmetry, the phase diagram is precisely known [46] (see the right hand side, real chemical potential, μ_R, part of fig 3.4). At low temperature, T, and density the preferred phase is characterized by a chiral symmetry breaking quark condensate. Note, the model does not include confinement.

In the holographic model we study the temperature transition is first order whilst the transition with chemical potential is continuous (in fact it splits into two continuous transitions one at which the mesons of the theory melt [63] and density switches on and a second at which chiral symmetry is restored). There are critical points for each transition. The theory, though distinct in detail from QCD, at least has some of the generic features of interest.

The following discussion mimicks that in the introduction but now with non-zero magnetic field. For completeness the whole calculation is presented.

At zero temperature we use an $AdS_5 \times S^5$ geometry with coordinates

$$ds^2 = \frac{\rho^2}{L^2} dx_4^2 + \frac{L^2}{\rho^2} \left(dr^2 + r^2 d\Omega_3^2 + dR^2 + R^2 d\Omega_1^2 \right) \tag{3.3}$$

where we have split the coordinates into the x_{3+1} of the gauge theory, the r and Ω_3 which will be on the D7 brane world-volume and two directions transverse to the D7, R, ϕ. The radial coordinate, $\rho^2 = r^2 + R^2$, corresponds to the energy scale of the gauge theory and radius of the space is $L^4 = 4\pi g_{uv}^2 N_c \alpha'^2$.

We will introduce a D7 probe brane into the geometry to include quarks - the probe approximation is equivalent to working in a quenched approximation. This system has a $U(1)_A$ axial symmetry on the quarks, corresponding to rotations in the angle ϕ, which will be broken by the formation of a quark condensate.

We seek D7 embedding functions $R(r)$ at some fixed ϕ. The Dirac Born Infeld action is

$$\begin{aligned} S_{D7} &= -N_f T_7 \int d^8\xi e^{\phi} \sqrt{-\det(P[G]_{ab} + 2\pi\alpha' F_{ab})} \\ &= -N_f \overline{T_7} \int d^4x\, dr\, r^3 \beta \sqrt{1 + (\partial_r R)^2} \end{aligned} \tag{3.4}$$

where $T_7 = 1/(2\pi)^7 \alpha'^4$ and $\overline{T_7} = 2\pi^2 T_7 / g_s$ after integrating over the 3-sphere on the D7. The factor of β appears when a magnetic field is introduced through eg $F_{12} = B/2\pi\alpha'$ [62]

$$\beta = \sqrt{1 + \frac{B^2 L^4}{(r^2 + R^2)^2}} \tag{3.5}$$

Note that it enters as an effective dilaton term although it's origin is in the DBI action.

The equation of motion for the embedding function is therefore

$$\partial_r \left[\frac{\beta r^3 \partial_r R}{\sqrt{1 + (\partial_r R)^2}} \right] - 2R r^3 \sqrt{1 + (\partial_r R)^2} \frac{\partial \beta}{\partial \rho^2} = 0 \tag{3.6}$$

As we have previously seen (2.63), the UV asymptotic of this equation has solutions of the form

$$R = m + \frac{c}{r^2} + ... \tag{3.7}$$

where we interpret m as the quark mass ($m_q = m/2\pi\alpha'$) and c is proportional to the quark condensate.

There is always a solution $R = 0$ which corresponds to a massless quark with zero quark condensate ($c = 0$). However, for forms of β such as that in (3.5) which grow near the origin there are symmetry breaking solutions that have $m = 0$ in the UV but bend off axis (at a particular, symmetry breaking, value of ϕ) to end on the R axis with $R'(0) = 0$. These "Minkowski" embeddings are the minimum of the effective

potential (computed by evaluating minus the action on the solution). The $R = 0$ embedding is a local maximum of the potential.

Temperature can be included in the theory by using the AdS-Schwarzschild black hole metric as proposed by Witten [32]. The metric is

$$ds^2 = -\frac{K(\rho)}{L^2}dt^2 + \frac{L^2}{K(\rho)}d\rho^2 + \frac{\rho^2}{L^2}d\vec{x}_3^2 + L^2 d\Omega_5^2 \tag{3.8}$$

$$K(\rho) = \rho^2 - \frac{\rho_H^4}{\rho^2}\,, \qquad \rho_H := \pi L^2 T\,. \tag{3.9}$$

where ρ_H is a dimension one parameter identified with temperature T.

It is helpful to make the coordinate transformation [64]

$$\frac{\rho d\rho}{(\rho^4 - \rho_H^4)^{1/2}} \equiv \frac{dw}{w} \tag{3.10}$$

$$2w^2 = \rho^2 + \sqrt{\rho^4 - \rho_H^4}\,, \tag{3.11}$$

with $\sqrt{2}w_H = \rho_H$. The metric becomes

$$\begin{aligned} ds^2 \;\; &= \;\; \tfrac{w^2}{L^2}(-g_t dt^2 + g_x d\vec{x}^2) \\ &\quad + \tfrac{L^2}{w^2}(dr^2 + r^2 d\Omega_3^2 + dR^2 + R^2 d\Omega_1^2), \end{aligned} \tag{3.12}$$

where

$$g_t = \frac{(w^4 - w_H^4)^2}{w^4(w^4 + w_H^4)}\,, \qquad g_x = \frac{w^4 + w_H^4}{w^4}\,. \tag{3.13}$$

$$w = \sqrt{r^2 + R^2}\,, \quad r = w\sin\theta\,. \quad R = w\cos\theta\,, \tag{3.14}$$

The Lagrangian for the magnetic field case becomes,

$$\begin{aligned} \mathcal{L} \;\; &= \;\; -\overline{T_7} r^3 \left(1 - \tfrac{w_H^4}{w^4}\right)\sqrt{1 + (\partial_r R)^2} \\ &\quad \times \sqrt{\left(1 + \tfrac{w_H^4}{w^4}\right)^2 + \tfrac{L^4 B^2}{w^4}} \end{aligned} \tag{3.15}$$

The embedding equation for $R(r)$ is straightforward to derive. Minkowski embeddings exist until the black hole horizon "eats" the central area of the $r - R$ plane. The flat $R = 0$ embedding always exists and so there is a first order transition from Minkowski to flat at a critical value of T [1, 64].

A chemical potential is introduced through the U(1) baryon number gauge field A_t component [65] which enters the DBI action as

$$\begin{aligned}\mathcal{L} &= -\overline{T_7} r^3 \left(1-\tfrac{w_H^4}{w^4}\right)\sqrt{\left(1+\tfrac{w_H^4}{w^4}\right)^2+\tfrac{L^4B^2}{w^4}} \\ &\quad \sqrt{1+(\partial_r R)^2)-\tfrac{w^4(w^4+w_H^4)}{(w^4-w_H^4)^2}(2\pi\alpha' A_t)^2}\end{aligned} \tag{3.16}$$

There is a conserved quantity d (the density) associated with A_t. We can Legendre transform the action to write A_t in terms of d leaving (after rescaling all dimensionful objects to be in units of $L\sqrt{B}$ donoted by the tildes)

$$\tilde{\mathcal{L}} = -\overline{T_7}\frac{\tilde{w}^4-\tilde{w}_H^4}{\tilde{w}^4}\sqrt{K(1+(\partial_{\tilde{r}}\tilde{R})^2)} \tag{3.17}$$

$$K = \tilde{r}^6\left(\frac{\tilde{w}^4+\tilde{w}_H^4}{\tilde{w}^4}\right)^2+\frac{\tilde{r}^6}{\tilde{w}^4}+\frac{\tilde{w}^4\tilde{d}^2}{\tilde{w}^4+\tilde{w}_H^4} \tag{3.18}$$

Given a solution for R at some T, d one can then find the chemical potential as

$$\tilde{\mu} = \tilde{d}\int_{\tilde{r}_H}^{\infty} d\tilde{r}\frac{\tilde{w}^4-\tilde{w}_H^4}{\tilde{w}^4+\tilde{w}_H^4}\sqrt{\frac{1+(\partial_{\tilde{r}}\tilde{R})^2}{K}} \tag{3.19}$$

At small T the appropriate solutions as d begins to grow from zero are solutions that end on the black hole horizon at the origin but "spike" up to the form of the Minkowski embedding. There is a corresponding non-zero critical μ for the on-set of d. There is a continuous transition here as the Minkowski embedding becomes a black hole ending embedding. As d then increases the black hole solution smoothly evoles to merge with the flat $R = 0$ embedding in a second continuous transition (where chiral symmetry breaking switches off) at a higher critical μ.

The full $\mu - T$ phase diagram is discussed in detail in [46]. Here we use two techniques to find the transition lines that will interest us:

1) To locate first order transitions: At a fixed T, d we seek Minkowski embeddings and then evaluate the difference in free energy between these and the $R = 0$ embedding. We then vary d to locate the first order transition point where these embeddings are degenerate in energy. One then repeats at all T.

2) To locate second order transitions: at fixed T, d we find embeddings shooting off the black hole surface from an angle θ and read off the UV asymptotic value of m. Now varying d we seek points where massless solutions merge with the flat embedding at $\theta = \pi/2$ or the Minkowski embedding at $\theta = 0$ or points where two new solutions emerge. Again one repeats at all T.

Before moving on it is worth pausing to write the phyiscal temperature and chemical potential in terms of μ, w_H and the physical B field that emerge from (3.17)

and (3.19). We have

$$T_{\rm phys} = \frac{\sqrt{2}\tilde{w}_H}{\pi L^2} L\sqrt{2\pi\alpha' B_{\rm phys}} = \frac{2\tilde{w}_H}{\sqrt{\pi}\lambda^{1/4}}\sqrt{B_{\rm phys}} \tag{3.20}$$

$$\mu_{\rm phys} = \frac{\tilde{\mu}}{2\pi\alpha'} L\sqrt{2\pi\alpha' B_{\rm phys}} = \frac{\tilde{\mu}\lambda^{1/4}}{\sqrt{2\pi}}\sqrt{B_{\rm phys}} \tag{3.21}$$

Note that these are independent of α' as they must be since $\alpha' \to 0$ in the supergravity limit. In our plots we plot $\mu_{\rm phys}/\lambda^{1/4}$ against $\lambda^{1/4}T_{\rm phys}$ and set $\sqrt{B_{\rm phys}} = 1$.

3.3 The Imaginary Phase Diagram

Imaginary chemical potential solutions are found by simply allowing $A_t \to iA_t$ or $d \to id$ and repeating the process. The lagrangian with imaginary chemical potential is unchange except in the factor K in equation (3.18) where $d^2 \to -d^2$.

A previous analysis [66] of the D3/D7 system (without a magnetic field) has concentrated on the Roberge-Weiss transitions [67] of such theories (see also the holographic work in [68, 69, 70] and most recently [71]). Here the key physics is that a spurious $U(1)_B$ transformation with parameter $\alpha = \mu_I x$ can remove the chemical potential from the action. The quark fields are rotated by $e^{i\alpha}$ such that the baryonic operators have a discontinuity in their boundary conditions around the thermal circle. In the case where the resulting phase difference is a multiple of $2\pi T/N_c$ (with N_c the number of colours) a gauge transformation that differs around the thermal circle by an element of the centre of the group can be used to remove μ_I completely. The $\mu_I = 0$ and $\mu_I = 2\pi T/N_c$ theories are therefore identical. The result is that there must be first order transitions at

$$\mu_I/T = (2k+1)\pi/N_c, \qquad k = 0, 1, 2... \tag{3.22}$$

At very large N_c these become very dense and begin essentially at $\mu_I = 0$. Our hope is that at lower N_c near, for example, $N_c = 3$ they become less dense and pushed out to large μ_I so they can be neglected. Nevertheless we hope that $N_c = 3$ is close enough to large N_c that aspects of our analysis remain useful. In particular in fig 3.4 the first transition occurs on the line,

$$\lambda^{1/4}T = \frac{N_c\lambda^{1/2}}{\pi} \quad \frac{\mu}{\lambda^{1/4}} \tag{3.23}$$

We have plotted the transition line for $N_c\lambda^{1/2} = 10\pi, 5\pi$ and 3π in fig 3.4 and for $N_c\lambda^{1/2} \leq 5\pi$ all the physics we will use is present. This is still strong coupling.

In practice we just concentrate on the role of μ_I in the DBI action for the probe branes in Schwarzschild AdS_5 describing the quarks. The result is shown on the left in fig 3.4 - the first order transition extends a little way into the μ_I piece of the $\mu - T$ plane before the theory becomes unstable. We have checked that the transition line is

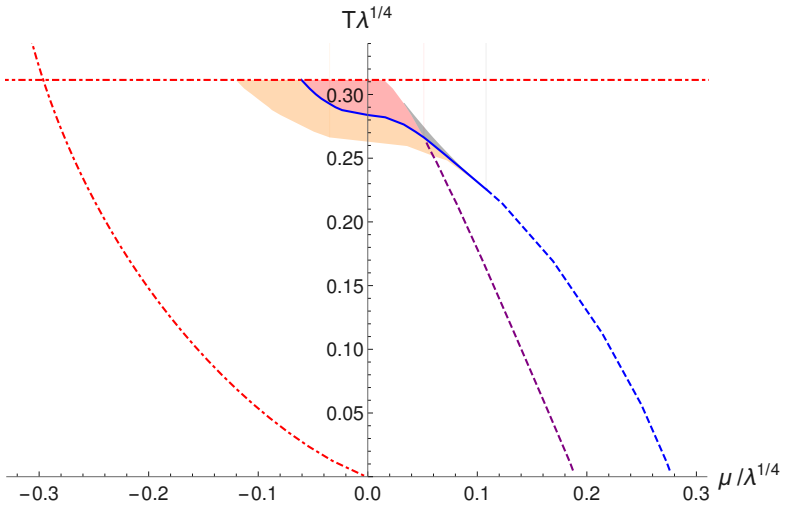

FIGURE 3.5: The phase diagram of the $\mathcal{N} = 2$ theory with B field from fig 3.4 but now in addition showing regions with metastable vacua. In the orange shaded region the chirally symmetric vacuum is metastable. In the red region the chirally broken vacuum with zero density is metastable. There is also a small grey region where a chirally broken, dense state is metastable which is addressed carefully in Section 3.3.1. The boundaries of the metastable regions and the transition lines themselves converge close to the region with the critcal points - the shaded region "points" to the critical point region.

linear in μ^2 across the $\mu = 0$ axis as one would expect. Instabilities exist at μ_I to the left or above the red dotted lines in fig 3.4 as we will discuss. Again if $N_c\lambda^{1/2} > 5\pi$ then the Roberge Weiss transition occurs before any of the instabilities set in and this may indicate that this is the smallest value of $N_c\lambda^{1/2}$ compatible with the large N_c analysis - this limit is sufficient for our purposes. As shown, at this stage, there is little to be deduced for the real chemcial potential, μ_R, region.

The theory, however, contains more information than just the ground state. We can find all turning points of the effective potential and it's interesting to track these and show in which regions of the parameter space there are metastable vacua (also sometimes called spinoidal regions - for example in [72, 73]). The metastable states exist in a band around the first order transition. This is shown in fig 3.5 where the shaded regions indicate the presence of metastable vacua. On the outer edges of this band the peak in the effective potential between the true vacuum and the false vacuum merge with the false vacuum (there is some structure to this boundary in this model that we will elaborate on in the following section) as the metastable vacuum disappears. These boundaries, which are distinct from the first order transition line, smoothly become the second order transition line(s) at the critical points. There are therefore actually three lines we can draw which must converge at, or near, the critical point. If one can identify these lines at finite μ_I or at low μ_R, as one can here, then extrapolation provides a sensible guess to the position of the critical point (one could reasonably estimate the T, μ values at the critical point at the 10% level).

Having just a single theory, of course, makes it hard to learn generic lessons but equally fully solvable models are scarce. Previously [74] applied some "bottom up" parameters to this model that allows us to move the position of the critical point and even change the order of the phase transitions. An example, that we will use here, is a parameter in the black hole emblackening factor which distorts the horizon from a sphere to an ellipse. Whilst this is not a full solution of the supergravity equations it does at least encode the breaking of the symmetry between the directions parallel and perpendicular to the D7 branes so may be indicative of the behaviour of a backreacted D3/D7 solution. The parameter can be used to move the chiral symmetry breaking critical point towards $\mu_R = 0$ and we show here it can even push it through the axis into the μ_I plane leaving the pure temperature transition second order. We repeat our study in some of these cases to show how generic our conclusions are and to display some other possible structures.

In the final section we will try to draw lessons on possible structures in both generic phase diagrams and for QCD. We speculate as to whether regions of the QCD phase diagram accessible to computation on the lattice might contain metastable vacua, in which case the boundarries of these regions could be used to point to the critical point. Also the second order transition line may separate in the μ_I plane into several transitions, including one for the onset of density and another for chiral symmetry restoration - these two lines might point to the critical point. In practice these transitions will be blurred into the crossover transition though and are likely very hard to spot even if they exist.

Heavy ion collision data might also be able to identify regions of the phase diagram with metastable vacua. In such regions there might be events in which the vacuum becomes caught for a period in the metastable state. It is possible that such states will hadronize differently and form an identifiably distinct set of events indicating that the theory is in a region with metastable vacua. This again might help distinguish boundaries of the regions with metastable vacua. See [75] for a recent summary of heavy ion collision searches for the QCD critical point.

3.3.1 The Phase Structure

To begin we present a detailed example of how we obtain the phase transitons. We take the case of $T = 0.26$ that can be seen in slice 4 in fig 3.8.

We plot example D7 embeddings in the left-hand figure in fig 3.6. In red is the Minkowski embedding with $\tilde{d} = 0$; orange is the flat embedding $\tilde{R} = 0$ with $\tilde{d} \neq 0$. In between we plot some black hole embedings. These are found from the right-hand plot in fig 3.6 - here at a given $\tilde{d}$ we shoot off the horizon at different angles θ and plot the resulting UV mass value $\tilde{m}$ - we seek solutions with $\tilde{m} = 0$. As can be seen between $\tilde{d} = 0.03$ and $\tilde{d} = 0.07$ the number of solutions change as the minimum of the curve passes through the $\tilde{m} = 0$ axis. This corresponds to the pair creation of two black hole solutions which we will call BH1 and BH2 - the two solutions emerge as the

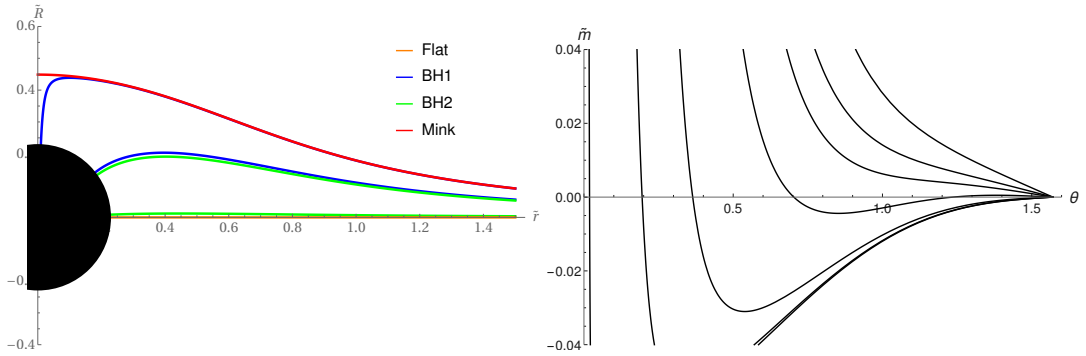

FIGURE 3.6: Detailed plots for the $\alpha = 1$ theory with T=0.26. (i)The top plot shows sample embedding functions (red Minkowski, Orange flat, BH1 in green and BH2 in blue. (ii) the second plot shows the UV mass of embeddings emerging at angle θ from the black hole as a function of d (for values d =0.001, 0.01, 0.03, 0.07, 0.1, 0.12, 0.15 from left to right)

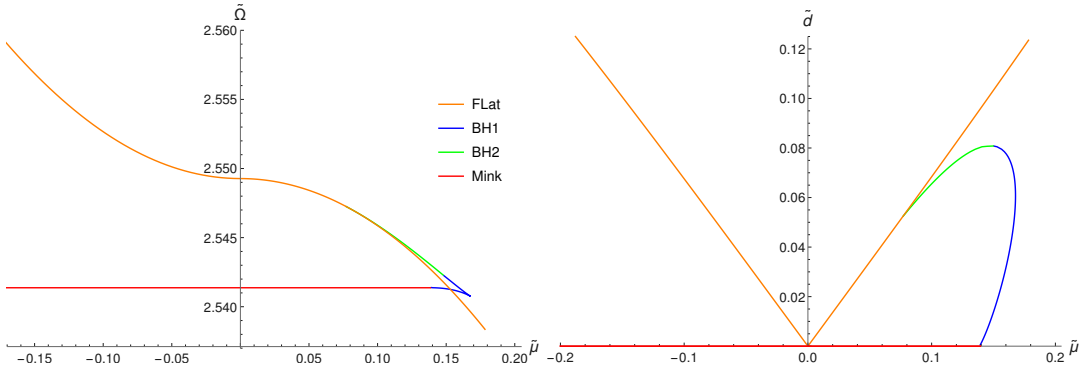

FIGURE 3.7: Detailed plots for the $\alpha = 1$ theory with T=0.26. (i) the third plot shows the free energy of the solutions against μ. (ii) the fourth plot shows d vs μ for the solutions.

closest green and blue black hole solutions in the top plot. By following the evolution of the two solutions in the second plot it can be seen that one moves to merge with the Minkowski embedding and the other with the flat embedding - the outer two blue and green embeddings in the top plot.

Now we can, embedding by embedding, compute $\tilde{\mu}$ from (3.19) and the free energy $\tilde{\Omega} = -\tilde{\mathcal{L}}$ in (3.16) . We plot $\tilde{\Omega}$ against $\tilde{\mu}$ for our solutions in the left-hand plot and $\tilde{d}$ versus $\tilde{\mu}$ in the right-hand plot in fig 3.7.

The free energy plot allows us to clearly see the phase structure along the slice, from left to right. At imaginary $\tilde{\mu}_I$ the Minkowski embedding is the lowest energy state and the flat embedding is the maxiumum of the potential. The first transition is where a BH2 solution emerges from the flat embedding - the flat embedding has become a local minimum of the potential. Next a BH1 solution emerges from thre Minkowski embedding and has lower energy - there is second order transition to the BH1 state as density switches on (we do not plot the continuation of the Minkowski embedding red line in the plot further to the right although it does continue to exist).

There is then a first order transition from the BH1 embedding to the flat embedding. The BH1 state is a metastable state briefly although with energy quite near the flat embedding of the true vacuum. Finally the BH1 solution ceases to exist merging with a BH1 solution that is the continuation of the BH2 state that is the local potential maximum. Note that the annihilation of the BH1 and BH2 solution as identified in the density plots is an innocuous transition when plotted with $\tilde{\mu}$.

Repeating the above contruction for all temperature slices we can build the phase diagram for the model in fig 3.4 (the positive μ axis is μ_R the negative axis μ_I). In the phase including $T = \mu = 0$ the vacuum is characterized by chiral symmetry breaking and zero density (it is a so called Minkowski embedding in the brane picture). At high T, μ_R the vacuum is a chirally symmetric state with generically melted mesons and non-zero density (these are flat embeddings). At low μ_R there is a first order thermal transition between these vacua as T grows. At larger μ_R there is a region with a third low T vacuum which has a density of deconfined quarks but which are still massive due to chiral symmetry breaking (a black hole embedding). The chiral restoration transition has a critical point where the transition becomes second order. The transition from the low T, μ_R phase to the deconfined massive quark phase is second order. The transition from that phase to the chirally symmetric phase is also second order.

Our first new results here are that we have extended the phase structure to imaginary chemical potential, μ_I. This is shown on the left hand side of fig 3.4. Note we have checked in all our figures to come that the transition line is linear in μ^2 across the $\mu = 0$ axis as one would expect. The first order chiral transition extends into the imaginary μ plane before coming to a halt on the line at T=0.311 (shown by a red dashed line in fig 3.4). Above this value of T the remnant of the low T, μ chiral symmetry breaking vacua ceases to be a turning point of the effective potential. The Minkowski embedding can not exist above this value of T because the black hole is too large and blocks the IR of the solution. Note this is independent of μ since the Minkowski embedding simply has $A_t = \mu$ which does not contribute to the action. At real μ_R this state is no longer the true vacuum and this line simply marks where the state ceases to be a turning point of the potential. At larger μ_I though below the T=0.311 line the Minkowski embedding (chiral symmetry breaking state) is the true vacuum yet it suddenly vanishes at higher T. The only explanation is that at higher T, for these μ_I, the effective potential becomes unbounded at large values of the condensate. Thus above the line $T = 0.311$ the theory is ill-defined for μ_I - we will henceforth not consider temperature above that value.

In fig 3.4 there is a second dashed red line emerging from the origin and cutting the $T - \mu_I$ plane. To the left of this line the flat or black hole embeddings do not exist because the action turns imaginary . To make this explicit consider the parameter K of (3.18) which is square rooted in the action (3.16) - we can evaluate it near the black hole horizon. We set $w_H \sim T$ and remember $\omega^2 = r^2 + R^2$, where at the black hole

horizon we have $r \sim T\sin\theta$ and $R \sim T\cos\theta$, we have

$$\begin{aligned} K &= (T\sin\theta)^6 \left(\frac{((T\sin\theta)^2+(T\cos\theta)^2)^2+T^4}{((T\sin\theta)^2+(T\cos\theta)^2)^2}\right)^2 \\ &\quad + \frac{(T\sin\theta)^6}{((T\sin\theta)^2+(T\cos\theta)^2)^2} \\ &\quad - \frac{((T\sin\theta)^2+(T\cos\theta)^2)^2 d^2}{((T\sin\theta)^2+(T\cos\theta)^2)^2+T^4} \end{aligned} \tag{3.24}$$

The final negative term is trying to force the action to become imaginary. The first two positive terms both go as $\sin\theta$ so for a given temperature increasing density forces the minimum value of θ to take on larger values. For large enough d this value becomes $\pi/2$ and above this value of d there can be no further flat or black hole solutions. The curved red dotted line in fig 3.4 is where this criteria is met. This corresponds to another instability of the effective potential against moving to larger density. Thus our analysis will be restricted to the part of the μ_I plane bounded by the red dashed lines in fig 3.4. We note that very close to this boundary there are some additional black hole solutions but we will not investigate these further since we wish to focus around the critical point. As we mentioned in the introduction if $N_c\lambda^{1/2} \geq 5\pi$ then the instability regions are not part of the true vacuum of the theory because to the left of the Roberge Weiss transitions there are just repeats of the phyiscs to the right of the transition line in fig 3.4. This may indicate that this value of $N_c\lambda^{1/2}$ is the minimum possible value compatible with the large N_c limit - that minimum value is sufficient for our discussions here.

Let us now imagine that some theorist can compute at imaginary μ_I and only very low μ_R values and they are hoping to understand the large μ_R structure to see if there are one or more critical points in this case. Looking at fig 3.4 there is little to guide this theorist - he could perform a fit to the first order chiral transition line as it crosses the T axis and perhaps do a reasonable job of predicting where the transition contour is at real μ but there is apparently no hint as to where the critical point must lie.

To gain more insight our putative theorist could make use of more information that is available to him. In particular the first order transition is associated with a crossing of two distinct vacua and to either side one or the other is a metastable vacuum state. We can ask the question where are there metastable vacua in the plane?

The answer in this case is illustrated in fig 3.5. Here the orange region is where the chirally symmetric vacuum (flat embedding) is metastable. In the red shaded region the Minkowski embedding (chirally broken, $d = 0$ phase) is metastable. In the small gray region a black hole embedding (chirally broken but $d \neq 0$) is metastable.

To understand this picture better it is helpful to use it to reconstruct the effective potential of the model across a number of fixed T slices - see fig 3.8 where we zoom in on the interesting structure.

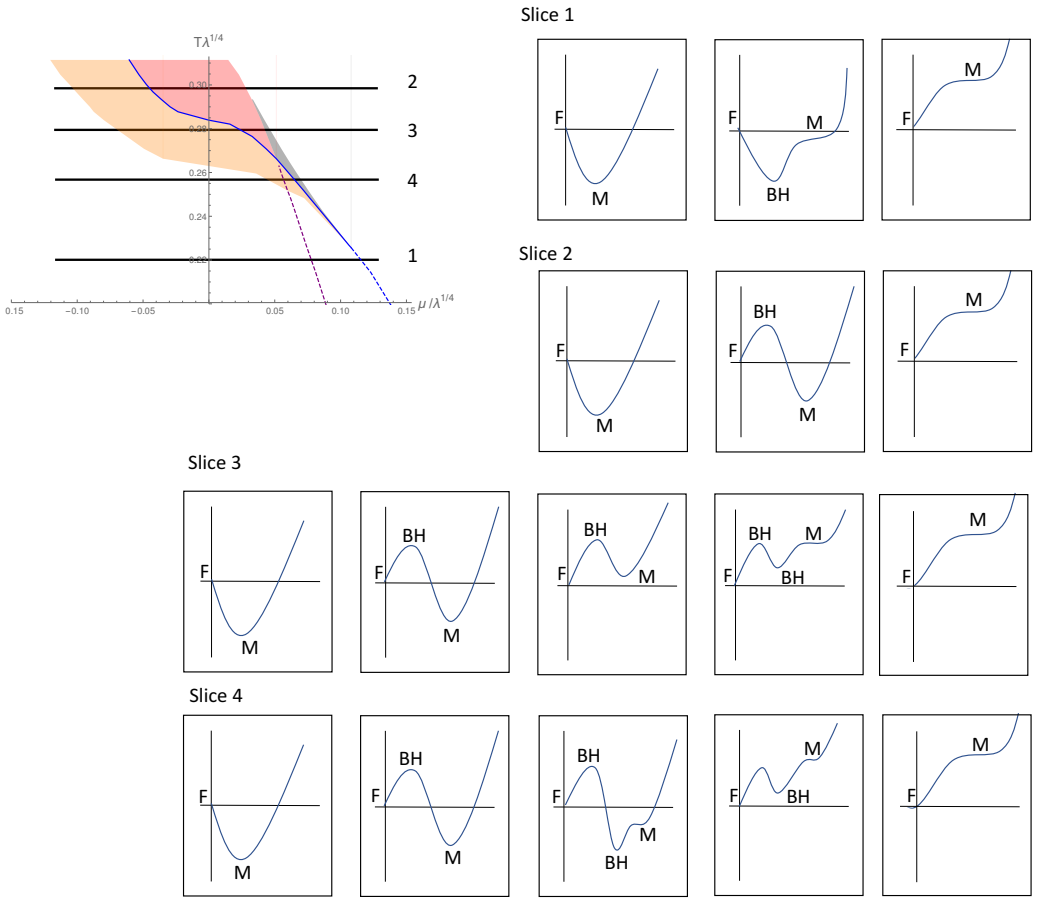

FIGURE 3.8: The structure of the effective potential against quark condensate as one moves from left to right across the phase diagram of the B field theory on a number of different T slices. Turning points of the potential are marked dependent by their nature: F (flat, chirally symmetric); BH (black hole, dense massive phase); M (Minkowski, chirally broken)

Slice one is at low temperature: starting at reasonably large imaginary μ_I the chiral symmetry breaking (zero density) phase is preferred (Minkowski embedding). As we track right a second order transition occurs to the deconfined massive quark phase (a black hole embedding emerges from the Minkowski embedding) - here we believe the chiral symmetry breaking vacuum turns into a point of inflection of the effective potential. Then sequentially a second order transition to the chirally symmetric (flat embedding) occurs - that is the black hole embedding merges with the flat embedding and then ceases to exist. Note here at no stage are there metastable vacua (we assume a point of inflection is insufficient to be visible either through lattice studies or by noticeable events in a heavy ion collider).

Moving now to large T - slice 2. To the left again the chirally broken vacuum dominates. As we track left to right the first event is that a peak in the effective

potential (black hole embedding) emerges from the chirally symmetric state as that state becomes a local minimum metastable vacuum. The chirally broken and chirally symmetric vacuum then interchange at a first order transition leaving the chirally broken phase as the metastable vacuum. The final change is that the chirally broken vacuum and the maximum of the potential merge to again leave the chirally broken phase remnant as a point of inflection.

Slices 3 and 4 show some more subtle structure around the critical points. Slice 3 follows slice 2 (moving to the right) until after the first order transition. Now the chirally broken remnant does not just merge with the potential peak but converts itself to a point of inflection throwing off a potential minimum that then moves to merge with the potential peak. In this intermediate region there is a metastable vacuum which is a deconfined massive quark phase (black hole embedding). Typically these minima are less deep than when the chirally broken or symmetric vacua are metastable. We show regions of the phase diagram with these metastable vacua in grey.

Slice 4 shows a further mixing of these events - the chirally broken vacuum converts to a deconfined massive quark phase at a second order transition before the first order transition. Thus the resulting first order transition is from the deconfined massive quark phase to the chirally symmetric phase.

A key observation is to follow the behaviour of the two boundaries where the chirally symmetric and chirally broken phase become metastable at high temperature - the boundaries of the red and orange regions. At each of these a black hole embedding merges with either the flat or Minkowski embedding. As one moves to lower T these boundaries become precisely the second order phase lines where again black hole embeddings merge with flat and Minkowski embeddings. Necessarily these boundaries of the metastable vacua region must join the transition lines at the critical points where the order of the transitions change. Further that these boundaries are distinct at high T naturally transforms to them being distinct at low T producing the three phases and two second order transitions we see.

The interesting thing about fig 3.5 in comparison to fig 3.4 is that whilst the latter simply has transition lines that apparently randomly convert their order, fig 3.5 essentially has arrows pointing to the critical points! In particular the boundary where the chirally broken phase becomes metastable and the transition line itself converge at the critical point for chiral symmetry breaking. Equally the boundary where the chirally symmetric phase becomes metastable and the transition line converge is the critical point on the transition line to the deconfined quark phase. Thus our putative theorist who can only compute at imaginary μ_I and low μ_R relative to T could try to identify the edges of the metastable regions and then extrapolate them to make an approximation as to the positions of the critical points.

If the theorist could also access heavy ion collision data from a variety of experiments then he could hope to identify whether in those experiments μ, T lie in

the metastable regions - for example one might expect two different categories of events, one which is ignorant of the metastable vacua and one of which got stuck in the metastable state for a period. These events could plausibly have different signatures even after hadronization. One might be able to further map out the metastable region even if the critical point had not been hit directly.

3.3.2 Horizon Deformed Theories

So far we have only considered a single phase structure so one might wonder how generic any of the features we see are. In principle it would be good to study many other such holographic set ups yet the number of fully understood ones are few and far between. In the future it would be interesting to construct more eg based on the D4/D6 system [76]. For now, we will add a "bottom-up" parameter to our probe D3/D7 system with a B field which was first introduced in [46]. Of course "bottom-up" is synonymous for an incomplete model but the trick we use is instructive and allows us to rather simply move the critical point.

The trick is to deform the spacetime geometry by making the substitution

$$w^2 \to r^2 + \frac{1}{\alpha} R^2, \qquad \alpha > 1 \tag{3.25}$$

into the metric factors in (3.13). This is not a solution of the Einstein equations but it breaks the $r - R$ symmetry which at least would happen were one to backreact the D7 branes (they are extended in r but point like in R). More practically by squashing the black hole horizon onto the R axis it is harder for the black hole to disturb the Minkowski embeddings that describe the chirally broken vacuum. This change tends to favour second order chiral transitions with temperature. The test of the use of this approach is rather in what one learns by doing it. In fig 3.9 we display (zoomed to the interesting segments) phase diagrams for a variety of α's.

If one first concentrates on the phase lines then the effect of growing α is to push the critical point on the chiral line towards the T axis. At $\alpha = 1$ the critical point on the chiral transition line lay after the separation of the density onset transition. By $\alpha = 1.12$ the critical points on both these lines have moved together. At larger α the density line shows a period of first order behaviour after separating from the chiral transition line at the critical point.

Previous analysis [46] had seen that for big enough α one could make the $\mu = 0$ chiral transition second order but now we see that in fact we have pushed the critical point into the imaginary μ_I plane. It's fascinating to think that some deformation might do this in QCD itself!

The region of metastable vacua broadly speaking moves with the points but there are some new features which we highlight by sketching the effective potential for a couple of slices in the $\alpha = 1.12$ case - see fig 3.10. The first slice just highlights the meaning of the grey zones around the edge of the full metastable region. Moving

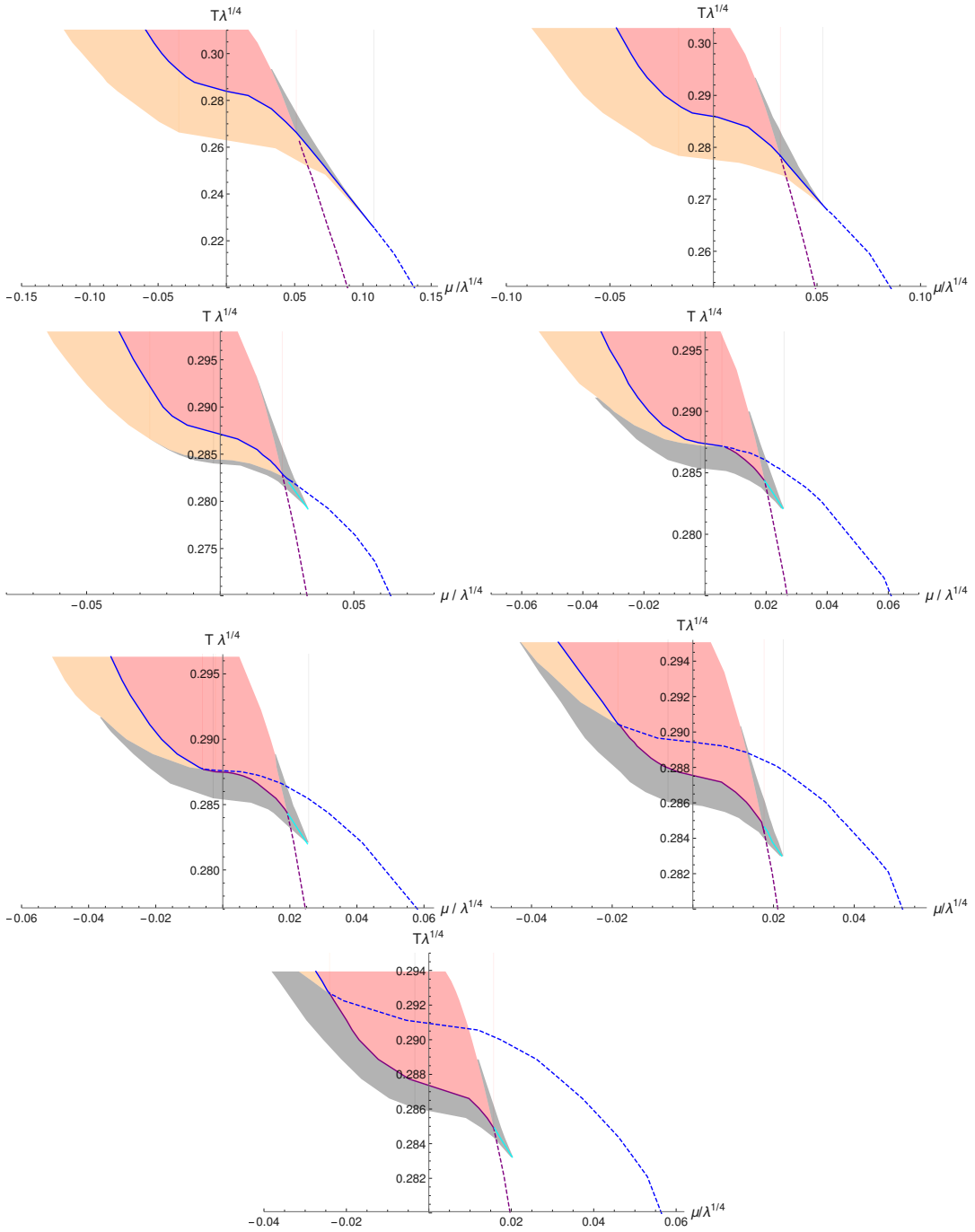

FIGURE 3.9: $T - \mu$ phase diagrams for the deformed theories with $\alpha = 1, 1.08, 1.12, 1.137, 1.139, 1.15, 1.16$.

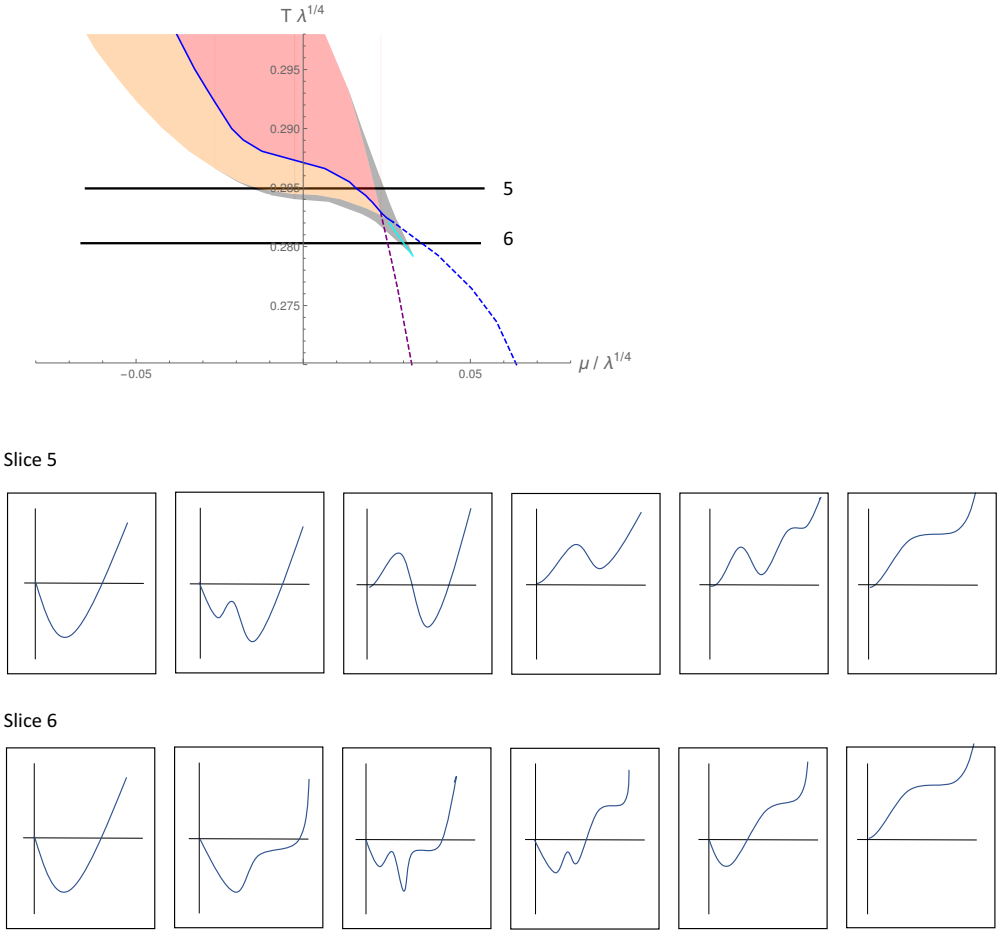

FIGURE 3.10: The effective potential evolution (vs c) from left to right as one moves along two T slices at $\alpha = 1.12$.

along slice 5 from the left to right the chirally symmetric embedding must become metastable from initially being a potential maximum. Previously it did this by casting out another maximum. Here however a maximum and a minimum pair create away from the chirally symmetric solution (both black hole solutions) and the minimum then merges with the chirally symmetric vacuum to convert it to a metastable minimum. Similarly after the first order transition the chirally broken remnant vacuum does not simply merge with the potential maximum but casts off another minimum (becoming a point of inflection) that annihilates the maximum. Thus in the grey zones there are metastable vacua with a massive deconfined quark phase. Since these are minima created between the previous maximum and minimum of the potential (the chirally broken and chiral restored vacua) the metastable vacuum is typically not very deep which suggest it would be harder to find either on the lattice or in heavy ion collision events.

Slice 6 shows a remnant of these "pair creation" events forming a "fishtail crossover" between the two second order transitions. Here after the chiral symmetry

breaking vacuum has second order transitioned to a massive deconfined quark phase a maximum and minium pair create. There is then a first order transition (the cyan line) between two massive deconfined quark phases. Finally the metastable vacuum annihilates with the maximum to allow a second order transition from the massive deconfined quark phase to the chirally symmetric phase. This explains the tail transition between the legs in these plots (which we view as a minor part of the story).

Let us again comment on the broad picture and lessons. The lines that mark the borders of where the chirally symmetric or chirally broken phases become metastable continue to play a crucial role. In all these phase diagrams these borders plus the first order phase line itself join at the critical points - in each case the two lines point at the critical point. Further these borders are distinct around the first order transition and then cross as they become the second order lines. Note even in the case where the two borders both cross at the critical point ($\alpha = 1.12$) they do not merge but separate again. This is the origin of the deconfined massive quark phase.

None of the cases we have seen have second order transitions at $\mu = 0$ and first order at $T = 0$ as expected in QCD. However, the cases where the critical point lies in the imaginary μ_I plane can allow us to speculate. Imagine now a putative theorist who (somehow) can only compute at real μ_R but not imaginary μ_I. In these cases the theorist would just see a second order chiral transition. In this model, however, if they could identify both the denisity onset transition and the chiral transition then those lines can be extrapolated to the critical point in the μ_I plane where he is ignorant.

3.3.3 General Lessons & Questions for the QCD Phase Strcuture

So far it has been interesting as a purely theoretical problem to investigate the structure in the phase diagram (extended to imaginary μ) of an exactly solvable gauge theory and amusing to look for signals of transitions and critical points in one part of the plane if one only had access to a sub-region. Have we learnt any lessons that could be applied more widely to a generic set of chiral symmetry breaking models (perhaps at large N_c) or even to QCD? We have concluded that looking for the regions of the phase diagram with metastable vacua can be used to identify the positions of the chiral critical point. Using this insight, in fig 3.11 we propose a number of qualitative pictures for theories where the transition is first order at at high μ_R and low T, but second order transitions at higher T and lower μ or at μ_I.

Let us begin by simply talking about theories without confinement that seem a natural extrapolation of the ones we have studied and ask in these worlds what lattice or heavy ion data could reveal. The first sketch in fig 3.11 shows the most pessimistic possible conclusion. Here we assume that the second order transitions (chiral cross over at finite mass) for density switching on and chiral restoration are degenerate and that the first order transition exists only at large real μ. The metastable region could be quite tightly positioned around the first order transition. Here there is little hope of using the lattice to idenitfy anything beyond the position of the second order line

which provides no information on the position of the critical point. Here one might hope to use heavy ion collisions at low T to identify T, μ points within the region with metastable vacua (again assuming that events that get stuck in the metastable vacua can be distinguished after hadronization).

The second sketch is a more hopeful speculation where the region with metastable vacua might be wider about the first order line - here one could hope to find regions of metastability at low T and low μ or even imaginary μ on the lattice. The second order phase transition line and the edge of the region of metastability converge at the critical point and could be used to point to it. Here we have also allowed a boundary region around the metastability region with a metastable massive deconfined quark phase. Tracking from left to right across the metastability region would have an effective potential that changes as in slice 5 of fig 3.10. Here the key question is whether the chirally symmetric vacuum converts from a maximum to a minimum directly by spitting out a maximum or whether a maximum and minimum are pair created elsewhere in the potential with that minimum then joining to the chirally symmetric vauum to make it a minimum. A priori both seem possible.

The third and fourth sketches show the structure one would expect if the chiral and density transitions separate. The critical line and one boundary of the metastable region meet at each critical point so could be used to predict its position.

Finally let us tentatively speculate for QCD. The first additional issue we must consider is confinement that is not included in the model we have used. We already know that at T=0 the first transition with μ is the first order switch on of baryon number. This transition might be distinct from the deconfined quark pictures we have drawn so far in which case the first 4 sketches could all lie to the right of the baryon onset transition. However, it also seems natural to associate the baryon density transition with the bottom of the density phase transition we have seen. The chiral transition is then separate but potentially also first order. We sketch such a set up in the final picture of fig 3.11. Here we appear to have drawn a deconfined, dense but chirally broken phase between two phase boundaries all along the transition. On the other hand we know that on the left hand boundary at low T these quarks should be confined and we should treat this as the baryonic phase. It is possible that within this region there is a transition where confinement switches off and a deconfined massive quark phase is realized (as speculated in [77]), but equally confinement may cover the whole phase region.

Note in this final picture the left hand red region is where the chirally broken vacua is metastable and the right most orange region where the chirally symmetric vacuum is metastable. The orange and red regions on the outer edges, in the language of our brane model, would be metastable dense and chirally broken vacua. If we believe our structures then these boundaries would continue beyond the critical region as further second order boundaries between a variety of dense yet chirally broken vacua. In QCD the full region between density switching on and chiral

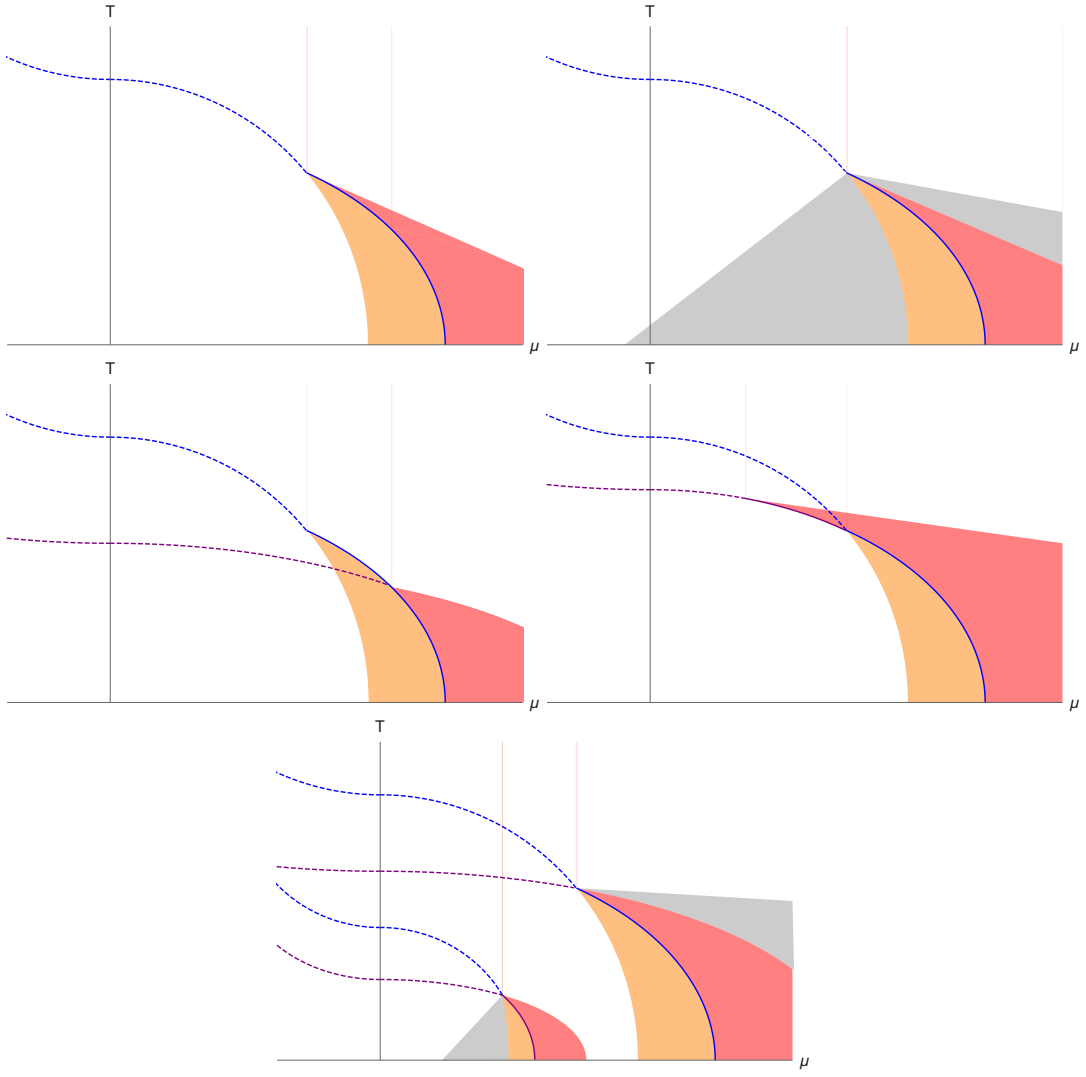

FIGURE 3.11: Here we present some speculative sketches for the phase diagrams of theories with first order transitions at high μ_R and low T, but second order transitions at higher T and lower μ or at μ_I. Here dashed lines are second order transitions; solid lines are first order transitions; in the red region the chiral symmetry breaking vacua is metastable; in the orange region the chirally symmetric vacuum is metastable; in grey regions dense massive quark phases are metastable. The final sketch shows the case that might apply to QCD where the density transition is linked to the known nuclear density onset and the chiral transition is separate (here the outer red and organge regions are metastable dense massive quark vacua).

symmetry being restored is the cross over region. Our model suggests there might be further second order transitions within that cross over region! In reality in QCD these are likely to be smoothed to cross overs and be very hard to spot if they exist at all. On the other hand at finite μ this cross over region might widen and allow more structure to be spotted (Fig 4 in [78] suggest the cross over region may widen at larger μ_R).

Finally we can again speculate that metastable vacua of some sort might exist over a wide region of the low T phase diagram that could be hunted for on the lattice at low μ_R or even at μ_I or that might display as new types of event in heavy ion collisions. Of course both are difficult and expensive technologies to use for such speculative searches.

To conclude we have seen that investigating the imaginary part of a completely soluble chiral symmetry breaking theory leads to the possibilities of new structure in the QCD phase diagram as well as potentially new methods to investigate its properties.

The first immediate thought to improve the model is to include confinement. This could be potentially achieved by considering soliton backgrounds where one of the spatial directions have been compactified. However to fully explore the transition between a soliton and black-hole background when using $D7$ branes would require backreaction. Other possibilities include studying 5D supergravity models as in [79]. Furthermore it would be interesting to explore other regions of the phase diagram such as in neutron-stars and the colour superconducting phase.

Ultimately the strongly-coupled region of the QCD phase diagram remains elusive. We hope by studying strongly-coupled theories like the one presented here that insight can be gained to the properties and structures hidden within the theory of QCD. Who knows what might be found.

Chapter 4

A Weyl-Semi Metal with Flavour

We construct a top-down holographic model of Weyl semimetal states using $(3+1)$-dimensional $\mathcal{N}=4$ supersymmetric $SU(N_c)$ Yang-Mills theory, at large N_c and strong coupling, coupled to a number $N_f \ll N_c$ of $\mathcal{N}=2$ hypermultiplets with mass m. A $U(1)$ subgroup of the R-symmetry acts on the hypermultiplet fermions as an axial symmetry. In the presence of a constant external axial gauge field in a spatial direction, b, we find the defining characteristic of a Weyl semi-metal: a quantum phase transition as m/b increases, from a topological state with non-zero anomalous Hall conductivity to a trivial insulator. The transition is first order. Remarkably, the anomalous Hall conductivity is independent of the hypermultiplet mass, taking the value dictated by the axial anomaly. At non-zero temperature the transition remains first order, and the anomalous Hall conductivity acquires non-trivial dependence on the hypermultiplet mass and temperature.

4.1 Strongly Coupled: CMT

In chapter 3 we saw that there are issues with standard techniques at strong coupling. These issues are not unique to QCD. Another field that struggles with non-perturbative physics is *condensed matter theory* (CMT), the field that aims at describing the phases of matter in different and often exotic materials. This is achieved by studying transport coefficients, sound modes and phase diagrams across the relevant parameter space of the system. In this introduction we give a short review of CMT and the issues at strong coupling.

CMT is a rich and diverse field with large potential. It has already helped explain phases of matter such as superconductors, superfluids, electron band structure, topological metals and more - often with symmetry (breaking) as its center pillar [17, 18, 80]. However, it relies on the assumption that the systems electrons are weakly interacting where effective field theory and quasiparticle descriptions are sufficient [17]. This is not the case when the electrons are strongly coupled. In fact there are few ways of describing strongly interacting condensed matter systems due to

the need of computing intractable microscopic Green's functions [1]. These systems often display exotic and intriguing behaviour making their theoretical understanding a priority in the field. Some examples include,

- *Quantum critical points*: Critical points of phase diagrams are of great interest. They mark the separation of different phase regimes and often have interesting properties. A quantum critical point (QCP) is one that occurs at zero temperature, where instead of the phase transition being thermally driven, it is driven by quantum fluctuations [48]. These points are spatially invariant (infinite coherence length) and often require strongly-coupled descriptions to extract important features such as transport. These QCP are also important away from zero temperature. In fact the phase regime dominated by the QCP can grow with temperature.

- *Non-BCS superconductors*: Bardeen-Cooper-Schrieffer theory is often used to describe superconductors where Fermi liquid theory (a brief introduction to Fermi liquid theory is given in chapter 5) is sufficient. These superconductors tend to have low-temperature transition between the superconducting phase and the normal phase. Non-BCS superconductors are so-called as they cannot be described using BCS theory [82]. An extreme example is the cuprate superconductors where the phase transition can occur at high temperatures, and since Fermi liquid theory (a weakly interacting model) fails it is dubbed a non-Fermi liquid.

- *Strange Metals* - Strange metals are a phase in heavy (i.e a very large effective mass) fermion compounds (and potentially also the cuprates above) that are realised by a QCP. They have strange non-Fermi liquid properties such as electrical resistivity scaling linearly with temperature [83]. They are often synonymous with non-Fermi liquids. More details of strange metals are given in chapter 5.

Clearly the cuprates, QCP and strange metals can be wrapped up as a single issue revolving around the break down of weakly interacting quasiparticle theory. It is also not difficult to imagine that these strongly coupled systems could unlock the next advancements in material science. Therefore it is of great interest to go beyond the weakly coupled paradigm and invent new theories that can make headway into understanding, and then manipulating, strongly coupled systems.

One possible route is to use the gauge/gravity duality. The duality is a good match for tackling strongly coupled CMT problems as many of the techniques used in CMT can be reproduced holographically. For example, in chapter 3 we were able to construct phase diagrams, and as outlined in the introduction transport coefficients

[1] Aside from holography the memory matrix method can be used, see [81] for details.

such as the conductivity can be calculated. In addition, the duality often relates to CFT such as those expected at QCP.

Once again it is worth pointing out that holography is looking for universalities or new structure. However since CMT utilises many effective descriptions this might alleviate the difficulty in matching to one theory alone, such as QCD or the standard model. One can even imagine that it may be possible to know which field theories admit a holographic dual. An experiment could then be devised whose effective description takes on a field theory with a known hologaphic dual, thus making experimental predictions of string theory a reality.

In this chapter we look at a recently-discovered class of materials: Weyl-semi metals, a sub-class of topological metals, and ask - what happens at strong coupling?

4.1.1 Topological Metals

Topological metals are metals that are...topologically protected.

To make this a little more concrete we consider the example of Weyl-semimetals, a class of recently-discovered materials in which two electronic bands touch at isolated points in momentum space at or near the Fermi surface, such that the low energy excitations near these nodal points are $(3+1)$-dimensional relativistic Weyl fermions, with the Fermi velocity playing the role of the speed of light [84, 85, 86, 87, 88].

If both parity (or inversion), $\mathcal{P}$, and time reversal, $\mathcal{T}$, are preserved then left- and right-handed Weyl fermions must appear in degenerate pairs. (For $\mathcal{T}$ this is the Kramers theorem.) Each such pair forms a Dirac fermion. To split the Dirac fermion into separate left- and right-handed Weyl fermions, either $\mathcal{T}$ or $\mathcal{P}$ must be broken. WSMs breaking either $\mathcal{P}$ or $\mathcal{T}$ have been experimentally discovered:
TaAs [10, 11, 12, 13] and its cousins TaP [89], NbAs [90], and NbP [89, 91] break $\mathcal{P}$ and preserve $\mathcal{T}$, whereas magnetic WSMs like $Co_3Sn_2S_2$ [92, 93] and Co_2MnGa [94] preserve $\mathcal{P}$ and break $\mathcal{T}$.

WSMs are "topological" materials in the following sense. Each Weyl point has an associated topological invariant: the integral of the Berry curvature over a surface enclosing the Weyl point is a Chern number ± 1, depending on the point's chirality, and zero otherwise [95]. This can be given formally as

$$C = \frac{1}{2\pi} \int \Omega(k) \cdot dS = \pm 1 \tag{4.1}$$

where $\Omega(k)$ is the Berry curvature in momentum space. The Weyl point can therefore be thought of as a source (+ chirality) or a sink (- chirality) of the Berry curvature.

The Weyl fermions are therefore topologically protected, meaning they cannot be destroyed by any continuous deformation that leaves the discrete symmetries unchanged.

In lattice systems, the Nielsen-Ninomiya theorem [96] guarantees zero net chirality in the Brillouin zone, or equivalently zero net Chern number. In lattice realisations of WSMs, Weyl fermions will thus always appear in positive and negative chirality pairs, and a Weyl point can disappear only by annihilating against another Weyl point of opposite chirality. In particular, a lattice system can never support a single isolated Weyl fermion.

The presence of Weyl points has (at least) two major phenomenological consequences. The first is Fermi arcs at the material's surface, meaning lines at or near the Fermi energy in the *surface* Brillouin zone, connecting the projections of the Weyl points [95]. Given that the bulk Weyl points are topologically protected, the existence of these Fermi arcs is as well. Fermi arc states can give rise to phenomena such as quantum oscillations [87]. The second consequence is exotic transport in the WSM's bulk, including the chiral magnetic effect, negative magneto-resistance, and the anomalous Hall effect [97]. These exotic effects arise in whole or in part from the $U(1)_A$ axial anomaly of the Weyl fermions.

As an example, consider a free Dirac fermion ψ, of mass m, with a non-dynamical background axial vector field A^5_j, where $j = x, y, z$ labels spatial coordinates. In units with $\hbar \equiv 1$ and the Fermi velocity $v_f \equiv 1$, the Lagrangian $\mathcal{L}$ of such a Dirac fermion is [98, 99]

$$\mathcal{L} = \bar{\psi}\left(i\gamma^\mu \partial_\mu - m + A^5_j \gamma^j \gamma^5\right)\psi, \tag{4.2}$$

where $\mu = t, x, y, z$ labels spacetime coordinates, γ^μ are the Dirac matrices, and $\gamma^5 \equiv i\gamma^t\gamma^x\gamma^y\gamma^z$. In eq. (4.2), on the right-hand-side the kinetic term and mass term each preserve $\mathcal{P}$ and $\mathcal{T}$, while the coupling to A^5_j preserves $\mathcal{P}$ but breaks $\mathcal{T}$. If we choose A^5_j to have constant magnitude $b/2$ (the factor of $1/2$ is for later convenience), and use rotational symmetry to orient it in the z direction, $A^5_j = b/2\,\delta_{jz}$, then the energy ε of the Dirac fermion is, for spatial momentum k_j,

$$\varepsilon = \pm\sqrt{k_x^2 + k_y^2 + \left(\frac{b^2}{4} \pm \sqrt{k_z^2 + m^2}\right)^2}, \tag{4.3}$$

where the $\pm$ signs are uncorrelated, so that eq. (4.3) describes four energy levels.

The qualitative form of the spectrum in eq. (4.3) depends on the dimensionless ratio $|m/b|$. If $|m/b| < 1/2$, then two of the four energy levels meet at two points in momentum space, $(k_x, k_y, k_z) = (0, 0, \pm\sqrt{(b/2)^2 - m^2})$. At these points, $\varepsilon = 0$. The effective theory governing the low energy excitations near these two nodal points is then a pair of Weyl fermions, and thus for $|m/b| < 1/2$ the system is a WSM. On the other hand, if $|m/b| > 1/2$ then an energy gap appears, and the system is a trivial insulator. At the critical point $|m/b| = 1/2$, a single node at $(k_x, k_y, k_z) = 0$ appears.

The $\mathcal{L}$ in eq. (4.2) is invariant under $U(1)_V$ vector transformations $\psi \to e^{i\alpha}\psi$ with constant α, and when $m = 0$ and $b = 0$ also under $U(1)_A$ axial transformations

$\psi \to e^{i\beta\gamma^5}\psi$, with constant β. The corresponding $U(1)_V$ and $U(1)_A$ currents are, respectively,

$$J^\mu = i\bar{\psi}\gamma^\mu\psi, \qquad J_5^\mu = i\bar{\psi}\gamma^\mu\gamma^5\psi. \tag{4.4}$$

However, $U(1)_A$ is anomalous: in the presence of a background $U(1)_V$ field strength $F_{\mu\nu}$, the axial current J_5^μ is not conserved. Moreover, non-zero m explicitly breaks $U(1)_A$. To be specific, if m and $F_{\mu\nu}$ are both non-zero, then the divergence of the $U(1)_A$ current is

$$\partial_\mu J_5^\mu = \frac{1}{16\pi^2}\,\epsilon^{\mu\nu\rho\sigma}F_{\mu\nu}F_{\rho\sigma} - 2m\,\bar{\psi}\gamma^5\psi. \tag{4.5}$$

As mentioned above, the $U(1)_A$ anomaly gives rise to exotic transport. Our focus will be the anomalous Hall effect: if we introduce $A_j^5 = b/2\,\delta_{jz}$, then a constant, external $U(1)_V$ electric field, E, in a perpendicular direction, say x, induces a $U(1)_V$ Hall current [99, 100],

$$J^y = \sigma_{yx}E, \qquad \sigma_{yx} = -\sigma_{xy} = \frac{1}{4\pi^2}\sqrt{b^2 - 4m^2}\,\Theta\left(|b| - 2|m|\right), \tag{4.6}$$

with $J^x = 0$ and $J^z = 0$. In eq. (4.6), the Heaviside step function $\Theta\left(|b| - 2|m|\right)$ makes manifest that the anomalous Hall effect occurs only when $|m/b| < 1/2$, in the WSM phase.

The free Dirac fermion theory of eq. (4.2) thus has a quantum phase transition as $|m/b|$ increases. As mentioned above, when $|m/b| < 1/2$ the system is a WSM, with $\mathcal{P}$ preserved and $\mathcal{T}$ broken at low energy, and an AHE with the $\sigma_{xy} \neq 0$ in eq. (4.6). When $|m/b| > 1/2$ the system is a trivial insulator, with both $\mathcal{P}$ and $\mathcal{T}$ preserved at low energy and $\sigma_{xy} = 0$. This quantum phase transition is second order, with a quantum critical point described by a conformal field theory (CFT), namely a free, massless Dirac fermion.

A crucial question is: what if the low-energy excitations of a material cannot be described by the free Dirac fermion theory of eq. (4.2)? In fact, what if the low-energy excitations cannot be described by band theory at all? What if the low-energy excitations are not weakly-interacting, long-lived quasi-particles? Are WSM states possible in strongly-correlated materials, and if so, then what are their properties?

Some phenomena of the free Dirac fermion theory are independent of interactions, as long as those interactions do not change the discrete symmetries—specifically phenomena that are topological and/or determined by the $U(1)_A$ anomaly in eq. (4.5). Examples include the presence of Weyl points in the Brillouin zone and the corresponding Fermi arcs, both of which are topological, and the anomalous Hall conductivity σ_{xy} in eq. (4.6) when $m = 0$, which is completely determined by the $U(1)_A$ anomaly.

However, practically any other property will be affected by interactions, including the exact shape and energy dispersion of Fermi arcs, the value of the anomalous Hall conductivity when $m \neq 0$, and the thermodynamic equation of state, which in turn determines the order of any (quantum) phase transition and the critical

value of $|m/b|$ at which it occurs. Indeed, effective field theory techniques have shown that with sufficiently strong *short-range* interactions a WSM will experience either a first-order transition to a band insulator or a continuous transition to a broken symmetry phase [101].

An alternative approach to strongly-interacting WSMs is via the gauge/gravity duality - this is the approach we take here.

4.2 Holographic Weyl-Semi Metal from probe D3/D7

The set-up to achieve a top-down holographic WSM with flavour follows from the previous chapters. Namely we have probe D7 branes in an $AdS_5 \times S^5$ background with $N_f \ll N_c$. To include the features expected in a WSM we turn on an axial $U(1)_A$ field $A^5_j = b/2\,\delta_{jz}$, that induces a non-zero Wess-Zumino term that, as we shall see, holographically encodes the $U(1)_A$ anomaly. Looking at the free energy of this set-up we have, as before, three distinct phases: a minkowski embedding, a black hole embedding and a critical solution. To see if we do indeed have a Weyl semimetal phase we turn on an electric field perpendicular to the axial field. We choose to align it along the x direction, $A_x = Et + a_x(r)$, where the first term introduces the electric field E and the second term allows for a non-zero current in the x-direction, $\langle J_x \rangle$. We also turn on $A_y = a_y(r)$ to allow for a non-zero $\langle J_y \rangle$. From this we can compute the anomouls hall conductivity, $\sigma_{xy} \sim \langle J_y \rangle / E$ and find that it is non-zero for the black-hole solutions and zero for the minkowski solutions indicating a phase transition between a Weyl semimetal phase, with $\mathcal{T}$ broken, and a trivial insulator phase, with $\mathcal{T}$ preserved - see fig 4.6a.

This set-up borrows some features from previous holographic WSM models. One such class of models [14, 15, 102, 103, 104, 105] consists of a bottom-up Einstein-Hilbert metric in 4+1 dimensions in asymptotic AdS, coupled to a complex scalar field and to $U(1)$ gauge fields, one of which has a five-dimensional Chern-Simons term. Upon introducing a non-zero m and b, most models in this class exhibit a quantum phase transition as $|m/b|$ increases. However, some models in this class have a first order QPT from a WSM to a Chern insulator, for suitable choices of scalar field couplings [103]. A key feature of these models is an anomalous Hall conductivity completely determined by the product of the Chern-Simons coefficient and the $U(1)_A$ gauge field's value at the black hole horizon [14, 15]. Models in this class have realised edge currents indicating Fermi arcs [106], odd viscosity [107], chaos [108], and much more [109, 110, 111, 112].

A second class of model that is top-down follows from the D3/D7 set-up we have seen previously. Using this holographic description, refs. [113, 114] showed that a $U(1)_V$ electric field rotating in space produced non-equilibrium steady states that were in fact WSMs, among other remarkable properties, such as an effective temperature and fluctuation-dissipation relation [113].

Both of the classes above are fully holographic. Another class of WSM models consists of fermions with strong interactions mediated by a holographic CFT [115, 116]. Such a mix of non-holographic fermions with a holographic CFT is called "semi-holographic" [117, 118]. These models behave as undoped WSMs exhibiting quantum criticality generically with non-integer scaling of the conductivity in frequency and T [115, 116].

Having reviewed the literature, we find that our model exhibits several remarkable phenomena distinct from all previous models. For example, when $T = 0$ we find a *first order* transition from a WSM to a trivial insulator as $|m/b|$ increases, in contrast to the second order transitions of most previous models, and to the first order transition to a Chern insulator of [103].

At $T = 0$ our small $|m/b|$ phase is a WSM with $\sigma_{xx} = 0$ and $\sigma_{xy} \neq 0$, signaling broken $\mathcal{T}$ at low energy, while the large $|m/b|$ phase is a trivial insulator with $\sigma_{xx} = 0$ and $\sigma_{xy} = 0$, signaling restored $\mathcal{T}$ at low energy. Most remarkably, at $T = 0$ in the WSM phase our σ_{xy} is *independent of* m, and in particular retains its $m = 0$ value, dictated by the $U(1)_A$ anomaly, for all $|m/b|$ in the WSM phase. To our knowledge such behaviour does not occur in any other model. We also find that at $T = 0$ in the WSM phase the low energy effective theory is a CFT, namely $\mathcal{N} = 4$ SYM coupled to *massless* probe hypermultiplets. In other words, the non-zero m in the ultraviolet (UV) is renormalised to zero in the infra-red (IR).

For any $T > 0$ we again find a first order transition, now from a WSM with $\sigma_{xx} \neq 0$ and $\sigma_{xy} \neq 0$ to a trivial insulator with $\sigma_{xx} = 0$ and $\sigma_{xy} = 0$. In other words, when $T > 0$ in the WSM phase $\sigma_{xx} \neq 0$ and $\sigma_{xy} \neq 0$ both acquire non-trivial dependence on m and T. We also explore our model's thermodynamics by computing our model's entropy density, heat capacity, and speed of sound. We find various curious features. For example, at sufficiently low T, in the WSM phase near the transition we find a rapid increase in the entropy density, presumably arising from the emergent IR CFT degrees of freedom.

Broadly speaking, individual holographic models can reveal what is possible with strong interactions, while families of holographic models can reveal what is universal with strong interactions. Our model shows that first order transitions from WSMs to trivial insulators are possible with strong interactions, accompanied by remarkable behaviour of thermodynamics and transport, and our model provides further evidence that transport properties controlled by anomalies are universal in the presence of strong interactions.

In the next section 4.2.1 we describe our model in detail. In section 4.2.2 we present our solutions for the D7-brane worldvolume fields, and use them to study the thermodynamics of our model. In section 4.2.5 we holographically compute the longitudinal and Hall conductivities of our model. We conclude in section 4.3 with a summary and outlook for future research using our model.

4.2.1 The holographic description

The holographic description follows form the previous sections with the distinction that by turning on A^5_j, A_x and A_y we have a non-zero Wess-Zumino term.

$$S_{\rm D7} = -N_f T_{\rm D7} \int d^8\xi \sqrt{-\det(P[G]+F)} + \frac{1}{2} N_f T_{\rm D7} \int P[C_4] \wedge F \wedge F, \tag{4.7}$$

where the D7-brane tension is $T_{\rm D7} = (2\pi)^{-7} g_s^{-1} \alpha'^{-4}$, ξ^a with $a = 1, 2, \ldots, 8$ are the worldvolume coordinates, $P[G]$ and $P[C_4]$ denote pullbacks of the bulk metric and four-form to the worldvolume, respectively, and $F = dA$ is the field strength of the $U(1)$ worldvolume gauge field A. Note, we have absorbed a factor of $(2\pi\alpha')$ into our F, which is thus dimensionless. The D7-branes' worldvolume $U(N_f)$ gauge invariance is dual to the $U(N_f)$ flavour symmetry, and in particular the $U(1)$ gauge field A is dual to the $U(1)_V$ current J^μ.

Furthermore, recall that by seperating the $D3$ and $D7$ branes in the (x_8, x_9) directions we break the $SO(2) \sim U(1)_A$ symmetry and introduce a hypermultiplet mass $m = R/(2\pi\alpha')$ with phase ϕ, where R is the seperation length and ϕ is the angle of separation in the (x_8, x_9) plane. In previous chapters ϕ played a minor role. Here, however, we shall see that it is pivatol in constructing our WSM model.

Being top-down, our model has the attractive feature that the Lagrangian is known: see for example refs. [119, 120] for explicit expressions. However, its full form is lengthy, so we will write only the terms we need, namely terms in the potential V that involve the complex hypermultiplet mass $m\, e^{i\phi}$,

$$V \supset m\bar{\psi} e^{i\phi\gamma^5}\psi - m q^\dagger \left(e^{i\phi}\Gamma^\dagger + e^{-i\phi}\Gamma\right) q - m\tilde{q}^\dagger \left(e^{i\phi}\Gamma^\dagger + e^{-i\phi}\Gamma\right)\tilde{q} + m^2\left(q^\dagger q + \tilde{q}^\dagger\tilde{q}\right), \tag{4.8}$$

with Γ a complex scalar field formed from two of the six real scalar fields of $\mathcal{N}=4$ SYM, q and $\tilde{q}$ the $\mathcal{N}=2$ scalars that, alongside the Dirac fermion ψ, make up the $\mathcal{N}=2$ hypermultiplet.

If we transform $\psi \to e^{-i\phi\gamma^5/2}\psi$, then the first term in eq. (4.8) becomes $m\,\bar{\psi}\psi$. Moreover, if ϕ depends on the field theory spacetime coordinates $(x_0, x_1, x_2, x_3) = (t, x, y, z)$ then the derivative in ψ's kinetic term will act on ϕ, producing a new term that we may include in the potential. The terms in V that depend only on ψ then become

$$V \supset \bar{\psi}\left(m - \frac{\partial_\mu\phi}{2}\gamma^\mu\gamma^5\right)\psi. \tag{4.9}$$

Comparing to the Dirac Lagrangian in eq. (4.2), in eq. (4.9) the second term on the right-hand side clearly represents a coupling to an external, non-dynamical $U(1)_A$ gauge field, $A^5_\mu = \partial_\mu\phi/2$. As in the effective theory of eq. (4.2), to produce a WSM we

will choose $\phi = b\,z$.[2] In the D-brane intersection, $\phi = b\,z$ corresponds to D7-branes spiraling around the D3-branes in the (x_8, x_9) plane as they extend along z.

The operators sourced by m and ϕ are, respectively,

$$\begin{aligned}\mathcal{O}_m &\equiv \frac{\partial V}{\partial m} = \bar{\psi} e^{i\phi\gamma^5}\psi - q^\dagger\left(e^{i\phi}\Gamma^\dagger + e^{-i\phi}\Gamma\right)q - \tilde{q}^\dagger\left(e^{i\phi}\Gamma^\dagger + e^{-i\phi}\Gamma\right)\tilde{q} + 2m\left(q^\dagger q + \tilde{q}^\dagger\tilde{q}\right),\\ \mathcal{O}_\phi &\equiv \frac{\partial V}{\partial \phi} = im\bar{\psi} e^{i\phi\gamma^5}\gamma^5\psi - imq^\dagger\left(e^{i\phi}\Gamma^\dagger - e^{-i\phi}\Gamma\right)q - im\tilde{q}^\dagger\left(e^{i\phi}\Gamma^\dagger - e^{-i\phi}\Gamma\right)\tilde{q}.\end{aligned} \tag{4.10}$$

The operator $\mathcal{O}_m$ is dimension 3, and when ϕ is constant is just the SUSY completion of the Dirac mass operator. The operator $\mathcal{O}_\phi$ is dimension 4, and obeys $\mathcal{O}_\phi \propto m$, so that if $m = 0$ then $\mathcal{O}_\phi = 0$.

As before, we parametrise the $D7$-branes worldvolume at non-zero temperature to be,

$$\begin{aligned}ds^2 &= \frac{\rho^2}{L^2}\left(-\frac{g^2(\rho)}{h(\rho)}dt^2 + h(\rho)d\vec{x}^2\right) + \frac{L^2}{\rho^2}\left(dr^2 + r^2 d\Omega_3^2 + dR^2 + R^2 d\phi^2\right),\\ C_4 &= \frac{\rho^4}{L^4}h^2(\rho)dt\wedge dx\wedge dy\wedge dz - \frac{L^4 r^4}{\rho^4}d\phi\wedge\omega(S^3),\end{aligned} \tag{4.11a}$$

$$\rho^2 = r^2 + R^2, \qquad g(\rho) \equiv 1 - \frac{\rho_H^4}{\rho^4}, \qquad h(\rho) \equiv 1 + \frac{\rho_H^4}{\rho^4}, \tag{4.11b}$$

where $\rho \in [\rho_H, \infty)$ with the black brane horizon at ρ_H and the asymptotic AdS_5 boundary at $\rho \to \infty$. The volume of a unit-radius S^3 is given by $\omega(S^3)$. Noticably, the pullback of the four-form is now non-zero.

The D7-branes are extended along $AdS_5 \times S^3$. We parametrise the D7-branes' worldvolume coordinates as $\xi^a = (t, x, y, z, r)$ plus the S^3 coordinates. The two worldvolume scalars are then R and ϕ, where R is holographically dual to $\mathcal{O}_m$ and ϕ is dual to $\mathcal{O}_\phi$ in eq. (4.10). More specifically, in the near-boundary region on the worldvolume, $r \to \infty$, the leading asymptotic values of R and ϕ determine the sources for $\mathcal{O}_m$ and $\mathcal{O}_\phi$, i.e. the modulus m and phase ϕ of the hypermultiplet mass, respectively, while the sub-leading behaviours determine the expectation values $\langle\mathcal{O}_m\rangle$ and $\langle\mathcal{O}_\phi\rangle$.

We will use the simplest ansatz for the worldvolume scalars that introduces the phase bz in the hypermutiplets' mass and allows for non-zero $\langle\mathcal{O}_m\rangle$ and $\langle\mathcal{O}_\phi\rangle$, namely $R(r)$ and $\phi(z, r) = bz + \Phi(r)$.[3] In practical terms, our goal will be to solve for $R(r)$ and $\Phi(r)$, and from these extract the dual flavour fields' thermodynamic and transport properties.

[2] In this model the effect of a $U(1)_A$ chemical potential μ_5, introduced as $\phi = 2\mu_5 t$, was studied holographically for example in refs. [121, 122].

[3] A similar ansatz for ϕ, in the presence of a magnetic field, has appeared in refs. [123, 124].

With our ansatz, the pullback of C_4 to the worldvolume becomes

$$P[C_4] = \frac{\rho^4}{L^4} dt \wedge dx \wedge dy \wedge dz - \frac{L^4 r^4}{\rho^4} \left(b\, dz + \frac{\partial \phi}{\partial r} dr \right) \wedge \omega(S^3), \tag{4.12}$$

and hence the WZ term in the action eq. (4.7) includes a term $\propto \int_{AdS_5} \frac{r^4}{\rho^4} b\, dz \wedge F \wedge F$, which holographically encodes the $U(1)_A$ anomaly.

Plugging our ansatz into the D7-branes' action eq. (4.7) gives

$$S_{\mathrm{D7}} = -\mathcal{N} \mathrm{vol}(\mathbb{R}^{1,3}) \int dr\, r^3\, g\, h \sqrt{\left(1 + \frac{L^4 b^2 R^2}{h \left(r^2 + R^2 \right)^2} \right) \left(1 + R'^2 \right) + R^2 \phi'^2}, \tag{4.13a}$$

$$\mathcal{N} \equiv 2\pi^2 N_f T_{\mathrm{D7}} = \frac{\lambda N_f N_c}{16 \pi^4} \frac{1}{L^8}, \tag{4.13b}$$

where $R' \equiv \partial R / \partial r$ and similarly for ϕ', and the factor $\mathrm{vol}(\mathbb{R}^{1,3})$ denotes the infinite volume of Minkowski space, arising from integration over the field theory directions (t, x, y, z). Starting now we will divide both sides of eq. (4.13a) by $\mathrm{vol}(\mathbb{R}^{1,3})$, so that S_{D7} will be an action *density*. Correspondingly, quantities derived from S_{D7} will be densities.

For our ansatz, the canonical momentum P_ϕ conjugate to ϕ is

$$P_\phi \equiv \frac{\delta S_{\mathrm{D7}}}{\delta \phi'} = -\mathcal{N} r^3\, g\, h \frac{R^2 \phi'}{\sqrt{\left(1 + \frac{L^4 b^2 R^2}{h (r^2 + R^2)^2} \right) \left(1 + R'^2 \right) + R^2 \phi'^2}}. \tag{4.14}$$

The equation of motion for ϕ is then $\partial_r P_\phi = 0$, so that P_ϕ is a constant of motion in the worldvolume holographic direction, r. We thus write the solution as $P_\phi = \mathcal{N} p_\phi$ where the factor of $\mathcal{N}$ is a convenient normalisation, and p_ϕ is a constant.

Plugging $P_\phi = p_\phi$ into eq. (4.14) and solving for ϕ'^2 gives

$$\phi'^2 = p_\phi \frac{\left[\left(r^2 + R^2 \right)^2 + L^4 b^2 R^2 \right] \left(1 + R'^2 \right)}{\left(r^2 + R^2 \right)^2 R^2 \left(R^2 r^6 - p_\phi^2 \right)}. \tag{4.15}$$

Subsequently plugging ϕ'^2 in eq. (4.15) into the action eq. (4.13a) and Legendre transforming with respect to ϕ then gives an effective action for $R(r)$ alone,

$$\begin{aligned} \tilde{S}_{\mathrm{D7}} &\equiv S_{\mathrm{D7}} - \int dr\, P_\phi \phi' \\ &= -\mathcal{N} \int dr\, r^3\, g\, h \sqrt{1 + R'^2} \sqrt{1 + \frac{L^4 b^2 R^2}{h \left(r^2 + R^2 \right)^2}} \sqrt{1 - \frac{p_\phi^2}{r^6 g^2 h^2 R^2}}, \end{aligned} \tag{4.16}$$

whose variation gives $R(r)$'s equation of motion.

The integrand of $\tilde{S}_{\mathrm{D7}}$ in eq. (4.16) includes a product of three square roots. For

both black hole and Minkowski embeddings, the arguments of the first and second square roots are positive for all r, hence both of these square roots are real-valued for all r.

However, if $p_\phi \neq 0$ then the third square root is never real-valued for all r. At the asymptotic AdS_5 boundary $r \to \infty$ the argument of the third square root is positive and hence the third square root is real-valued. For black hole embeddings, the argument of the third square root diverges to negative infinity at r_H because $g(\rho_H) = 0$, while for Minkowski embeddings it diverges to negative infinity at $r = 0$. In each case the argument of the third square root must change sign at some r between the asymptotic AdS_5 boundary and the horizon or brane endpoint, so for some values of r the third square root always acquires a non-zero imaginary part. As a result, $\tilde{S}_{\rm D7}$ acquires a non-zero imaginary part, which signals a tachyonic instability with decay rate $\propto |\mathrm{Im}\, \tilde{S}_{\rm D7}|$ [125, 126, 127].

Similar tachyons appear in other probe brane systems, when a square root factor acquires a non-zero imaginary part: see for example refs. [128, 129, 121, 122]. In those cases we can "fix the problem," i.e. prevent the instability, by adding to our ansatz non-zero components of the worldvolume gauge field A. These come with their own integration constants, and typically produce additional factors under the square root that can be arranged such that the action remains real. Indeed, we will do precisely this in section 4.2.5, where we will introduce a constant, non-dynamical, external $U(1)_V$ electric field E, and to avoid a tachyonic instability we introduce components of A. In field theory terms, we will introduce E which will in turn induce $U(1)_V$ currents.

However, that strategy does not work when $E = 0$ and $p_\phi \neq 0$. In that case, even if we introduce all components of A in field theory directions, $(A_t(r), A_x(r), A_y(r), A_z(r))$, then the corresponding integration constants cannot be arranged to keep the square root real for all r. In particular, these integration constants appear in the Legendre-transformed action under the third square root as terms added to those in eq. (4.16), but with powers of r sub-leading compared to the p_ϕ term at small r. As a result, these integration constants cannot be adjusted to keep the square root real for all r.

The upshot is that we will set $p_\phi = 0$ in all that follows, to guarantee that $\tilde{S}_{\rm D7}$ in eq. (4.16) is always real, and hence no tachyonic instability appears. In appendix 4.3 we perform the holographic renormalisation of our model and find $\langle \mathcal{O}_\phi \rangle = P_\phi = p_\phi$, so our choice $p_\phi = 0$ means $\langle \mathcal{O}_\phi \rangle = 0$.

With our choice $p_\phi = 0$, the near-boundary asymptotic expansion of $R(r)$ is

$$R(r) = ML^2 \left(1 - \frac{L^4 b^2}{2r^2} \log(r/L)\right) + C\,\frac{L^6}{r^2} + \mathcal{O}\left(\frac{\log(r/L)}{r^4}\right), \tag{4.17}$$

where we see a similar relation to what we had in previous sections (4.17) albeit with an addition factor due to the non-zero b. Indeed, the asymptotic separation $\lim_{r\to\infty} R(r) = ML^2$ determines $m = ML^2/(2\pi\alpha') = M\sqrt{\lambda}/(2\pi)$. In appendix 4.3 we

show that M and the sub-leading asymptotic coefficient C together determine $\langle \mathcal{O}_m \rangle$ as

$$\langle \mathcal{O}_m \rangle = \frac{\sqrt{\lambda} N_f N_c}{8\pi^3} \left[-2C + \frac{b^2 M}{2} + b^2 M \log(ML) \right]. \tag{4.18}$$

4.2.2 Thermodynamics

In this section we will explore our model's thermodynamics. Specifically, for different classes of solutions of $R(r)$, characterised by boundary conditions, we will compute the hypermultiplets' contribution to the (Helmholtz) free energy density, f. Given f we can also compute the thermal expectation value $\langle \mathcal{O}_m \rangle = \partial f / \partial m$, which in terms of the near-boundary asymptotic coefficients M and C is given by eq. (4.18), and the hypermultiplets' contribution to the entropy density, s, and heat capacity density, c_V,

$$s = -\frac{\partial f}{\partial T}, \qquad c_V = T \frac{\partial s}{\partial T}. \tag{4.19}$$

In our case, where all chemical potentials vanish, we can also compute the speed of sound, v, from these thermodynamic quantities, as follows. The entropy density of the $\mathcal{N} = 4$ SYM fields is $s_{\rm YM} = \frac{\pi^2}{2} N_c^2 T^3$ and their heat capacity density is $c_V^{\rm YM} = 3\, s_{\rm YM}$ [130]. The total entropy density and heat capacity density are then $s_{\rm tot} = s_{\rm YM} + s$ and $c_V^{\rm tot} = c_V^{\rm YM} + c_V$, respectively. The speed of sound is then given by

$$v^2 = \frac{s_{\rm tot}}{T} \frac{\partial T}{\partial s_{\rm tot}} = \frac{s_{\rm tot}}{c_V^{\rm tot}} = \frac{s_{\rm YM} + s}{c_V^{\rm YM} + c_V} = v_{\rm YM}^2 + \delta v^2 + \mathcal{O}\left(N_f^2 / N_c^2 \right), \tag{4.20}$$

where in the final equality we expanded in the probe limit $N_f \ll N_c$, with leading term $v_{\rm YM}^2 = s_{\rm YM} / c_V^{\rm YM}$, which takes the value required for a $(3+1)$-dimensional CFT, $v_{\rm YM}^2 = 1/3$, and the $\mathcal{O}\left(N_f / N_c\right)$ correction due to the hypermultiplets is

$$\delta v^2 = \frac{s_{\rm YM}}{c_V^{\rm YM}} \left(\frac{s}{s_{\rm YM}} - \frac{c_V}{c_V^{\rm YM}} \right). \tag{4.21}$$

Given f we can thus compute s and c_V, and hence δv^2.

In holography, f is simply minus the on-shell D7-brane action $S_{\rm D7}$ in eq. (4.7) (not $\tilde{S}_{\rm D7}$ in eq. (4.16)) in Euclidean signature [42]. In the appendix for this section we show that

$$\begin{aligned} f = \frac{\lambda N_f N_c}{16\pi^4 L^8} \lim_{r_c \to \infty} \Bigg[\int^{r_c} dr\, r^3\, g\, h \sqrt{1 + \frac{L^4 b^2 R^2}{h \left(r^2 + R^2\right)^2}} \sqrt{1 + R'^2} \\ - \frac{r_c^4}{4} - \frac{L^8 b^2 M^2}{2} \log(r_c / L) + \frac{L^8 b^2 M^2}{4} \left(1 + 2\log(ML)\right) \Bigg], \end{aligned} \tag{4.22}$$

where r_c is a large-r cutoff, and the lower endpoint of integration is r_H for black hole embeddings and $r = 0$ for Minkowski embeddings.

In the field theory the free parameters are m, b, and T, all with dimensions of mass. We will plot most physical quantities in units of b, and specifically as functions of the dimensionless ratios T/b and $m/(b\sqrt{\lambda}) = M/(2\pi b)$. Most of our results will be numerical, although we will obtain closed-form results in certain limits.

As mentioned in the introduction, our main result is that for all T/b we find a first-order transition as $m/(b\sqrt{\lambda})$ increases. In holographic terms, the transition is from black hole to Minkowski embeddings. In CFT terms, we find that f is of course continuous, but has a discontinuous first derivative $\langle \mathcal{O}_m \rangle = \partial f/\partial m$ at the transition. Our results are summarised in the phase diagram of figure 4.4. In section 4.2.5, by computing the conductivity we show that the transition is in fact from a WSM to a trivial insulator.

4.2.3 Phase Transition at Zero Temperature

We start with $T/b = 0$, in which case the only scale in the field theory is $m/(b\sqrt{\lambda})$. When $T = 0$ we have that $g = 1$ and $h = 1$ in eq. (4.11). Taking also $p_\phi = 0$, the equation of motion for $R(r)$ following from the Legendre transformed action $\tilde{S}_{\rm D7}$ in eq. (4.16) is

$$R'' + \left(\frac{3}{r} - \frac{2L^4b^2rR^2}{(r^2+R^2)\left[(r^2+R^2)^2+L^4b^2R^2\right]}\right) R'(1+R'^2) + \frac{L^4b^2R(R^2-r^2)}{(r^2+R^2)\left[(r^2+R^2)^2+L^4b^2R^2\right]}(1+R'^2) = 0. \quad (4.23)$$

Without a horizon, all embeddings reach $r = 0$. We can divide the embeddings into two classes, distinguished by whether $R_0 \equiv R(r=0)$ vanishes. In the first class of embeddings, $R_0 \neq 0$. Specifically, by expanding $R(r)$ around $r = 0$ in eq. (4.23) we find

$$R(r) = R_0 - \frac{L^4b^2r^2}{8R_0\left(L^4b^2+R_0^2\right)} + \mathcal{O}(r^4). \quad (4.24a)$$

These are Minkowski embeddings: at $r = 0$ we have $\rho = R_0 \neq 0$. In the second class of embeddings $R_0 = 0$, and in fact from eq. (4.23) we find $R(r)$ vanishes exponentially quickly as $r \to 0$,

$$R(r) = \eta \frac{e^{-L^2b/r}}{\sqrt{r}}\left[1+\mathcal{O}(r^2)\right], \quad (4.24b)$$

where η is a constant. These are analogous to $T > 0$ black hole embeddings. These two classes are separated by a critical embedding, $R_{\rm c}(r)$, which from eq. (4.23) we find approaches $R_0 = 0$ linearly in r,

$$R_{\rm c}(r) = \frac{r}{\sqrt{3}} - \frac{32r^3}{27\sqrt{3}L^4b^2} + \mathcal{O}(r^5). \quad (4.24c)$$

For any value of b, eq. (4.23) admits a trivial solution, $R(r) = 0$, which has $R_0 = 0$ and in eq. (4.17) also $M = 0$ and $C = 0$. As a result, this solution describes $m = 0$ and $\langle \mathcal{O}_m \rangle = 0$, and a straightforward calculation shows that also $f = 0$.

We can obtain approximate solutions with non-zero m in two limits, large m and small m. More precisely, large mass means $m/(b\sqrt{\lambda}) \gg 1$. In that limit, following ref. [131] we take $R(r) = ML^2 + \delta R(r)$ and linearise the equation of motion eq. (4.23) in δR, also keeping only leading-order terms in $1/\left(L^4M^2 + r^2\right)$, with the result

$$\delta R'' + \frac{3}{r}\delta R' + \frac{L^6 b^2 M\left(M^2 - r^2\right)}{\left(L^4M^2 + r^2\right)^3} = 0, \qquad \frac{m}{b\sqrt{\lambda}} \gg 1. \tag{4.25}$$

The solution of eq. (4.25) regular as $r \to 0$ and with the large-r asymptotics of eq. (4.17) is

$$R(r) \approx L^2 M + \frac{L^6 b^2 M}{4}\left[\frac{1}{L^4M^2 + r^2} - \frac{1}{r^2}\log\left(1 + \frac{r^2}{L^4M^2}\right)\right], \qquad \frac{m}{b\sqrt{\lambda}} \gg 1. \tag{4.26}$$

This solution has $R_0 = L^2 M \neq 0$, as in eq. (4.24a), and is therefore a Minkowski embedding. This solution has the large-r asymptotics of eq. (4.17), with

$$C = \frac{1}{4} M b^2 \left[1 + 2\log(ML)\right], \qquad \frac{m}{b\sqrt{\lambda}} \gg 1. \tag{4.27}$$

Substituting this into eq. (4.18) then gives $\langle \mathcal{O}_m \rangle = 0$. Integrating $\langle \mathcal{O}_m \rangle$ over m then trivially gives a free energy independent of m, as expected in the limit $\frac{m}{b\sqrt{\lambda}} \gg 1$ where the hypermultiplets decouple. Concretely, we find $f \to -b^4 N_f N_c/(512\pi^4)$ as $m/(b\sqrt{\lambda}) \to \infty$.

Small mass means $m/(b\sqrt{\lambda}) \ll 1$, where we may linearise the equation of motion eq. (4.23) in $R(r)$, finding

$$R'' + \frac{3}{r}R' - \frac{L^4 b^2}{r^4} R = 0, \qquad \frac{m}{b\sqrt{\lambda}} \ll 1. \tag{4.28}$$

The solution of eq. (4.28) regular as $r \to 0$ and with large-r asymptotics as in eq. (4.17) is

$$R(r) \approx \frac{L^4 b M}{r} K_1(L^2 b/r), \qquad \frac{m}{b\sqrt{\lambda}} \ll 1, \tag{4.29}$$

with modified Bessel function K_1. This solution vanishes exponentially as $r \to 0$, as in eq. (4.24b), with $\eta = L^3 M\sqrt{\pi b/2}$, and hence is analogous to a $T > 0$ black hole embedding. This solution has the large-r asymptotics of eq. (4.17), with

$$C = \frac{1}{4} b^2 M\left[2\log\left(bL/2\right) 2 - 1 + 2\gamma_{\mathrm{E}}\right], \qquad \frac{m}{b\sqrt{\lambda}} \ll 1, \tag{4.30}$$

with Euler-Mascheroni constant $\gamma_{\rm E} \approx 0.577$. Using $m = M\sqrt{\lambda}/2\pi$, eq. (4.18) then gives

$$\langle \mathcal{O}_m \rangle \approx \frac{N_f N_c}{4\pi^2}\, m\, b^2 \left[\log\left(\frac{4\pi m}{b\sqrt{\lambda}}\right) + 1 - \gamma_{\rm E} \right], \qquad \frac{m}{b\sqrt{\lambda}} \ll 1. \tag{4.31}$$

We then obtain f by integrating eq. (4.31) with respect to m, fixing the integration constant using the fact that the trivial solution $R(r) = 0$ has $f = 0$, with the result

$$f \approx \frac{N_f N_c}{16\pi^2}\, m^2\, b^2 \left[2\log\left(\frac{4\pi m}{b\sqrt{\lambda}}\right) + 1 - 2\gamma_{\rm E} \right], \qquad \frac{m}{b\sqrt{\lambda}} \ll 1. \tag{4.32}$$

We will obtain more general solutions with non-zero m numerically, by shooting from $r = 0$, with the boundary conditions in eq. (4.24), towards the asymptotic AdS_5 boundary $r \to \infty$. For solutions obeying eq. (4.24a) we impose $R'(r = 0) = 0$ and choose the free parameter $R_0 \neq 0$. For solutions obeying eq. (4.24b) we impose $R(r) = \eta L (2b/\pi)^{1/2} r^{-1} K_1(L^2 b/r)$ at small r, with free parameter η.[4] In each case, for a given value of R_0 or η, we numerically integrate to large r, and then perform a numerical fit to the large-r asymptotic form in eq. (4.17), and extract M and C. Since every solution is determined by a single parameter, R_0 or η, the asymptotic coefficient C will always implicitly depend on M. For given values of M and C, we compute $\langle \mathcal{O}_m \rangle$ from eq. (4.18), and for a given numerical solution for $R(r)$ we compute f by performing the integral in eq. (4.22) numerically. For the unique, critical solution $R_{\rm c}(r)$ obeying eq. (4.24c) we have $R_0 = 0$ and $R_c'(r = 0) = 1/\sqrt{3}$, which map to the unique values

$$M_{\rm c} = 0.4875, \qquad C_{\rm c} = -0.07804, \tag{4.33a}$$

$$\langle \mathcal{O}_m \rangle_{\rm c} = 0.04965\, b^3\, \frac{\sqrt{\lambda}\, N_f N_c}{8\pi^3}, \qquad f_{\rm c} = -0.02671\, b^4\, \frac{\lambda\, N_f N_c}{16\pi^4}. \tag{4.33b}$$

Figure 4.1a shows examples of our $T/b = 0$ numerical solutions for $R(r)/(L^2 b)$. The dashed blue, solid orange, and dot-dashed black lines correspond to the $r = 0$ boundary conditions in eq. (4.24a) ($R_0 \neq 0$, Minkowski), eq. (4.24b) (exponential, black-hole-like), and (4.24c) (critical), respectively. The limiting value that each solution approaches on the right-hand side of figure 4.1a determines m as $\lim_{r\to\infty} R(r) = ML^2 = (2\pi\alpha')m$. Figure 4.1a shows that, broadly speaking, the dashed blue Minkowski embeddings only exist for large enough m, i.e. they describe large mass, while the solid orange black-hole-like embeddings only exist for small enough m, i.e. they describe small mass. Figure 4.1a also shows that both classes of embeddings produce the same values of m for a range of m near the critical solution, which will be crucially important when we consider f below.

As previously discussed, the holographic coordinate ρ encodes the field theory energy scale, with the UV near the AdS_5 boundary $\rho \to \infty$ and the IR near $\rho = 0$. Given a value of the UV parameter $m/(b\sqrt{\lambda})$, the solution $R(r)$ encodes the

[4] This is the correct small-r behaviour of solutions obeying eq. (4.24b), up to corrections of order $e^{-3L^2 b/r}$.

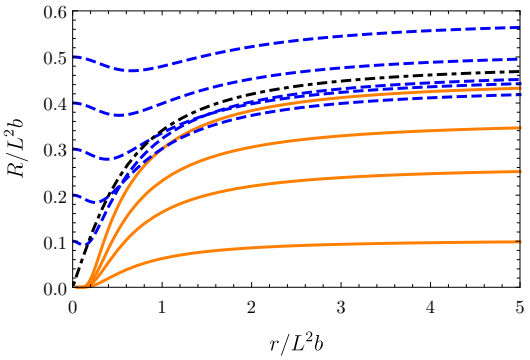

(A) Embeddings at $T/b = 0$

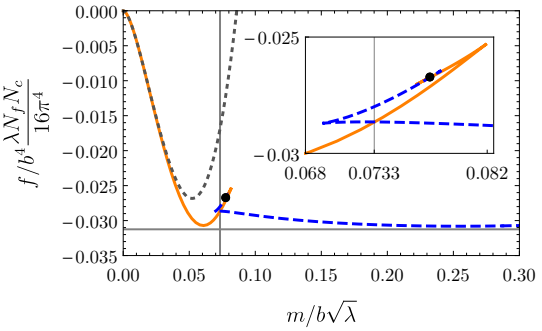

(B) Free energy density at $T/b = 0$

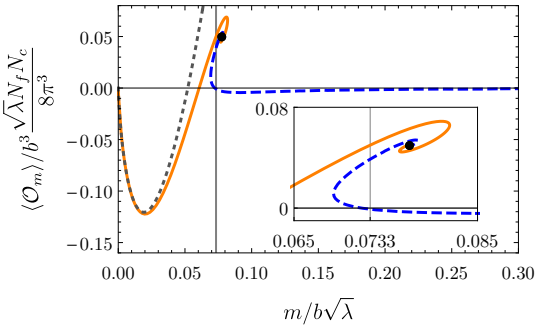

(C) $\langle\mathcal{O}_m\rangle$ at $T/b = 0$

FIGURE 4.1: **(a)** Examples of our numerical solutions for $R(r)/(L^2b)$ as functions of $r/(L^2b)$, at $T/b = 0$. The dashed blue, solid orange, and dot-dashed black lines are solutions obeying the $r \to 0$ boundary conditions in eqs. (4.24a) (Minkowski), (4.24b) (black-hole-like), and (4.24c) (critical), respectively. **(b)** Our numerical result for the free energy density $f/(b^4\frac{\lambda N_f N_c}{16\pi^4})$, as a function of $m/(b\sqrt{\lambda})$, at $T/b = 0$, with the same colour coding as (a). The dotted gray line is the small mass approximation in eq. (4.32). The black dot indicates the critical solution, and the inset is a close-up near the critical solution, showing the "swallow tail" shape characteristic of a first-order transition. The first order transition at $m/(b\sqrt{\lambda}) \approx 0.0733$ is indicated by the vertical grey line. The horizontal grey line shows the large $m/(b\sqrt{\lambda})$ limit of the free energy, $f \approx -b^4 N_f N_c/(512\pi^4)$. **(c)** The expectation value $\langle\mathcal{O}_m\rangle/(b^3\frac{\lambda N_f N_c}{8\pi^3})$ as a function of $m/(b\sqrt{\lambda})$, at $T/b = 0$, with the same colour coding as (a) and (b). The dotted gray line is the small mass approximation in eq. (4.31). The inset is a close-up of the spiral behaviour near the phase transition.

corresponding renormalisation group (RG) flow, where the $r \to 0$ behaviours in eq. (4.24) encode the IR degrees of freedom.

For example, the Minkowski embeddings obey eq. (4.24a) and hence the $S^3 \in S^5$ collapses at $\rho = R_0 \neq 0$, as described above. As a result, the D7-branes are absent for $\rho < R_0$. The holographically dual statement is that sufficiently heavy hypermultiplets decouple at sufficiently low energy, and so disappear from the IR. Indeed, for Minkowski embeddings we expect the spectrum of linearised worldvolume excitations to be gapped and discrete [132].

In contrast, the black-hole-like embeddings have the exponential decay of

eq. (4.24b), so that $\lim_{r\to 0} R(r) = 0$. The D7-branes thus reach the AdS_5 Poincaré horizon at $\rho = 0$, as described above. The holographically dual statement is that for sufficiently light hypermultiplets the RG flow is to a gapless IR. Indeed, for black-hole-like embeddings we expect the spectrum of linearised worldvolume excitations to be gapless and continuous [132].

In fact, for the black-hole-like embeddings we can say more: a straightforward exercise shows that as $r \to 0$ the D7-branes' worldvolume metric approaches that of $AdS_5 \times S^3$, with the same radius of curvature as that of the $r \to \infty$ region. The holographically dual statement is that the RG flow leads to an emergent conformal symmetry in the IR, and in fact the IR CFT is simply *massless* probe hypermultiplets coupled to $\mathcal{N} = 4$ SYM at large N_c and large coupling.

For the critical solution, which has the linear in r behaviour near $r = 0$ of eq. (4.24c), as $r \to 0$ the D7-branes' worldvolume metric approaches

$$P[G]_{ab}d\xi^a d\xi^b \approx L^2\frac{dr^2}{r^2} + \frac{4}{3}\frac{r^2}{L^2}\left(-dt^2 + dx^2 + dy^2\right) + \frac{1}{4}b^2 L^2 dz^2 + \frac{3}{4}L^2 ds^2_{S^3}, \qquad (4.34)$$

which we recognise as that of AdS_4 with coordinates (r, t, x, y) and radius L, times $\mathbb{R}$ with coordinate z, times S^3 with radius $L\sqrt{\frac{3}{4}}$. The holographically dual statement is that the RG flow leads to an emergent $(2+1)$-dimensional conformal symmetry in the IR, dual to the AdS_4 isometry, with a non-compact $U(1)$ symmetry, dual to translations in z, plus an $SO(4)$ symmetry, dual to the S^3 isometry. In other words, the critical RG flow leads to an emergent $(2+1)$-dimensional CFT. The fully holographic, bottom-up models of refs. [14, 15, 102, 104, 105] have a similar critical solution, but with IR Lifshitz symmetry in which z scales with a different power from (t, x, y). In both our model and those models, the choice $\phi = b\,z$ breaks $SO(3)$ rotational symmetry of (x, y, z) down to $SO(2)$ rotational symmetry of (x, y), allowing for a lower-dimensional CFT or Lifshitz scaling in the IR.

Since only black-hole-like embeddings exist for sufficiently small $m/(b\sqrt{\lambda})$, and only Minkowski embeddings exist for sufficiently large $m/(b\sqrt{\lambda})$, as we increase $m/(b\sqrt{\lambda})$ a transition from black-hole-like to Minkowski embeddings must necessarily occur. A key question is the nature of that transition, including in particular its order.

Figure 4.1b shows our numerical results for the free energy density f, in units of b and normalised by $\frac{\lambda N_f N_c}{16\pi^4}$, as a function of $m/(b\sqrt{\lambda})$. The colour coding is the same as in figure 4.1a, while the black dot represents the critical solution and the dotted grey line is the small-m approximation in eq. (4.32), showing excellent agreement with our numerics when $m/(b\sqrt{\lambda}) \ll 1$. The horizontal grey line in the figure shows the analytic approximation for the free energy in the large-m limit, $f \approx -b^4 N_f N_c/(512\pi^4)$, which agrees well with our numerics when $m/(b\sqrt{\lambda}) \gg 1$.

The inset in figure 4.1b shows f near the critical solution, which clearly exhibits the "fish tail" shape characteristic of a first-order transition. Specifically, for a range of

$m/(b\sqrt{\lambda})$ near the critical solution, f is multi-valued, with both black-hole-like and Minkowski embeddings available to the system. The thermodynamically preferred solution is that with the lowest f. As we increase $m/(b\sqrt{\lambda})$ black-hole-like embeddings are preferred until $m/(b\sqrt{\lambda}) \approx 0.0733$, denoted by the vertical line in figure 4.1b, after which Minkowski embeddings are preferred. The first derivative $\partial f/\partial m$ is discontinuous at the transition, thus the transition is first order. The critical solution is never thermodynamically preferred.

Figure 4.1c shows some of our numerical results for $\langle \mathcal{O}_m \rangle = \partial f/\partial m$, in units of b and normalised by $\frac{\lambda N_f N_c}{8\pi^3}$, with the same colour coding as figs. 4.1a and 4.1b. At large m clearly $\langle \mathcal{O}_m \rangle \to 0$, as discussed below eq. (4.27), and the small-m approximation of eq. (4.31) appears as the dotted grey line. The transition point $m/(b\sqrt{\lambda}) \approx 0.0733$ is denoted by the vertical line. As expected, near the critical solution $\langle \mathcal{O}_m \rangle$ is multi-valued, and as $m/(b\sqrt{\lambda})$ increases, at the transition point $\langle \mathcal{O}_m \rangle$ jumps discontinuously from black-hole-like to Minkowski embeddings.

In figure 4.1c the inset is a close-up showing that $\langle \mathcal{O}_m \rangle$ executes a spiral when approaching the critical solution, $R_c(r)$. Such behaviour is familiar for probe branes, and arises from a discrete scale invariance of near-critical solutions, producing self-similarity [133, 47, 134, 1, 135, 136]. This discrete scale invariance explains why the transition is first order: discrete scale invariance of near-critical solutions implies that $\langle \mathcal{O}_m \rangle$ executes a spiral and hence f is multi-valued near the critical solution, which then guarantees that the transition is first order. We will not use the scaling symmetry here, so we will just sketch the derivation of the scaling exponents and self-similarity, leaving the details to refs. [133, 47, 134, 1, 135, 136]. The discrete scaling symmetry is manifest when we linearise the equation of motion eq. (4.23) in $R(r)$ about the critical solution, $R_c(r)$, which at small r gives

$$R(r) \approx R_c(r) + B\, r^{\nu_+} + B^*\, r^{\nu_-}, \tag{4.35}$$

with constant B and $\nu_\pm = -\frac{1}{2} \pm \frac{i}{2}\sqrt{23}$. The near-critical solutions have the scaling symmetry $R(r) \to \zeta R(r)$ and $r \to \zeta r$ with real, positive ζ, under which $B \to \zeta^{1-\nu_+} B$. Since we have linearised the equation of motion, the map from the $r \to 0$ coefficients B and B^* to the $r \to \infty$ coefficients M and C is linear, which implies

$$M - M_c \approx \kappa_1\, \zeta^{1-\nu_+} + \kappa_1^*\, \zeta^{1-\nu_-}, \qquad C - C_c \approx \kappa_2\, \zeta^{1-\nu_+} + \kappa_2^*\, \zeta^{1-\nu_-}, \tag{4.36}$$

with constants κ_1 and κ_2. Inserting eq. (4.36) into eq. (4.18) we obtain a curve for $\langle \mathcal{O}_m \rangle$ as a function of m, parametrised by ζ. Re-writing

$$\zeta^{1\pm\nu_\pm} = e^{(1\pm \mathrm{Re}\,\nu_\pm)\ln\zeta} \left[\cos\left(\mathrm{Im}\,\nu_\pm \ln\zeta\right) + i \sin\left(\mathrm{Im}\,\nu_\pm \ln\zeta\right)\right], \tag{4.37}$$

then shows that if we approach the critical solution by sending $\zeta \to 0$, then $\langle \mathcal{O}_m \rangle$ as a function of m will trace a spiral of decaying amplitude, with period $2\pi/\mathrm{Im}\,\nu_\pm$. In

contrast, real-valued exponents $\nu_\pm$ would lead to single-valued $\langle \mathcal{O}_m \rangle$ as a function of m and hence a transition of second order or higher [135].

4.2.4 Phase Transition at Non-Zero Temperature

When $T > 0$ the field theory has two free parameters, $m/(b\sqrt{\lambda})$ and T/b. The equation of motion for $R(r)$ derived from eq. (4.16) when $T/b > 0$ and $p_\phi = 0$ is cumbersome and unilluminating, so we will not write it here.

When $T/b > 0$ we know one exact solution for $R(r)$, namely the trivial solution $R(r) = 0$, which is a black hole embedding, intersecting the horizon at $r = \rho_H$. The trivial solution describes $m = 0$ and $\langle \mathcal{O}_m \rangle = 0$, but has non-zero free energy density eq. (4.22),

$$f = -\frac{\lambda N_f N_c}{16\pi^4}\frac{\pi^4}{8}T^4. \tag{4.38}$$

Plugging this f into eqs. (4.19) and (4.20), we obtain the corresponding entropy density, heat capacity density, and correction to the sound speed squared, respectively,

$$s = \frac{\lambda N_f N_c}{16\pi^4}\frac{\pi^4}{2}T^3, \qquad c_V = 3\,s, \qquad \delta v^2 = 0. \tag{4.39}$$

These results are the same as for hypermultiplets with $m = 0$ and $b = 0$. That is no surprise: the solution $R(r) = 0$, and thus the Legendre-transformed action eq. (4.16) evaluated on $R(r) = 0$, is independent of both m and b. As a result, for the trivial solution all physical quantities are proportional to a power of T dictated by dimensional analysis. Moreover, the sound speed squared v^2 must take the value required by $(d+1)$-dimensional scale invariance, $v^2 = 1/\sqrt{d}$, explaning why the $\mathcal{O}\left(N_f/N_c\right)$ correction vanishes, $\delta v^2 = 0$.

We obtain solutions for $R(r)$ describing non-zero m numerically as in chapter 3. Figure 4.2 shows examples of our $T/b > 0$ numerical solutions for $R(r)/(L^2 b)$, where the dashed blue, solid orange, and dot-dashed black lines correspond to Minkowski, black hole, and the critical embeddings, respectively. Similar to the $T/b = 0$ case of section 4.2.3, Minkowski embeddings only exist for large enough m while black hole embeddings only exist for small enough m, and both classes of embeddings exist for a range of m near the critical embedding.

Among the black hole embeddings we find solutions whose boundary conditions approach the exponential behaviour of eq. (4.24b) as $T/b \to 0$. Examples of these appear in figure 4.2a for $T/b = 0.05$, as the three lowest solid orange lines, corresponding to the three lowest values of m, or in figure 4.2b for $T/b = 0.1$ as the lowest few solid orange lines. These solutions describe RG flows to the IR CFT with non-zero temperature, i.e. massless hypermultiplets with $T/b > 0$. In other words, some of the solutions with exponential boundary conditions at $T/b = 0$, which describe RG flows to massless hypermultiplets, survive at sufficiently small non-zero T/b. However, as T/b increases the horizon eventually "hides" any exponential

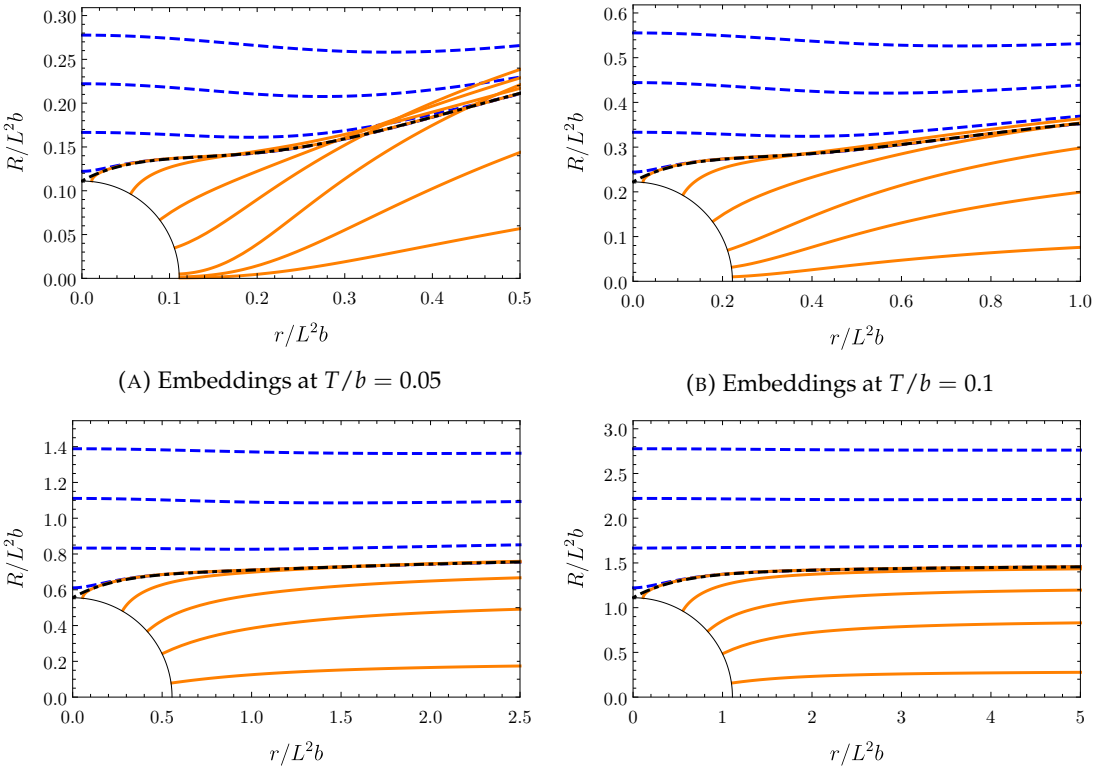

(A) Embeddings at $T/b = 0.05$

(B) Embeddings at $T/b = 0.1$

(C) Embeddings at $T/b = 0.25$

(D) Embeddings at $T/b = 0.5$

FIGURE 4.2: Examples of our numerical solutions for $R(r)/(L^2b)$ as functions of $r/(L^2b)$ when $T/b > 0$. In each plot, the solid black quarter-circle is the horizon ρ_H, given by $\rho_H^2 = r^2 + R^2 = \pi^2 L^4 T^2/2$. The dashed blue, solid orange, and dot-dashed black lines are Minkowski, black hole, and the critical embeddings, respectively, for **(a)** $T/b = 0.05$, **(b)** $T/b = 0.1$, **(c)** $T/b = 0.25$, and **(d)** $T/b = 0.5$.

behaviour. In CFT terms, once T is sufficiently large compared to m, the IR CFT is "washed out" in the plasma.

For a given solution $R(r)$ we perform a numerical fit to the large-r asymptotics in eq. (4.17), extract M and C, and plug these into eq. (4.18) to obtain $\langle \mathcal{O}_m \rangle$. We then calculate f by performing the integral in eq. (4.22) numerically.

Figure 4.3 shows some of our numerical results for f, normalised by $\frac{\lambda N_f N_c}{16\pi^4}$, and for $\langle \mathcal{O}_m \rangle$, normalised by $\frac{\lambda N_f N_c}{8\pi^3}$, both in units of b, as functions of $m/(b\sqrt{\lambda})$. Figure 4.3 has the same colour coding as figure 4.2, and the black dot denotes the critical solution. Our results show clearly that the first-order transition we found at $T/b = 0$ persists to $T/b > 0$, with the same qualitative characteristics. In particular, for some range of $m/(b\sqrt{\lambda})$ near the critical solution both f and $\langle \mathcal{O}_m \rangle$ are multi-valued, and the insets in figure 4.3 are close-ups near the critical solution showing that f exhibits a "fish tail" shape and $\langle \mathcal{O}_m \rangle$ exhibits a spiral shape, similar to the $T/b = 0$ case in figure 4.1. Clearly, as we increase $m/(b\sqrt{\lambda})$ a transition from a black hole to a Minkowski embedding occurs in which f is continuous but its first derivative $\langle \mathcal{O}_m \rangle = \partial f/\partial m$ is not. In figure 4.3 we denote the transition point with a vertical line. The critical embedding is never thermodynamically preferred.

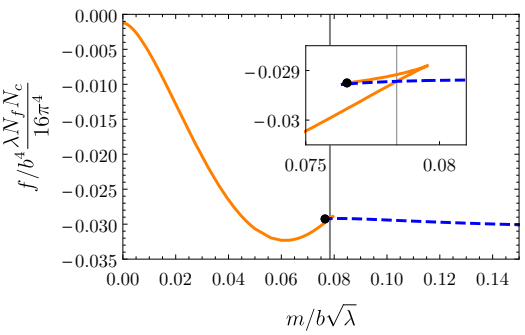

(A) Free energy density at $T/b = 0.1$.

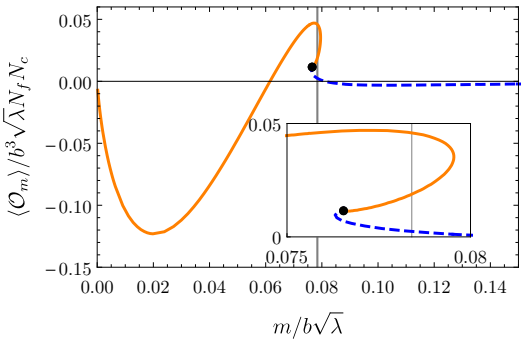

(B) $\langle\mathcal{O}_m\rangle$ at $T/b = 0.1$.

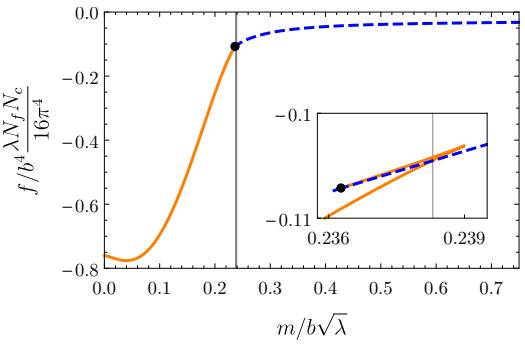

(C) Free energy density at $T/b = 0.5$.

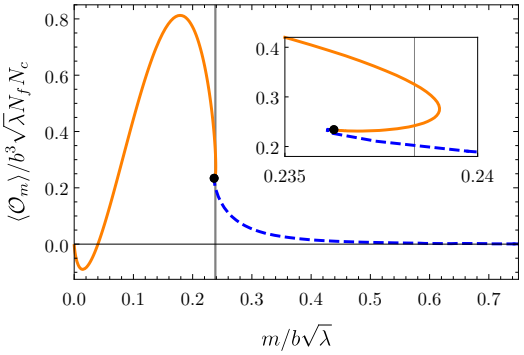

(D) $\langle\mathcal{O}_m\rangle$ at $T/b = 0.5$.

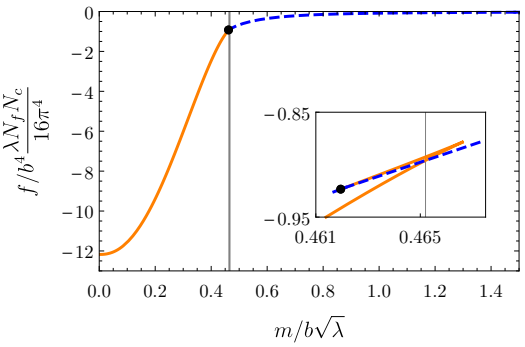

(E) Free energy density at $T/b = 1$.

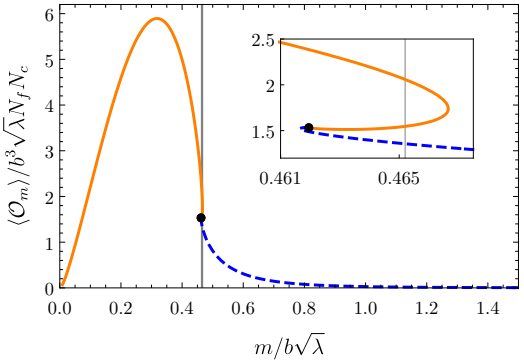

(F) $\langle\mathcal{O}_m\rangle$ at $T/b = 1$.

FIGURE 4.3: Our numerical results for the free energy density $f/(b^4\frac{\lambda N_f N_c}{16\pi^4})$ and for $\langle\mathcal{O}_m\rangle/(b^3\frac{\lambda N_f N_c}{8\pi^3})$ as functions of $m/(b\sqrt{\lambda})$, for **(a)** and **(b)** $T/b = 0.1$, **(c)** and **(d)** $T/b = 0.5$, and **(e)**, and **(f)** $T/b = 1$. As in figs. 4.1 and 4.2, the solid orange and dashed blue lines correspond to black hole and Minkowski embeddings, respectively, and the black dots denote critical embeddings. The insets are close-ups near critical embeddings, showing f's "swallow tail" and $\langle\mathcal{O}_m\rangle$'s spiral, both characteristic of first-order transitions. The vertical gray lines indicate the values of $m/(b\sqrt{\lambda})$ at the first-order transitions.

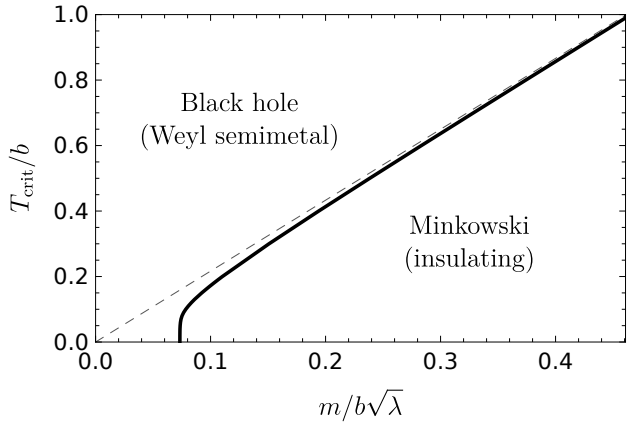

FIGURE 4.4: The phase diagram of our holographic model. The solid black line is the critical temperature $T_{\rm crit}$, in units of b, where we find a first-order transition from black hole to Minkowski embeddings, as a function of $m/(b\sqrt{\lambda})$. To the left of this line, black hole embeddings are thermodynamically preferred, whereas to the right of this line, Minkowski embeddings are thermodynamically preferred. In section 4.2.5 we show the black hole embeddings are dual to WSM states, while Minkowski embeddings are dual to trivially insulating states. The dashed gray line shows the $b = 0$ result $T_{\rm crit} \approx 2.166\, m/\sqrt{\lambda}$ of ref. [1], which our transition line approaches as $m/(b\sqrt{\lambda}) \to \infty$.

We find that the first-order transition persists to all T/b. Figure 4.4 is the phase diagram of our model, showing our numerical result for the critical temperature of the first-order transition, $T_{\rm crit}$, in units of b, as a function of $m/(b\sqrt{\lambda})$. As we found in section 4.2.3, at $T/b = 0$ the transition occurs at $m/(b\sqrt{\lambda}) \approx 0.0733$, and as $m/(b\sqrt{\lambda})$ increases, $T_{\rm crit}/b$ increases. As both m and $T_{\rm crit}$ grow, we expect the influence of b to fade, and the first-order transition to approach that at $b = 0$ [47, 1]. Figure 4.4 confirms that expectation: the dashed grey line denotes the $b = 0$ transition at $T_{\rm crit}/(m/\sqrt{\lambda}) \approx 2.166$ [1][5], which our $T_{\rm crit}$ indeed approaches as $m \to \infty$.

To calculate the entropy density, s we have to differentiate the free energy (4.78) with respect to temperature. It is easiest to do this in steps. First, we have the contribution coming from the endpoints of integration, and second from the integrand itself. The upper bound for both the Minkowski and black hole embeddings has no temperature dependence, nor does the lower bound for the Minkowski solution. This leaves the contribution from the lower bound for the black hole embedding, $r_0 = \frac{\pi L^2}{\sqrt{2}} T \sin\theta$,

$$s_{r_0} = -\frac{\lambda N_c N_f}{16\pi^4 L^8}\left[r_0^3 g(\rho_0)h(\rho_0)\sqrt{1+\frac{L^4 b^2 R^2}{\rho_0^4 h(\rho_0)}}\sqrt{1+R'^2}\right]. \tag{4.40}$$

As $g(\rho_0)h(\rho_0) = 0$ this contribution is zero, $s_{r_0} = 0$. As a result, only the contribution from the integrand itself contributes:

[5]The definition of the 't Hooft coupling λ in ref. [1] is smaller than ours by a factor of 2.

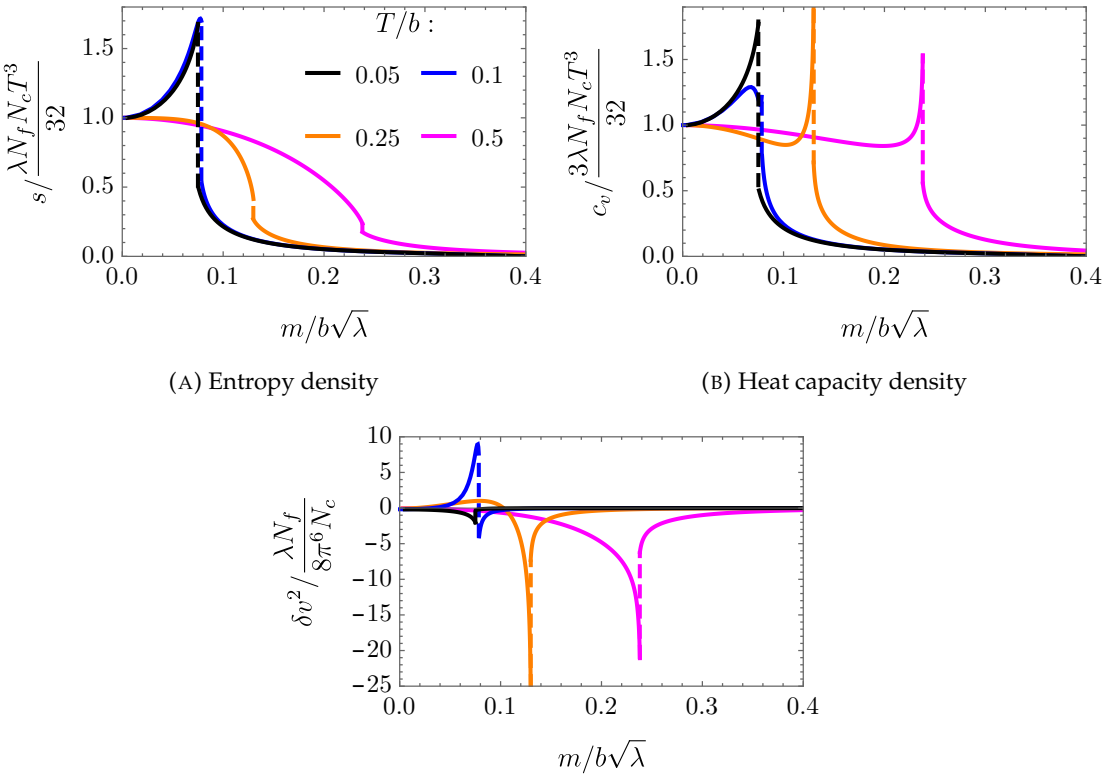

(A) Entropy density

(B) Heat capacity density

(C) Correction to the sound speed squared, δv^2

FIGURE 4.5: (a) Our numerical results for the entropy density, s, normalised by its $m = 0$ value in eq. (4.39), $\lambda N_f N_c T^3/32$, as a function of $m/(b\sqrt{\lambda})$, for $T/b = 0.05$ (solid black), 0.1 (solid blue), 0.25 (solid orange), and 0.5 (solid pink). (b) Our numerical results for the heat capacity density, c_V, normalised by its $m = 0$ value in eq. (4.39), $3\lambda N_f N_c T^3/32$, as a function of $m/(b\sqrt{\lambda})$, for the same values of T/b as in (a). (c) Our numerical results for the $\mathcal{O}\left(N_f/N_c\right)$ correction to the sound speed squared, δv^2 in eq. (4.21), as a function of $m/(b\sqrt{\lambda})$, for the same values of T/b as in (a) and (b). In each case the dashed vertical lines denote a first-order phase transition.

$$s = -\frac{\lambda N_c N_f}{16\pi^4 L^8}\left[\int_{r_0}^{r_c} dr\, \frac{\partial}{\partial T}\left(r^3 g(\rho)h(\rho)\sqrt{1+\frac{L^4 b^2 R^2}{\rho^4 h(\rho)}}\sqrt{1+R'^2}\right)\right]. \tag{4.41}$$

All three of ρ_H, R and R' have T dependence. We can therefore split the differentiation into two parts, one where we vary ρ_H while holding R, R' constant, and another where we vary R, R' while holding ρ_H constant. The former contribution is

$$s_i = -\frac{\lambda N_c N_f}{16\pi^4 L^8}\left[\int_{r_0}^{r_c} dr\, r^3\sqrt{1+R'^2}\,\frac{\partial}{\partial T}\left(g(\rho)h(\rho)\sqrt{1+\frac{L^4 b^2 R^2}{\rho^4 h(\rho)}}\right)\Bigg|_{R,R'}\right], \tag{4.42}$$

where the differentiation can be explicitly performed. The latter contribution is

$$s_{ii} = -\frac{\lambda N_c N_f}{16\pi^4 L^8}\left[\int_{r_0}^{r_c} dr\, \frac{\partial}{\partial T}\left(r^3\sqrt{1+R'^2}\,g(\rho)h(\rho)\sqrt{1+\frac{L^4 b^2 R^2}{\rho^4 h(\rho)}}\right)\Bigg|_{\rho_0}\right]. \tag{4.43}$$

Following ref. [1] this term can be simplified by noticing that the differentiation with temperature can be viewed as a variation δR. Given that the entropy is evaluated on-shell this means we only have to calculate a boundary term,

$$s_{ii} = -\frac{\lambda N_c N_f}{16\pi^4 L^8}\frac{r^3}{\sqrt{1+R'^2}}g(\rho)h(\rho)\sqrt{1+\frac{L^4b^2R^2}{\rho^4 h(\rho)}}R'\frac{\partial R}{\partial T}\Big|_{r_0}^{r_c}, \tag{4.44}$$

where we have three cases to consider. First is the case where the lower bound is $r_0 = 0$, i.e the Minkowksi embedding. We then have the boundary condition $R(0) = R_0$ where R_0 is a constant, hence $R' = 0$ and the contribution to the entropy density is zero. Next we consider the lower bound for the black hole embeddings, where $r_0 = \frac{\pi L^2}{\sqrt{2}}T\sin\theta$. However, as above this implies $g(\rho_0)h(\rho_0) = 0$, so the contribution to the entropy density is zero. Finally we have the upper bound r_c. As this is at the asymptotically AdS_5 boundary we can use the embedding's asymptotic expansion in eq. (4.17),

$$R = L^2 M\left(1 - L^4b^2\frac{\log(r/L)}{2r^2}\right) + \frac{L^6 C}{r^2} + \dots. \tag{4.45}$$

This term has no temperature dependence and so $\frac{\partial R}{\partial T} = 0$, and again the contribution to the entropy density is zero. Ultimately, then, the total entropy density is given by eq. (4.42),

$$s = -\frac{\lambda N_c N_f}{16\pi^4 L^8}\left[\int_{r_0}^{r_c} dr\, r^3\sqrt{1+R'^2}\frac{\partial}{\partial T}\left(g(\rho)h(\rho)\sqrt{1+\frac{L^4b^2R^2}{\rho^4 h(\rho)}}\right)\Big|_{R,R'}\right], \tag{4.46}$$

From s we then compute heat capacity density c_V numerically using finite differences, and from s and c_V we compute the $\mathcal{O}\left(N_f/N_c\right)$ correction to the sound speed squared, δv^2 via eq. (4.21). Figure 4.5 shows some of our numerical results for s, c_V, and δv^2 as functions of $m/(b\sqrt{\lambda})$ for several values of T/b. Both s and c_V take forms characteristic of a first-order transition, for example c_V grows rapidly when approaching the transition.

Exceptional behaviour appears in s, which at low T/b exhibits a dramatic increase as $m/(b\sqrt{\lambda})$ approaches the transition from below: see figure 4.5a with $T/b = 0.05$ (solid black) and 0.1 (solid blue). These results arise from solutions with exponential behaviour at low T/b, namely those we discussed in figures 4.2a and 4.2b. In CFT terms these are cases where the IR is the massless hypermultiplet CFT. Recalling that s counts thermodynamic degrees of freedom, the rise in s at $T/b = 0.05$ or 0.1 presumably comes from these additional massless degrees of freedom. More generally, such increases or spikes in s may serve as signals of emergent massless degrees of freedom.

Figure 4.5c shows that in the conformal limits $m/(b\sqrt{\lambda}) \to 0$ or $\to \infty$ we find $\delta v^2 \to 0$, as expected. In most cases, for $m/(b\sqrt{\lambda})$ near the transition δv^2 spikes down

to negative values. However, for some T/b, near the transition δv^2 becomes positive: in figure 4.5c see $T/b = 0.1$ (solid blue) and 0.25 (solid orange). In those cases the sound speed squared in eq. (4.20) is greater than the conformal value, $v^2 > 1/3$, thus violating the bound conjectured for v^2 in ref. [137]. The significance of such behaviour, if any, we leave for future research.

4.2.5 Conductivity

In this section we compute our system's $U(1)_V$ DC longitudinal and Hall conductivities, σ_{xx} and σ_{xy}, respectively. To do so, we use the method of refs. [128, 129], wherein we introduce a non-dynamical, constant $U(1)_V$ electric field in the x direction, E, compute the resulting expectation values of $U(1)_V$ currents, $\langle J_x \rangle$ and $\langle J_y \rangle$, and from these extract σ_{xx} and σ_{xy}.

As before, we parameterize the D7-branes' worldvolume coordinates as $\xi^a = (t, x, y, z, r)$ plus the S^3 coordinates. Our ansatz for the worldvolume fields again includes $R(r)$ and $\phi(z, r) = bz + \Phi(r)$. As mentioned in section 4.2.1, the $U(1)_V$ current is dual to the D7-brane's $U(1)$ worldvolume gauge field, so now our ansatz also includes two gauge field components. The first is $A_x = Et + a_x(r)$, where the first term introduces the electric field E in the x direction, while the second term, $a_x(r)$, allows for a non-zero $\langle J_x \rangle$. We use rotational symmetry in the xy-plane to set $E > 0$. Second is $A_y(r)$, which allows for a non-zero $\langle J_y \rangle$. The D7-brane action (4.7) evaluated on this ansatz is

$$S_{\rm D7} = -\mathcal{N} \int dr \left(\sqrt{w_1(r) \left(h + hR'^2 + A_y'^2 \right) + w_2(r)\phi'^2 + w_3(r) A_x'^2} - w_4(r) A_y' \right), \tag{4.47a}$$

$$w_1 \equiv r^6 \left(h + \frac{L^4 b^2 R^2}{(r^2+R^2)^2} \right) \left(g^2 - \frac{L^4 E^2}{(r^2+R^2)^2} \right), \tag{4.47b}$$

$$w_2 \equiv r^6 h^2 R^2 \left(g^2 - \frac{L^4 E^2}{(r^2+R^2)^2} \right), \tag{4.47c}$$

$$w_3 \equiv r^6 g^2 \left(h + \frac{L^4 b^2 R^2}{(r^2+R^2)^2} \right), \tag{4.47d}$$

$$w_4 \equiv \frac{L^4 r^4}{(r^2+R^2)^2}\, b\, E, \tag{4.47e}$$

where $R' \equiv \partial R/\partial r$, and similarly for the other fields. The action in eq. (4.47a) depends on ϕ', A_x', and A_y' and not on ϕ, A_x, or A_y. As a result, the equations of motion imply that the corresponding canonical momenta are independent of r. To be explicit, the

canonical momenta conjugate to ϕ, A_x, and A_y are, respectively,

$$P_\phi \equiv \frac{\delta S_{\rm D7}}{\delta \phi'} = -\mathcal{N}\frac{w_3\phi'}{\sqrt{w_1(r)\left(h+hR'^2+A_y'^2\right)+w_2(r)\phi'^2+w_3(r)A_x'^2}}, \tag{4.48a}$$

$$P_x \equiv \frac{\delta S_{\rm D7}}{\delta A_x'} = -\mathcal{N}\frac{w_2A_x'}{\sqrt{w_1(r)\left(h+hR'^2+A_y'^2\right)+w_2(r)\phi'^2+w_3(r)A_x'^2}}, \tag{4.48b}$$

$$P_y \equiv \frac{\delta S_{\rm D7}}{\delta A_y'} = -\mathcal{N}\frac{w_1A_y'}{\sqrt{w_1(r)\left(h+hR'^2+A_y'^2\right)+w_2(r)\phi'^2+w_3(r)A_x'^2}}+\mathcal{N}w_4, \tag{4.48c}$$

and the corresponding Euler-Lagrange equations are, respectively, $\partial_r P_\phi = 0$, $\partial_r P_x = 0$, and $\partial_r P_y = 0$. We therefore write the canonical momenta as $P_\phi = \mathcal{N}p_\phi$, $P_x = \mathcal{N}j_x$ and $P_y = \mathcal{N}j_y$ with constants p_ϕ, j_x and j_y. In the appendix for this section we show that these constants determine the one-point functions of the dual operators: we again have $\langle \mathcal{O}_\phi \rangle = \mathcal{N}p_\phi$, while

$$\langle J_x \rangle = -\left(2\pi\alpha'\right)\mathcal{N}j_x, \qquad \langle J_y \rangle = -\left(2\pi\alpha'\right)\mathcal{N}j_y. \tag{4.49}$$

To obtain an action for $R(r)$ alone, we use a similar strategy to that in section 4.2.1, eliminating ϕ, A_x, and A_y in favour of P_ϕ, P_x, and P_y by a Legendre transform. To be explicit, we insert $P_\phi = \mathcal{N}p_\phi$, $P_x = \mathcal{N}j_x$ and $P_y = \mathcal{N}j_y$ into eq. (4.48), solve for ϕ', A_x', and A_y', plug these solutions into the action eq. (4.47a), and then Legendre transform with respect to ϕ, A_x, and A_y. The result is

$$\begin{aligned}\tilde{S}_{\rm D7} &\equiv S_{\rm D7} - \int dr\left(\phi' P_\phi + A_x'P_x + A_y'P_y\right)\\ &= -\mathcal{N}\int dr\,\sqrt{h}\sqrt{1+R'^2}\sqrt{w_1(r)-\frac{w_1(r)}{w_2(r)}p_\phi^2-\frac{w_1(r)}{w_3(r)}j_x^2-\left[j_y-w_4(r)\right]^2},\end{aligned} \tag{4.50}$$

Similar to $\tilde{S}_{\rm D7}$ in eq. (4.16) , the integrand of $\tilde{S}_{\rm D7}$ in eq. (4.50) includes a product of three square roots. The first two of these, $\sqrt{h}$ and $\sqrt{1+R'^2}$, are manifestly real for all r. However the third square root is not necessarily real for all r. To see why in detail, we re-write the factors under the third square root,

$$\tilde{S}_{\rm D7} = -\mathcal{N}\int dr\,\sqrt{h}\sqrt{1+R'^2}\sqrt{\alpha(r)\beta(r)-\gamma(r)}, \tag{4.51a}$$

$$\alpha(r) \equiv g^2 - \frac{L^4 E^2}{\left(r^2+R^2\right)^2}, \tag{4.51b}$$

$$\beta(r) \equiv r^6\left(h + \frac{L^4 b^2 R^2}{\left(r^2+R^2\right)^2}\right) - \frac{j_x^2}{g^2}, \tag{4.51c}$$

$$\gamma(r) \equiv \frac{p_\phi^2}{h^2}\left(\frac{h}{R^2} + \frac{L^4 b^2}{\left(r^2+R^2\right)^2}\right) + \left(j_y - \frac{L^4 r^4 b E}{\left(r^2+R^2\right)^2}\right)^2. \tag{4.51d}$$

Clearly $\gamma(r) \geq 0$ for all r. However, $\alpha(r)$ and $\beta(r)$ can change sign. For example, if $T > 0$ then each of $\alpha(r)$ and $\beta(r)$ is positive at the AdS_5 boundary, $r \to \infty$, and negative at the horizon, where $g = 0$. Each must therefore change sign at some r in between. If one of $\alpha(r)$ or $\beta(r)$ changes sign and the other does not, then $\alpha(r)\beta(r) - \gamma(r) < 0$ for some range of r (until the other also changes sign). In that case, $\tilde{S}_{\rm D7}$ acquires a non-zero imaginary part, signaling a tachyonic instability, as mentioned in section 4.2.1. The method of refs. [128, 129] is to adjust p_ϕ, j_x, and j_y such that $\alpha(r)$ and $\beta(r)$ change sign at the same value of r, such that $\alpha(r)\beta(r) - \gamma(r) \geq 0$ for all r, thus avoiding the instability. With $\langle J_x\rangle = -(2\pi\alpha')j_x$ and $\langle J_y\rangle = -(2\pi\alpha')j_y$ thus fixed, we extract the DC conductivities via

$$\sigma_{xx} = \lim_{E\to 0}(2\pi\alpha')\langle J_x\rangle/E, \qquad \sigma_{xy} = -\sigma_{yx} = -\lim_{E\to 0}(2\pi\alpha')\langle J_y\rangle/E, \tag{4.52}$$

where the factors of $(2\pi\alpha')$ come from our normalisation of the D7-brane's worldvolume gauge field, described below eq. (4.7).

We will thus impose the conditions $\alpha(r_*) = 0$, $\beta(r_*) = 0$, and $\gamma(r_*) = 0$ at some r_*. The location r_* is in fact a horizon of the open string metric on the D7-brane worldvolume [138, 139]. This horizon has an associated Hawking temperature,[6] in general larger than the background AdS_5 black hole's Hawking temperature T. The difference in temperatures signals that these solutions do not describe thermal equilibrium states, since heat will flow from the D7-brane to the background black hole. In fact, stationary solutions with $E > 0$ describe non-equilibrium steady states. For a review of their physics, see refs. [138, 139] and references therein. We will ultimately take $E \to 0$, as in eq. (4.52), so we only use the $E > 0$ solutions in intermediate steps. However, the effect of $b > 0$ on solutions with $E > 0$ is worth studying in future research, as we discuss in section 4.3.

Not all D7-brane embeddings have a worldvolume horizon when $E > 0$. In particular, in some Minkowski embeddings the D7-brane ends before either $\alpha(r)$ or $\beta(r)$ changes sign. Whether a worldvolume horizon appears thus depends on the boundary conditions, which in turn depend on T. We consider $T = 0$ first, in section 4.2.6, and then $T > 0$ in section 4.2.7.

[6] Whether any entropy can be associated with this horizon is an open question [140, 141, 138, 139].

4.2.6 Conductivity at Zero Temperature

If $T = 0$ then $g = 1$ and $h = 1$. We first consider D7-brane embeddings with a worldvolume horizon at some r_*, the value of which is fixed by $\alpha(r_*) = 0$. With the notation $R_* \equiv R(r_*)$ we have from eq. (4.51b)

$$1 - \frac{L^4 E^2}{(r_*^2 + R_*^2)^2} = 0 \qquad \Rightarrow \qquad r_*^2 + R_*^2 = L^2 E. \tag{4.53}$$

In the (r, R) plane the worldvolume horizon is thus a circle of radius $L\sqrt{E}$. The conditions $\beta(r_*) = 0$ and $\gamma(r_*) = 0$ then give, respectively,

$$r_*^6 \left(1 + \frac{L^4 b^2 R_*^2}{(r_*^2 + R_*^2)^2}\right) - j_x^2 = 0, \tag{4.54a}$$

$$p_\phi^2 \left(\frac{1}{R_*^2} + \frac{L^4 b^2}{(r_*^2 + R_*^2)^2}\right) + \left(j_y - \frac{L^4 r_*^4 b E}{(r_*^2 + R_*^2)^2}\right)^2 = 0, \tag{4.54b}$$

In eq. (4.54b) the left-hand side is a sum of squares, which vanishes if and only if each term in the sum vanishes independently. The first term vanishes only if $p_\phi = 0$, which implies $\langle \mathcal{O}_\phi \rangle = 0$. We thus take $p_\phi = 0$ henceforth. In that case eqs. (4.54a) and (4.54b) determine j_x and j_y, and thus $\langle J_x \rangle$ and $\langle J_y \rangle$ via eq. (4.49), giving

$$\langle J_x \rangle = (2\pi\alpha')\, r_*^3 \sqrt{1 + \frac{L^4 b^2 R_*^2}{(r_*^2 + R_*^2)^2}}, \tag{4.55a}$$

$$\langle J_y \rangle = -(2\pi\alpha')\, L^4\, b\, E \frac{r_*^4}{(r_*^2 + R_*^2)^2}. \tag{4.55b}$$

We now need r_* and R_*, at least in the limit $E \to 0$. If $E = 0$ then clearly eq. (4.53) implies $r_* = 0$ and $R_* = 0$, or in other words $R_0 \equiv R(r = 0) = 0$. We thus learn that when $E \to 0$ the solutions with worldvolume horizon reduce to the black-hole like embeddings with the exponential boundary condition in eq. (4.24b). As discussed in section 4.2.3, these embeddings describe RG flows to an IR CFT, the massless probe hypermultiplet CFT.

To determine r_* and R_* at small E we expand $R(r) = R^{(0)}(r) + R^{(1)}(r) + \ldots$, where $R^{(0)}(r)$ is the solution at $E = 0$, $R^{(1)}(r)$ is the first correction at small non-zero E, and so on. All we will need to know about the terms in this expansion is that $R^{(0)}$ obeys the boundary condition of eq. (4.24b), and in particular $R^{(0)}(r) \propto \exp\left(-L^2 b/r\right)$ at small r. At leading order in small E, eq. (4.54a) becomes

$$r_*^2 + R^{(0)}(r_*)^2 \approx L^2 E. \tag{4.56}$$

When $E \to 0$ we have $r_* \to 0$, but $R^{(0)}(r_*) \propto \exp\left(-L^2 b/r_*\right) \to 0$ more quickly, so to leading approximation eq. (4.56) gives $r_* \approx L\sqrt{E}$ and $R^{(0)}(r_*) \approx 0$, and hence $R_* \approx 0$.

Plugging these into eq. (4.55) gives

$$\langle J_x \rangle = (2\pi\alpha')\, L^3\, E^{3/2} \tag{4.57a}$$

$$\langle J_y \rangle = -(2\pi\alpha')\, L^4\, b\, E. \tag{4.57b}$$

Given that our IR is a CFT, the powers of E in eq. (4.57) are dictated by dimensional analysis and the fact that $\langle J_y \rangle$ must be proportional to the $\mathcal{T}$-breaking parameter b. Plugging eq. (4.57) into eq. (4.52) we obtain

$$\sigma_{xx} = 0, \qquad \sigma_{xy} = \frac{N_f N_c}{4\pi^2}\, b. \tag{4.58}$$

We thus find that the black-hole like embeddings with the exponential boundary condition in eq. (4.24b) describe RG flows from small values of $m/(b\sqrt{\lambda})$ in the UV to massless hypermultiplets in the IR, with vanishing DC longitudinal conductivity, $\sigma_{xx} = 0$, and an anomalous Hall conductivity, $\sigma_{xy} \neq 0$. The latter indicates that $\mathcal{T}$ is broken in the IR.

Remarkably, our σ_{xy} in eq. (4.58) is *independent* of the hypermultiplet mass m. In fact, it takes the value determined by the $U(1)_A$ anomaly when $m = 0$, but now extended to cases with small $m/(b\sqrt{\lambda})$, described by our black-hole like embeddings. In contrast, σ_{xy} of the free Dirac fermion in eq. (4.6) and of previous holographic models [14, 15, 102, 103, 104, 105] depended on m, and in particular decreased as m increased, reaching $\sigma_{xy} = 0$ at a quantum critical point. The reason for this difference is clear from a holographic perspective. In previous holographic models, σ_{xy} was proportional to the product of the Chern-Simons coefficient and the value of the $U(1)_A$ gauge field at the horizon. Our result in eq. (4.58) has the same form, but in our case the $U(1)_A$ gauge field is $\partial_\mu \phi/2$, as mentioned below eq. (4.9). Our ansatz is $\phi(z, r) = bz + \Phi(r)$, and our solution includes $p_\phi = 0$, which implies $\phi(z, r)$ is actually independent of r and hence $\Phi(r) = 0$. As a result, our $U(1)_A$ gauge field is simply $A_z^5 = \partial_z \phi/2 = b/2$, leading to our m-independent result for σ_{xy} in eq. (4.58). Crucially, this m-independence is not required by any symmetry, and is not determined by the $U(1)_A$ anomaly alone, but comes from dynamics, and specifically from the fact that we had to take $p_\phi = 0$ to avoid a tachyonic instability, as explained above.

We now consider the case where the D7-brane has no worldvolume horizon. These embeddings are necessarily Minkowski, and in particular the D7-brane should reach $r = 0$ outside of the worldvolume horizon described by the semicircle in eq. (4.53). Indeed, demanding $\alpha(r) \geq 0$ for all r gives $r^2 + R(r)^2 \geq L^2 E$ for all r. Evaluating this at $r = 0$ gives $R_0 > L\sqrt{E}$. Similarly we demand $\beta(r) \geq 0$ for all r. Evaluating this at $r = 0$ gives $\beta(0) = -j_x^2 \geq 0$, which implies $j_x = 0$, so that in fact $\beta(0) = 0$. Finally we demand $\alpha(r)\beta(r) - \gamma(r) \geq 0$ for all r. Evaluating this at $r = 0$ gives $-\gamma(0) \geq 0$, where

$$\gamma(0) = \frac{p_\phi^2}{R_0^2}\left(1 + \frac{L^4 b^2}{R_0^2}\right) + j_y^2. \tag{4.59}$$

Clearly $-\gamma(0) \geq 0$ is possible if and only if $p_\phi = 0$ and $j_y = 0$, so that in fact $\gamma(0) = 0$. We thus find that Minkowski embeddings with $R_0 \geq L\sqrt{E}$ have $p_\phi = 0$, $j_x = 0$, and $j_y = 0$, implying $\langle \mathcal{O}_\phi \rangle = 0$, $\langle J_x \rangle = 0$, and $\langle J_y \rangle = 0$, respectively. As a result, $\sigma_{xx} = 0$ and $\sigma_{xy} = 0$, so that these embeddings describe trivially insulating states.

If we now take $E \to 0$, then $R_0 \geq L\sqrt{E}$ becomes simply $R_0 \geq 0$. The $E \to 0$ limit of embeddings with no worldvolume horizon thus correspond to the Minkowski embeddings with the $r \to 0$ boundary condition in eq. (4.24a), describing large values of $m/(b\sqrt{\lambda})$. We have therefore learned that the large $m/(b\sqrt{\lambda})$ phase exhibits no current flow in response to an applied electric field, as both the longitudinal and Hall conductivities vanish, $\sigma_{xx} = 0$ and $\sigma_{xy} = 0$, respectively. The latter indicates that $\mathcal{T}$ is preserved in the IR.

To summarise, when $T = 0$ and $E = 0$ we find that $\langle \mathcal{O}_\phi \rangle = 0$ and $\sigma_{xx} = 0$ for all $m/(b\sqrt{\lambda})$, while σ_{xy} takes the non-zero value in eq. (4.58) at small $m/(b\sqrt{\lambda})$, dual to black-hole-like embeddings, but vanishes at large $m/(b\sqrt{\lambda})$, dual to Minkowski embeddings. In section 4.2.3 we found a first-order transition from black hole-like embeddings to Minkowski embeddings at $m/(b\sqrt{\lambda}) \approx 0.0733$, so the Hall conductivity in our model is

$$\sigma_{xy} = \begin{cases} \dfrac{N_f N_c}{4\pi^2}\, b, & m/(b\sqrt{\lambda}) \lesssim 0.0733, \\ 0, & m/(b\sqrt{\lambda}) \gtrsim 0.0733, \end{cases} \tag{4.60}$$

and correspondingly in the IR $\mathcal{T}$ is broken when $\sigma_{xy} \neq 0$ and is preserved when $\sigma_{xy} = 0$. Remarkably, σ_{xy} when $m/(b\sqrt{\lambda}) \lesssim 0.0733$ is independent of m, in contrast to the free Dirac fermion in eq. (4.6) and previous holographic models [14, 15, 102, 103, 104, 105]. This σ_{xy} is precisely the value dictated by the $U(1)_A$ anomaly when $m = 0$, but now extended to $m/(b\sqrt{\lambda}) \lesssim 0.0733$. We thus identify the $m/(b\sqrt{\lambda}) \lesssim 0.0733$ phase as a WSM and the $m/(b\sqrt{\lambda}) \gtrsim 0.0733$ phase as a trivial insulator, as indicated in our phase diagram, figure 4.4.

4.2.7 Conductivity at Non-Zero Temperature

At $T > 0$ we first consider embeddings with a worldvolume horizon at r_*, determined by $\alpha(r_*) = 0$. Denoting the values of R and g at r_* as R_* and g_*, respectively, and using the definition of $\alpha(r)$ in eq. (4.51b) and g in eq. (4.11), we find

$$g_*^2 - \frac{L^4\, E^2}{(r_*^2 + R_*^2)^2} = 0, \qquad \Rightarrow \qquad r_*^2 + R_*^2 = L^2\, E/2 + \sqrt{L^4\, E^2/4 + \rho_H^4}. \tag{4.61}$$

In the (r, R) plane the worldvolume horizon is thus again a semicircle, which at $E = 0$ coincides with the AdS_5-Schwarzschild horizon ρ_H, and as E grows, monotonically moves to larger r. In particular, $r_*^2 + R_*^2 \geq \rho_H^2$ for all r, i.e. the worldvolume horizon is always coincident with or outside the AdS_5-Schwarzschild horizon. In general, when

$T > 0$ and $E > 0$, embeddings with a worldvolume horizon fall into two categories. The first are black hole embeddings. The second are Minkowski embeddings in which the D7-brane has a worldvolume horizon but ends before reaching the black hole horizon.

Denoting the value of h at r_* as h_*, $\beta(r_*) = 0$ and $\gamma(r_*) = 0$ give, respectively,

$$r_*^6 \left(h_* + \frac{L^4 b^2 R_*^2}{(r_*^2 + R_*^2)^2} \right) - \frac{j_x^2}{g_*^2} = 0, \tag{4.62a}$$

$$\frac{p_\phi^2}{h_*^2} \left(\frac{h_*}{R_*^2} + \frac{L^4 b^2}{(r_*^2 + R_*^2)^2} \right) + \left(j_y - \frac{L^4 r_*^4 \, b \, E}{(r_*^2 + R_*^2)^2} \right)^2 = 0. \tag{4.62b}$$

Similar to the $T = 0$ case, in eq. (4.62b) the left-hand side is a sum of squares, which vanishes if and only if each term in the sum vanishes independently. The first term vanishes only if $p_\phi = 0$, so we take $p_\phi = 0$ henceforth, and thus $\langle \mathcal{O}_\phi \rangle = 0$. In that case eqs. (4.62a) and (4.62b) determine j_x and j_y, and thus $\langle J_x \rangle$ and $\langle J_y \rangle$,

$$\langle J_x \rangle = (2\pi\alpha') \, r_*^3 \, \frac{L^2 E}{r_*^2 + R_*^2} \sqrt{h_* + \frac{L^4 b^2 R_*^2}{(r_*^2 + R_*^2)^2}}, \tag{4.63a}$$

$$\langle J_y \rangle = -(2\pi\alpha') \, L^4 \, b \, E \frac{r_*^4}{(r_*^2 + R_*^2)^2}. \tag{4.63b}$$

We are interested in the limit $E \to 0$. As mentioned above, when $E = 0$ the worldvolume horizon coincides with the black hole horizon, or in other words, only black hole embeddings have a worldvolume horizon, which is at r_H. When $E \to 0$ we thus have $r_* \to r_H$ and $r_*^2 + R_*^2 \to r_H^2 + R(r_H)^2 = \rho_H^2$. Expanding $\langle J_x \rangle$ and $\langle J_y \rangle$ in eq. (4.63) in E, and using $\rho_H = \pi L^2 T / \sqrt{2}$, we thus find

$$\langle J_x \rangle = (2\pi\alpha') \, r_H^3 \, \frac{4E}{\pi^4 L^4 T^4} \sqrt{\frac{1}{2} \pi^4 L^4 T^4 + b^2 \, R(r_H)^2} + \mathcal{O}(E^2), \tag{4.64a}$$

$$\langle J_y \rangle = -(2\pi\alpha') \, L^4 \, b \, E \frac{4 r_H^4}{\pi^4 L^8 T^4} + \mathcal{O}(E^2). \tag{4.64b}$$

Using eq. (4.52) we then find

$$\sigma_{xx} = \frac{N_f N_c}{4\pi^2} \, r_H^3 \, \frac{4}{\pi^4 L^8 T^4} \sqrt{\frac{1}{2} \pi^4 L^4 T^4 + b^2 R(r_H)^2}, \tag{4.65a}$$

$$\sigma_{xy} = \frac{N_f N_c}{4\pi^2} \, b \, \frac{4 \, r_H^4}{\pi^4 L^8 T^4}. \tag{4.65b}$$

In general, we must determine σ_{xx} and σ_{xy} as functions of $m/(b\sqrt{\lambda})$ numerically. In particular, as explained at the beginning of section 4.2.4, for black hole embeddings we choose r_H, which determines $R(r_H) = \sqrt{\rho_H^2 - r_H^2}$, and impose $R'(r_H) = 0$, numerically solve the equation of motion, and then from the large-r asymptotics we extract

$m/(b\sqrt{\lambda})$.

However, we know one black hole embedding exactly, namely the trivial solution $R(r) = 0$, corresponding to $m = 0$. The trivial solution has $r_H = \rho_H$, so from eq. (4.65) we find

$$\sigma_{xx} = \frac{N_f N_c}{4\pi^2}\,\pi T, \qquad \sigma_{xy} = \frac{N_f N_c}{4\pi^2}\,b, \qquad m = 0. \tag{4.66}$$

Clearly when $m = 0$ all b dependence disappears from σ_{xx}, which takes the $b = 0$ and $m = 0$ value of ref. [128], and all T dependence disappears from σ_{xy}, which takes the value we found in eq. (4.58) at $T = 0$ and small $m/(b\sqrt{\lambda})$.

We now consider the case where the D7-brane has no worldvolume horizon. Our arguments here are very similar to the $T = 0$ case, so we will be brief. These embeddings are necessarily Minkowski, with the D7-brane ending at $r = 0$ outside of the worldvolume horizon in eq. (4.61). We demand $\alpha(r) \geq 0$ and $\beta(r) \geq 0$ for all $r \in [0, \infty)$. The condition $\beta(0) \geq 0$ is satisfied if and only if $j_x = 0$, so that in fact $\beta(0) = 0$. We also demand $\alpha(r)\beta(r) - \gamma(r) \geq 0$ for all $r \in [0, \infty)$, which when evaluated at $r = 0$ becomes $-\gamma(0) \geq 0$, which is satisfied if and only if $p_\phi = 0$ and $j_y = 0$. As a result, embeddings without a worldvolume horizon describe states with $\langle \mathcal{O}_\phi \rangle = 0$, $\langle J_x \rangle = 0$, and $\langle J_y \rangle = 0$, and hence $\sigma_{xx} = 0$ and $\sigma_{xy} = 0$, i.e. trivially insulating states.

Figure 4.6 shows some of our numerical results for σ_{xx} and σ_{xy}, normalised by their $m = 0$ values in eq. (4.66). Figures 4.6a and 4.6b show $\sigma_{xx}/(N_f N_c T/4\pi)$ and $\sigma_{xy}/(N_f N_c/(4\pi^2))$ as functions of $m/(b\sqrt{\lambda})$, for sample values of T/b. In both figures the vertical dashed lines indicate the first order phase transition of figure 4.4. For small T/b, such as for example $T/b = 0.1$ (blue in figure 4.6a), as we increase $m/(b\sqrt{\lambda})$ we find σ_{xx} exhibits a maximum just below the transition. Such behaviour likely indicates a pole in J_x's retarded two-point function in Fourier space near the origin of the complex frequency plane, and may be related to the IR CFT, similar to what we discussed for the entropy density in figure 4.5. At larger T/b however, σ_{xx} decreases monotonically, reaching $\sigma_{xx} = 0$ at the transition. In contrast, for all $T/b > 0$ we find σ_{xy} decreases monotonically as $m/(b\sqrt{\lambda})$ increases, reaching $\sigma_{xy} = 0$ at the transition. For $m/(b\sqrt{\lambda})$ above the transition, $\sigma_{xx} = 0$ and $\sigma_{xy} = 0$.

Figures 4.6c and 4.6d show 3D plots of σ_{xx} and σ_{xy}, normalised by their $m = 0$ values in eq. (4.66), as functions of $m/(b\sqrt{\lambda})$ and T/b. These plots summarise all of our main results. For example, the phase diagram of figure 4.4 is apparent in the plane of $m/(b\sqrt{\lambda})$ and T/b, the step-function in σ_{xy} of eq. (4.60) is obvious in figure 4.6d at $T = 0$, and so on. Figure 4.6c also shows a spike in σ_{xx} at low T/b and $m/(b\sqrt{\lambda})$ near the transition, consistent with the maximum in figure 4.6a. As mentioned above, this spike likely comes from a pole in J_x's retarded two-point function near the origin of the complex frequency plane.

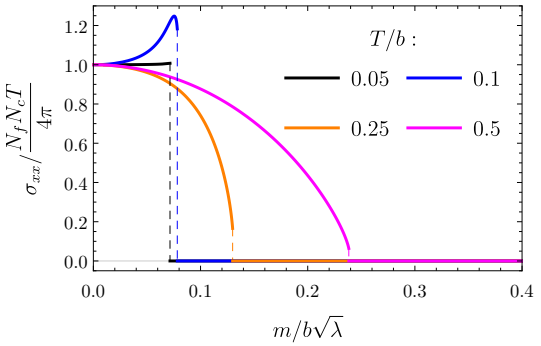

(A) Longitudinal conductivity σ_{xx}.

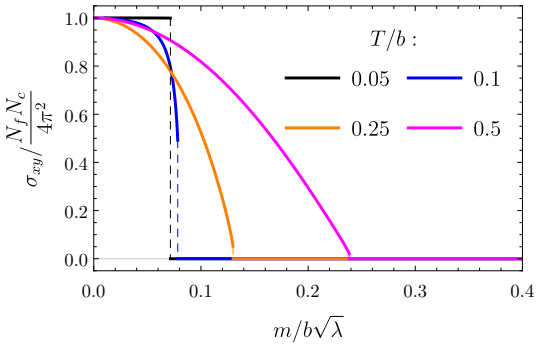

(B) Hall conductivity σ_{xy}.

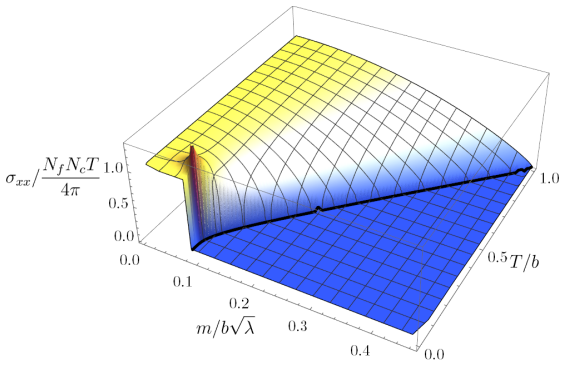

(C) Longitudinal conductivity σ_{xx}.

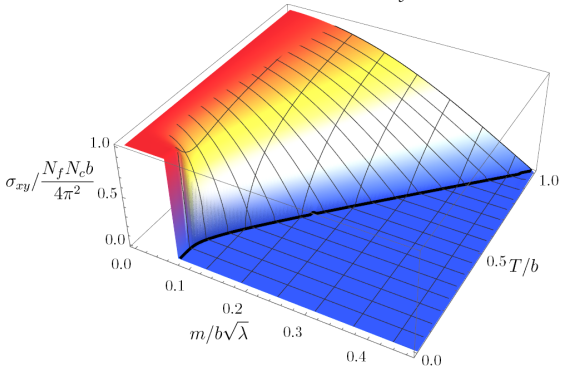

(D) Hall conductivity σ_{xy}.

FIGURE 4.6: Our numerical results for **(a)** the DC longitudinal conductivity, $\sigma_{xx}/(N_f N_c T/4\pi)$, and **(b)** the DC Hall conductivity, $\sigma_{xy}/(N_f N_c/(4\pi^2))$, as functions of $m/(b\sqrt{\lambda})$, for $T/b = 0.05$ (black) 0.1 (blue), 0.25 (orange), and 0.5 (purple). In each case the vertical dashed line indicates the first order phase transition of figure 4.4. As $m/(b\sqrt{\lambda})$ approaches the transition from below, σ_{xy} decreases monotonically for all T/b, reaching $\sigma_{xy} = 0$ at the transition. In contrast, σ_{xx} decreases monotonically for larger T/b, but exhibits a maximum near the transition at small T/b. For $m/(b\sqrt{\lambda})$ above the transition, $\sigma_{xx} = 0$ and $\sigma_{xy} = 0$. **(c)** and **(d)** 3D plots of our numerical results for $\sigma_{xx}/(N_f N_c T/4\pi)$ and $\sigma_{xy}/(N_f N_c b/(4\pi^2))$, respectively, as functions of $m/(b\sqrt{\lambda})$ and T/b.

4.3 Discussion

In this section we studied a top-down holographic model of a WSM, namely probe D7-branes in the $AdS_5 \times S^5$ background of type IIB supergravity, dual to probe hypermultiplets in $\mathcal{N} = 4$ SYM at large N_c and large coupling λ, with worldvolume fields describing non-zero hypermultiplet mass m and background spatial $U(1)_A$ gauge field b. The latter explicitly breaks time reversal symmetry, $\mathcal{T}$.

At zero temperature, $T = 0$, we found that sufficiently small values of $m/(b\sqrt{\lambda})$ in the UV renormalise to zero mass in the IR, so that the IR is a CFT, namely $\mathcal{N} = 4$ SYM coupled to massless probe hypermultiplets. As we increased $m/(b\sqrt{\lambda})$ we found a first-order quantum phase transition, at $m/(b\sqrt{\lambda}) \approx 0.0733$. When $m/(b\sqrt{\lambda}) \lesssim 0.0733$, we found a WSM with $\sigma_{xx} = 0$ but non-zero anomalous Hall conductivity σ_{xy}, and hence broken $\mathcal{T}$ in the IR. Remarkably, this σ_{xy} at $T = 0$ was

independent of $m/(b\sqrt{\lambda})$, retaining its $m = 0$ value, determined by the $U(1)_A$ anomaly, for all $m/(b\sqrt{\lambda}) \lesssim 0.0733$. When $m/(b\sqrt{\lambda}) \gtrsim 0.0733$ we found a trivial insulator with $\sigma_{xx} = 0$ and $\sigma_{xy} = 0$, and hence restored $\mathcal{T}$ in the IR. The first order transition survived for all $T/b > 0$, as summarised in our phase diagram, figure 4.4. The biggest effect of $T/b > 0$ was the fact that both σ_{xx} and σ_{xy} acquired non-trivial dependence on $m/(b\sqrt{\lambda})$ and T/b in the WSM phase, though both still vanished in the trivial insulator phase, as summarised in figure 4.6. We also studied our model's thermodynamics, finding among other things a rise in the entropy density at low T/b for $m/(b\sqrt{\lambda})$ just below the transition, presumably coming from the emergent IR CFT degrees of freedom.

Our model had several non-trivial features distinct from previous models, such as the free Dirac fermion model and previous holographic models that we discussed in the introduction. Chief among these differences was our first order transition for all T/b, including $T/b = 0$, in contrast to the second-order (quantum) phase transitions of most previous models, as well as the fact that our $T = 0$ anomalous Hall conductivity was independent of m.

These results raise many crucial questions for future research on this model. For example, what is the spectrum of excitations of our model? In particular, how do the retarded Green's functions in the probe sector depend on $m/(b\sqrt{\lambda})$ and T/b? Where are their poles, representing the excitations of the system? How do the corresponding spectral functions behave? How does the IR CFT affect these? Does a pole in the retarded two-point function of the $U(1)_V$ current produce the maximum we saw in σ_{xx} at sufficiently small $m/(b\sqrt{\lambda})$ and T/b in figure 4.6? More generally, the spectrum of excitations could reveal whether our model has perturbative instabilities, long-lived propagating modes, the expected Fermi surfaces and associated topological invariants, and more.

Particularly important excitations characterising the WSM phase are of course Fermi arcs. Does our model support Fermi arcs? These may be "washed out" at strong coupling, nevertheless boundary currents required by the $U(1)_A$ anomaly, and hence topologically protected, should still appear [106]. Does our model support such boundary currents?

Holographic models also revealed an anomalous Hall viscosity in WSMs [107]. Does our model support an anomalous Hall viscosity? From the holographic perspective this phenomenon arises from a mixed $U(1)_A$-gravitational Chern-Simons term [107]. The D7-brane WZ terms indeed includes a term of the correct form [142], which however comes with an additional factor of $\alpha'^2 = L^4/\lambda$ compared to the WZ term we included in eq. (4.7), and hence is suppressed when $\lambda \gg 1$. We therefore expect that our model indeed exhibits anomalous Hall viscosities, albeit vanishing as $1/\lambda$ at strong coupling.

Holographic probe brane models exhibit several special phenomena, especially in transport. For example, in our model a non-zero electric field, $E > 0$, can induce

negative differential conductivity, in which the longitudinal conductivity σ_{xx} is a *decreasing* function of the electric field [143]. In contrast, in typical metals an increasing electric field produces a larger current. For a WSM in parallel electric and magnetic fields, the $U(1)_A$ anomaly can induce negative magneto-resistance, in which σ_{xx} is an *increasing* function of the magnetic field, in contrast to typical metals [144]. Remarkably, our model exhibits negative magneto-resistance already when $b = 0$ [145, 146]. How does non-zero b affect these phenomena? Could this model suggest any unusual transport in real strongly-coupled WSMs?

More generally, this work opens the way for top-down holographic probe brane models of many semi-metal phenomena, such as type II WSMs, nodal line semi-metals, nodal loop semi-metals, and more.

4.A Holographic Renormalisation

On-shell Action

For the purposes of holographic renormalization, it will be convenient to replace r and R with new coordinates $u = L^2/\sqrt{r^2+R^2}$ and $\theta = \arctan(R/r)$. The inverse transformation is $r = L^2 u^{-1}\cos\theta$, $R = L^2 u^{-1}\sin\theta$. It will also be convenient to use units in which the AdS radius is $L \equiv 1$, restoring factors of L by dimensional analysis at the end. In these coordinates, the asymptotically $AdS_5 \times S^5$ black brane background in eq. (4.11) becomes

$$\begin{aligned} ds^2 &= \frac{1}{u^2}\left[-\frac{g^2(u)}{h(u)}dt^2 + h(u)d\vec{x}^2 + du^2\right] + d\theta^2 + \sin^2\theta\, d\phi^2 + \cos^2\theta\, ds^2_{S^3} \\ C_4 &= \frac{1}{u^4}h^2(u)dt\wedge dx\wedge dy\wedge dz - \cos^4\theta\, d\phi\wedge ds_{S^3}, \end{aligned} \tag{4.67}$$

where in a slight abuse of notation we have defined $g(u) \equiv 1-\rho_0^4 u^4$ and $h(u) \equiv 1+\rho_0^4 u^4$. The boundary is at $u=0$, while the horizon of the black brane is at $u = 1/\rho_0$.

In this coordinate system, our ansatz for the D7-brane embedding becomes

$$\theta = \theta(u), \quad \phi = bz + \Phi(u). \tag{4.68}$$

From the near-boundary expansion of $R(r)$ in eq. (4.17) we can find the near-boundary expansion of $\theta(u)$,

$$\theta(u) = M\left(u + \frac{b^2}{2}u^3\log u\right) + \left(C + \frac{M^3}{6}\right)u^3 + \dots\,. \tag{4.69}$$

Solving eq. (4.14) for ϕ' in terms of $p_\phi = P_\phi/\mathcal{N}$ and R, replacing (r,R) with (u,θ), and using $\theta(u)$'s near-boundary expansion in eq. (4.69), we also find ϕ's near-boundary expansion,

$$\phi = bz - \frac{p_\phi}{2}u^2 + \dots\,. \tag{4.70}$$

The D7-brane action evaluated on the ansatz in eq. (4.68) is

$$S_{\rm D7} = -\mathcal{N}\int du \frac{\cos^3\theta}{u^5}g(u)h(u)\sqrt{\left(1+\frac{b^2u^2\sin^2\theta}{h(u)}\right)(1+u^2\theta'^2) + u^2\sin^2\theta\,\phi'^2}. \tag{4.71}$$

If we plug in the near-boundary expansions in eqs. (4.69) and (4.70), then we find that the integrand diverges near $u=0$. We regularize this divergence by introducing a small-u cutoff at $u=\epsilon$. We then find that the on-shell action is

$$S^\star_{\rm D7} = \mathcal{N}\left[-\frac{1}{4\epsilon^4} + \frac{M^2}{2\epsilon^2} + b^2M^2\log\epsilon + \mathcal{O}(\epsilon^0)\right], \tag{4.72}$$

where the $\mathcal{O}(\epsilon^0)$ term cannot be determined from the near-boundary analysis.

To have a well-defined variational principle we need to remove the small-ϵ divergences in eq. (4.72) by the addition of counterterms to the action. The full D7-brane action is then $S = S_{\rm D7} + S_{\rm ct}$ where the counterterms are given by $S_{\rm ct} = \sum_i S_{{\rm ct},i}$ with [147, 148, 122, 149]

$$S_{\rm ct,1} = \mathcal{N}\frac{1}{4}\sqrt{-\gamma}, \qquad S_{\rm ct,2} = -\mathcal{N}\frac{1}{2}\sqrt{-\gamma}|\Theta|^2, \qquad S_{\rm ct,3} = \mathcal{N}\frac{5}{12}\sqrt{-\gamma}|\Theta|^4,$$
$$S_{\rm ct,4} = \mathcal{N}\frac{1}{2}\sqrt{-\gamma}\Theta^*\Box_\gamma\Theta\log|\Theta|, \qquad S_{\rm ct,5} = \mathcal{N}\frac{1}{4}\sqrt{-\gamma}\Theta^*\Box_\gamma\Theta. \tag{4.73}$$

where $\Theta \equiv \theta e^{i\phi}$, $\gamma_{\mu\nu} = \epsilon^{-2}\eta_{\mu\nu}$ is the induced metric on the intersection of the brane with the cutoff surface at $u = \epsilon$, and $\Box_\gamma\Theta = \frac{1}{\sqrt{-\gamma}}\partial_\mu\left(\sqrt{-\gamma}\,\gamma^{\mu\nu}\partial_\nu\Theta\right)$. Evaluating these counterterms using the small-u expansions in eqs. (4.69) and (4.70), we find

$$S_{\rm ct} = \mathcal{N}\left[\frac{1}{4\epsilon^4} - \frac{M^2}{2\epsilon^2} - b^2M^2\log\epsilon - MC + \frac{M^2}{4}\left(M^2 - b^2\right) - \frac{1}{2}b^2M^2\log M\right], \tag{4.74}$$

where we have suppressed terms that vanish when $\epsilon \to 0$. The counterterms cancel the divergences in the bulk action eq. (4.72), as expected, and also provide a finite contribution to the action.

The contribution of the D7-branes to free energy density in the dual field theory is given by its on-shell action density in Euclidean signature. Since our solutions are time-independent, this is just minus the on-shell action density in Lorentzian signature, $f = -S^\star = -(S^\star_{\rm D7} + S^\star_{\rm ct})$. The bulk D7-brane action's contribution may be found from eq. (4.13a), by substituting our numerical solution for $R(r)$ up to some large-r cutoff r_c,[7]

$$S^\star_{\rm D7} = -\mathcal{N}\int_{r_0}^{r_c} dr\, r^3 g(\rho)h(\rho)\sqrt{1 + \frac{b^2R^2}{\rho^4 h(\rho)}}\sqrt{1 + R'^2}, \tag{4.75}$$

where the lower limit of integration is $r = 0$ for Minkowski embeddings, and is $r = r_H$ for black hole embeddings.

The contribution from the counterterms may be obtained by exchanging the small-u cutoff ϵ in eq. (4.74) for the large-r cutoff r_c. To do so, we expand the relation $\epsilon = 1/\sqrt{r_c^2 + R(r_c)^2}$ for r_c, making use of R's near boundary expansion in eq. (4.17) to find

$$\frac{1}{\epsilon} = r_c + \frac{M^2}{2r_c} - \frac{b^2M^2}{2r_c^3}\log r_c + \frac{M}{r_c^3}\left(C - \frac{M^3}{8}\right) + \dots\,. \tag{4.76}$$

Substituting this into eq. (4.74) we find that the counterterm contribution is

$$S^\star_{\rm ct} = \mathcal{N}\left[\frac{r_c^4}{4} + \frac{b^2M^2}{2}\log r_c - \frac{b^2M^2}{4}\left(1 + 2\log M\right)\right]. \tag{4.77}$$

[7] Since all of our solutions have $p_\phi = 0$, they also have $\phi' = 0$ by eq. (4.14).

Combining this with eq. (4.75) we find an expression for the free energy density

$$f = \mathcal{N}\Big[\int^{r_c} dr\, r^3 g(\rho)h(\rho)\sqrt{1+\frac{b^2R^2}{\rho^4 h(\rho)}}\sqrt{1+R'^2} - \frac{r_c^4}{4} - \frac{b^2M^2}{2}\log r_c + \frac{b^2M^2}{4}(1+2\log M)\Big]. \tag{4.78}$$

Using dimensional analysis to restore factors of L and taking $\mathcal{N} = \lambda N_c N_f/(16\pi^4 L^8)$ from eq. (4.13b) then yields eq. (4.22).

Scalar One-point Functions

The one-point functions of the operators $\mathcal{O}_m$ and $\mathcal{O}_\phi$ defined in eq. (4.10) are proportional to the functional derivatives of the on-shell action with respect to the boundary values of θ and ϕ,

$$\langle\mathcal{O}_m\rangle = -2\pi\alpha' \lim_{\epsilon\to 0}\epsilon\frac{\delta S}{\delta\theta(\epsilon)}, \quad \langle\mathcal{O}_\phi\rangle = -\lim_{\epsilon\to 0}\frac{\delta S}{\delta\phi(\epsilon)}. \tag{4.79}$$

In order to compute $\langle\mathcal{O}_m\rangle$, let us consider a small variation $\theta(u)\to\theta(u)+\delta\theta(u)$. Writing $S_{\rm D7} = \int du\,\mathcal{L}$, the resulting variation in the action is

$$\delta S_{\rm D7} = \int_\epsilon du\left[\frac{\partial\mathcal{L}}{\partial\theta'(u)}\delta\theta'(u) - \frac{\partial\mathcal{L}}{\partial\theta(u)}\delta\theta(u)\right] = -\left.\frac{\partial\mathcal{L}}{\partial\theta'(u)}\delta\theta(u)\right|_{u=\epsilon}. \tag{4.80}$$

The second equality is obtained using integration by parts and the Euler-Lagrange equation for θ. The derivative $\partial\mathcal{L}/\partial\theta'(u)$ may be computed from the action in eq. (4.71). Inserting the near-boundary expansions in eqs. (4.69) and (4.70) gives a result that diverges as ϵ^{-3}. The ϵ^{-3} and an $\epsilon^{-1}\log\epsilon$ divergence are cancelled by the variation of the counterterms in eq. (4.73), so we obtain a finite result from eq. (4.79),

$$\langle\mathcal{O}_m\rangle = 2\pi\alpha'\mathcal{N}L^6\left[-2C + \frac{b^2M}{2} + b^2M\log(ML)\right], \tag{4.81}$$

where we used dimensional analysis to restore factors of L on the right-hand side. Using $\mathcal{N} = \lambda N_c N_f/(16\pi^4 L^8)$ from eq. (4.13b) and $L^4 = \alpha'^2\lambda$ then yields eq. (4.18).

Similarly under a small variation $\phi\to\phi+\delta\phi$ we find

$$\delta S_{\rm D7} = -\left.\frac{\partial\mathcal{L}}{\partial\phi'}\delta\phi\right|_{u=\epsilon} = -\mathcal{N}p_\phi\,\delta\phi(\epsilon), \tag{4.82}$$

where we have used $\partial\mathcal{L}/\partial\phi' \equiv P_\phi = \mathcal{N}p_\phi$. In this case the counterterms do not contribute to the one-point function, and we can read off $\langle\mathcal{O}_\phi\rangle$ from eq. (4.82) using eq. (4.79),

$$\langle\mathcal{O}_\phi\rangle = \mathcal{N}p_\phi. \tag{4.83}$$

Since $p_\phi = 0$ in all the embeddings we consider, all phases of our model have $\langle \mathcal{O}_\phi \rangle = 0$.

Current One-point Functions

In order to compute the one-point functions of the current, we need to allow for non-zero A_x and A_y,

$$\theta = \theta(u), \quad \phi = bz + \Phi(u), \quad A_x = Et + a(u), \quad A_y = A_y(u). \tag{4.84}$$

Non-zero A changes the coefficient of the $\log \epsilon$ divergence of the D7-brane action. This change is cancelled by an additional counterterm [147, 148, 122, 149],

$$S_{\text{ct},6} = -\mathcal{N}\frac{1}{4}\sqrt{-\gamma}F^{\mu\nu}F_{\mu\nu}\log\epsilon. \tag{4.85}$$

The one-point functions of the currents are given by

$$\langle J^\mu \rangle = 2\pi\alpha' \lim_{\epsilon\to 0}\frac{\delta S^\star}{\delta A_\mu(\epsilon)}. \tag{4.86}$$

The calculation proceeds similarly to that of $\langle \mathcal{O}_\phi \rangle$. We find that the the small variation in the bulk D7-brane action resulting from $A_\mu \to A_\mu + \delta A_\mu$ is

$$\delta S_{\text{D7}} = -\left.\frac{\partial \mathcal{L}}{\partial A'_\mu(u)}\right|_{u=\epsilon} \delta A_\mu(\epsilon). \tag{4.87}$$

The variation of the counterterms vanishes at leading order in δA_μ, so eq. (4.87) is the only contribution to the one-point function. Using $\partial\mathcal{L}/\partial A'_\mu = \mathcal{N} j_\mu$, we then find

$$\langle J_x \rangle = -2\pi\alpha'\mathcal{N} j_x, \quad \langle J_y \rangle = -2\pi\alpha'\mathcal{N} j_y. \tag{4.88}$$

Chapter 5

Translational Symmetry Breaking of Holographic Zero Sound

We study the sound modes of a probe brane holographic model in 2+1 field theory dimensions with translational symmetry breaking (TSB). The TSB is introduced in the simplest possible case, where the metric itself remains translationally invariant while other fields break translational symmetry, parameterised by the dimensionfull quantities α_1 and α_2 with mass dimension [1] and [2] respectively. This system contains two sound modes at non-zero temperature T and chemical potential μ, holographic zero sound (HZS, that persists to zero temperature) and the hydrodynamic diffusive mode. Our goal here is to study the effect that the TSB parameters α_1 and α_2 have on these sound modes. We find that the dispersion relation for HZS takes the form of a damped harmonic oscillator with k-gap given by $k_g = 1/2v\tau$. We also find the analytic form of the relaxation timescale τ by comparing expressions derived from a gradient expansion electric field, $\mathcal{E}$ with a linearised fluctuation electric field E. We find the expected response of the sound modes, namely that with increasing symmetry breaking the propagating holographic zero sound mode transitions to the diffusive mode. Moreover, we study the effect the TSB has on the k-gap as well as the AC and DC conductivities, where in general we find that with increasing TSB the conductivities decrease until they saturate a lower bound.

5.1 Strongly Coupled: (non)-Hydrodynamic Fluctuations

We have already seen some aspects of hydrodynamics in preceding sections in the form of the conductivity transport coefficient. Here, instead, we take a closer look at the kinds of *modes* that can be found in a strongly coupled system. The reason for doing so, and the reason for turning to the duality, follows the same argument as in chapter 4: weakly coupled systems described by quasiparticle interactions display collective excitations (we shall see one such example in section 5.2 in the form of Landua zero sound, when we briefly outline Fermi liquid theory) and since we expect

the quasiparticle picture to break down at strong coupling we are then left without theory in a bid to describe the possibilities of strongly coupled propagating modes. Instead, a good place to start, is by revisiting an old theory - hydrodynamics.

Hydrodynamics [48, 17, 150] is an effective description of a system near thermal equilibrium at long time times and large distances. In other words, hydrodynamics is valid when the characteristic energy, ω and momentum, k is small compared to some scale set by the microscopic theory. Since hydrodynamics is at long times, the system will be dominated by dynamics that 'survive' the longest: the conserved quantities of the system. For a system respecting Poincaré symmetry and a global $U(1)$ we have the conservation of the energy-momentum tensor and a $U(1)$ current respectively,

$$\partial_\mu T^{\mu\nu} = 0 \qquad \partial_\mu J^\mu = 0 \tag{5.1.1}$$

Crucially, in hydrodynamics $T^{\mu\nu}$ and J^μ can be written in terms of a few slowly varying parameters: a local temperature $T(x)$, a local fluid velocity $v(x)$ and a local chemical potential, $\mu(x)$, also known as the hydrodynamic variables [17]. Without this simplification the hydrodynamic equations would not be solvable. We then perform a gradient expansion in these hydrodynamic variables. The reason being that including gradients will induce dissipation in the system, and since we are at long wavelengths the gradients will in general be small, allowing for an expansion. The hydrodynamic expansion of the conserved currents will then order itself into zeroth order $\mathcal{O}(T, v, \mu)$, first order $\mathcal{O}(\partial(T, v, \mu))$, second order $\mathcal{O}(\partial^2(T, v, \mu))$ and so on. An immediate question is the regime of validity of such an expansion, or more precisely, what is its radius of convergence? Recently this was answered holographically by studying the collision of the hydrodynamic and non-hydrodynamic quasi-normal modes [151, 152].

Each term in the expansion will come with some coefficient, called transport coefficients, that can only be found analytically by studying the microscopic theory, namely by calculating the two point functions of the conserved currents. Furthermore, as mentioned in section 2.3.3, the poles of the two point functions give the dispersion relation related to the long-wavelength fluctuations associated with each conserved current. For example from the conservation of the longitudinal stress energy components (T^{00}, T^{03} and T^{33}) we get sound waves with dispersion relation,

$$\omega = \pm v_s k - i\Gamma_s k^2 + \mathcal{O}(k^3/T^3) \tag{5.1.2}$$

with speed v_s and attenuation Γ_s given by,

$$v_s^2 = \frac{\partial p}{\partial \epsilon} \qquad \Gamma_s = \frac{2(d-2)\eta + (d-1)\zeta}{2(d-1)(\epsilon + p)} \tag{5.1.3}$$

where ϵ is the equilibrium energy density, p the equilibrium pressure, η is the shear viscosity and ζ the bulk viscosity.

The shear modes correspond to fluctuations of the T^{0i} and T^{3i} currents. They are diffusive modes (rather than propagating as in the sound modes) and are given by,

$$\omega = -i\Gamma_p k^2 + \mathcal{O}(k^3/T^3) \tag{5.1.4}$$

with attenuation,

$$\Gamma_p = \frac{\eta}{\epsilon + p} \tag{5.1.5}$$

From the conserved $U(1)$ current we instead get a longitudinal diffusive mode associated with the conserved charge,

$$\omega = -iDk^2 + \mathcal{O}(k^3/T^3) \tag{5.1.6}$$

with diffusion constant D. There is also the scalar channel of the stress energy tensor and the transverse channel of the conserved current.

All of the modes above are in the hydrodynamic limit, $\omega\tau \ll 1$, where τ, the relaxation timescale, is small. What about in the opposite limit, when $\omega\tau \gg 1$? We discuss such a limit in the next section where we introduce Fermi-liquid theory and a collective quasiparticle excitation called Landau zero sound.

5.2 Fermi-Liquid Theory and Landau Zero Sound

To formulate a theory of interacting fermions in a metal is exceedingly difficult - ultimately this is a many-body quantum problem. However, in 1956 Lev Landau made use of the non-interacting (ideal) Fermi gas and the Pauli exclusion principle (PEP) to develop Fermi-liquid theory (LFL) [17, 18].

The ground state of a Fermi gas at zero temperature organises itself according to the PEP; states fill up all energy levels below the Fermi energy (which at zero temperature is just the chemical potential) such that in momentum space we have the notion of a Fermi surface – a surface that separates occupied and unoccupied states. The Fermi-Dirac distribution function is therefore either 1 inside the surface, or 0 outside. At non-zero temperature a state can then be excited above the Fermi surface leaving behind a *hole* in its absence.

We then slowly (adiabatically) turn on interactions such that we get a one-to-one correspondence between the non-interacting and interacting system, and further assume that the ground states are also one-to-one. Now, imagine an excitation in the non-interacting case and slowly turn on the interactions. The *bare* fermion will start to interact with its surroundings. Instead of trying to work out the precise details of how the fermion is interacting, we can instead dress the bare fermion with a renormalised mass and charge. The fermion is now a *quasiparticle*. Alternatively we could have created a hole, in which case we would get a *quasihole*. To make sure the system has time to turn interactions on adiabatically the quasiparticles have to be long-lived $\tau \gg 1$, which in turn means that quasiparticles are excited only near the Fermi

surface. We can then imagine the quasiparticle as a deviation from the thermal equilibrium ground state distribution [18],

$$n_p = n_p^0 + \delta n_p \tag{5.2.7}$$

where $n_p(t, x)$ is the distribution function specifying the number of quasiparticles per unit momentum and obeying the Boltzmann equation.

We can then ask, is it possible for a bunch of the quasiparticles to form collective excitations? - the answer is yes. There are two cases to consider; hydrodynamic first sound and Landau zero sound.

First Sound - This mode dominates when there are lots of collisions between the quasiparticles, that is in the limit $\omega \ll v$, where v is the frequency of the collisions. It is a longitudinal wave where an element of the collective excitation has an increase in density that pushes neighboring particles through collisions. This is essentially when δn_p is small as the quasiparticles are constantly being returned to the equilibrium state.

Zero Sound - In the collisionless regime, $\omega \gg v$, neighboring quasiparticles are instead driven by an effective force between the quasiparticles. The effective force is proportional to δn_p and arises because the departure from the Fermi surface can be equated to a change in the free energy, where the quasiparticles are moving from one region to another. In other words, zero sound arises due to the fluctuation of the Fermi surface. The dispersion relation for zero sound is given by,

$$\omega = \pm vk - i\Gamma k^2 + \mathcal{O}(k^3/\epsilon_F^3) \tag{5.2.8}$$

where ϵ_F is the Fermi energy. We see that it takes the form of a damped propagating mode.

Since zero sound is in the collisionless regime, we should expect to see it dominate at low temperatures, whereas as temperature is increased the mode should transition to first sound. Note, however, that even at zero temperature the zero sound attenuation is not zero but instead takes on a constant value. This is because of multipair decay between quasiparticle and quasihole pairs. At low temperatures collisions from thermally excited quasiparticles are fairly infrequent, this results in the dominating part of the zero sound attenuation still being from multi-pair decay. This is the 'quantum collisionless' regime, $0 \leq \pi T/\mu < \omega/\mu$, with attenuation $\Gamma \propto \omega^2/\mu$.

As temperature is increased the collisions start to dominate, $\omega/\mu < \pi T/\mu < \sqrt{\omega/\mu}$, with the attenuation proportional to the collision rate $\Gamma \propto (\pi T)^2/\mu$. This is called the thermal collisionless regime. Finally, at high enough temperatures, the dominante mode switches from zero sound to first sound that has an attenuation proportional to $\Gamma \propto \mu\omega^2/T^2$. Therefore a peak should develop in the attenuation of a Fermi liquid as a function of temperature. Indeed, zero sound was

experimentally found in helium-3 at a temperature of 4k (below this helium-3 becomes a superfluid) and the resulting attenuation showed a peak at the crossover between the two competing modes [153].

5.3 Holographic Zero Sound

LFLs are examples of compressible matter, meaning the density is a non-zero, smooth function of the chemical potential μ, with non-zero first derivative. Holography has also revealed suggestive patterns in strongly-coupled compressible quantum matter. In such holographic systems sound modes are common, if not universall [16, 154, 155, 156, 157, 158, 159, 160, 161, 162, 163, 164, 165, 166, 167, 168, 169, 170, 171, 172, 173, 174, 175, 176, 177, 178, 179, 180, 181, 182].

To be specific, sound modes appear in two classes of holographic compressible quantum matter. The first class is described by charged black holes in Einstein-Hilbert gravity coupled to a $U(1)$ gauge field, and possibly scalar fields. The central example is the AdS-Reissner-Nordström solution.

The second class comes from probe branes in holographic spacetimes, such as the systems we have encountered in previous chapters. In the $T = 0$, $\langle J_t \rangle \neq 0$ scenario sound modes appear as poles in J^μ's retarded two-point function.

In both classes of holographic compressible quantum matter the sound modes appear in states with no broken symmetries, and in particular with neither Translational Symmetry Breaking (TSB) nor spontaneous breaking of the $U(1)$, i.e. no superfluidity. As a result, compared to textbook examples of compressible quantum matter, the microscopic origin of these holographic sound modes is mysterious: they cannot be phonons, as occur in solids, nor can they be superfluid phonons, as occur in Bose-Einstein-condensates. Perhaps, then, it is possible that the sound mode is related to the zero sound found in LFL. However, the holographic sound modes cannot be LFL zero sound either. Charged black holes can support Fermi surfaces, but with volume smaller than $\langle J^t \rangle$ by powers of N, thus violating Luttinger's theorem. Many probe brane models show no signs of a Fermi surface at all. As a result, the holographic sound modes are called "holographic zero sound" (HZS) to emphasise their similarity to, but difference from, LFL zero sound.

The differences with LFL zero sound are even more pronounced when $T > 0$. As we saw in the introduction there were three regimes of interest in a LFL characterised by the attenuations dependence on temperature; quantum collisionless ($\Gamma \propto \omega^2/\mu$), thermal collisionless ($\Gamma \propto (\pi T)^2/\mu$) and hydrodynamic ($\Gamma \propto \mu\omega^2/T^2$). AdS-Reissner-Nordström at low T/μ has a near-horizon AdS_2, indicating that the holographic dual's effective description is a $d = 1$ CFT. Correspondingly the sound mode crossover differs significantly from a LFL. At low T/μ the sound mode has $\Gamma \propto T^0$, similar to the LFL quantum collisionless regime. However, as T/μ increases Γ scales as a power of T less than the T^2 of the LFL thermal collisionless regime, and in

the high-T/μ hydrodynamic regime $\Gamma \propto T^{-1}$, unlike the T^{-2} of the LFL hydrodynamic regime [165].

In probe brane models, although the sound mode behaves identically to LFL zero sound in the quantum and thermal collisionless regimes [164, 181], the hydrodynamic regime is strikingly different. In particular, in the probe limit the sound mode appears as a pole in correlators of J^μ, and not in those of the stress-energy tensor. As a result, in probe brane systems at high T/μ the crossover is not to the hydrodynamic sound mode, but to the charge diffusion mode, in stark contrast to a LFL.

To be explicit, the low-T effective theory of the holographic systems is different from those of solids, BECs, or LFLs. For probe branes in translationally- and rotationally-invariant backgrounds with Lifshitz dynamical exponent < 2, the low-T effective theory that describes correlators of J^μ is

$$\partial_t d + \partial_i J^i = 0, \tag{5.3.9a}$$

$$\partial_t J^i + v^2 \partial_i d = -\frac{J^i}{\tau}, \tag{5.3.9b}$$

where J^i is the charge current, $J^t = d$ is the charge density, v is the HZS speed and τ is a coefficient that represents damping due to loss of energy and momentum from the probe sector into the background. Eq. (5.3.9) describes a current that is "quasi-conserved" rather than conserved, due to this damping. If we Fourier transform eq. (5.3.9), using the same symbols for J^t and J^i and their Fourier transforms, and then solve eq. (5.3.9a) for J^i, plug the result into eq. (5.3.9b), and demand a solution with $J^t \neq 0$, then we find

$$\omega^2 + \frac{i}{\tau}\omega - v^2 k^2 = 0. \tag{5.3.10}$$

Eq. (5.3.10) determines the dispersion relation of the longest-lived modes, and in fact appears in a wide variety of systems, such as damped harmonic oscillators, the electromagnetic skin effect, the Sine-Gordon model, and more [183]. The key feature of the dispersion relation that arises from eq. (5.3.10) is a "momentum gap" or "k-gap": solving eq. (5.3.10) for ω gives

$$\omega = -\frac{i}{2\tau} \pm v\sqrt{k^2 - k_g^2}, \tag{5.3.11}$$

where the k-gap, k_g, is

$$k_g \equiv \frac{1}{2v\tau}. \tag{5.3.12}$$

In the thermal collisionless regime, where $k > k_g$, eq. (5.3.11) describes sound modes: if we Taylor expand eq. (5.3.11) in $k/k_g \gg 1$ then we find

$$\omega = \pm v\,k - \frac{i}{2\tau} + \mathcal{O}\left(\frac{v\,k_g^2}{k}\right). \tag{5.3.13}$$

As k decreases, the crossover from the thermal collisionless to the hydrodynamic regime occurs when $k = k_g$. In more detail, as $k \to k_g$, the two sound modes approach the $\mathrm{Im}(\omega)$ axis, and collide there when $k = k_g$. When $k < k_g$ this double pole splits into two purely imaginary modes, one of which moves up the $\mathrm{Im}(\omega)$ axis while the other remains in place as k continues to decrease. The pole moving up the $\mathrm{Im}(\omega)$ axis is the hydrodynamic charge diffusion mode. To be explicit, if we Taylor expand eq. (5.3.11) in $k/k_g \ll 1$ then we find

$$\omega = \begin{cases} -\frac{i}{\tau} + \mathcal{O}\left(\frac{k^2}{k_g^2}\right), \\ -iD\,k^2 + \mathcal{O}\left(\frac{k^4}{k_g^4}\right), \end{cases} \tag{5.3.14}$$

where the latter mode is the hydrodynamic charge diffusion mode, with diffusion constant

$$D \equiv v^2\tau. \tag{5.3.15}$$

In short, eq. (5.3.10) describes the crossover from the high-momentum thermal collisionless regime, which supports sound modes, to the low-momentum hydrodynamic regime, which supports a charge diffusion mode and a second, k-independent, purely imaginary mode. The name "k-gap" describes how propagating modes appear only for sufficiently large k, while at small k both modes are completely damped.

To summarise, holography provides solvable models of strongly-interacting quantum compressible matter that can reveal general principles applicable to real systems. For example, sound modes are common, if not ubiquitous, in holographic quantum compressible matter, and have microscopic origins and effective descriptions different from those in solids, BECs, and LFLs. How common are sound modes in real strongly-interacting quantum compressible matter? What microscopic mechanisms could produce them? What kinds of effective theories give rise to such sound modes? To take a small step in understanding the microscopic origins we construct an analysis on the effect of translational symmetry breaking on holograhpic zero sound.

5.4 Translational Symmetry Breaking

An important element that is missing from the preious analysis is translational symmetry breaking (TSB). TSB is important in many physical systems to model the damping that would occur due to the crystaline structure of metals or from doping. As noted, there is already an attenuation factor in the dispersion relation of HZS above, however this is from the lack of back-reaction and does not come from any broken symmetries. In this section we instead wish to study how explicit TSB, affects HZS in probe brane models. To do so, we will use the simplest models of TSB in holography, in which the metric itself remains translationally invariant while other fields break translational symmetry. We restrict to $d = 3$ although qualitatively we

expect our results to generalise to any d. Examples include exactly massless scalar fields linear in a CFT spatial coordinate [21], massless two-form fields linear in a CFT spatial coordinate [22], or giving the graviton a mass term that breaks the bulk diffeomorphisms holographically dual to translations [20], some details of these models are given in appendix 5.A. In all of these cases the metric $g_{\mu\nu}$ with $\mu, \nu = 0, \ldots, 3$ of the bulk asymptotically AdS_{d+1} black brane spacetime takes the form

$$ds^2 = g_{\mu\nu}dx^\mu dx^\nu = \frac{L^2}{z^2}\left(\frac{dz^2}{f(z)} - f(z)dt^2 + d\vec{x}^2\right) \tag{5.4.16a}$$

$$f(z) = 1 + \alpha_1 z + \alpha_2 z^2 - mz^3, \tag{5.4.16b}$$

with coordinates x^μ, including time t, CFT spatial coordinates $\vec{x}$, and the holographic coordinate z. These metrics describe black brane spacetimes with a planar horizon at $z = z_H$, given by the smallest zero of the equation $f(z_H) = 0$, and an asymptotic AdS_{d+1} region with radius L at $z \to 0$. Note that compared to previous sections we have made the transformation $r \to L^2/z$ with the boundary now located at $z \to 0$. In the blackening factor $f(z)$ in eq. (5.4.16), m determines the black brane mass density while α_1 and α_2 arise from the TSB. For example, Vegh's model had $\alpha_1 \neq 0$ and $\alpha_2 \neq 0$ [19, 20] while both the Andrade-Withers [21] and Poovuttikul-Grozdanov [22] models had $\alpha_1 = 0$ and $\alpha_2 \neq 0$. We will treat α_1 and α_2 as free parameters, to encompass all of the models above. However, we will restrict to $d = 3$, although qualitatively we expect our results to generalise to any d.

Our model will be the DBI action that we have seen in previous chapters,

$$S = -\mathcal{N}\int d^{d+1}\xi\sqrt{-\det(g^*_{ab} + F_{ab})} \tag{5.4.17}$$

This is, in fact, not the most general choice. For example, in the Andrade-Withers model, general covariance and $U(1)$ gauge invariance would allow arbitrary functions of the massless scalars to appear in eq. (5.4.17) multiplying F_{ab} and multiplying the square root. We restrict to the action in eq. (5.4.17) as a simple starting point.

In our model the probe brane will only "know" about TSB through the metric's dependence on α_1 and α_2. As a result, we are guaranteed to obtain the same effective theory as eq. (5.3.9), but now with values of v and τ that depend on α_1 and α_2. (Crucially, τ is non-zero even when $\alpha_1 = 0$ and $\alpha_2 = 0$, that is, in our model damping occurs even without TSB, because of the probe limit.) Indeed, our main objective will be to determine how v and τ depend on α_1 and α_2.

Intuitively, we can think of α_1 and α_2 as measures of the strength of TSB. For example, we can think of $\alpha_1 \neq 0$ and/or $\alpha_2 \neq 0$ as arising from a concentration of impurities smeared to produce a continuum. We thus expect non-zero values of α_1 and α_2 to dampen the HZS. Broadly speaking, we find that this intuition is correct.

The rest of this section is organised as follows. In 5.4.1 we outline the thermodynamics of the system, finding that the α's are constrained by temperature

and null-energy bounds. In 5.4.2 we set out the DBI action and conserved currents, as well as discuss the holographic renormalisation in appendix B that leads to the Gibbs free energy. In section 5.4.3 we derive the constituent equations and analytic dispersion relation that is then compared to the numeric solutions. Finally, in secion 5.4.4 we calculate the effect the α's have on the AC and DC conductivities.

5.4.1 Thermodynamics

The black brane with metric in eq. (5.4.16) has the Hawking temperature

$$T = \frac{|f'(z_H)|}{4\pi} = \frac{1}{4\pi z_H}\left[3 + 2\alpha_1 z_H + \alpha_2 z_H^2\right]. \tag{5.4.18}$$

The black brane also has a Bekenstein-Hawking entropy, proportional to the horizon area, and a free energy, given by minus the on-shell Euclidean action. Via holography we identify the black brane's T, Bekenstein-Hawking entropy, and free energy as the temperature, entropy, and free energy of the dual field theory. For what follows, we will not need explicit expressions of the black brane entropy or free energy.

Eq. (5.4.18) is a quadratic equation for z_H, with solutions (when $\alpha_2 \neq 0$)

$$z_H^{\pm} = \frac{2\pi T - \alpha_1}{\alpha_2} \pm \frac{1}{\alpha_2}\sqrt{(2\pi T - \alpha_1)^2 - 3\alpha_2} \tag{5.4.19a}$$

$$= \frac{1 - \frac{\alpha_1}{2\pi T}}{\frac{\alpha_2}{2\pi T}} \pm \frac{1}{\frac{\alpha_2}{2\pi T}}\sqrt{\left(1 - \frac{\alpha_1}{2\pi T}\right)^2 - \frac{3\,\alpha_2}{(2\pi T)^2}}. \tag{5.4.19b}$$

Clearly in eqs. (5.4.18) and (5.4.19) some values of α_1 and α_2 produce $T < 0$ and/or $z_H < 0$, which is obviously unphysical. To avoid these and various other pathologies, we will impose two constraints on α_1 and α_2, following refs. [20, 19]. First, we will demand that $(2\pi T)z_H^{\pm} \geq 0$. The resulting allowed values of α_1 and α_2 appear in fig. 5.1. In particular, fig. 5.1 (a) shows that $(2\pi T)z_H^{+} \geq 0$ only when $\alpha_2 \geq 0$. In that regime, $z_H^{-} < z_H+$, that is, z_H^{-} is the smaller root of $f(z_H) = 0$ and is thus the horizon, so we can already discard z_H^{+}.

Our second constraint will provide an additional reason to discard z_H^{+}, and will further constrain z_H^{-}: we impose the null energy condition on the Ricci tensor computed from the metric in eq. (5.4.16), which gives

$$\alpha_2 + \frac{\alpha_1}{z} \leq 0. \tag{5.4.20}$$

We will impose eq. (5.4.20) for all $z \in [0, z_H]$, where the endpoints $z = 0$ and $z = z_H$ produce the most stringent constraints. Eq. (5.4.20) with $z = z_H$ is the stability condition of refs. [20, 19]. Violating this condition causes various pathologies, including a negative graviton mass squared [20, 19]. The values of α_1 and α_2 obeying this stability condition for each of $z_H^{\pm}$ appear in fig. 5.2. Figs. 5.1 and 5.2 show that no values of α_1 and $\alpha_2 \neq 0$ can simultaneously satisfy both $(2\pi T)z_H^{+} \geq 0$ and the stability

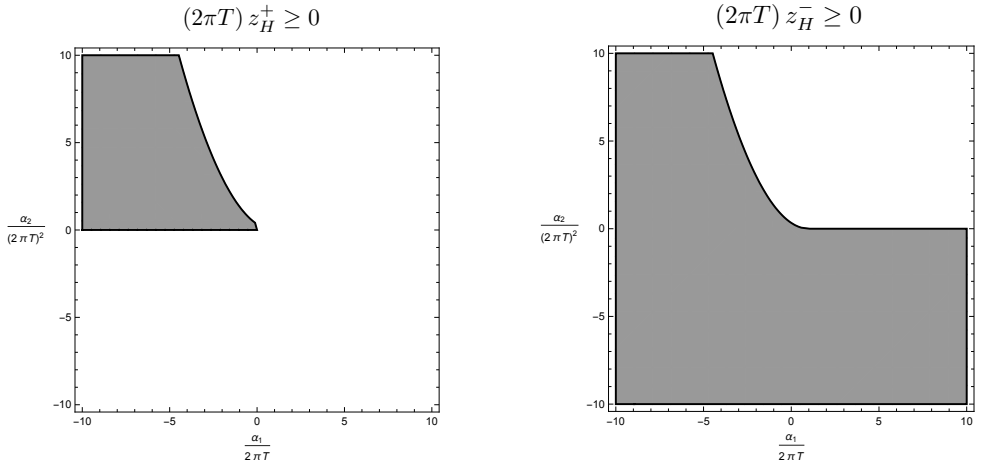

(A) (B)

FIGURE 5.1: The regions in the $\left(\frac{\alpha_1}{2\pi T}, \frac{\alpha_2}{(2\pi T)^2}\right)$-plane where $(2\pi T)\, z_H^{\pm} \geq 0$, for the two branches of solutions in eq. (5.4.19), (a) z_H^+, and (b) z_H^-.

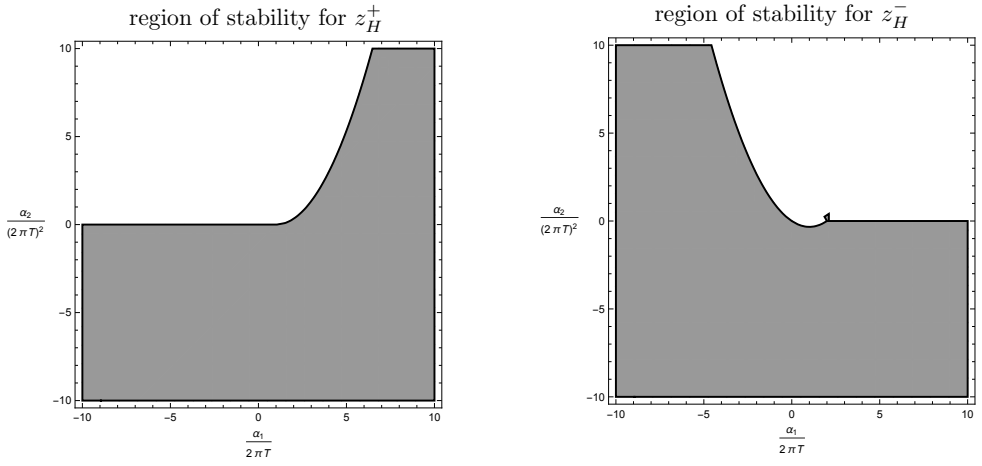

(A) (B)

FIGURE 5.2: The regions in the $\left(\frac{\alpha_1}{2\pi T}, \frac{\alpha_2}{(2\pi T)^2}\right)$-plane obeying the stability condition given by eq. (5.4.20) with $z = z_H$, for the two branches of solutions in eq. (5.4.19), (a) z_H^+, and (b) z_H^-.

condition of eq. (5.4.20) with $z = z_H^+$, so as mentioned above our second constraint provides another reason to discard z_H^+. We thus restrict to z_H^-, and from now on, z_H will refer only to z_H^-. Finally, eq. (5.4.20) with $z = 0$ gives $\alpha_1 \leq 0$, which we will impose from now on.

Fig. 5.3 summarises our constraints by combining fig. 5.1 (b), fig. 5.2 (b), and $\frac{\alpha_1}{2\pi T} \leq 0$. In what follows, we will restrict to values of α_1 and $\alpha_2 \neq 0$ in the region shown in fig. 5.3.

In fact, for simplicity, in all of our numerics we will set one of α_1 or α_2 to zero,

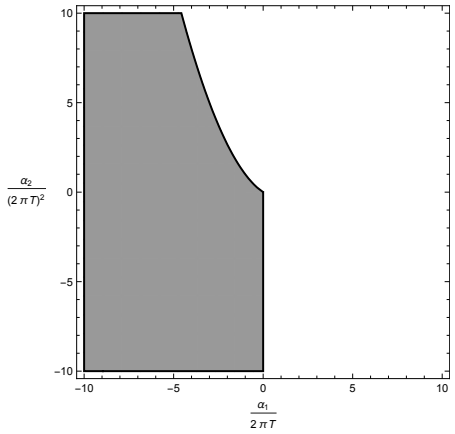

FIGURE 5.3: The region in the $\left(\frac{\alpha_1}{2\pi T}, \frac{\alpha_2}{(2\pi T)^2}\right)$-plane where three conditions are simultaneously satisfied: $(2\pi T)\, z_H^- \geq 0$, the stability condition given by eq. (5.4.20) with $z = z_H^-$, and $\frac{\alpha_1}{(2\pi T)} \leq 0$. This region is the overlap of the region in fig. 5.1 (b), the region in fig. 5.2 (b), and $\frac{\alpha_1}{(2\pi T)} \leq 0$. In what follows we will always restrict to values of α_1 and α_2 in this region.

with the other non-zero. If $\alpha_1 = 0$ then eq. (5.4.20) becomes simply $\alpha_2 \leq 0$, which is also sufficient to guarantee $(2\pi T) z_H \geq 0$. When $\alpha_1 = 0$ we will thus always restrict to $\alpha_2 \leq 0$. If $\alpha_2 = 0$, then eq. (5.4.20) gives $\alpha_1 \leq 0$, which we will always impose, as mentioned above.

The nature of the extremal limit, $T \to 0$, depends on whether α_1 and α_2 are both zero. If $\alpha_1 = 0$ and $\alpha_2 = 0$, then $T = 3/(4\pi z_H)$, so $T = 0$ implies $z_H = \infty$, meaning no horizon is present. In the dual field theory, this means that when $T = 0$, no entropy is present. This makes sense, since in those limits the geometry is exactly that of AdS_4, so the dual CFT is in its conformal vacuum. However if α_1 and/or α_2 is non-zero, then a horizon survives down to $T = 0$. In this case, the dual field theory has non-zero entropy of order N^2, even when $T = 0$, due to the TSB induced by α_1 and/or α_2. When either or both of α_1 and α_2 is non-zero, the location of the extremal horizon is, from eq. (5.4.19a),

$$z_{\text{ext}} = \lim_{T\to 0} z_H^- = -\frac{\alpha_1}{\alpha_2}\left[1 - \sqrt{1 - \frac{3\alpha_2}{\alpha_1^2}}\right]. \tag{5.4.21}$$

Near the extremal horizon the geometry is approximately $AdS_2 \times \mathbb{R}^2$, indicating that in the dual field theory at $T = 0$ the low-energy effective description is a $d = 1$ CFT.

An extremal horizon implies a non-zero Bekenstein-Hawking entropy at $T = 0$, and hence a large degeneracy of $T = 0$ ground states. Such a degeneracy is at risk of instability, since generically any perturbation will break the degeneracy and drive the system to a new, and presumably unique, ground state. Such instabilities often depend on the detailed dynamics of the particular (super-)gravity theory. To our knowledge, the massive gravity and scalar or two-form theories in refs. [20, 19, 21, 195, 22] are stable, at least under linear perturbations in the regimes of α_1 and α_2 shown in fig. 5.3,

so in what follows we will assume that the geometry is stable at $T = 0$.

5.4.2 The Probe Sector

In the probe sector of the dual field theory we want to introduce a non-zero charge density, $\langle J^t \rangle \neq 0$. The charge density operator, J^t, is holographically dual to A_t, the time component of the $U(1)$ gauge field in the DBI action eq. (5.4.17). Since in our model the DBI action is sensitive only to the metric in eq. (5.4.16), which is translationally and rotationally invariant, our ansatz for A_t will depend only on z. We will also work in the gauge $A_z = 0$, in which case the only non-zero components of the $U(1)$ field strength are $F_{zt}(z) = -F_{tz}(z) = \partial_z A_t(z) \equiv A_t'(z)$. With these choices the DBI action becomes

$$S = -\mathcal{N} \int_0^{z_H} dz\, g_{xx} \sqrt{|g_{tt}| g_{zz} - A_t'^2} \tag{5.4.22}$$

This action depends only on A_t' and not A_t, hence we have a constant of integration, which is in fact the charge density in the dual field theory,

$$\langle J^t \rangle = \frac{\delta S}{\delta A_t'} = \frac{\mathcal{N}\, g_{xx}\, A_t'}{\sqrt{|g_{tt}| g_{zz} - A_t'^2}}. \tag{5.4.23}$$

We can solve eq. (5.4.23) for A_t', with the result

$$A_t' = d \sqrt{\frac{|g_{tt}| g_{zz}}{g_{xx}^2 + d^2}}, \qquad d \equiv \langle J^t \rangle / \mathcal{N}. \tag{5.4.24}$$

We define the chemical potential to be the work done to add a unit charge to the system by moving it from the horizon to the boundary against the electric field,

$$\mu = \int_{z_H}^{0} dz\, F_{tz} = \int_0^{z_H} dz\, A_t' = \int_0^{z_H} dz\, \frac{d}{\sqrt{1 + d^2 z^4}} \tag{5.4.25}$$

$$= \frac{\sqrt{d}}{4} B\left(\frac{1}{4}, \frac{1}{4}\right) - \frac{1}{z_H}\, {}_2F_1\left(\frac{1}{4}, \frac{1}{2}; \frac{5}{4}, -d^{-2} z_H^{-4}\right), \tag{5.4.26}$$

where $B\left(\frac{1}{4}, \frac{1}{4}\right)$ is a Beta function.

The probe contribution to the grand canonical (Gibbs) free energy density, Ω, is minus the on-shell probe brane action density. Plugging the solution for A_t' from eq. (5.4.24) into the action density $\hat{S}$ in eq. (5.4.22), we find the on-shell probe brane action density,

$$\hat{S}\big|_{\text{on-shell}} = -\mathcal{N} \int_0^{z_H} dz\, g_{xx}^2 \sqrt{\frac{|g_{tt}| g_{zz}}{g_{xx}^2 + d^2}} \tag{5.4.27a}$$

$$= -\mathcal{N} \int_0^{z_H} dz\, z^{-4} \left(1 + d^2 z^4\right)^{-1/2}. \tag{5.4.27b}$$

The integral in eq. (5.4.27) clearly diverges as $-\frac{1}{3}\mathcal{N}z^{-3}$ at the $z \to 0$ endpoint, that is, near the asymptotically AdS_4 boundary. To obtain a finite result, and more generally to guarantee a well-defined variational problem, we must holographically renormalise the on-shell action [184, 185, 186, 147, 187]. To do so, we first regulate the divergence by integrating not to $z = 0$ but to a cutoff surface $z = \varepsilon$, leading to a regulated action, S_{reg}. On the surface $z = \varepsilon$ we then introduce a counterterm action, S_{CT}, built from objects invariant under the system's symmetries, such as the diffeomorphisms preserved by α_1 and α_2. These counterterms cancel the $\varepsilon \to 0$ divergences in S_{reg} and may also contain contributions that remain finite as $\varepsilon \to 0$. We then define the renormalised action as $S_{\text{ren}} \equiv \lim_{\varepsilon\to 0}\left(S_{\text{reg}} + S_{\text{CT}}\right)$, and corresponding renormalised action density, $\hat{S}_{\text{ren}}$.

We present the details of the holographic renormalisation for the probe brane in the background of eq. (5.4.16) in Appendix 5.B. Here we will just highlight the main differences between the cases with and without α_1 and α_2. When $\alpha_1 = 0$ and $\alpha_2 = 0$, the $\varepsilon \to 0$ divergence in S_{reg} is $-\frac{1}{3}\mathcal{N}\varepsilon^{-3}$, as mentioned above, and S_{CT} consists of a single term proportional to the volume of the $z = \varepsilon$ surface, whose only non-zero contribution as $\varepsilon \to 0$ is $+\frac{1}{3}\mathcal{N}\varepsilon^{-3}$, which precisely cancels the divergence in S_{reg} [147]. When α_1 and/or α_2 is non-zero, the $\varepsilon \to 0$ divergence in S_{reg} is still $-\frac{1}{3}\mathcal{N}\varepsilon^{-3}$, however the volume counterterm in S_{CT} now acquires new divergences with coefficients that depend on α_1 and α_2. Cancelling these requires additional counterterms, which also make finite contributions to S_{ren} when $\varepsilon \to 0$, which depend on α_1 and α_2. Ultimately, for the probe contribution to the grand canonical free energy density we find

$$\Omega = -\mathcal{N}\frac{1}{12}B\left(\frac{1}{4},\frac{1}{4}\right)d^{3/2} - \mathcal{N}\frac{1}{5}\frac{1}{z_H^5\, d}\,{}_2F_1\left(\frac{5}{4},\frac{1}{2},\frac{9}{4};-\frac{1}{d^2\, z_H^4}\right) \tag{5.4.28a}$$

$$-\mathcal{N}\frac{5}{48}\alpha_1^3 + \mathcal{N}\frac{1}{4}\alpha_1\alpha_2 + \mathcal{N}\frac{1}{6}\left(\frac{1}{z_H^3} + \frac{\alpha_1}{z_H^2} + \frac{\alpha_2}{z_H}\right), \tag{5.4.28b}$$

where $B\left(\frac{1}{4},\frac{1}{4}\right)$ is a Beta function. In eq. (5.4.28), the first line is the contribution from the bulk integral in eq. (5.4.27). As described above, in Appendix 5.B we show that S_{CT} cancels the divergent contribution from the $z = \varepsilon$ endpoint of the bulk integral, and also contributes the finite terms in the second line of eq. (5.4.28). In Ω, α_1 and α_2 enter explicitly in the finite terms in the second line of eq. (5.4.28) and implicitly through z_H, via eq. (5.4.19).

In general, the hypergeometric functions in (5.4.26) and (5.4.28) will prove difficult to work with, it will therefore be prudent to apply an approximation. Since the hypergeometric function is a function of $d\, z_H^2$, the only two options are $d\, z_H^2 \gg 1$ and $d\, z_H^2 \ll 1$.

If $\alpha_1 = 0$ and $\alpha_2 = 0$, then $z_H = 3/(4\pi T)$, and so $d\, z_H^2 \propto d/T^2$. As a result, $d\, z_H^2 \gg 1$ and $\ll 1$ are the high- and low-density limits, respectively. We are interested primarily in the high-density, or quantum compressible, limit, $d/T^2 \gg 1$. However, we will have $\alpha_1 \neq 0$ and/or $\alpha_2 \neq 0$, in which case z_H is not simply $\propto 1/T$, but rather is

the more complicated combination of T, α_1, and/or α_2 in eq. (5.4.19). As a result, $d\,z_H^2 \gg 1$ and $\ll 1$ are not necessarily the high- and low-density limits, respectively. In fact, with the constraints in sec 5.4.1, $d^2 z_H^4 \gg 1$ will always be a high-density limit, but when $d^2 z_H^4 \ll 1$ we can still reach $d/T^2 \gg 1$. Nevertheless, in what follows we will primarily be interested in the $d\,z_H^2 \gg 1$ limit. It would be interesting to explore the $d\,z_H^2 \ll 1$ limit in future work.

5.4.3 Spectrum of Fluctuations

Unlike in a back-reacted model we only have access to a subset of the spectrum of fluctuations, namely we do not have access to the modes found in the sound, shear and scalar channel, calculated by looking at variations of the metric. Instead, in a probe brane system we can calculate the holographic zero sound and diffusive mode. There are multiple ways to do this, for example in [16, 160] the holographic zero sound dispersion relation at vanishing temperature is found via the fluctuation method as poles in the two point retarted Green's function (we will use this method to calculate the numerics). In [181] a different approach is taken where instead a quasi-conserved constituent equation is derived using a linearised gradient expansion. Here we will combine aspects of both methods.

Concretely, we derive the constituent equation (5.3.9b) by comparing two electric fields, a gauge-invariant electric field derived as a solution to its equation of motion, that we shall call E, with a solution of the electric field derived from a combination of field theory gauge fields, $\mathcal{E}$ obtained from a zeroth order gradient expansion. As with previous calculations, the solutions are derived in a near horizon low frequency limit.

We start with the later, where we define $\mathcal{E} = \partial_i A_t - \partial_t A_i$. A_t and A_i can be calculated by looking for saddle point solutions of the DBI action,

$$\partial_a \left(\sqrt{-det(g_{ab} + F_{ab})} (g_{ab} + F_{ab})^{-1} \right) = 0 \tag{5.4.29}$$

and taking a gradient expansion in the field theory co-ordinates μ. Noting the gauge choice $A_z = 0$ we can write the 0^{th} order i and t-components of (5.4.29) as:

$$\partial_z \left(A_i' f(z) \sqrt{1 + d^2 z^4} \right) = \mathcal{O}(\partial_\mu^2) \tag{5.4.30a}$$

$$\partial_z \left(\frac{A_t'}{\sqrt{1 - z^4 A_t'^2 + A_i'^2 f(z) z^4}} \right) = \mathcal{O}(\partial_\mu^2) \tag{5.4.30b}$$

where $\mathcal{O}(\partial_\mu^2)$ denotes higher order terms in the gradient expansion. Alternatively, subbing in the conserved constants, and taking $J^i = 0$ to be

infinitesimal, we can instead write:

$$\partial_z\left(A_i' f(z)\sqrt{1+d^2z^4}\right) = \mathcal{O}(\partial_\mu^2) \tag{5.4.31a}$$

$$\partial_z\left(A_t'\sqrt{1+d^2z^4}\right) = \mathcal{O}(\partial_\mu^2) \tag{5.4.31b}$$

with solutions,

$$A_t' = -\frac{d}{\sqrt{1+d^2z^4}} \qquad A_i' = \frac{J_i}{f\sqrt{1+d^2z^4}} \tag{5.4.32}$$

where J_i is the charge current and d the charge density defined in eq. (5.4.24). To find A_t and A_i we now need to integrate both sides of the equations in eq. (5.4.32). Starting with A_t we have,

$$A_t(z) = A_t^0 - d\int_0^z dr \frac{1}{\sqrt{1+d^2r^4}} \tag{5.4.33}$$

where the integral, evaluated at $z = z_H$, is the chemical potential derived in eq. (5.4.26),

$$\mu = \frac{\sqrt{d}}{4}B\left(\frac{1}{4},\frac{1}{4}\right) - \frac{1}{z_H}{}_2F_1\left(\frac{1}{4},\frac{1}{2};\frac{5}{4},-d^{-2}z_H^{-4}\right) \tag{5.4.34}$$

Near the horizon, for the regime of parameters that we are interested in, $d^2z_H^4$ is, in general, large. Hence we can expand the second term,

$$\mu = \frac{\sqrt{d}}{4}B\left(\frac{1}{4},\frac{1}{4}\right) - \frac{1}{z_H} + ... \tag{5.4.35}$$

such that A_t becomes,

$$A_t(z) = A_t^0 - \frac{\sqrt{d}}{4}B\left(\frac{1}{4},\frac{1}{4}\right) + \frac{1}{z_H} \tag{5.4.36}$$

Similarly the A_i term can be derived as,

$$\begin{aligned} A_i(z) &= A_i^0 + J_i\int_0^z dr \frac{1}{f(r)\sqrt{1+d^2r^4}} \\ &= A_i^0 + J_i\int_0^z \frac{dr}{\sqrt{1+d^2r^4}} + J_i\int_0^z \frac{dr}{\sqrt{1+d^2r^4}}\frac{1-f(r)}{f(r)} \\ &= A_i^0 + \frac{J_i}{4\sqrt{d}}B\left(\frac{1}{4},\frac{1}{4}\right) - \frac{J_i}{dz_H} + J_i\int_0^z \frac{dr}{\sqrt{1+d^2r^4}}\frac{1-f(r)}{f(r)} \end{aligned} \tag{5.4.37}$$

Where in the second line we have simply re-written the integral and in the third used the expansion above. The remaining integral is difficult to compute, however it turns out that the integral contains a logarithmic divergence near the horizon [181],

and so by expanding near the horizon, where d^2r^4 is large, it can be approximated,

$$\int_0^z \frac{dr}{\sqrt{1+d^2r^4}}\frac{1-f(r)}{f(r)} \approx Log\left|\frac{z_H}{z_H-z}\right|\left(\frac{1}{dz_H(3+2\alpha_1 z_H+\alpha_2 z_H^2)}\right)\left(1-\frac{1}{2d^2z_H^4}+\frac{3}{8d^4z_H^8}-...\right)+const. \tag{5.4.38}$$

For simplicity, we write (5.4.38) as $A\text{Log}\frac{z_H}{z_H-z}+D$ and drop the A_μ^0 terms. The A_i component then becomes,

$$A_i(z)=J_iA\text{Log}\frac{z_H}{z_H-z}+\frac{J_i}{4\sqrt{d}}B\left(\frac{1}{4},\frac{1}{4}\right)+J_i\left(D-\frac{1}{dz_H}\right) \tag{5.4.39}$$

We are also interesting in the case with a vanishing horizon - ultimately this means taking $A=D=0$,

$$A_i(z_H\to\infty)=\frac{J_i}{4\sqrt{d}}B\left(\frac{1}{4},\frac{1}{4}\right)-\frac{J_i}{dz_H} \tag{5.4.40}$$

We can now write down the electric field. For the case with a horizon we have,

$$\mathcal{E}=-A\text{Log}\frac{z_H}{z_H-z}\partial_tJ_i-\left(\frac{1}{2}\partial_id+\partial_tJ^i\right)\left(\frac{B(\frac{1}{4},\frac{1}{4})}{4\sqrt{d}}\right)-\left(D-\frac{1}{dz_H}\right)\partial_tJ_i \tag{5.4.41}$$

where we have a logarithmic piece as $z\to z_H$, terms independent of z_H and terms subleading in z_H. From now on we drop the subleading terms for the case with a horizon.

For the horizonless case we instead have,

$$\mathcal{E}_{z_H\to\infty}=-\left(\frac{1}{2}\partial_id+\partial_tJ^i\right)\left(\frac{B(\frac{1}{4},\frac{1}{4})}{4\sqrt{d}}\right)+\frac{1}{dz_H}\partial_tJ_i \tag{5.4.42}$$

where we now only have terms that go as $\frac{1}{z_H}$ and a z_H-independent term. Keeping track of the z_H dependence will be important later.

We now construct a second electric field E by taking the action to second order in fluctuation with respect to the $U(1)$ gauge field. The fluctuations are,

$$A_\mu\to A_\mu(z)+a_\mu(z,t,x). \tag{5.4.43}$$

Due to invariance under rotations, and noting as a gauge choice $a_z=0$, we only have to consider the fluctuations a_t and a_x. It is then easiest to proceed by Fourier transforming the fluctuations and combining them to create a gauge invariant electric field, $E=\omega a_x+ka_t$. To find solutions for E we have to solve the linearized equations of motion for the electric field, the action of which, to quadratic order, is [160]

$$S = \frac{\mathcal{N}}{2}\int dz d\omega dk \frac{g_{xx}^{-1/2} g_{zz}^{1/2}}{u}\left[E^2 + \frac{|g_{tt}|}{g_{zz}(u^2k^2 - \omega^2)}E'^2\right] \tag{5.4.44}$$

with,

$$u = \sqrt{\frac{|g_{tt}|}{g_{xx}}}(1 + d^2 g_{xx}^{-2})^{-1/2} \tag{5.4.45}$$

The equation of motion for E can then be written as:

$$\partial_z\left[\frac{|g_{tt}|}{u\sqrt{g_{zz}g_{xx}}}\frac{\omega}{(u^2k^2 - \omega^2)}E'\right] - \sqrt{\frac{g_{zz}}{g_{xx}}}\frac{\omega}{u}E = 0 \tag{5.4.46}$$

We will solve this in two ways, first with a finite horizon, and second with a vanishing horizon (that is, with $\alpha_1 = \alpha_2 = T = 0$). In both cases we will solve the equation of motion in a near horizon, low frequency limit. Using our metric factors eq. (5.4.46) becomes:

$$\partial_z\left(\frac{f(z)^{3/2}\omega}{u(u^2k^2 - \omega^2)}E'\right) = \frac{\omega}{\sqrt{f}u}E \tag{5.4.47}$$

We first look at the case with no horion where we can set $f(z) = 1$. In the 'near horizon' limt of $z_H \to \infty$ the equation simplifies to:

$$E'' + \frac{2}{z}E' + \omega^2 E = 0 \tag{5.4.48}$$

The solution is of Hankel form,

$$E = C\left(\frac{\omega z}{2}\right)^{-\frac{1}{2}} H^{(1)}_{-\frac{1}{2}}(\omega z) \tag{5.4.49}$$

where we have chosen the in-going wave solution, $E \sim z^{-1}e^{i\omega z}$. We now take frequency and momentum small such that the solution becomes,

$$E_{z_H\to\infty} = C\Gamma\left(\frac{3}{2}\right)^{-1} - i\frac{2C}{\pi\omega}\Gamma\left(\frac{1}{2}\right)\frac{1}{z} \tag{5.4.50}$$

where we see that we have a part that is independent of z and a part that goes as $\frac{1}{z}$ - this will come in useful when we match to our previous electric field.

We now look at the case with a horizon. Taking a near horizon expansion we obtain,

$$\begin{aligned}\sqrt{f}u\partial_z\left(\frac{f^{3/2}}{u\omega}E'\right) &= -\omega E \\ f^2E'' + E'ff' + \frac{2f^2}{z}E' &= -\omega^2 E\end{aligned} \tag{5.4.51}$$

We can see that this result reduces to (5.4.48) in the horizonless limit. It would be interesting to be able to solve this equation in its current form, however for now it will

suffice to again invoke a near horizon approximation and take only the leading term in E'

$$f\partial_z(fE') = -\omega^2 E \tag{5.4.52}$$

or, by undoing the Fourier transform,

$$f\partial_z(fE') = \partial_t^2 E \tag{5.4.53}$$

To simplify this further, we can expand the emblackening factor near the horizon,

$$f(z) \approx \left(\frac{3}{z_H} + 2\alpha_1 + \alpha_2 z_H\right)(z_H - z) + \mathcal{O}((z_H - z)^2) \tag{5.4.54}$$

and defining

$$R = \frac{1}{4\pi T}\text{Log}\frac{z_H}{z_H - z} \tag{5.4.55}$$

where, as in (5.4.18), we use:

$$4\pi T = \frac{1}{z_H}[3 + 2\alpha_1 z_H + \alpha_2 z_H^2] \tag{5.4.56}$$

We then have,

$$\partial_R^2 E = \partial_t^2 E, \tag{5.4.57}$$

of which the regular, in-falling, solution is of Fourier form,

$$E \approx \int d\omega C(\omega) e^{i\omega(R-t)} \tag{5.4.58}$$

To write this solution for the electric field in a more useful way we Taylor expand in the limit of small frequency and small momentum,

$$E \approx C - \frac{\partial_t C}{4\pi T}\log\frac{z_H}{z_H - z} + \mathcal{O}(\partial_t^2) \tag{5.4.59}$$

Where we note there is a part independent of z_H and a part that has a logarithmic divergence as $z \to z_H$.

We now have two electric fields worked out from the fluctuation EOM that we can now compare to our previous electric field, $\mathcal{E}$. In the vanishing horizon case we match equation (5.4.42) and (5.4.50), where we match the terms that go as $1/z$ together and the terms that are independent of z in the near horizon limit $z \to z_H$:

$$-\frac{\Gamma(\frac{3}{2})B(\frac{1}{4},\frac{1}{4})}{8\sqrt{d}}\partial_i d - \frac{\Gamma(\frac{3}{2})B(\frac{1}{4},\frac{1}{4})}{4\sqrt{d}}\partial_t J_i = i\frac{\pi\omega}{2\Gamma(\frac{1}{2})d}\partial_t J_i \tag{5.4.60}$$

or

$$v^2\partial_i d + \partial_t J_i = -\frac{i}{\tau}\partial_t J_i \tag{5.4.61}$$

where we have defined velocity and dissipation rate as,

$$v^2 = \frac{1}{2} \qquad \frac{1}{\tau} = \frac{4}{B(\frac{1}{4},\frac{1}{4})\sqrt{d}}\omega^2 \tag{5.4.62}$$

where we see that we have the conformal value $1/\sqrt{2}$ for the speed of sound. To find the dispersion relation we combine the above quasi-conserved constituent relation with the conserved charge equation, $\partial_\mu J^\mu = 0$, and look for solutions that go as $J_\mu \sim e^{i(kx-\omega t)}$. The result is,

$$v^2k^2 = \omega^2\left(1 + \frac{i}{\omega\tau}\right) \tag{5.4.63}$$

As expect this matches the result of [160], that is, even without a horizon there is still a non-zero dissipation due to the probe limit.

The constituent equation for the horizon case can be found by matching (5.4.41) and (5.4.59) and following the same steps as the horizonless case, but now matching the logarithmic divergent terms together as well as the terms independent of z_H. We have as our dispersion relation,

$$v^2k^2 = \omega^2\left(1 + \frac{i}{\tau\omega}\right) \tag{5.4.64}$$

where now we have,

$$v^2 = \frac{1}{2} \qquad \frac{1}{\tau} = \frac{4}{B(\frac{1}{4},\frac{1}{4})\sqrt{d}}\frac{1}{z_H^2} \tag{5.4.65}$$

Note, we have again used the conformal speed of sound, however since we have now included temperature and the symmetry breaking factors it may prove useful to amend the conformal value. Furthermore, we notice the attenuation clearly vanishes in the horizonless limit $z_H \to \infty$. However, as we have seen in the vanishing horizon case there is in fact a finite damping factor. Therefore the two solutions will clearly cross over at some small but finite temperature. Since we are primarily interested in the thermal colisionless to hydrodynamic crossover, we leave the transition to the quantum collisionless regime for future work.

The dispersion relation in eq. (5.4.64) can be written as,

$$\omega = -\frac{i}{2\tau} \pm \sqrt{k^2v^2 - \frac{1}{4\tau^2}} \tag{5.4.66}$$

where we see that there is a k-gap - a finite, non-zero amount of momentum is required before the mode begins to propagate. This is not uncommon and is in fact characteristic of a system that resembles a damped harmonic oscillator, a system with some form of momentum dissipation.

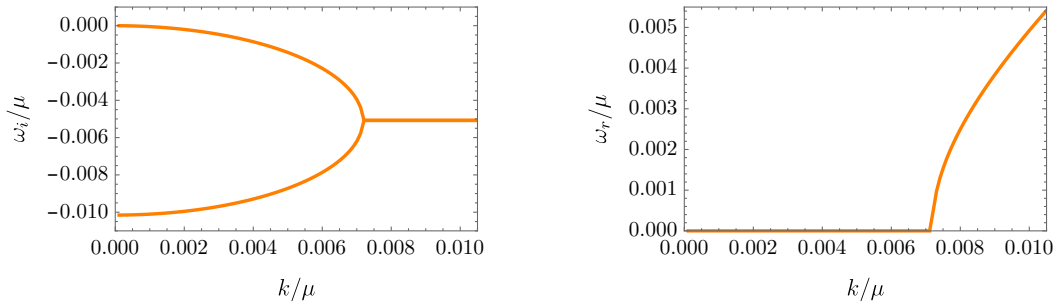

FIGURE 5.4: Example of QNM k-dependence for $\alpha_1/\mu = -1/30$ and $\alpha_2/\mu^2 = 0$. As momentum is decreased the real part of the mode goes to zero thus indicating the existance of a k-gap.

An example of the quasi-normal mode dependence on momentum is given in Fig 5.4 for the case of $\alpha_1/\mu = -1/30$ and $\alpha_2/\mu^2 = 0$. The HZS mode starts as a propagating mode at $k/\mu = 1/100$. As momentum is decreased the HZS modes collide on the imaginary axis where one pole subsequently moves up the axis until it reaches $\omega_{Re} = \omega_{Im} = 0$, whereas the other pole moves down the axis. In other words, a propagating mode has turned into a diffusive mode. This means that the sound modes require a minimum amount of momentum before they can start propagating i.e a k-gap.

The k-gap can be calculated as,

$$k_g = \frac{1}{2\tau v} \tag{5.4.67}$$

It explicitly depends on the momentum relaxation scale τ. Therefore with stronger symmetry breaking factors we should see that more momentum is required before the sound modes start propagating. The left/right hand plot of Fig 5.5 shows the analytic k-gap using the values of τ and v at various α_1/μ and α_2/μ^2 values respectively (note the analytics have also been checked against the numerics in the subsequent section). For larger values of α_1 and α_2 the k-gap is pushed to higher momentum. This intuitively makes sense. With larger symmetry breaking the mode is pushed further into the diffusive regime, therefore more momentum is required to transition the mode into the propagating regime.

Before moving on to take a closer look at the quasi-normal modes and the numerics, we also calculate the analytic diffusive dispersion relation defined by,

$$\omega = -iDk^2 \tag{5.4.68}$$

Where D can be calculated from [188],

$$D = \sqrt{1 + d^2 z_H^4}\, z_H F\left(\frac{3}{2}, \frac{1}{4}, \frac{5}{4}; -d^2 z_H^4\right) \tag{5.4.69}$$

The diffusive constant can also be written in terms of the relaxation scale via the

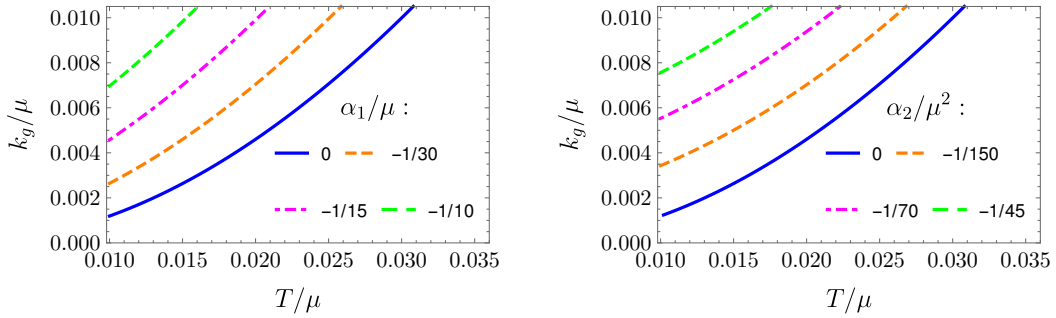

FIGURE 5.5: Plot of k-gap against temperature for various values of $\alpha_{1/2}$. Left plot, $\alpha_2 = 0$, right plot, $\alpha_1 = 0$. We see that with increasing $\alpha_{1/2}$ k_g is pushed to higher values, indicating that with more momentum dissipation, more momentum is needed before the mode starts propagating.

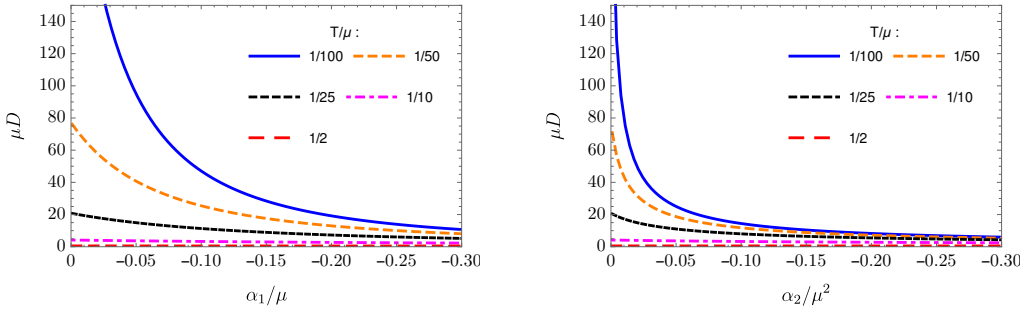

FIGURE 5.6: Diffusivity constant D plotted as a function of $\alpha_{1/2}$ at various temperatures. We see that the symmetry breaking pushes the purely imaginary mode towards the origin.

relation $D = v^2\tau$. If we take the limit $d^2z_H^4 \gg 1$ in eq. (5.4.69) we that that the result matches that of τ in eq. (5.4.65) up to the factor v^2.

In fig 5.6 we take a look at how the translational symmetry breaking affects the diffusivity constant D. In agreement with the k-gap, the affect of the symmetry breaking is to push the mode towards the diffusive pole at $\omega_R = \omega_i = 0$ for any temperature.

5.4.3.1 Numerics

Now that we have analytic solutions we can proceed to calculate the numerics. The zero sound mode should show up as the pole of the two point retarded correlator that can be calculated from the fluctuations:

$$G_{ii} = \frac{\delta^2 S}{\delta a(\epsilon)_i^2} = \left(\frac{\delta E}{\delta a(\epsilon)_i}\right)^2 \frac{\delta^2 S}{\delta E(\epsilon)^2} \tag{5.4.70}$$

where ϵ indicates near boundary values of a_μ. Thus, numerically solving E's EOM and looking for solutions that vanish at the boundary is sufficient to find the quasi-normal modes. Our numerics follow the shooting/Frobenius method where the solution

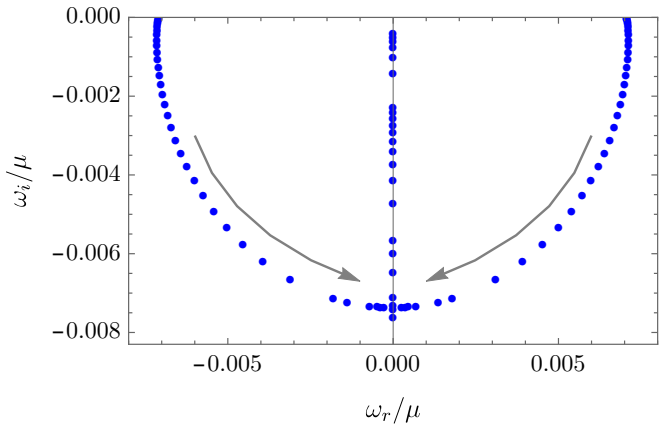

FIGURE 5.7: QNM with $\alpha_1/\mu = \alpha_2/\mu^2 = 0$ while varying temperature. The critical temperature is given by $T_c/\mu = 0.029$.

'shoots' out of the black hole horizon with initial conditions specified by a power series expansion near the horizon.

To keep everything consistent we scale by the chemical potential and, using $\frac{k}{\mu} = \frac{1}{100}$ throughout we plot various QNM with different T/μ, α_1/μ and α_2/μ^2. Note we keep $\frac{T}{\mu} > \frac{1}{100}$ due to discrepancies in the numeric and analytical results below this temperature. Future work would be to extend the results to this very low temperature regime, as well as finding the attenuation cross-over in the analytical solutions.

As a first example we plot the QNM of $\frac{\alpha_1}{\mu} = \frac{\alpha_2}{\mu^2} = 0$ in Fig. 5.7. The holographic zero sounds (HZS) mode starts at $\frac{T}{\mu} = \frac{1}{100}$ with a small, but non-zero, imaginary frequency - it is a long lived excitation with a real frequency dependent only on the value of momentum and the propagating speed, v, which conformally is given in (2+1)-dimesions by $v = \frac{1}{\sqrt{2}}$. As temperature is increased we move from the near quantum regime, into the thermo collisionless regime and finally into the hydrodynamic regime. We see that the modes become increasing damped until they collide on the imaginary axis, whereupon one mode moves down the imaginary axis to become the diffusive mode and the other dissapears up the axis. The temperature at which the modes collide is the crossover between the thermo-collisionless and hydrodynamic regimes and henceforth will be called the critical temperature, T_c. The value of T_c in this case is 0.029 in units of μ. We note that the shape of the evolution, an approximate semi-circle, is characteristic of a damped harmonic oscillator.

Next we plot a variety of QNM with various fixed $\alpha_{1/2}$ and T values. In fig. 5.8 we fix α_1/μ while varying temperature, in fig. 5.9 we fix temperature while vary α_1/μ, in fig 5.10 we fix α_2/μ^2 while varying temperature, and finally in fig. 5.11 we fix temperature while vary α_2/μ^2.

Let's take a closer look at fig. 5.8. There are a few features to point out. First, the location of the low temperature modes, $T/\mu = 1/100$, no longer reach the real frequency axis when there is explicit symmetry breaking - there no longer exists near-infinite long lived modes. With increasing symmetry breaking these low

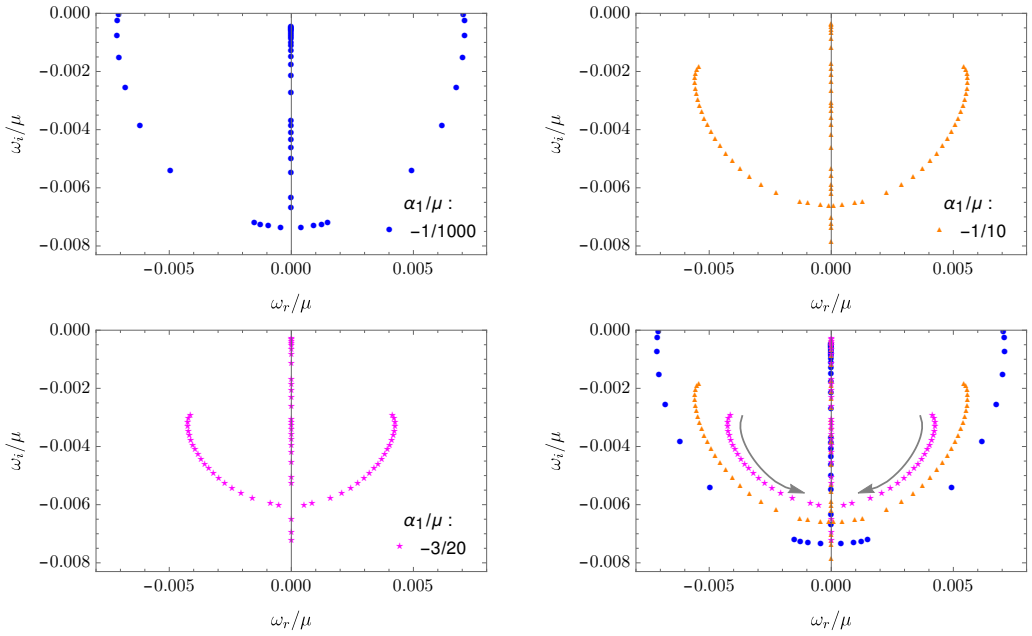

FIGURE 5.8: Various QNM numerics at fixed α_1/μ with varying temperature.

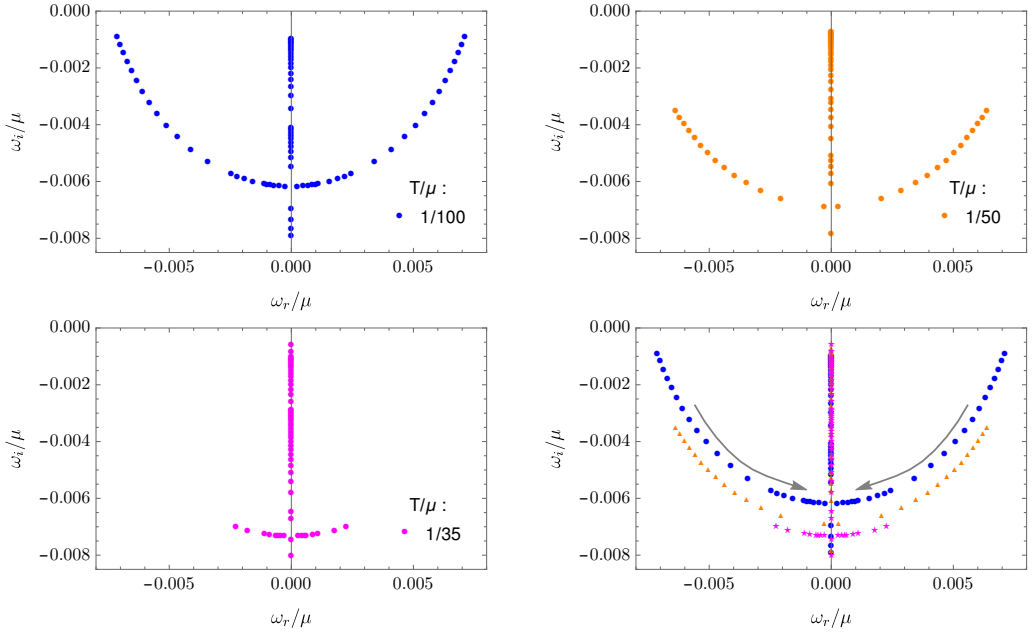

FIGURE 5.9: Various QNM numerics at fixed temperature while varying α_1/μ.

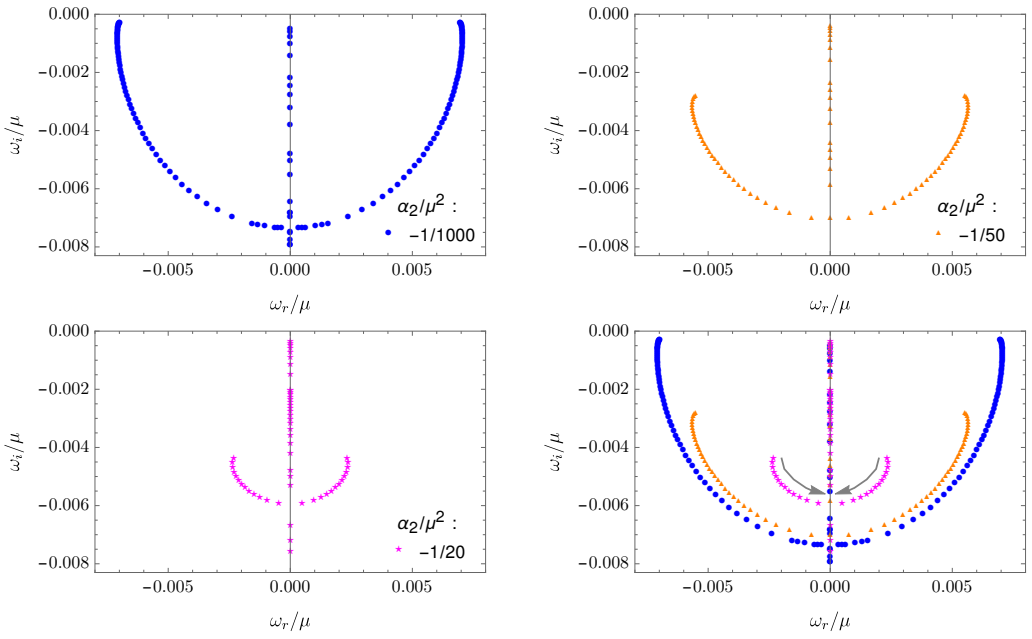

FIGURE 5.10: Various QNM numerics at fixed α_2/μ^2 with varying temperature.

temperature modes becomes increasingly damped, as expected. We do not know the precise end point of these semi-circles as we keep $T/\mu > 1/100$ due to numerical and analytical inconsistency. It would be interesting to see where these modes end and if there is new behaviour at very low temperature. Secondly, the size of the semi-circle is reduced as the strength of the symmetry breaking is increased, this indicates that eventually there will be no propagating modes at any temperature. Thirdly, as the semi-circle reduces in size the location of the critical temperature is at smaller imaginary frequency, it is also at a lower critical temperature as can be seen in the plots. None of this is surprising, with increased symmetry breaking there will be increased momentum dissipation in any propagating mode, thus turning the mode diffusive. It is worth noting that if the QNM started on the imaginary axis, i.e those modes with $T/\mu > 0.029$ for the case with no symmetry breaking, then the effect of the symmetry breaking is to move one of the modes toward the diffusive pole and the other further along the imaginary axis.

In fig. 5.9 we instead fix temperature and vary α_1/μ. The starting point for each fixed T/μ semi-circle is with $\alpha = -1/1000$ in units of μ. We then increase α_1/μ, the effect of which is to move the mode in a semi-circle until it collides on the imaginary axis at some critical α_1/μ. Again, one mode will then move down to the diffusive pole as the other moves up. This makes clear that with enough symmetry breaking even a very low temperature mode will eventually move to the diffusive pole.

In fig. 5.10 and fig. 5.11 we repeat the analysis but now with α_2/μ^2 - the numerics follow a similar trend, however in the case of fixing α_2/μ^2 it is clear that smaller values of α_2/μ^2 are required to have the same damping effect as α_1/μ. We can therefore say that the effect of α_2/μ^2 is 'stronger' than that of α_1/μ on the quasi-normal modes.

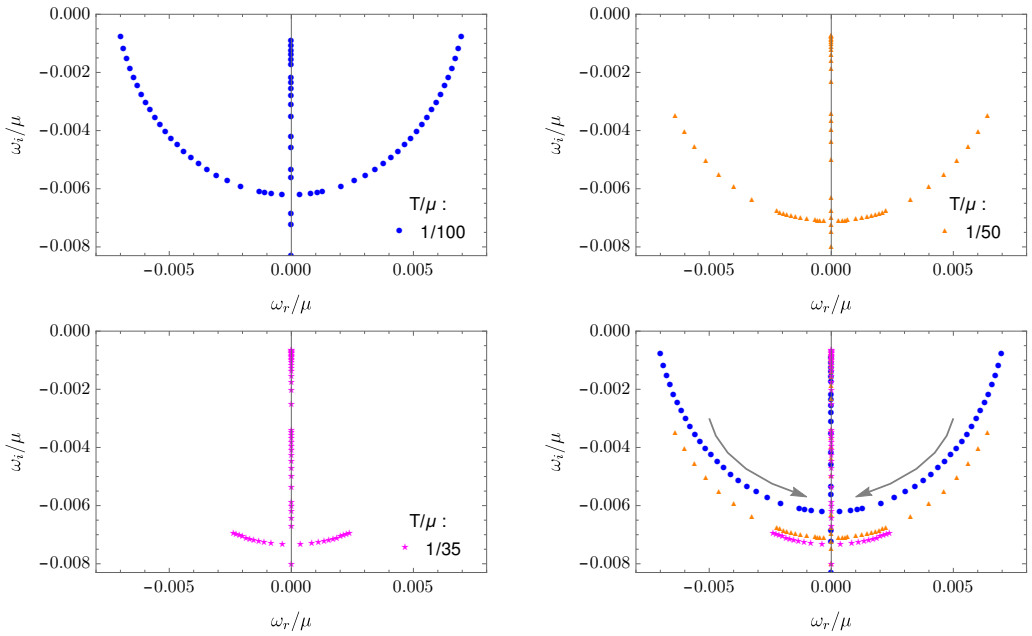

FIGURE 5.11: Various QNM numerics at fixed temperature while varying α_2/μ^2.

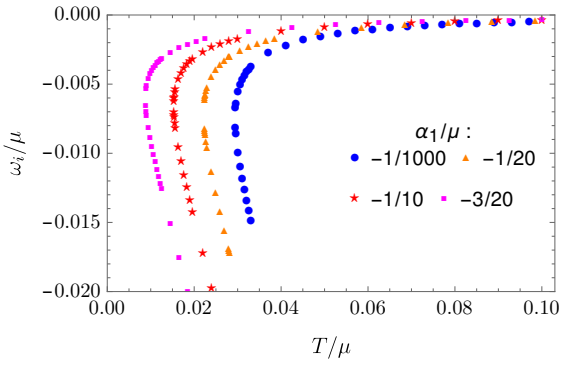

FIGURE 5.12: The purely damped modes for fixed α_1/μ with varying temperature. The lower modes are those that tend to the diffusive pole, whereas the higher are those that move down the imaginary axis.

It is difficult to see the α/T dependence of the QNM when they have no real part. In fig 5.12 we plot ω_{Im}/μ against T/μ for various fixed values of α_1/μ. Each curve is plotted with QNM values immediately after T_c, that is there are two modes, one moves to higher ω_{Im} values and the other to the diffusive pole. We see that at lower temperatures the value of α_1/μ has a distinct effect on the location of the QNM. However as temperature is increased the QNM begin to overlap, and coincide as the diffusive pole is neared. In other words, small perturbations around the diffusive mode are independent of the strength of the symmetry breaking factor.

Finally, it is worth checking the accuracy of our numerics. In fig. 5.13 and fig. 5.14 we plot the real and imaginary parts of the QNM for $\alpha_1/\mu = -1/100, -1/20, -1/10$ and $\alpha_2/\mu^2 = -1/200, -1/50, -1/20$ respectively. The blue dots are the numerics, the

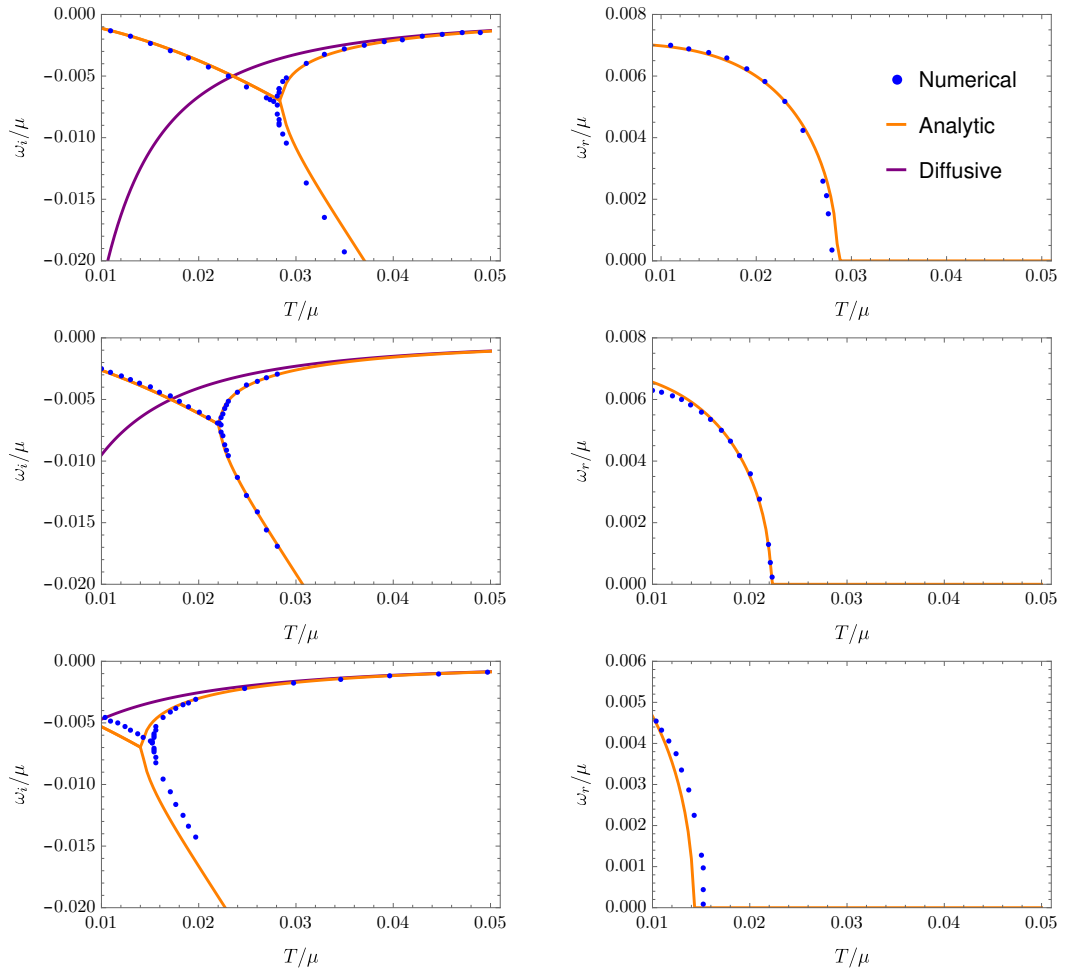

FIGURE 5.13: Analytic and numeric comparison for $\alpha_1 = \frac{-1}{100}, \frac{-1}{20}$ and $\frac{-1}{10}$. The left-/right hand plots show the imaginary/real components of the QNM.

orange line is the analytics as worked out via the conserved charge equations, and the purple line is the diffusive analytics. In both cases we see good agreement between all of the numerics and analytics in the parameter regime that we have been interested in, namely $T/\mu > 1/100$. To capture the analytics and numerics at lower temperatures would require a second numerical method more suited to low temperature analysis, as well as further investigation into the low temperature/ high $\alpha_{1/2}$ analytics. Nevertheless, the conserved charge analytics not only captures the holographic zero sound regime, but also the crossover (that is around T_c) as well as the diffusive regime as is confirmed by the overlap with the diffusive results.

To emphasis the accuracy of the conserved charge analytics we plot the critical temperature versus $\alpha_{1/2}$ in fig. 5.15. The vertical axis here is taken to be either α_1 or α_2 in units of μ. The blue dots are the numerical critical temperatures with only α_2, the black triangles are the numerics for α_1. The solid orange line is the analytics for α_2 and the dashed red line is the analytical result for α_1. Again we note good agreement between numerics and analytics with $T/\mu > 1/100$. As mentioned previously the

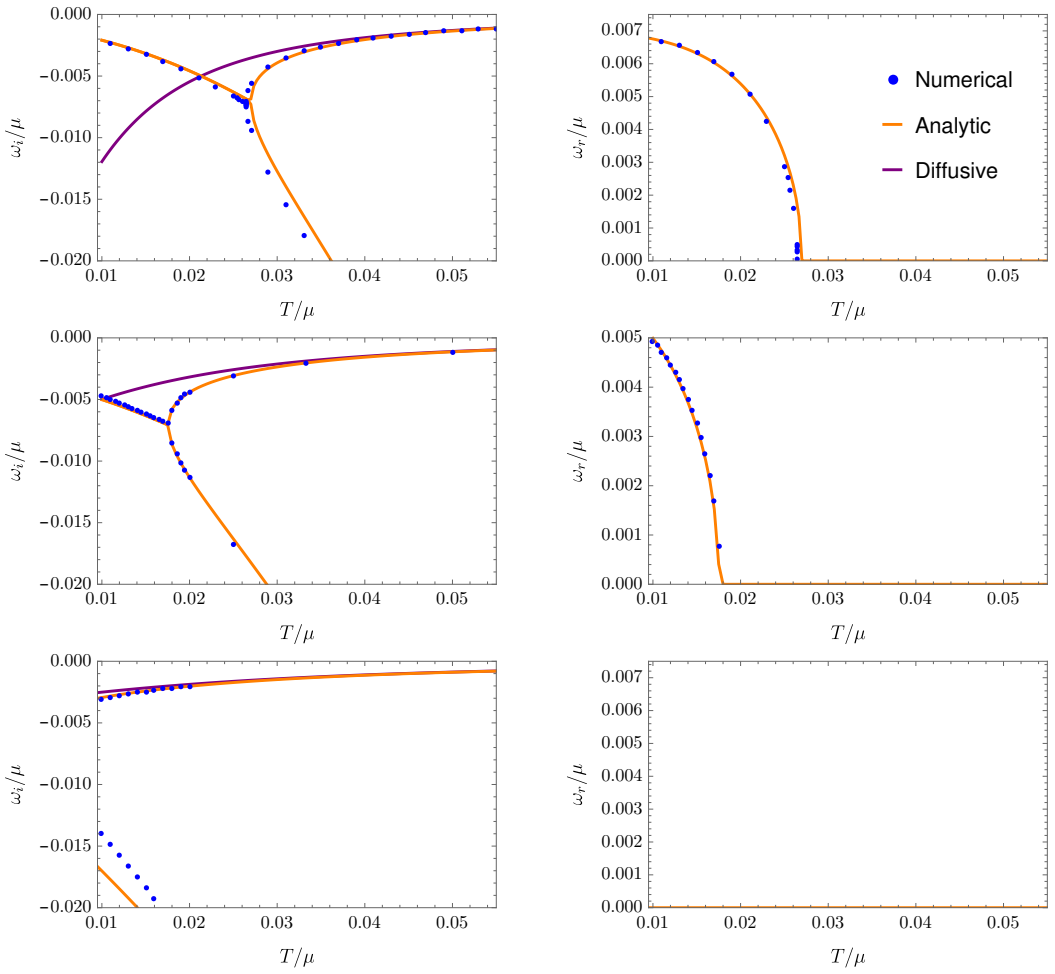

FIGURE 5.14: Analytic and numeric comparison for $\alpha_2 = \frac{-1}{200}, \frac{-1}{50}, \frac{-1}{20}$. The left/right hand plots show the imaginary/real components of the QNM.

'strength' of α_2 is greater than that of α_1 and the net effect of the explicit symmetry breaking is to lower the critical temperature. The numerics and analytics presented here are not restricted to the case of $\alpha_{1/2} = 0$. 3D plots can be constructed with both $\alpha_{1/2}$, again showing agreement between numerics and analytics.

To summerise, the effect of the explicit symmetry breaking parameters are to damp the holographic zero mode. With enough symmetry breaking the mode will stop propagating and move toward the diffusive pole. With larger symmetry breaking the critical temperature is reduced, and eventually with enough symmetry breaking there are no propagating modes at any temperature.

5.4.4 Conductivity

In this section we present the effect that explicit symmetry breaking has on AC and DC conductivity. We start with the AC conductivity:

$$\sigma_{AC} = -\frac{i}{\omega} G_{xx} = -\frac{i}{\omega}\omega^2 \frac{\delta^2 S}{\delta E^2} = -i\omega\Pi \tag{5.4.71}$$

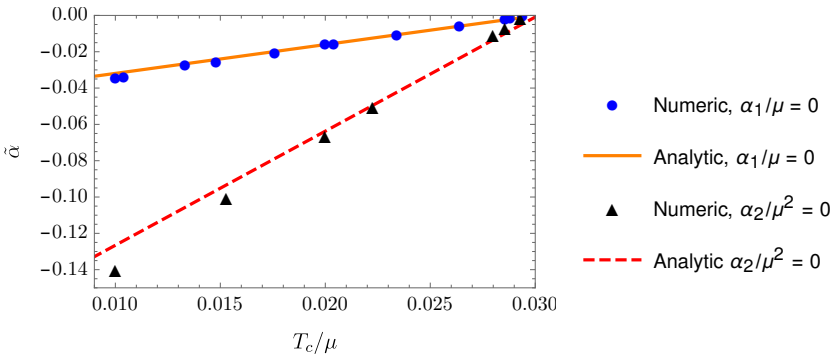

FIGURE 5.15: Numeric and analytic critical temperature. $\tilde{\alpha}$ is the dimensionless α's, that is both α_1/μ and α_2/μ^2.

where the Greens function is defined in (5.4.70). From the electric field's EOM we can obtain numerical results for the AC conductivity by setting $k = 0$. In Fig 5.16 we show the case with no α's at a temperature of $T/\mu = 1/50$. The left/right plots are the real/imaginary parts of the conductivity, and the solid blue line is the numerical result. To confirm our numerics we also include two analytic calculations. The first is from the analytic DC conductivity (calculated in the next section) that takes a normalised value of 48.696 and is labelled as a black dot in the figure with excellent agreement with the numerical solution when $\omega_{Re} \to 0$. The second is from a low frequency, low temperature analytic result for the AC conductivity [160]. At low temperature and at $k = 0$ Π is derived as,

$$\Pi = -\frac{2d\Gamma(\frac{1}{2})\Gamma(\frac{3}{2})}{\pi}\frac{\mathcal{N}}{i\omega^3 + \omega^2\beta} \tag{5.4.72}$$

where

$$\beta = \frac{d^{1/2}}{2\pi}\Gamma\left(\frac{1}{2}\right)\Gamma\left(\frac{3}{2}\right)B\left(\frac{1}{4},\frac{1}{4}\right) \tag{5.4.73}$$

Therefore the AC conductivity becomes,

$$\sigma_{AC} = i\mathcal{N}\frac{2d\Gamma(\frac{1}{2})\Gamma(\frac{3}{2})}{\pi}\frac{\omega}{i\omega^3 + \omega^2\beta} \tag{5.4.74}$$

That can be expanded at low frequency,

$$\frac{\sigma_{AC}}{\mathcal{N}} = i\frac{A}{\beta\omega} + \frac{A}{\beta^2} + \mathcal{O}(\omega) \tag{5.4.75}$$

with $A = \frac{2\tilde{d}\Gamma(\frac{1}{2})\Gamma(\frac{3}{2})}{\pi}$. This low frequency, low temperature result is plotted in dashed orange in Fig 5.16. We see that the analytic AC results agree with the numerics except at very small frequency where the analytic result diverges. This confirms the statement of the different limits in [160]: the $\omega \to 0$ and $T \to 0$ limits do not commute. The DC analytics are calculated taking $\omega \to 0$ first (the collision dominated limit

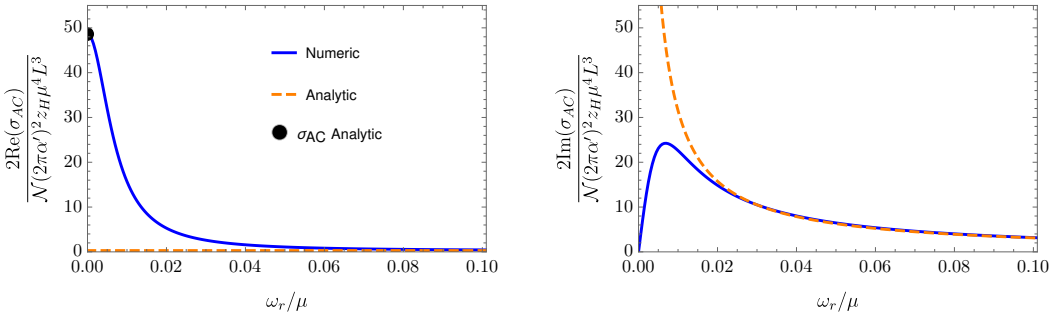

FIGURE 5.16: Real and Imaginary conductivity for $\frac{T}{\mu} = \frac{1}{50}$ and no explicit symmetry breaking. DC conductivity is 48.696.

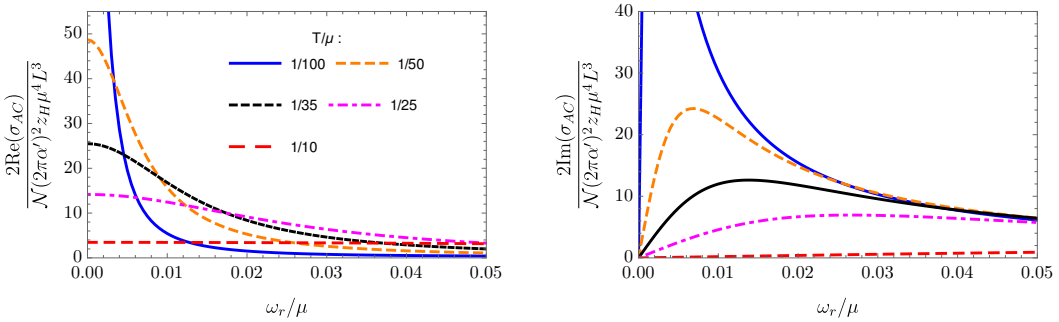

FIGURE 5.17: $\alpha_1/\mu = \alpha_2/\mu^2 = 0$

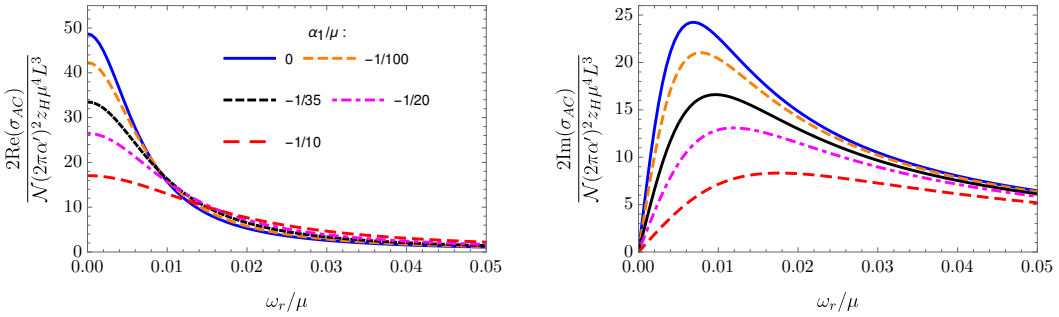

FIGURE 5.18: $\alpha_2 = 0$ AC conductivity at varying α_1 values at $T = \frac{1}{50}$

$\omega/T \to 0$) whereas the AC conductivity takes $T \to 0$ first (the collisionless limit $\omega/T \to \infty$). The numerical solution interpolates well between these two limits.

Before turning on the α's we first take a look at the effect that temperature has on the AC conductivity in fig. 5.17. We first note that the high frequency limit is largely independent of the temperature. At lower frequencies we see that as temperature is increased the imaginary component approaches zero, whereas the real part approaches a lower bound. For a discussion on lower bounds in probe brane systems see [189, 190] where it is conjectured that $\sigma \geq 1$ in appropriate units.

We turn on the symmetry breaking factors in Fig 5.18, Fig 5.19 and Fig 5.20. Fig 5.18 and Fig 5.19 are both at a fixed temperature of $T/\mu = 1/50$ with varying α_1/μ

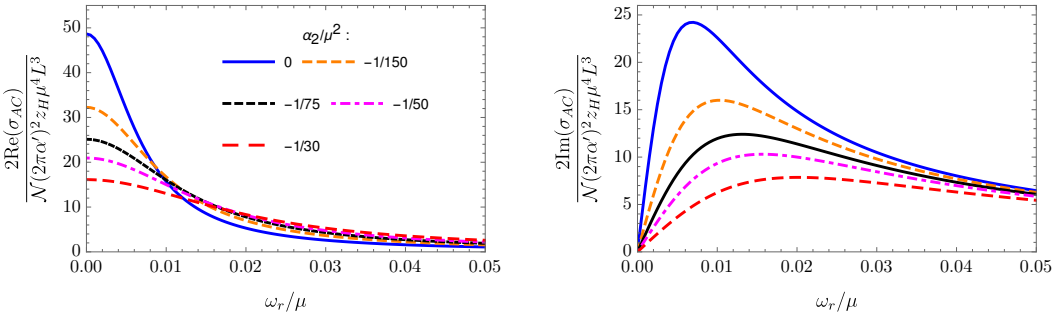

FIGURE 5.19: $\alpha_1 = 0$ AC conductivity at varying α_2 values at $T = \frac{1}{50}$

and α_2/μ^2 respectively. The effect is the same as with increasing temperature, that is the real and imaginary parts of the conductivity are decreased. In Fig 5.20 we plot various temperatures with four fixed α_2/μ^2 values, $-1/10, -1/5, -1, -5$. At extremely high α_2 values we see that the result is independent of temperature and the conductivity saturates the bound outlined above.

From [191] the DC conductivity for a probe brane in a (2+1)-dimensional field theory is:

$$\sigma_{DC} = \mathcal{N}\sqrt{1 + d^2 z^4} \tag{5.4.76}$$

The left/right plots in fig. 5.21 plot the DC conductivity against $\alpha_1\mu$ and α_2/μ^2 respectively at different temperature values. Fig 5.22 shows the opposite, the x-axis is now temperature and the left/right plots are with various fixed α_1/μ and α_2/μ^2 values. We see that the behaviour is the same as in the AC conductivity: increasing the symmetry breaking factors and/or temperature lowers the DC conductivity. We have also checked that in all the AC conductivity plots, the $\omega_{Re} \to 0$ limit matches the DC values in this section.

5.5 Discussion

In this chapter we have investigated the effect that translational symmetry breaking has on the current-current two point probe sound modes, namely the holographic zero sound mode and the diffusive mode. Specifically, we have been interested in the thermo-collisionless to hydrodynamic crossover. We found that the dispersion relation for HZS mode takes the form of a damped harmonic oscillator with k-gap given by $k_g = 1/2v\tau$. We also found the analytic form of the relaxation timescale τ by comparing expressions derived from a gradient expansion electric field, $\mathcal{E}$ with a linearised fluctuation electric field E. In section 5.4.1 we also looked at the allowed values of the α's, bounded by temperature and null-energy constraints. In appendix 5.B we outlined the necessary holographic renormalisation contributions required to make the DBI action finite.

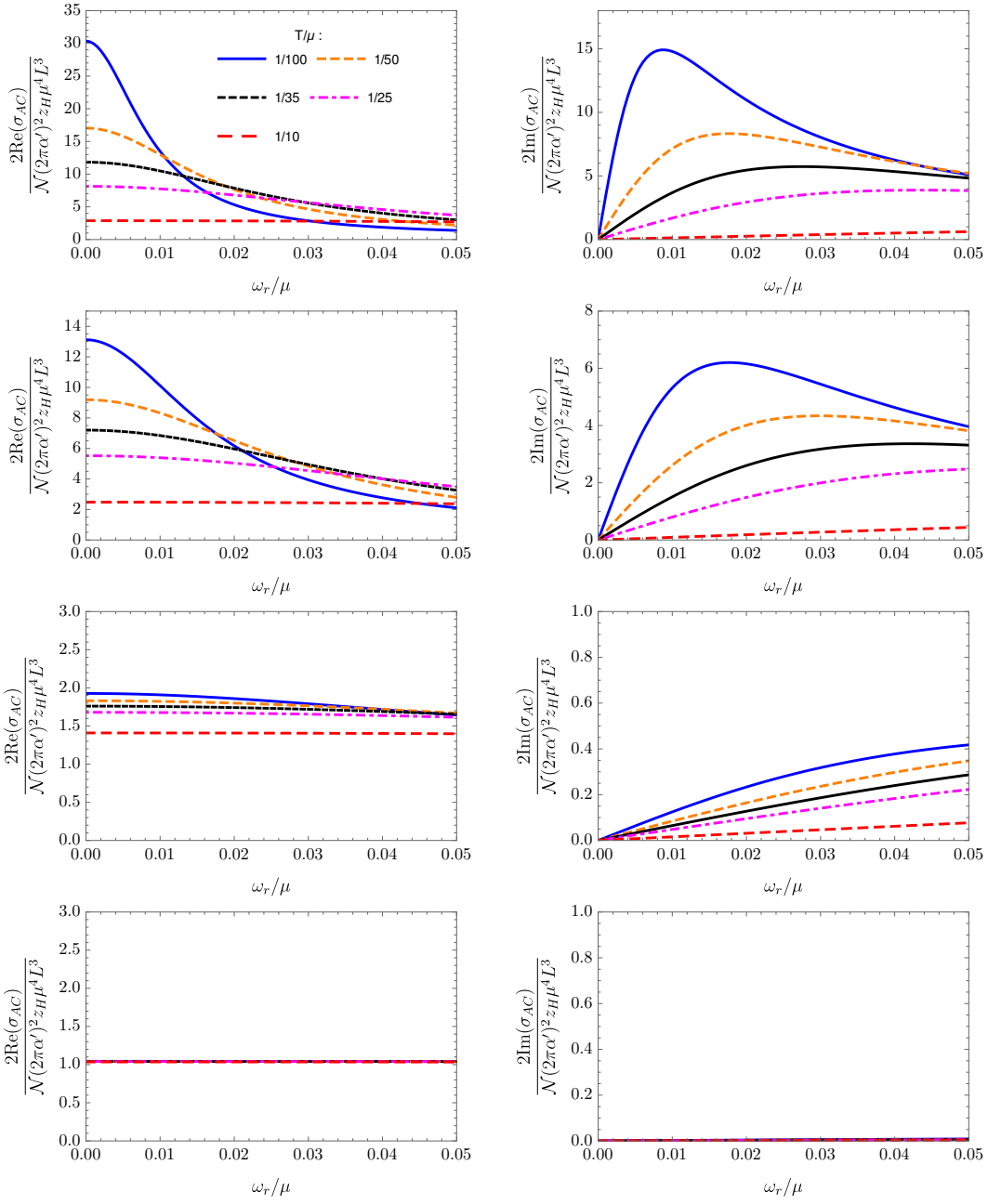

FIGURE 5.20: AC conductivity, varying temperature with $\alpha_2/\mu^2 = 0$ and $\alpha_1/\mu = -1/10, -1/5, -1, -5$

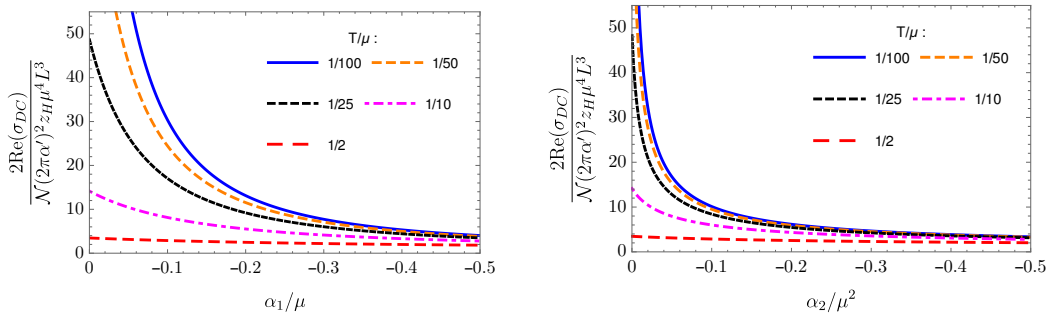

FIGURE 5.21: DC conductivity at $k = 0$. The left/right plots show the DC conductivity as a function of $\alpha_1/\mu/\alpha_2/\mu^2$ respectively at various fixed temperatures.

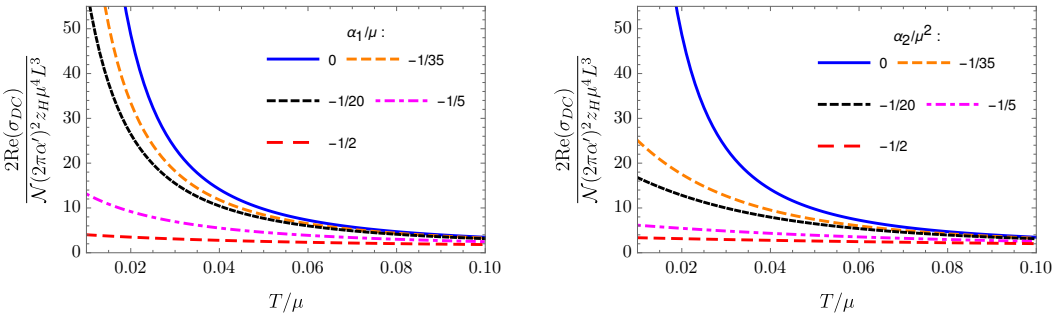

FIGURE 5.22: DC conductivity at $k = 0$ as a function of temperature. The left hand plot

In particular, we found that for fixed α's, k_g increases as T/μ increases, as expected. For fixed T/μ, k_g increases as the α's increase. As a result, even with fixed T/μ, as the α's increase, the transition occurs, that is the sound modes stop propagating. Furthermore the diffusive constant D decreases as the α's increase, as does the AC and DC conductivities until they saturate the lower bound. In summary, all the results we have found agree with the intuition of a momentum dissipating system.

The results we have found have been focused on the thermo-collisonless to hydrodynamic crossover. It would also be interesting to study the transition to the quantum collisionless regime at low temperatures, as well as the zero temperature result where a horizon would persist due to the α's contribution to the emblackening factor in eq. (5.4.16). Since the horizonless case involved the matching of a sub-leading $1/z_H$ terms, it is possible that extending the horizon case to that order would produce the necessary extra contributions to extend the analytic results into low temperature. This would most likely require solving eq. (5.4.51) in its full form. Furthermore, we have used a conformal value of $1/2$ for v^2 throughout, however at non-zero T, α's we might find that we depart from this value. Since the dispersion relation depends on the value of v^2 as well as τ, more accurate analytics could be found. Finally, taking motivation from chapter 3 it could be of interest to plot the phase diagram for this

model, this could be achieved by simply including the D7 embedding function in the DBI action.

5.A Holographic TSB Models

In this appendix we give some more details of previous holographic translational symmetry breaking models.

dRGT Massive Gravity

In de Rham, Gabadadze, Tolley (dRGT) massive gravity [192], the graviton is given a mass term such that it breaks the bulk diffeomorphisms while avoiding the difficulties normally associated with massive gravity (i.e ghosts). It has subsequently been studied holographically [20, 19]. For the case of AdS_4 dual to a 3d field theory, the dRGT action is given by an Einstein-Maxwell term plus a massive gravity term,

$$S_{Bulk} = \frac{1}{16\pi G_N}\int d^4x\sqrt{-g}\left[R - 2\Lambda - \frac{L^2}{4}\mathcal{F}^2 + M^2\sum_{i=1}^{4} C_i\mathcal{U}_i\right] \tag{5.5.77}$$

$$ds^2 = \frac{L^2}{z^2}\left(\frac{dz^2}{f(z)} - f(z)dt^2 + dx^2 + dy^2\right) \tag{5.5.78}$$

$$f(z) = 1 + C_1\frac{LM^2}{2}z + C_2M^2z^2 - mz^3 + \frac{\mu_B z^4}{4z_H^2} \tag{5.5.79}$$

where $\Lambda = -d(d-1)/2L^2 = -6/L^2$ is the cosmological constant, $\mathcal{F}$ is a background electromagnetic tensor, R is the Ricci scalar, M is a dimension 1 term that can be related to the graviton mass and the C_i are dimensionless constants. The massive gravity term is made up of polynomials $\mathcal{U}_i$,

$$\begin{aligned}
\mathcal{U}_1 &= [\mathcal{K}] \\
\mathcal{U}_2 &= [\mathcal{K}]^2 - [\mathcal{K}^2] \\
\mathcal{U}_3 &= [\mathcal{K}]^3 - 3[\mathcal{K}][\mathcal{K}^2] + 2[\mathcal{K}^3] \\
\mathcal{U}_4 &= [\mathcal{K}]^4 - 6[\mathcal{K}^2][\mathcal{K}]^2 + 8[\mathcal{K}^3][\mathcal{K}] + 3[\mathcal{K}^2]^2 - 6[\mathcal{K}^4]
\end{aligned} \tag{5.5.80}$$

where $\mathcal{K} = \sqrt{g^{\mu\alpha}}\sqrt{f_{\alpha\nu}}$ and $f_{\mu\nu} = \partial_\mu\phi^a\partial_\nu\phi^b\eta_{ab}$ is called the reference metric. To make sure we only break the spatial diffeomorphism, and to keep the model simple, the scalar fields are set to be $\phi^x = x$ and $\phi^y = y$, such that the reference metric reads $(0,0,1,1)$ in the (t,z,x,y) basis. For this model $\mathcal{U}_3$ and $\mathcal{U}_4$ are zero, $\mathcal{U}_1 = 2z/L$ and $\mathcal{U}_2 = 2z^2/L^2$. Therefore the mass term becomes,

$$M^2(C_1\mathcal{U}_1 + C_2\mathcal{U}_2) = M^2C_1\frac{2z}{L} + M^2C_2\frac{2z^2}{L^2} \tag{5.5.81}$$

If we define dimensionful parameters as,

$$\alpha_1 = C_1\frac{LM^2}{2} \qquad \alpha_2 = C_2M^2 \tag{5.5.82}$$

and set $\mu_B = 0$ we then get the emblackening factor defined in (5.4.16), with $[\alpha_1] = 1$ and $[\alpha_2] = 2$.

Stuckleberg Fields

An alternative method [21] is to look at what the stress energy tensor looks like when massless scalar fields linear in a CFT spatial coordinate are introduced.

$$\nabla\langle T^{ij}\rangle = \nabla^j \psi^{(0)}\langle \mathcal{O}\rangle + F^{(0)ij}\langle J_i\rangle \tag{5.5.83}$$

where the first term is the coupling between an operator that is sourced by the scalar field, and the second term is if a gauge field is turned on in the bulk. The reason the scalar fields are restricted is to keep the model simple, that is to make sure that the tensor does not depend on the boundary coordinates and that the metric remains translationally invariant. The holographic action used is then given by,

$$S_{Bulk} = \frac{1}{16\pi G_N}\int d^4x\sqrt{-g}\Big[R - 2\Lambda - \frac{L^2}{4}\mathcal{F}^2 - \frac{L^2}{2}\sum_I^2(\partial\psi_I)^2\Big] \tag{5.5.84}$$

$$ds^2 = \frac{L^2}{z^2}\left(\frac{dz^2}{f(z)} - f(z)dt^2 + dx^2 + dy^2\right) \qquad \psi_I = \beta_{Ia}x^a \tag{5.5.85}$$

$$f(z) = 1 - \frac{1}{2}\beta^2 L^2 z^2 - mz^3 + \frac{\mu_B^2 z^4}{4z_H^2} \tag{5.5.86}$$

where

$$\beta^2 \equiv \frac{1}{2}\sum_a^2\sum_I \beta_{Ia}\beta_{Ib} \tag{5.5.87}$$

This looks simlar to the metric we have before but now with $\alpha_1 = 0$ and $\alpha_2 = -\beta^2 L^2/2$. The emblackening factor becomes,

$$f(z) = 1 + \alpha_2 z^2 - mz^3 + \frac{\mu_B^2 z^4}{4z_H^2} \tag{5.5.88}$$

It should therefore be possible to cast the momentum dissipating term, $\alpha_2 = -\beta^2 L^2/2$, in terms of the notation used in the dGRT model. Noting the following,

$$
\begin{aligned}
-\frac{L^2}{2}\sum_{I=1}^{2}\Big(\partial\psi_I\Big)^2 &= -\frac{L^2}{2}\sum_{I=1}^{2} g^{\mu\nu}\partial_\mu\psi_I\partial_\nu\psi_I \\
&= -\frac{L^2}{2}g^{\mu\mu}\Big(\partial_\mu(\beta_{1a}\phi^a)\partial_\mu(\beta_{1a}\phi^a)+\partial_\mu(\beta_{2a}\phi^a)\partial_\mu(\beta_{2a}\phi^a)\Big) \\
&= -\frac{L^2}{2}g^{\mu\mu}\Big(\beta_{1a}\beta_{1a}\partial_\mu(\phi^a)\partial_\mu(\phi^a)+\beta_{2a}\beta_{2a}\partial_\mu(\phi^a)\partial_\mu(\phi^a)\Big) \\
&= -\frac{L^2}{2}g^{\mu\mu}\beta^2\partial_\mu\phi^a\partial_\mu\phi^a \\
&= -\frac{1}{2}L^2\beta^2[g^{xx}\partial_x\phi^a\partial_x\phi^a+g^{yy}\partial_y\phi^a\partial_y\phi^a] \\
&= \alpha_2\frac{2z^2}{L^2} \\
&= M^2C_2\mathcal{U}_2
\end{aligned}
\tag{5.5.89}
$$

where we have used that $-\frac{1}{2}L^2\beta^2=\alpha_2=M^2C_2$, $\beta_{1a}\beta_{1a}+\beta_{2a}\beta_{2a}=\sum_I^2\beta_{Ia}\beta_{Ia}=\overline{\beta}_a\cdot\overline{\beta}_a=\beta^2$ and $g^{ii}=z^2/L^2$ we do indeed see that the two models are related.

5.B Holographic Renormalisation

In this appendix we perform the holographic renormalisation of the action S in eq. (5.4.17) in the background spacetime with metric in eq. (5.4.16). More specifically, we determine the counterterm action, $S_{\rm CT}$, localised on the cutoff surface $z=\varepsilon$, as mentioned in sec. 5.4.1. In principle we could fix $S_{\rm CT}$ by demanding a well-posed variational problem [184, 185, 186, 147, 187], however, by exploiting a special feature of our system we have found a simple argument that gives $S_{\rm CT}$ easily, as follows.

The key observation is that when the field strength vanishes, $F_{ab}=0$, the action S of the space-filling brane can be viewed as a contribution to the cosmological constant. We may thus use known results for the counterterms of a bulk theory that gives rise to the metric in eq. (5.4.16), split that theory's cosmological constant into "background" and "brane" contributions, with the latter proportional to the branes prefactor, $\mathcal{N}$, and then take a probe limit, meaning expand in $\mathcal{N}$ and retain the terms $\propto\mathcal{N}$. The order $\mathcal{N}$ counterterms that we obtain must be our $S_{\rm CT}$ for the probe brane action S. Since F_{ab} will play no role in what follows, and in particular our non-zero F_{zt} makes no contributions to the $z=\varepsilon$ endpoint of integration in S, we will set $F_{ab}=0$ in the rest of this appendix.

The background dRGT massive gravity action (5.5.77) must be amended by two types of terms at the $z=\varepsilon$ surface. First is the Gibbons-Hawking term,

$$
S_{\rm GH}=-\frac{2}{16\pi G_N}\int_{z=\varepsilon}d^3x\,\sqrt{-\gamma}\,K, \tag{5.5.90}
$$

where $\gamma \equiv \det(\gamma_{ij})$ and K is the trace of the second fundamental form on the $z = \varepsilon$ surface (with outward-pointing normal vector). Second are the counterterms, which for massive gravity in $d = 4$ were determined by ref. [193, 194]:

$$S_{\rm CT}^{\rm grav} = -\frac{1}{16\pi G_N}\int_{z=\varepsilon} d^3x\,\sqrt{-\gamma}\,\left[\sum_{j=1}^{5}\mathcal{L}_j^{\rm grav}\right], \tag{5.5.91a}$$

$$\mathcal{L}_1^{\rm grav} = \frac{4}{\ell}, \qquad \mathcal{L}_2^{\rm grav} = \ell\, R_\gamma, \tag{5.5.91b}$$

$$\mathcal{L}_3^{\rm grav} = \frac{\ell}{2}M^2\,C_1\,\mathcal{U}_1, \qquad \mathcal{L}_4^{\rm grav} = \ell\,M^2\,C_2\,\mathcal{U}_2, \qquad \mathcal{L}_5^{\rm grav} = -\frac{\ell^3}{16}\,M^4\,C_1^2\,\mathcal{U}_2, \tag{5.5.91c}$$

where R_γ is the Ricci scalar computed from γ_{ij}. The counterterms in eq. (5.5.91b) are those required for holographic renormalisation of the Einstein-Hilbert action, while the counterterms in eq. (5.5.91c) are the "extra" counterterms required for massive gravity.

As mentioned above, our holographic renormalisation for the probe brane action begins with the observation that if we split the cosmological constant into two contributions,

$$\Lambda \equiv \Lambda' + (16\pi G_N)\,\mathcal{N}, \tag{5.5.92}$$

then the bulk action of massive gravity becomes

$$\begin{aligned} S_{\rm grav} &= \frac{1}{16\pi G_N}\int d^4x\sqrt{-g}\,\left(R - \Lambda' + M^2\,C_1\,\mathcal{U}_1 + M^2\,C_2\,\mathcal{U}_2\right) && \text{(5.5.93a)}\\ &- \mathcal{N}\int d^4x\sqrt{-g}, && \text{(5.5.93b)} \end{aligned}$$

where in the second line we recognise the probe brane action S in eq. (5.4.17), with $F_{ab} = 0$. We can correspondingly define a new radius of curvature, L,

$$\Lambda' \equiv -\frac{6}{L^2}, \tag{5.5.94}$$

so that eq. (5.5.92) becomes

$$-\frac{6}{\ell^2} = -\frac{6}{L^2} + (16\pi G_N)\,\mathcal{N}, \tag{5.5.95}$$

or equivalently,

$$\ell = L\left(1 - \frac{L^2}{6}\,(16\pi G_N)\,\mathcal{N}\right)^{-1/2}. \tag{5.5.96}$$

As mentioned previously, the probe limit consists of expanding in $(16\pi G_N)\,\mathcal{N} \ll 1$ and retaining the leading contribution in $\mathcal{N}$. Expanding eq. (5.5.96) in the probe limit gives

$$\ell = L + \frac{L^3}{12}\,(16\pi G_N)\,\mathcal{N} + \mathcal{O}\left(((16\pi G_N)\,\mathcal{N})^2\right). \tag{5.5.97}$$

To obtain the counterterms for the probe brane, we simply plug the probe limit

expansion for ℓ in eq. (5.5.97) into the counterterms for massive gravity, eq. (5.5.91), and extract the terms $\propto \mathcal{N}$, with the result

$$S_{\rm CT} = -\mathcal{N}\int_{z=\varepsilon} d^3x\,\sqrt{-\gamma}\,\left[\sum_{j=1}^{5}\mathcal{L}_j\right], \tag{5.5.98a}$$

$$\mathcal{L}_1 = -\frac{L}{3}, \qquad \mathcal{L}_2 = \frac{L^3}{12}R_\gamma, \tag{5.5.98b}$$

$$\mathcal{L}_3 = \frac{L^3}{24}M^2\,C_1\,\mathcal{U}_1, \qquad \mathcal{L}_4 = \frac{L^3}{12}M^2\,C_2\,\mathcal{U}_2, \qquad \mathcal{L}_5 = -\frac{L^5}{64}M^4\,C_1^2\,\mathcal{U}_2. \tag{5.5.98c}$$

The counterterms in eq. (5.5.98b) are those required for holographic renormalisation of a spacetime-filling probe brane in Einstein-Hilbert gravity [147], while the counterterms in eq. (5.5.98c) are the "extra" counterterms required for a probe brane in massive gravity.

The counterterms in eq. (5.5.98) are the main result of this appendix. They are applicable to any spacetime-filling probe brane with action of the form in eq. (5.4.17), with $F_{ab} = 0$, in any asymptotically AdS_4 solution of the massive gravity theory of eq. (5.5.78). They are also applicable to probe branes in solutions of massive gravity that can be mapped to other systems, such as massless scalar or two-form fields linear in a CFT spatial coordinate [21, 195, 22], and to probe branes whose F_{ab} is non-zero but decays sufficiently quickly asymptotically as to not introduce further divergences when $z \to 0$.

Restricting the solutions to the case we investigated, that is with a reference metric of $f_{\mu\nu} = \mathrm{diag}(0,0,1,1)$ where only $\mathcal{U}_{1/2}$ survive and using the dimensionful paramters α_1 and α_2, we have that the regulated on-shell probe brane action is then

$$S_{\rm reg} = -\mathcal{N}\int d^4x\sqrt{-g} = -\mathcal{N}\int d^3x\int_\varepsilon^{z_H} dz\,\frac{L^4}{z^4} = -\mathcal{N}\int d^3x\,\frac{L^4}{3}\left(\frac{1}{\varepsilon^3}-\frac{1}{z_H^3}\right), \tag{5.5.99}$$

where, as mentioned in sec. 5.4.2, the term $-\mathcal{N}\frac{L^4}{3}\frac{1}{\varepsilon^3}$ that diverges as $\varepsilon \to 0$ is independent of T, α_1, and α_2. On the $z = \varepsilon$ surface we then have

$$\gamma_{ij} = \frac{L^2}{\varepsilon^2}\,\mathrm{diag}\left(-f(\varepsilon),1,1\right)_{ij}, \tag{5.5.100a}$$

$$\sqrt{-\gamma} = \frac{1}{\varepsilon^3}L^3 + \frac{1}{\varepsilon^2}\frac{L^3}{2}\alpha_1 - \frac{1}{\varepsilon}\frac{L^3}{8}\left(\alpha_1^2-4\alpha_2\right) + \frac{L^3}{16}\left(\alpha_1^3-4\alpha_1\alpha_2-8m\right)+\mathcal{O}\left(\varepsilon\right), \tag{5.5.100b}$$

and $R_\gamma = 0$. Plugging our values for the symmetry breaking factors eq. (5.5.82) as well as using $\mathcal{U}_1 = 2z/L$ and $\mathcal{U}_2 = 2z^2/L^2$ into eq. (5.5.98), we thus find the counterterms

that renormalise the probe brane action in this case:

$$S_{\rm CT} = \sum_{j=1}^{5} S_j, \tag{5.5.101a}$$

$$S_1 = -\mathcal{N}\int d^3x\sqrt{-\gamma}\left(-\frac{L}{3}\right) \tag{5.5.101b}$$

$$= -\mathcal{N}\int d^3x\left(-\frac{1}{\varepsilon^3}\frac{L^4}{3}-\frac{1}{\varepsilon^2}\frac{L^4}{6}\alpha_1+\frac{1}{\varepsilon}\frac{L^4}{24}\left(\alpha_1^2-4\alpha_2\right)-\frac{L^4}{48}\left(\alpha_1^3-4\alpha_1\alpha_2-8m\right)+\mathcal{O}\left(\varepsilon\right)\right),$$

$$S_2 = -\mathcal{N}\int d^3x\sqrt{-\gamma}\left(\frac{L^3}{12}R_\gamma\right)=0, \tag{5.5.101c}$$

$$S_3 = -\mathcal{N}\int d^3x\sqrt{-\gamma}\left(\frac{L^3}{24}M^2C_1\mathcal{U}_1\right), \tag{5.5.101d}$$

$$= -\mathcal{N}\int d^3x\left(\frac{1}{\varepsilon^2}\frac{L^4}{6}\alpha_1+\frac{1}{\varepsilon}\frac{L^4}{12}\alpha_1^2-\frac{L^4}{48}\alpha_1\left(\alpha_1^2-4\alpha_2\right)+\mathcal{O}\left(\varepsilon\right)\right), \tag{5.5.101e}$$

$$S_4 = -\mathcal{N}\int d^3x\sqrt{-\gamma}\left(\frac{L^3}{12}M^2C_2\mathcal{U}_2\right), \tag{5.5.101f}$$

$$= -\mathcal{N}\int d^3x\left(\frac{1}{\varepsilon}\frac{L^4}{6}\alpha_2+\frac{L^4}{12}\alpha_1\alpha_2+\mathcal{O}\left(\varepsilon\right)\right), \tag{5.5.101g}$$

$$S_5 = -\mathcal{N}\int d^3x\sqrt{-\gamma}\left(-\frac{L^5}{64}M^4C_1^2\mathcal{U}_2\right) \tag{5.5.101h}$$

$$= -\mathcal{N}\int d^3x\left(-\frac{1}{\varepsilon}\frac{L^4}{8}\alpha_1^2-\frac{L^4}{16}\alpha_1^3+\mathcal{O}\left(\varepsilon\right)\right). \tag{5.5.101i}$$

As mentioned in sec. 5.4.2, the volume counterterm, S_1, cancels the divergence in the bulk action but also includes divergences of lower order in $1/\varepsilon$ whose coefficients are non-zero when $\alpha_1 \neq 0$ and/or $\alpha_1 \neq 0$. The latter are cancelled by the other counterterms, and specifically the order $1/\varepsilon^2$ divergences cancel between S_1 and S_3 while the order $1/\varepsilon$ divergences cancel among S_1, S_3, S_4, and S_5. All of the counterterms also contribute terms that remain finite as $\varepsilon \to 0$. Adding eq. (5.5.99) for $S_{\rm reg}$ and eq. (5.5.101) for $S_{\rm CT}$, and taking the $\varepsilon \to 0$ limit, we find for the renormalised on-shell probe brane action

$$S_{\rm ren} = \lim_{\varepsilon\to 0}\left(S_{\rm reg}+S_{\rm CT}\right) \tag{5.5.102a}$$

$$= -\mathcal{N}\int d^3x\left(-\frac{L^4}{3}\frac{1}{z_H^3}-\frac{5L^4}{48}\alpha_1^3+\frac{L^4}{4}\alpha_1\alpha_2+\frac{L^4}{6}m\right). \tag{5.5.102b}$$

Chapter 6

Conclusions

Thales took us to Democritus took us to Dalton took us to Feynman, and in the search for the Fundamental a most miraculous duality was discovered. If one went looking for such a duality at the outset, it seems unlikely that it would ever have been found. It is almost inconceivable [1] that a CFT without gravity in a lower dimension can be related to a quantum theory of gravity, and moreover that that quantum theory arises simply from studying what happens to pieces of string. It is hard to imagine what would be more surreal, that the Fundamental is a piece of string, or that the whole of string theory mathematically exists but is not realised in nature, that the duality does not exist.

However, from what we have seen in this thesis there is strong evidence that it does indeed exist. Leaving the question of what CFT we have aside, we have seen remarkable cross-disciplanarity that even the most synergy mad politician would be proud of. We have seen that chiral symmetry can be related to D-branes bulking in the bulk, Weyl semi-metal phase transitions analogous to whether a D-brane falls into a black hole or not and simulating momentum dissipation in lattice systems by turning on a graviton mass. To pull together experts from various fields is one of the dualities greatest achievments, that string theoriest and black hole experts can feature in the same conference alongside condensed matter physicists, phenomenologists, quantum computer scientists and AI magicians. It seems natural to conclude that only with such an array of expertise will humanity make tractable progress towards the Fundamental.

How then can the duality be improved upon? First, as we have seen in this thesis, the quest for universalities and exploring the possibilities of duality models will go on. For example - adding confinement to the model in chapter 3 or exploring the neutron star phase of the QCD phase diagram, where strongly coupled deconfined quarks might exist; or that the symmetry breaking model of chapter 5 could be combined with the analysis of chapter 3 to produce crystalline phase structures; or exploring the quasi-normal mode spectrum of the Weyl semi-metal of chapter 4 to quantify the odd peaks seen in the conductivity and the exponentially decaying

[1] We have checked that this is the correct use of the word.

solutions. Even if we do not arrive at univeralities, such exploration can nevertheless pave the way to new ideas and directions of research for theoreticians and experamentalists alike.

Second, is the study of the duality itself. A major step forward would be to prove which CFTs (and deformations thereof) give rise to holographic duals [196]. Improving our understanding of string theory and moving away from the vanishing g_s and α' would also allow for a greater exploration of the parameter space of the dual field theory, perhaps attainable through the study of bulk amplitudes [197].

Recently, new directions of collaboration have emerged, such as the view that holography is related to quantum error correction code [198], and that using ideas from the duality, if not the duality itself, can make progress in old problems such as the Hawking-Page curve [199, 200].

The duality has proven to be one of the most incredible discovories of the late twentith century and shows no signs of slowing down in the twenty-first. It once again shows that we simple do not know where the next advancement might come from and often stumple across it in our ignorance - hence the everlasting need to study the elusive Fundamental for its own sake, and from it who knows what might be found. It is difficult to pose the correct question that will reveal all of nature in one swoop, instead it is often better simply to be curious and then tenacious.

References

[1] D. Mateos, R. C. Myers and R. M. Thomson, *Thermodynamics of the brane*, *JHEP* **05** (2007) 067, [hep-th/0701132].

[2] MUON $g-2$ COLLABORATION collaboration, B. Abi, T. Albahri, S. Al-Kilani, D. Allspach, L. P. Alonzi, A. Anastasi et al., *Measurement of the positive muon anomalous magnetic moment to 0.46 ppm*, *Phys. Rev. Lett.* **126** (Apr, 2021) 141801.

[3] L. collaboration, R. Aaij, C. A. Beteta, T. Ackernley, B. Adeva, M. Adinolfi et al., *Test of lepton universality in beauty-quark decays*, 2021.

[4] G. Hooft, *A planar diagram theory for strong interactions*, *Nuclear Physics B* **72** (1974) 461–473.

[5] L. Susskind, *The world as a hologram*, *Journal of Mathematical Physics* **36** (Nov, 1995) 6377–6396.

[6] J. M. Maldacena, *The Large N limit of superconformal field theories and supergravity*, *Int. J. Theor. Phys.* **38** (1999) 1113–1133, [hep-th/9711200].

[7] J. Rafelski, *Melting hadrons, boiling quarks*, *The European Physical Journal A* **51** (Sep, 2015) .

[8] C. Ratti, *Lattice qcd and heavy ion collisions: a review of recent progress*, *Reports on Progress in Physics* **81** (Jul, 2018) 084301.

[9] M. Stephanov, K. Rajagopal and E. Shuryak, *Signatures of the tricritical point in qcd*, *Physical Review Letters* **81** (Nov, 1998) 4816–4819.

[10] S.-Y. Xu, I. Belopolski, N. Alidoust, M. Neupane, G. Bian, C. Zhang et al., *Discovery of a Weyl fermion semimetal and topological Fermi arcs*, *Science* **349** (Aug., 2015) 613–617, [1502.03807].

[11] L. Lu, Z. Wang, D. Ye, L. Ran, L. Fu, J. D. Joannopoulos et al., *Experimental observation of Weyl points*, *Science* **349** (Aug., 2015) 622–624, [1502.03438].

[12] B. Q. Lv, H. M. Weng, B. B. Fu, X. P. Wang, H. Miao, J. Ma et al., *Experimental Discovery of Weyl Semimetal TaAs*, *Physical Review X* **5** (July, 2015) 031013, [1502.04684].

[13] B. Q. Lv, N. Xu, H. M. Weng, J. Z. Ma, P. Richard, X. C. Huang et al., *Observation of Weyl nodes in TaAs*, *Nature Physics* **11** (Sept., 2015) 724–727, [1503.09188].

[14] K. Landsteiner and Y. Liu, *The holographic Weyl semi-metal*, *Phys. Lett. B* **753** (2016) 453–457, [1505.04772].

[15] K. Landsteiner, Y. Liu and Y.-W. Sun, *Quantum phase transition between a topological and a trivial semimetal from holography*, *Phys. Rev. Lett.* **116** (2016) 081602, [1511.05505].

[16] A. Karch, D. T. Son and A. O. Starinets, *Holographic quantum liquid*, *Physical Review Letters* **102** (Feb, 2009) .

[17] E. Lifshitz and L. Pitaevskii, *Statistical Physics: Theory of the Condensed State*. No. pt. 2 in Course of Theoretical Physics. Elsevier Science, 2013.

[18] P. Nozieres and D. Pines, *Theory Of Quantum Liquids*. Advanced Books Classics. Avalon Publishing, 1999.

[19] R. A. Davison, *Momentum relaxation in holographic massive gravity*, *Physical Review D* **88** (Oct, 2013) .

[20] D. Vegh, *Holography without translational symmetry*, 2013.

[21] T. Andrade and B. Withers, *A simple holographic model of momentum relaxation*, *Journal of High Energy Physics* **2014** (May, 2014) .

[22] S. Grozdanov and N. Poovuttikul, *Generalized global symmetries in states with dynamical defects: The case of the transverse sound in field theory and holography*, *Physical Review D* **97** (May, 2018) .

[23] C. Montonen and D. Olive, *Magnetic monopoles as gauge particles?*, *Physics Letters B* **72** (1977) 117–120.

[24] N. Seiberg, *Electric-magnetic duality in supersymmetric non-abelian gauge theories*, *Nuclear Physics B* **435** (Feb, 1995) 129–146.

[25] D. Tong, *Gauge theory*, 2018.

[26] D. Mateos, *String theory and quantum chromodynamics*, *Classical and Quantum Gravity* **24** (Oct, 2007) S713–S739.

[27] T.-P. Cheng, L.-F. Li and D. Gross, *Gauge theory of elementary particle physics*, *Physics Today - PHYS TODAY* **38** (12, 1985) .

[28] K. Becker, M. Becker and J. H. Schwarz, *String theory and M-theory: A modern introduction*. Cambridge University Press, 12, 2006.

[29] M. Ammon and J. Erdmenger, *Gauge/gravity duality: Foundations and applications*. Cambridge University Press, Cambridge, 4, 2015.

[30] O. Aharony, S. S. Gubser, J. Maldacena, H. Ooguri and Y. Oz, *Large n field theories, string theory and gravity*, *Physics Reports* **323** (Jan, 2000) 183–386.

[31] S. Gubser, I. R. Klebanov and A. M. Polyakov, *Gauge theory correlators from noncritical string theory*, *Phys. Lett. B* **428** (1998) 105–114, [hep-th/9802109].

[32] E. Witten, *Anti-de Sitter space and holography*, *Adv. Theor. Math. Phys.* **2** (1998) 253–291, [hep-th/9802150].

[33] E. Witten, *String theory dynamics in various dimensions*, *Nuclear Physics B* **443** (Jun, 1995) 85–126.

[34] P. Hořava and E. Witten, *Heterotic and type i string dynamics from eleven dimensions*, *Nuclear Physics B* **460** (Feb, 1996) 506–524.

[35] M. Duff and J. Lu, *The self-dual type iib superthreebrane*, *Physics Letters B* **273** (1991) 409–414.

[36] P. Ginsparg, *Applied conformal field theory*, 1988.

[37] C. Fefferman and C. R. Graham, *Conformal invariants*, in *Élie Cartan et les mathématiques d'aujourd'hui - Lyon, 25-29 juin 1984*, no. S131 in Astérisque. Société mathématique de France, 1985.

[38] I. R. Klebanov and E. Witten, *Ads/cft correspondence and symmetry breaking*, *Nuclear Physics B* **556** (Sep, 1999) 89–114.

[39] P. Breitenlohner and D. Z. Freedman, *Stability in gauged extended supergravity*, *Annals of Physics* **144** (1982) 249–281.

[40] P. Breitenlohner and D. Z. Freedman, *Positive energy in anti-de sitter backgrounds and gauged extended supergravity*, *Physics Letters B* **115** (1982) 197–201.

[41] S. S. Gubser, I. R. Klebanov and A. W. Peet, *Entropy and temperature of black 3-branes*, *Physical Review D* **54** (Sep, 1996) 3915–3919.

[42] E. Witten, *Anti-de Sitter space, thermal phase transition, and confinement in gauge theories*, *Adv. Theor. Math. Phys.* **2** (1998) 505–532, [hep-th/9803131].

[43] C. P. Burgess, N. R. Constable and R. C. Myers, *The free energy of n = 4 super-yang-mills and the ads/cft correspondence*, *Journal of High Energy Physics* **1999** (Aug, 1999) 017–017.

[44] A. Karch and E. Katz, *Adding flavor to AdS / CFT*, *JHEP* **06** (2002) 043, [hep-th/0205236].

[45] A. Karch and L. Randall, *Open and closed string interpretation of susy cft's on branes with boundaries*, *Journal of High Energy Physics* **2001** (Jun, 2001) 063–063.

[46] N. Evans, A. Gebauer, K.-Y. Kim and M. Magou, *Holographic description of the phase diagram of a chiral symmetry breaking gauge theory*, *Journal of High Energy Physics* **2010** (Mar, 2010) .

[47] D. Mateos, R. C. Myers and R. M. Thomson, *Holographic phase transitions with fundamental matter*, *Phys. Rev. Lett.* **97** (2006) 091601, [hep-th/0605046].

[48] S. A. Hartnoll, *Lectures on holographic methods for condensed matter physics*, *Classical and Quantum Gravity* **26** (Oct, 2009) 224002.

[49] D. T. Son and A. O. Starinets, *Minkowski space correlators in AdS / CFT correspondence: Recipe and applications*, *JHEP* **09** (2002) 042, [hep-th/0205051].

[50] C. Herzog and D. Son, *Schwinger-Keldysh propagators from AdS/CFT correspondence*, *JHEP* **03** (2003) 046, [hep-th/0212072].

[51] K. Skenderis, *Lecture notes on holographic renormalization*, *Classical and Quantum Gravity* **19** (Nov, 2002) 5849–5876.

[52] S. de Haro, K. Skenderis and S. N. Solodukhin, *Holographic reconstruction of spacetime¶and renormalization in the ads/cft correspondence*, *Communications in Mathematical Physics* **217** (Mar, 2001) 595–622.

[53] P. K. Kovtun and A. O. Starinets, *Quasinormal modes and holography*, *Physical Review D* **72** (Oct, 2005) .

[54] J. Greensite, *An introduction to the confinement problem*. Springer, 01, 2011.

[55] S. Scherer and M. R. Schindler, *A chiral perturbation theory primer*, 2005.

[56] G. Aarts, *Introductory lectures on lattice qcd at nonzero baryon number*, *Journal of Physics: Conference Series* **706** (Apr, 2016) 022004.

[57] E. S. Bowman and J. I. Kapusta, *Critical points in the linear model with quarks*, *Physical Review C* **79** (Jan, 2009) .

[58] S. Ejiri, *Canonical partition function and finite density phase transition in lattice qcd*, *Physical Review D* **78** (Oct, 2008) .

[59] T. K. Nayak, *Phases of nuclear matter*, *Current Science* **103** (2012) 888–894.

[60] L. McLerran and R. D. Pisarski, *Phases of dense quarks at large*, *Nuclear Physics A* **796** (Nov, 2007) 83–100.

[61] M. G. Alford, A. Schmitt, K. Rajagopal and T. Schäfer, *Color superconductivity in dense quark matter*, *Reviews of Modern Physics* **80** (Nov, 2008) .

[62] V. G. Filev, C. V. Johnson, R. C. Rashkov and K. S. Viswanathan, *Flavoured largengauge theory in an external magnetic field*, *Journal of High Energy Physics* **2007** (Oct, 2007) 019–019.

[63] C. Hoyos, K. Landsteiner and S. Montero, *Holographic meson melting*, *Journal of High Energy Physics* **2007** (Apr, 2007) 031–031.

[64] J. Babington, J. Erdmenger, N. Evans, Z. Guralnik and I. Kirsch, *Chiral symmetry breaking and pions in nonsupersymmetric gauge/gravity duals*, *Physical Review D* **69** (Mar, 2004) .

[65] S. Kobayashi, D. Mateos, S. Matsuura, R. C. Myers and R. M. Thomson, *Holographic phase transitions at finite baryon density*, *Journal of High Energy Physics* **2007** (Feb, 2007) 016–016.

[66] G. Aarts, S. P. Kumar and J. Rafferty, *Holographic roberge-weiss transitions*, *Journal of High Energy Physics* **2010** (Jul, 2010) .

[67] A. Roberge and N. Weiss, *Gauge theories with imaginary chemical potential and the phases of qcd*, *Nuclear Physics B* **275** (1986) 734–745.

[68] J. Rafferty, *Holographic roberge weiss transitions ii: Defect theories and the sakai sugimoto model*, *Journal of High Energy Physics* **2011** (Sep, 2011) .

[69] F. Bigazzi and A. L. Cotrone, *Holographic qcd with dynamical flavors*, *Journal of High Energy Physics* **2015** (Jan, 2015) .

[70] H. Isono, G. Mandal and T. Morita, *Thermodynamics of qcd from sakai-sugimoto model*, *Journal of High Energy Physics* **2015** (Dec, 2015) 1–19.

[71] K. Ghoroku, K. Kashiwa, Y. Nakano, M. Tachibana and F. Toyoda, *Extension to imaginary chemical potential in a holographic model*, *Physical Review D* **102** (Aug, 2020) .

[72] D. Nickel, *Inhomogeneous phases in the nambu–jona-lasinio and quark-meson model*, *Physical Review D* **80** (Oct, 2009) .

[73] N. Kovensky and A. Schmitt, *Heavy holographic qcd*, *Journal of High Energy Physics* **2020** (Feb, 2020) .

[74] N. Evans, A. Gebauer, K.-Y. Kim and M. Magou, *Towards a holographic model of the qcd phase diagram*, *Journal of Physics G: Nuclear and Particle Physics* **39** (Apr, 2012) 054005.

[75] M. Gazdzicki, M. Gorenstein and P. Seyboth, *Brief history of the search for critical structures in heavy-ion collisions*, *Acta Physica Polonica B* **51** (2020) 1033.

[76] M. Kruczenski, D. Mateos, R. C. Myers and D. J. Winters, *Towards a holographic dual of large-ncqcd*, *Journal of High Energy Physics* **2004** (May, 2004) 041–041.

[77] K. B. Fadafan, J. C. Rojas and N. Evans, *Deconfined, massive quark phase at high density and compact stars: A holographic study*, *Physical Review D* **101** (Jun, 2020) .

[78] R. Bellwied, S. Borsanyi, Z. Fodor, J. Günther, S. D. Katz, C. Ratti et al., *The qcd phase diagram from analytic continuation*, 2015.

[79] Y. Yang and P.-H. Yuan, *Qcd phase diagram by holography*, 2020.

[80] C. Kittel, *Kittel's Introduction to Solid State Physics*. Wiley, 2018.

[81] D. Forster, *Hydrodynamic Fluctuations, Broken Symmetry, And Correlation Functions*. CRC Press, 2018.

[82] G. R. Stewart, *Unconventional superconductivity*, *Advances in Physics* **66** (Apr, 2017) 75–196.

[83] S. Adachi, Y. Murai and K. Tanabe, *Synthesis and characterization of (ba, sr)fe2(as, p)2 iron pnictide superconductors*, *Physica C: Superconductivity* **483** (Dec, 2012) 67–70.

[84] B. Yan and C. Felser, *Topological materials: Weyl semimetals*, *Annual Review of Condensed Matter Physics* **8** (Mar, 2017) 337–354.

[85] M. Z. Hasan, S.-Y. Xu, I. Belopolski and S.-M. Huang, *Discovery of weyl fermion semimetals and topological fermi arc states*, *Annual Review of Condensed Matter Physics* **8** (Mar, 2017) 289–309.

[86] A. Burkov, *Weyl metals*, *Annual Review of Condensed Matter Physics* **9** (Mar, 2018) 359–378.

[87] N. Armitage, E. Mele and A. Vishwanath, *Weyl and dirac semimetals in three-dimensional solids*, *Reviews of Modern Physics* **90** (Jan, 2018) .

[88] H. Gao, J. W. Venderbos, Y. Kim and A. M. Rappe, *Topological semimetals from first principles*, *Annual Review of Materials Research* **49** (Jul, 2019) 153–183.

[89] Z. Liu, L. Yang, Y. Sun, T. Zhang, H. Peng, H. Yang et al., *Evolution of the fermi surface of weyl semimetals in the transition metal pnictide family.*, *Nature materials* **15** (2016) 27–31.

[90] S.-Y. Xu, N. Alidoust, I. Belopolski, Z. Yuan, G. Bian, T.-R. Chang et al., *Discovery of a weyl fermion state with fermi arcs in niobium arsenide*, *Nature Physics* **11** (Aug, 2015) 748–754.

[91] I. Belopolski, S.-Y. Xu, D. S. Sanchez, G. Chang, C. Guo, M. Neupane et al., *Criteria for directly detecting topological fermi arcs in weyl semimetals*, *Physical Review Letters* **116** (Feb, 2016) .

[92] N. Morali, R. Batabyal, P. K. Nag, E. Liu, Q. Xu, Y. Sun et al., *Fermi-arc diversity on surface terminations of the magnetic weyl semimetal co3sn2s2*, *Science* **365** (2019) 1286–1291, [1903.00509].

[93] D. F. Liu, A. J. Liang, E. K. Liu, Q. N. Xu, Y. W. Li, C. Chen et al., *Magnetic weyl semimetal phase in a kagomé crystal*, *Science* **365** (2019) 1282–1285, [1909.09580].

[94] I. Belopolski, K. Manna, D. S. Sanchez, G. Chang, B. Ernst, J. Yin et al., *Discovery of topological weyl fermion lines and drumhead surface states in a room temperature magnet*, *Science* **365** (2019) 1278–1281, [2004.00004].

[95] X. Wan, A. M. Turner, A. Vishwanath and S. Y. Savrasov, *Topological semimetal and fermi-arc surface states in the electronic structure of pyrochlore iridates*, *Phys. Rev. B* **83** (May, 2011) 205101.

[96] H. Nielsen and M. Ninomiya, *Absence of neutrinos on a lattice: (ii). intuitive topological proof*, *Nuclear Physics B* **193** (1981) 173 – 194.

[97] F. D. Haldane, *Berry Curvature on the Fermi Surface: Anomalous Hall Effect as a Topological Fermi-Liquid Property*, *"Phys. Rev. Lett."* **93** (Nov., 2004) 206602, [cond-mat/0408417].

[98] D. Colladay and V. Kostelecky, *Lorentz violating extension of the standard model*, *Phys. Rev. D* **58** (1998) 116002, [hep-ph/9809521].

[99] A. G. Grushin, *Consequences of a condensed matter realization of Lorentz violating QED in Weyl semi-metals*, *Phys. Rev. D* **86** (2012) 045001, [1205.3722].

[100] P. Goswami and S. Tewari, *Axionic field theory of (3+1)-dimensional Weyl semimetals*, *Phys. Rev. B* **88** (2013) 245107, [1210.6352].

[101] B. Roy, P. Goswami and V. Juričić, *Interacting weyl fermions: Phases, phase transitions, and global phase diagram*, *Physical Review B* **95** (May, 2017) .

[102] C. Copetti, J. Fernández-Pendás and K. Landsteiner, *Axial Hall effect and universality of holographic Weyl semi-metals*, *JHEP* **02** (2017) 138, [1611.08125].

[103] Y. Liu and J. Zhao, *Weyl semimetal/insulator transition from holography*, *JHEP* **12** (2018) 124, [1809.08601].

[104] K. Landsteiner, Y. Liu and Y.-W. Sun, *Holographic topological semimetals*, *Sci. China Phys. Mech. Astron.* **63** (2020) 250001, [1911.07978].

[105] V. Juričić, I. Salazar Landea and R. Soto-Garrido, *Phase transitions in a holographic multi-Weyl semimetal*, *JHEP* **07** (2020) 052, [2005.10387].

[106] M. Ammon, M. Heinrich, A. Jiménez-Alba and S. Moeckel, *Surface States in Holographic Weyl Semimetals*, *Phys. Rev. Lett.* **118** (2017) 201601, [1612.00836].

[107] K. Landsteiner, Y. Liu and Y.-W. Sun, *Odd viscosity in the quantum critical region of a holographic Weyl semimetal*, *Phys. Rev. Lett.* **117** (2016) 081604, [1604.01346].

[108] M. Baggioli, B. Padhi, P. W. Phillips and C. Setty, *Conjecture on the Butterfly Velocity across a Quantum Phase Transition*, *JHEP* **07** (2018) 049, [1805.01470].

[109] G. Grignani, A. Marini, F. Pena-Benitez and S. Speziali, *AC conductivity for a holographic Weyl Semimetal*, *JHEP* **03** (2017) 125, [1612.00486].

[110] M. Ammon, M. Baggioli, A. Jiménez-Alba and S. Moeckel, *A smeared quantum phase transition in disordered holography*, *JHEP* **04** (2018) 068, [1802.08650].

[111] Y. Liu and Y.-W. Sun, *Topological invariants for holographic semimetals*, *JHEP* **10** (2018) 189, [1809.00513].

[112] M. Baggioli and D. Giataganas, *Detecting Topological Quantum Phase Transitions via the c-Function*, 2007.07273.

[113] K. Hashimoto, S. Kinoshita, K. Murata and T. Oka, *Holographic Floquet states I: a strongly coupled Weyl semimetal*, *JHEP* **05** (2017) 127, [1611.03702].

[114] S. Kinoshita, K. Murata and T. Oka, *Holographic Floquet states II: Floquet condensation of vector mesons in nonequilibrium phase diagram*, *JHEP* **06** (2018) 096, [1712.06786].

[115] U. Gursoy, V. Jacobs, E. Plauschinn, H. Stoof and S. Vandoren, *Holographic models for undoped Weyl semimetals*, *JHEP* **04** (2013) 127, [1209.2593].

[116] V. Jacobs, P. Betzios, U. Gursoy and H. Stoof, *Electromagnetic response of interacting Weyl semimetals*, *Phys. Rev. B* **93** (2016) 195104, [1512.04883].

[117] T. Faulkner and J. Polchinski, *Semi-Holographic Fermi Liquids*, *JHEP* **06** (2011) 012, [1001.5049].

[118] U. Gursoy, E. Plauschinn, H. Stoof and S. Vandoren, *Holography and ARPES Sum-Rules*, *JHEP* **05** (2012) 018, [1112.5074].

[119] P. Chesler and A. Vuorinen, *Heavy flavor diffusion in weakly coupled N=4 super Yang-Mills theory*, *JHEP* **11** (2006) 037, [hep-ph/0607148].

[120] J. Erdmenger, N. Evans, I. Kirsch and E. Threlfall, *Mesons in Gauge/Gravity Duals - A Review*, *Eur. Phys. J. A* **35** (2008) 81–133, [0711.4467].

[121] S. R. Das, T. Nishioka and T. Takayanagi, *Probe Branes, Time-dependent Couplings and Thermalization in AdS/CFT*, *JHEP* **07** (2010) 071, [1005.3348].

[122] C. Hoyos, T. Nishioka and A. O'Bannon, *A Chiral Magnetic Effect from AdS/CFT with Flavor*, *JHEP* **10** (2011) 084, [1106.4030].

[123] D. E. Kharzeev and H.-U. Yee, *Chiral helix in AdS/CFT with flavor*, *Phys. Rev. D* **84** (2011) 125011, [1109.0533].

[124] Y. Bu and S. Lin, *Holographic magnetized chiral density wave*, *Chin. Phys. C* **42** (2018) 114104, [1807.00330].

[125] K. Hashimoto and T. Oka, *Vacuum Instability in Electric Fields via AdS/CFT: Euler-Heisenberg Lagrangian and Planckian Thermalization*, *JHEP* **10** (2013) 116, [1307.7423].

[126] K. Hashimoto, T. Oka and A. Sonoda, *Magnetic instability in AdS/CFT: Schwinger effect and Euler-Heisenberg Lagrangian of supersymmetric QCD*, *JHEP* **06** (2014) 085, [1403.6336].

[127] K. Hashimoto, T. Oka and A. Sonoda, *Electromagnetic instability in holographic QCD*, *JHEP* **06** (2015) 001, [1412.4254].

[128] A. Karch and A. O'Bannon, *Metallic AdS/CFT*, *JHEP* **09** (2007) 024, [0705.3870].

[129] A. O'Bannon, *Hall Conductivity of Flavor Fields from AdS/CFT*, *Phys. Rev. D* **76** (2007) 086007, [0708.1994].

[130] S. Gubser, I. R. Klebanov and A. Peet, *Entropy and temperature of black 3-branes*, *Phys. Rev. D* **54** (1996) 3915–3919, [hep-th/9602135].

[131] V. G. Filev, C. V. Johnson, R. Rashkov and K. Viswanathan, *Flavoured large N gauge theory in an external magnetic field*, *JHEP* **10** (2007) 019, [hep-th/0701001].

[132] C. Hoyos-Badajoz, K. Landsteiner and S. Montero, *Holographic meson melting*, *JHEP* **04** (2007) 031, [hep-th/0612169].

[133] V. P. Frolov, A. Larsen and M. Christensen, *Domain wall interacting with a black hole: A New example of critical phenomena*, *Phys. Rev. D* **59** (1999) 125008, [hep-th/9811148].

[134] V. P. Frolov, *Merger Transitions in Brane-Black-Hole Systems: Criticality, Scaling, and Self-Similarity*, *Phys. Rev. D* **74** (2006) 044006, [gr-qc/0604114].

[135] A. Karch, A. O'Bannon and L. G. Yaffe, *Critical Exponents from AdS/CFT with Flavor*, *JHEP* **09** (2009) 042, [0906.4959].

[136] K. Bitaghsir Fadafan, J. Cruz Rojas and N. Evans, *Holographic description of color superconductivity*, *Phys. Rev. D* **98** (2018) 066010, [1803.03107].

[137] A. Cherman, T. D. Cohen and A. Nellore, *A Bound on the speed of sound from holography*, *Phys. Rev. D* **80** (2009) 066003, [0905.0903].

[138] A. Kundu, *Effective Thermal Physics in Holography: A Brief Review*, 1812.09447.

[139] A. Kundu, *Steady States, Thermal Physics, and Holography*, *Adv. High Energy Phys.* **2019** (2019) 2635917.

[140] J. Sonner, *Holographic Schwinger Effect and the Geometry of Entanglement*, *Phys. Rev. Lett.* **111** (2013) 211603, [1307.6850].

[141] A. O'Bannon, J. Probst, R. Rodgers and C. F. Uhlemann, *First law of entanglement rates from holography*, *Phys. Rev. D* **96** (2017) 066028, [1612.07769].

[142] C. V. Johnson, *D-brane primer*, in *Theoretical Advanced Study Institute in Elementary Particle Physics (TASI 99): Strings, Branes, and Gravity*, pp. 129–350, 7, 2000, hep-th/0007170, DOI.

[143] S. Nakamura, *Negative Differential Resistivity from Holography*, *Prog. Theor. Phys.* **124** (2010) 1105–1114, [1006.4105].

[144] D. T. Son and B. Z. Spivak, *Chiral anomaly and classical negative magnetoresistance of weyl metals*, *Physical Review B* **88** (Sep, 2013) .

[145] M. Ammon, T. H. Ngo and A. O'Bannon, *Holographic Flavor Transport in Arbitrary Constant Background Fields*, *JHEP* **10** (2009) 027, [0908.2625].

[146] A. Baumgartner, A. Karch and A. Lucas, *Magnetoresistance in relativistic hydrodynamics without anomalies*, *JHEP* **06** (2017) 054, [1704.01592].

[147] A. Karch, A. O'Bannon and K. Skenderis, *Holographic renormalization of probe D-branes in AdS/CFT*, *JHEP* **04** (2006) 015, [hep-th/0512125].

[148] A. Karch and A. O'Bannon, *Chiral transition of N=4 super Yang-Mills with flavor on a 3-sphere*, *Phys. Rev. D* **74** (2006) 085033, [hep-th/0605120].

[149] C. Hoyos, A. O'Bannon and J. M. Wu, *Transport and zero sound in holographic strange metals*, *J. Phys. Conf. Ser.* **287** (2011) 012029.

[150] L. P. Kadanoff and P. C. Martin, *Hydrodynamic equations and correlation functions*, *Annals of Physics* **24** (1963) 419–469.

[151] S. Grozdanov, P. K. Kovtun, A. O. Starinets and P. Tadić, *The complex life of hydrodynamic modes*, *Journal of High Energy Physics* **2019** (Nov, 2019) .

[152] M. Baggioli, *How small hydrodynamics can go*, 2021.

[153] W. R. Abel, A. C. Anderson and J. C. Wheatley, *Propagation of zero sound in liquid* he^3 *at low temperatures*, *Phys. Rev. Lett.* **17** (Jul, 1966) 74–78.

[154] M. Kulaxizi and A. Parnachev, *Remarks on fermi liquid from holography*, *Physical Review D* **78** (Oct, 2008) .

[155] M. Kulaxizi and A. Parnachev, *Holographic responses of fermion matter*, *Nuclear Physics B* **815** (Jul, 2009) 125–141.

[156] K.-Y. Kim and I. Zahed, *Baryonic response of dense holographic qcd*, *Journal of High Energy Physics* **2008** (Dec, 2008) 075–075.

[157] A. Karch, D. T. Son and A. O. Starinets, *Holographic quantum liquid*, *Phys. Rev. Lett.* **102** (Feb, 2009) 051602.

[158] M. Kaminski, K. Landsteiner, J. Mas, J. P. Shock and J. Tarrío, *Holographic operator mixing and quasinormal modes on the brane*, *Journal of High Energy Physics* **2010** (Feb, 2010) .

[159] M. Edalati, J. I. Jottar and R. G. Leigh, *Holography and the sound of criticality*, *Journal of High Energy Physics* **2010** (Oct, 2010) .

[160] C. Hoyos, A. O'Bannon and J. M. S. Wu, *Zero sound in strange metallic holography*, *Journal of High Energy Physics* **2010** (Sep, 2010) .

[161] D. Nickel and D. T. Son, *Deconstructing holographic liquids*, *New Journal of Physics* **13** (Jul, 2011) 075010.

[162] B.-H. Lee, D.-W. Pang and C. Park, *Zero sound in effective holographic theories*, *Journal of High Energy Physics* **2010** (Nov, 2010) .

[163] M. Ammon, J. Erdmenger, S. Lin, S. Müller, A. O'Bannon and J. P. Shock, *On stability and transport of cold holographic matter*, *Journal of High Energy Physics* **2011** (Sep, 2011) .

[164] R. A. Davison and A. O. Starinets, *Holographic zero sound at finite temperature*, *Physical Review D* **85** (Jan, 2012) .

[165] R. A. Davison and N. K. Kaplis, *Bosonic excitations of the ads 4 reissner-nordstrom black hole*, *Journal of High Energy Physics* **2011** (Dec, 2011) .

[166] N. Jokela, G. Lifschytz and M. Lippert, *Magnetic effects in a holographic fermi-like liquid*, *Journal of High Energy Physics* **2012** (May, 2012) .

[167] M. Goykhman, A. Parnachev and J. Zaanen, *Fluctuations in finite density holographic quantum liquids*, *Journal of High Energy Physics* **2012** (Oct, 2012) .

[168] D. K. Brattan, R. A. Davison, S. A. Gentle and A. O'Bannon, *Collective excitations of holographic quantum liquids in a magnetic field*, *Journal of High Energy Physics* **2012** (Nov, 2012) .

[169] N. Jokela, M. Järvinen and M. Lippert, *Fluctuations and instabilities of a holographic metal*, *Journal of High Energy Physics* **2013** (Feb, 2013) .

[170] D.-W. Pang, *Probing holographic semilocal quantum liquids with d-branes*, *Physical Review D* **88** (Aug, 2013) .

[171] P. Dey and S. Roy, *Zero sound in strange metals with hyperscaling violation from holography*, *Physical Review D* **88** (Aug, 2013) .

[172] M. Edalati and J. F. Pedraza, *Aspects of current correlators in holographic theories with hyperscaling violation*, *Physical Review D* **88** (Oct, 2013) .

[173] D. K. Brattan and G. Lifschytz, *Holographic plasma and anyonic fluids*, *Journal of High Energy Physics* **2014** (Feb, 2014) .

[174] R. A. Davison, M. Goykhman and A. Parnachev, *Ads/cft and landau fermi liquids*, *Journal of High Energy Physics* **2014** (Jul, 2014) .

[175] B. S. DiNunno, M. Ihl, N. Jokela and J. F. Pedraza, *Holographic zero sound at finite temperature in the sakai-sugimoto model*, *Journal of High Energy Physics* **2014** (Apr, 2014) .

[176] N. Jokela and A. V. Ramallo, *Universal properties of cold holographic matter*, *Physical Review D* **92** (Jul, 2015) .

[177] G. Itsios, N. Jokela and A. V. Ramallo, *Collective excitations of massive flavor branes*, *Nuclear Physics B* **909** (Aug, 2016) 677–724.

[178] N. Jokela, J. Järvelä and A. V. Ramallo, *Non-relativistic anyons from holography*, *Nuclear Physics B* **916** (Mar, 2017) 727–768.

[179] S. A. Hartnoll, A. Lucas and S. Sachdev, *Holographic quantum matter*, 2018.

[180] D. Roychowdhury, *Probing deformed backgrounds with dp branes*, *Physics Letters B* **778** (Mar, 2018) 167–173.

[181] C.-F. Chen and A. Lucas, *Origin of the drude peak and of zero sound in probe brane holography*, *Physics Letters B* **774** (Nov, 2017) 569–574.

[182] N. I. Gushterov, A. O'Bannon and R. Rodgers, *Holographic zero sound from spacetime-filling branes*, *Journal of High Energy Physics* **2018** (Oct, 2018) .

[183] M. Baggioli, M. Vasin, V. V. Brazhkin and K. Trachenko, *Gapped momentum states*, *Phys. Rept.* **865** (2020) 1–44, [1904.01419].

[184] S. de Haro, S. N. Solodukhin and K. Skenderis, *Holographic reconstruction of space-time and renormalization in the AdS / CFT correspondence*, *Commun. Math. Phys.* **217** (2001) 595–622, [hep-th/0002230].

[185] M. Bianchi, D. Z. Freedman and K. Skenderis, *Holographic renormalization*, *Nucl. Phys. B* **631** (2002) 159–194, [hep-th/0112119].

[186] I. Papadimitriou and K. Skenderis, *AdS / CFT correspondence and geometry*, *IRMA Lect. Math. Theor. Phys.* **8** (2005) 73–101, [hep-th/0404176].

[187] I. Papadimitriou, *Holographic renormalization as a canonical transformation*, *JHEP* **11** (2010) 014, [1007.4592].

[188] J. Mas, J. P. Shock and J. Tarrío, *A note on conductivity and charge diffusion in holographic flavor systems*, *Journal of High Energy Physics* **2009** (Jan, 2009) 025–025.

[189] S. Grozdanov, A. Lucas, S. Sachdev and K. Schalm, *Absence of disorder-driven metal-insulator transitions in simple holographic models*, *Physical Review Letters* **115** (Nov, 2015) .

[190] T. N. Ikeda, A. Lucas and Y. Nakai, *Conductivity bounds in probe brane models*, *Journal of High Energy Physics* **2016** (Apr, 2016) 1–18.

[191] A. Karch and A. O'Bannon, *Metallic ads/cft*, *Journal of High Energy Physics* **2007** (Sep, 2007) 024–024.

[192] C. de Rham, G. Gabadadze and A. J. Tolley, *Resummation of massive gravity*, *Physical Review Letters* **106** (Jun, 2011) .

[193] M. Blake and D. Tong, *Universal Resistivity from Holographic Massive Gravity*, *Phys. Rev. D* **88** (2013) 106004, [1308.4970].

[194] L.-M. Cao and Y. Peng, *Counterterms in Massive Gravity Theory*, *Phys. Rev. D* **92** (2015) 124052, [1509.08738].

[195] M. Taylor and W. Woodhead, *Inhomogeneity simplified*, *Eur. Phys. J. C* **74** (2014) 3176, [1406.4870].

[196] S. El-Showk and K. Papadodimas, *Emergent spacetime and holographic cfts*, *Journal of High Energy Physics* **2012** (Oct, 2012) .

[197] F. Aprile, J. M. Drummond, H. Paul and M. Santagata, *The virasoro-shapiro amplitude in ads$_5\times s^5$ and level splitting of 10d conformal symmetry*, 2020.

[198] A. Almheiri, X. Dong and D. Harlow, *Bulk locality and quantum error correction in ads/cft*, *Journal of High Energy Physics* **2015** (Apr, 2015) .

[199] G. Penington, *Entanglement wedge reconstruction and the information paradox*, 2020.

[200] A. Almheiri, N. Engelhardt, D. Marolf and H. Maxfield, *The entropy of bulk quantum fields and the entanglement wedge of an evaporating black hole*, *Journal of High Energy Physics* **2019** (Dec, 2019) .